



**Nanoscale and macroscale characterization of the dielectric  
charging phenomenon and stiction mechanisms for  
electrostatic MEMS/NEMS reliability**

by

**Usama Zaghoul Heiba**

A thesis submitted to  
THE UNIVERSITY OF TOULOUSE  
Université Toulouse III - Paul Sabatier  
in partial satisfaction of the requirements for the degree of

Doctor of Philosophy

in

Electrical Engineering, Electronics, and Telecommunications  
Discipline: Design of microelectronic circuits and Microsystems

Research unit: LAAS-CNRS, MINC group  
(Micro and Nano-systems for Wireless Telecommunication)

Toulouse 2011





# THÈSE

En vue de l'obtention du

**DOCTORAT DE L'UNIVERSITÉ DE TOULOUSE**

Délivré par l'Université Toulouse III - Paul Sabatier

Discipline: Conception des Circuits Microélectroniques et Microsystèmes

**Présentée et soutenue par Usama Zaghoul Heiba**

**Caractérisation à l'échelle nanométrique et macroscopique, des phénomènes de chargement des diélectriques et des mécanismes d'adhérence pour la fiabilité des micro-nano systèmes à actionnement électrostatique**

Ecole Doctorale: Génie Electrique, Electronique, Télécommunications (GEET)

Unité de recherche: LAAS-CNRS, groupe MINC

(Micro et Nanosystèmes pour les Communications sans fils)

Toulouse 2011



## **COMPOSITION DU JURY**

### **DIRECTEUR DE THÈSE**

Robert PLANA, Professeur, Université Paul Sabatier, LAAS-CNRS

Co-Directeur: Fabio COCCETTI, Docteur, NOVAMEMS, Toulouse

### **RAPPORTEURS**

Ingrid DE WOLF, Professeur, Catholic University of Leuven, Belgique

Pierre BLONDY, Professeur, Université de Limoges, XLIM-CNRS

### **EXAMINATEURS**

Bharat BHUSHAN, Professeur, The Ohio State University, USA

George PAPAIOANNOU, Professeur, University of Athens, Greece

Didier THERON, Directeur de Recherche, IEMN-CNRS, Lille

Olivier VENDIER, Docteur, Thales Alenia Space, Toulouse

### **MEMBRES**

Patrick PONS, Chargé de Recherche, LAAS-CNRS

Thesis submitted to The University of Toulouse for the degree of Doctor of Philosophy

*This thesis is dedicated to*

*My Parents*

*My Wife*

*and*

*My Lovely Daughter, Noor*

### Acknowledgements

When I decided to go for the Ph.D. and leave industry, SoftMEMS, back in May 2007, my main goal was to make a different and high-level thesis, and this is what I kept telling myself all the time during the last four years. Today, I'm so happy that the defense committee recommends my thesis for the competition of the annual prize of the Ecole Doctoral in France. I tried hard to report most of the results we had, and I only omitted the secrets behind each characterization method we proposed for a possible Startup in the future. I hope you find this thesis interesting.

Well, the work presented in this thesis is basically the outcome of a very fruitful cooperation between three distinguished institutions. The first one is the Laboratory for Analysis and Architecture of Systems (LAAS - CNRS) in Toulouse, France under the supervision of Prof. Robert Plana, Dr. Fabio Coccetti, and Dr. Patrick Pons. The second institution is the Nanoprobe Laboratory for Bio- and Nanotechnology & Biomimetics (NLBB), The Ohio State University in Columbus, Ohio, USA under the guidance of Prof. Bharat Bhushan. The third one is the Physics Department, Solid State Physics Section of the University of Athens, Greece under the supervision of Prof. George Papaioannou. I consider myself very fortunate to work closely with these big names and to learn a lot from their own experiences, both personally and scientifically. I met Robert in July 2007 during the AMICOM summer school where he offered me a Ph.D. scholarship in his wonderful group, MINC. Thank you Robert for your trust! One thing I like a lot about Robert is his strategic view and brilliant guidance. As a student with young experience and thinking only from his point view, it is common to face some difficulties and to commit some mistakes. So do I, especially in the beginning of my Ph.D. Here, I found Fabio and Patrick always giving me a hand to overcome that and to keep going forward. One phrase I learned from Fabio was "*think always about time, schedule, and plan*" while from Patrick I learned "*how to think from different views and simply put myself in others' shoes*". Thank you, Fabio and Patrick!

I started the Ph.D. research in January 2008, and now I find it obvious to divide this period into two main stages. The first stage is from the beginning until November 2009 where the work was done mainly at LAAS with continuous support from George, while the second stage starts from December 2009 to June 2011 where I joined NLBB, which I consider the key turning point in my Ph.D. During the first stage, I went through an intensive training on the fabrication process of MEMS switches, followed by fabricating the investigated samples used in this study including bare dielectrics, MIM capacitors, and MEMS switches in the clean room of LAAS. While working with technology, I had wonderful help and guidance from my colleagues in the clean room, Dr. Christina Villeneuve, Laurent Bouscayrol, David Bourrier, Samuel Charlot, and Pierre-François Calmon. Our initial trials for the KPFM measurements were also done during this stage, where I had preliminary instructions from my previous colleague, Dr.

Aissa Belarni, followed by an extensive training given by Veeco (now Bruker) with Mickael Febvre. The DCT measurements were also done at LAAS during this stage where I had unique support from Nicolas Mauran, while the TSDC measurements were performed at the University of Athens by my colleagues there, mainly Matroni Koutsourelis (Roni). Later, while at Athens, Roni gave me comprehensive training on this kind of measurements, followed by conducting several measurements together. Thank you, Roni, for your efforts and kind help while at Greece. The correlation between the different characterization techniques was made for the first time during this stage as well. Throughout this work, I have always had concrete guidance from George who introduced me to the field of Solid state physics and who was pushing me all the time to *'think in-depth'* and to *'understand'* the physics behind each single result we had. I really found it very interesting and fruitful to work with him; thank you so much, George. A special thanks is given to my LAAS colleague, Dr Haixia Wang. Her deep knowledge in material science was very helpful in understanding the behavior of the different dielectric materials we investigated. We have done also a lot of work related to the packaging of RF MEMS devices which is beyond the scope of the present thesis and so it was not included in this manuscript.

The major turning point in my Ph.D. was actually in September 2009 when Patrick introduced me to Prof. Bhushan where the second stage of my Ph.D. started. Since December 2009, I have had several long internships at NLBB. During these internships, the actual KPFM based characterization methods were developed and optimized under controlled environments and were used to study the effect of numerous parameters on charging. Moreover, the influence of environment gases, humidity, and contaminants was investigated using KPFM for the first time there. The different stiction mechanisms were also studied in-depth for the first time during this period. Finally, the FDC based characterization techniques were invented at NLBB. The beauty in NLBB is that one has the chance to interact with experts from different scientific domains: chemistry, physics, material science, electrical and mechanical engineering, which certainly helps to have a broad view of the research topic one is tackling, and consequently, pushes one forward to think differently. Basically, more than 90 % from the results presented in this thesis comes from those multiple visits to NLBB. Such an amount of work has been achieved in a very limited time thanks to the high support from Prof. Bhushan who gave me the chance to access the AFMs for very long durations, in some cases for continuous weeks. I have even done many other measurements there which are not included in the thesis because there was no time for the data analysis. While at NLBB, I attended two impressive courses taught by Prof. Bhushan related to Bio/Nanotechnology, Biomimetics, and Nanotribology where I really learned a lot. Thank you, Prof. Bhushan, for your wonderful support, for teaching me the art of writing a high-quality paper, and for opening my eyes to this fascinating world, Nanotechnology and Nanotribology! I'm also very grateful to my colleagues there at NLBB, Dr. Manuel Palacio (Manny) and Dr. Hyungoo Lee, for the intensive training they gave me on numerous kinds of AFM measurements. Well, I'm not a native English speaker and I consider myself lucky to have our wonderful secretary Caterina Runyon-Spears correcting the English of all papers I have written, the thing which helps me improving my technical writing skills. Thank you, Caterina!

## ACKNOWLEDGEMENTS

---

On the personal side, I believe no one can live a happy and successful life without sharing love with family members. While at France or USA, I have always my small family with me, my wife and my lovely daughter, Noor. I remember well how much my wife suffered being alone with our baby in foreign countries while I'm always at work. I even had to leave her shortly after putting our first child there at Columbus to go to the lab for urgent measurements! Back to my home country, Egypt, I have there a wonderful and large family. I'm really grateful to my parents, brothers, and sisters for their love and continuous support. Thank you all, and I promise to give you more time in the future.

Finally, the financial support for this work came from the following projects: the French ANR project FAME (PNANO-059), POLYNOE project funded by European Defense Agency (B-0035-IAP1-ERG), and the SYMIAE project funded by the Fondation STAE. Much of the funding for my stay and research at NLBB in Columbus, Ohio, was provided by the NLBB laboratory.

USAMA ZAGHLOUL HEIBA

Usama.zaghloul@ieee.org

Toulouse, France

September 2011



Université  
de Toulouse



Université  
Paul Sabatier  
T O U L O U S E

DOCTORAT DE L'UNIVERSITE DE TOULOUSE  
délivré par l'Université Toulouse III – Paul Sabatier

Spécialité : *Génie Électrique, Électronique,  
Télécommunications*

RAPPORT DE SOUTENANCE

Nom du (ou de la) candidat(e) : *Usama ZAGHLOUL HEIBA*  
Date de soutenance : *16 septembre 2011*  
Président du jury : *Didier THERON*

The jury appreciated the excellent presentation of Mr Usama ZAGHLOUL HEIBA. It was a clear, didactical and synthetic communication of the results obtained during his PhD work. It also translated the large amount of work in the multi-disciplinary domain of nanocharacterization and MEMS devices. The presentation was very dynamic and the jury was convinced of the scientific maturity that the candidate has reached today.

Mr ZAGHLOUL answered to all the question with a lot of detailed arguments and a complete honesty. He was very fluent, explained very easily his arguments and was completely open to the discussion. Here again the jury was convinced that the candidate had a deep understanding and a full master of his research field. During the deliberation, the jury unanimously recommended without hesitation his work to the competition for the prize of the "Ecole Doctorale".

Le jury a apprécié l'excellente présentation de Mr Usama ZAGHLOUL HEIBA. Les résultats de son travail de thèse ont été communiqués de façon très claire, didactique et synthétique. Cette présentation a témoigné de la grande quantité de travail effectué dans le domaine multi-disciplinaire de la nanocaractérisation et des composants MEMS. Elle a également témoigné du dynamisme du candidat et le jury a pu constater la maturité scientifique qu'il a acquis désormais.

Mr ZAGHLOUL a répondu à toutes les questions de façon très détaillée et avec une parfaite honnêteté. La discussion a été très ouverte et le candidat a montré une très grande aisance dans l'expression de ses arguments. Le jury a ainsi constaté la profonde compréhension et la maîtrise de son domaine de recherche. Lors de la délibération, le jury a recommandé de façon unanime et sans aucune hésitation que son travail participe au concours pour le prix de l'Ecole Doctorale.

Le diplôme national de Docteur est délivré par l'Université Toulouse III – Paul Sabatier sans aucune mention.

Les Membres du Jury :

Nom	Signature	Nom	Signature
<i>Ingrid De Wolf</i>	<i>[Signature]</i>	Blondy	<i>[Signature]</i>
PLATA Robert	<i>[Signature]</i>	A. Papaioannou	<i>[Signature]</i>
Bhavat Bhushan	<i>[Signature]</i>	Olivia Vendin	<i>[Signature]</i>
Fabio COCCETTI	<i>[Signature]</i>	THERON Didier	<i>[Signature]</i>

## **Abstract**

The reliability of electrostatically actuated micro- and nano-electromechanical systems (MEMS and NEMS) is determined by several failure modes which originate from different failure mechanisms. Among various reliability concerns, the dielectric charging constitutes major failure mechanism which inhibits the commercialization of several electrostatic MEMS devices. In electrostatic capacitive MEMS switches, for example, the charging phenomenon results in shifting the electrical characteristics and leads to stiction causing the device failure. In spite of the extensive study done on this topic, a comprehensive understanding of the charging phenomenon and its relevant failure mechanisms are still missing. The characterization techniques employed to investigate this problem, though useful, have serious limitations in addition to the missing correlation between their results. On the other hand, recent studies show that tribological phenomena such as adhesion and friction are crucial in MEMS/NEMS devices requiring relative motion and could affect their performance. Since the operation of MEMS switch is based on intermittent contact between two surfaces, the movable electrode and the dielectric, critical tribological concerns may also occur at the interface and influence the device reliability. These concerns have not been investigated before, and consequently, micro/nanotribological studies are needed to develop a fundamental understanding of these interfacial phenomena. Also, the multiphysics coupling between the charging phenomena and those expected tribological effects needs to be studied.

This thesis addresses the abovementioned weaknesses and presents numerous novel characterization techniques to study the charging phenomenon based on Kelvin probe force microscopy (KPFM) and, for the first time, force-distance curve (FDC) measurements. These methods were used to study plasma-enhanced chemical vapor deposition (PECVD) silicon nitride films for application in electrostatic capacitive MEMS switches. The proposed methods are performed on the nanoscale and take the advantage of the atomic force microscope (AFM) tip to simulate a single asperity contact between the switch movable electrode and the dielectric surface. Different device structures were characterized including bare dielectric films, MIM capacitors, and MEMS switches. In addition, the charge/discharge current transients (C/DCT) and thermally stimulated depolarization current (TSDC) assessment methods were used to study the charging/discharging processes in metal-insulator-metal (MIM) capacitors. A comparison

and correlation between the results from the investigated characterization techniques were performed. Moreover, a correlation between the obtained nanoscale/macroscale results and the literature reported data obtained from device level measurements of actual MEMS devices was made.

The influence of several key parameters on the charging/discharging processes was investigated. This includes the impact of the dielectric film thickness, dielectric deposition conditions, and substrate. SiN<sub>x</sub> films with different thicknesses were deposited over metal layers and over silicon substrates to study the effect of the dielectric thickness. The impact of the dielectric deposition conditions was investigated through depositing SiN<sub>x</sub> films using different gas ratio, temperature, power, and RF modes. To study the influence of the substrate, SiN<sub>x</sub> layers were deposited on evaporated gold, electrochemically-deposited gold, evaporated titanium layers, and over bare silicon substrates. Fourier transform infra-red spectroscopy (FT-IR) and X-ray photoelectron spectroscopy (XPS) material characterization techniques were used to determine the chemical bonds and compositions, respectively, of the investigated SiN<sub>x</sub> films. The obtained data from these techniques were used to explain the electrical characterization results. The impact of electrical charge injection conditions, which are the voltage amplitude, polarity and duration, was also explored. Finally, the influence of the relative humidity, environment medium, and contaminants on the charging phenomenon was studied.

Furthermore, the thesis investigates different tribological phenomena at the interface between the two contacting surfaces of electrostatic MEMS switches as well as their multiphysics coupling with the dielectric charging failure mechanism. The adhesive and friction forces were measured on the nanoscale under different electrical stress conditions and relative humidity levels using an AFM to study different stiction mechanisms. In these devices, stiction can be caused by two main mechanisms: dielectric charging and meniscus formation resulting from the adsorbed water layer at the interface. The effect of each mechanism as well as their multiphysics interaction and impact on the overall adhesion or stiction was quantified. Finally, the impact of the dielectric charging on the friction force between the two contacting surfaces of the switch has been studied.

## Résumé

Les phénomènes de chargement des diélectriques constituent l'un des principaux mécanismes de défaillance des microsystèmes à actionnement électrostatique, ce qui limite la commercialisation de ce type de dispositifs. Par exemple, dans le cas de micro-commutateurs capacitifs ce chargement entraîne des problèmes de collage entre la membrane actionnable et la surface du diélectrique qui recouvre l'électrode d'actionnement. Malgré de nombreux travaux réalisés dans le monde, les phénomènes de chargement des diélectriques sont encore mal compris aujourd'hui et les mécanismes de défaillances associés peu explicités. Par ailleurs de nombreuses méthodes de caractérisation ont été développées afin d'étudier ces phénomènes : capacité/tension dans les micro-commutateurs capacitifs, courant/tension dans les capacités MIM (Métal-Isolant-Métal). Bien que très souvent utilisées, ces méthodes donnent des résultats qui dépendent fortement de la nature du dispositif utilisé. Dans les capacités MIM par exemple, la décharge a lieu en situation de court-circuit et les charges injectées dans le diélectrique sont collectées seulement par l'électrode qui a servi à réaliser l'injection. Cette configuration est l'inverse de celle qui a lieu réellement dans les microsystèmes pour lesquels les charges sont injectées par la membrane actionnable et collectées par l'électrode d'actionnement, puisque la membrane ne touche pas le diélectrique lorsque la tension est supprimée. Par ailleurs les mécanismes de défaillances sont souvent liées à des phénomènes multi-physiques (électrique, mécanique, thermique). Ainsi le chargement des diélectriques peut être couplé notamment à des problèmes de fatigue mécanique de la membrane, ce qui peut fausser les interprétations. Des études récentes ont par ailleurs montré que les phénomènes tribologiques, comme l'adhésion et la friction, sont cruciaux pour les MEMS/NEMS et peuvent affecter radicalement leurs performances. Les micro-commutateurs RF étant basés sur le contact intermittent entre deux surfaces (membrane métallique et diélectrique), la fiabilité des ces composants est également impactée par ces phénomènes de surface. Des études sur la micro-nanotribologie appliquée aux micro-commutateurs RF sont donc nécessaires pour comprendre les phénomènes qui se passent aux interfaces et pour coupler ces phénomènes avec le chargement des diélectriques.

Les travaux sur le chargement des diélectriques présentés dans ce mémoire sont basés sur la microscopie à force atomique (KPFM, FDC) et permettent de supprimer les inconvénients des méthodes conventionnelles. Le diélectrique étudié est le nitrure de silicium obtenu par PECVD

pour des micro-commutateurs RF à contact capacitif. Les méthodes utilisées permettent de réaliser l'étude des diélectriques à l'échelle nanométrique grâce à l'utilisation de l'AFM dont la dimension de la pointe est comparable aux aspérités des microstructures. Différentes structures de tests ont été caractérisées incluant des films diélectriques, des capacités MIM et des micro-commutateurs. La pointe de l'AFM est utilisée pour réaliser l'injection des charges (comme dans le cas d'une aspérité en contact avec le diélectrique), mais également pour mesurer le potentiel de surface et la force d'adhésion. Les résultats obtenus ont été comparés à des mesures de charges et décharges plus conventionnelles sur des capacités MIM et sur des micro-commutateurs RF. Tous ces résultats ont également été comparés à des données de la littérature provenant de différents composants.

L'influence de plusieurs paramètres clés sur le chargement des diélectriques a également été étudiée. Différentes épaisseurs de  $\text{SiN}_x$  déposées sur de l'or (évacués et électrodéposés), sur du Titane et sur du silicium ont été analysées. Différents modes d'élaboration du  $\text{SiN}_x$  PECVD ont été utilisés en changeant le ratio des gaz, la température de dépôt, la puissance et la fréquence RF. Des analyses physico-chimiques ont également été menées pour déterminer les liaisons chimiques et les compositions des films de  $\text{SiN}_x$  (FTIR, XPS). Ces données ont été utilisées pour expliquer les résultats électriques obtenus. Différentes conditions de chargement ont également été explorées : amplitude, durée et polarité de la tension, taux d'humidité, contamination dues aux hydro-carbones. Les différents phénomènes tribologiques (adhésion, friction) ont aussi été étudiés à l'échelle nanométrique sous différentes tensions et pour différents taux d'humidité. A partir de ces études, deux principaux mécanismes de collage dans les microsystèmes à actionnement électrostatique ont ainsi été explicités : le chargement des diélectriques et la formation d'un ménisque d'eau. L'interaction entre ces deux mécanismes a également été mise en évidence et a permis de mieux comprendre les phénomènes de collage dans les MEMS à actionnement électrostatique.

*It is important that students bring a certain ragamuffin, barefoot irreverence to their studies; they are not here to worship what is known, but to question it.*

*Jacob Bronowski  
1908 – 1974, British mathematician and biologist  
in “The Ascent of Man”*

## Contents

Acknowledgements.....	iv
Abstract.....	viii
Résumé.....	x
List of papers.....	xvi
1 Thesis organisation .....	1
2 Review of present knowledge.....	3
2.1 Introduction .....	3
2.2 General introduction to MEMS Reliability .....	3
2.3 Reliability of electrostatic MEMS switches.....	6
2.4 Dielectric polarization/charging.....	10
2.4.1 Polarization/Charging mechanisms .....	10
2.4.2 Charge injection mechanisms .....	12
2.5 Investigated dielectric materials in electrostatic MEMS.....	15
2.6 Available characterization techniques for the dielectric charging .....	17
2.6.1 MEMS-based characterization methods .....	17
2.6.2 MIM-based characterization methods.....	18
2.6.3 KPFM-based characterization.....	19
2.7 State-of-the-art knowledge and open issues.....	21
2.7.1 Effect of dielectric deposition conditions on charging .....	21
2.7.2 Effect of substrate charging .....	22
2.7.3 Effect of packaging environment.....	22
2.7.4 Effect of tribological phenomena.....	23
2.8 Summary and motivation .....	25
3 Experimental context .....	27
3.1 Introduction .....	27
3.2 Investigated samples .....	27
3.3 KPFM-based characterization .....	33
3.3.1 KPFM theory .....	33
3.3.2 KPFM-TF technique .....	36

3.3.3	KPFM measurement parameters.....	37
3.3.4	KPFM-MEMS, KPFM-MIM characterization techniques .....	42
3.4	FDC-based characterization .....	44
3.4.1	Induced adhesive force and surface potential measurements using FDC.....	44
3.4.2	FDC-based different characterization techniques.....	46
3.4.3	Environment control system .....	49
3.5	DCT-based characterization.....	50
3.5.1	Charge/discharge current transient (C/DCT).....	50
3.5.2	Thermally Stimulated Depolarization Current (TSDC).....	51
3.6	Physical material characterization.....	52
3.7	Summary .....	53
4	Correlation and comparison between electrical characterization techniques .....	54
4.1	Introduction .....	54
4.2	DCT-based assessment methods .....	54
4.3	KPFM-based characterization and correlation to DCT.....	57
4.3.1	KPFM-TF: example of results and the influence of the AFM tip.....	58
4.3.2	Correlation between KPFM and DCT based methods.....	59
4.4	FDC-based characterization techniques .....	65
4.4.1	Experimental .....	65
4.4.2	FDC-TF results .....	66
4.4.3	FDC-MIM results.....	70
4.4.4	FDC-MEMS results .....	72
4.5	Summary .....	73
5	Charging/discharging processes in SiN <sub>x</sub> films with various interfacial structures.....	75
5.1	Introduction .....	75
5.2	Experimental .....	75
5.3	Influence of SiN <sub>x</sub> film thickness .....	77
5.3.1	KPFM results .....	77
5.3.2	FDC results .....	80
5.3.3	C/DCT results .....	81
5.3.4	Influence on material stoichiometry .....	84
5.3.5	Discussion.....	87
5.4	Influence of substrate and underlying metal layers.....	91
5.4.1	SiN <sub>x</sub> over silicon substrate versus SiN <sub>x</sub> over Au .....	91
5.4.2	KPFM and FDC results.....	92
5.4.3	Discussion.....	95
5.4.4	Influence of underlying metal layer.....	96
5.4.5	KPFM and FDC results.....	98
5.4.6	Discussion.....	99
5.5	Influence of bias polarity.....	100
5.5.1	KPFM and FDC results.....	100
5.5.2	Discussion.....	103
5.6	Impact of charge injection duration, T <sub>p</sub> .....	106
5.7	HF versus LF SiN <sub>x</sub> .....	107
5.7.1	KPFM results .....	107
5.7.2	FDC results .....	109

## CONTENTS

---

5.7.3	C/DCT results .....	111
5.7.4	Influence on material stoichiometry .....	113
5.7.5	Discussion .....	113
5.8	Summary .....	116
6	Influence of deposition reactive gas ratio, RF power and substrate temperature on charging/discharging processes in SiN <sub>x</sub> films.....	118
6.1	Introduction .....	118
6.2	Experimental .....	119
6.3	Effect of reactive gas ratio .....	121
6.3.1	KPFM results .....	121
6.3.2	FDC results .....	124
6.3.3	Influence on material stoichiometry .....	126
6.3.4	Discussion .....	127
6.4	Effect of RF power .....	129
6.4.1	KPFM results .....	129
6.4.2	FDC results .....	131
6.4.3	Influence on material stoichiometry .....	133
6.4.4	Discussion .....	134
6.5	Effect of deposition temperature .....	136
6.5.1	KPFM results .....	136
6.5.2	FDC results .....	137
6.5.3	Influence on material stoichiometry .....	139
6.5.4	Discussion .....	140
6.6	Summary .....	143
7	The influence of environment medium, relative humidity, and contaminants on charging/discharging processes .....	145
7.1	Introduction .....	145
7.2	Experimental .....	145
7.3	Impact of relative humidity on KPFM measurement accuracy.....	146
7.4	Air versus nitrogen under different relative humidity levels .....	149
7.4.1	Surface potential distribution (FWHM).....	149
7.4.2	Surface potential amplitude (U <sub>s</sub> ).....	151
7.4.3	Surface potential decay .....	155
7.4.4	Lateral charge redistribution (FWHM evolution with time).....	159
7.5	Influence of oxygen, organics and hydrocarbon contaminants.....	164
7.5.1	Impact on charging process .....	165
7.5.2	Impact on discharging process.....	166
7.6	Summary .....	168
8	Characterization of different stiction mechanisms .....	170
8.1	Introduction .....	170
8.2	Experimental .....	171
8.2.1	Adhesive force and water film thickness measurements .....	171
8.2.2	Friction force and coefficient of friction.....	173
8.3	Effect of meniscus formation when no bias is applied.....	173
8.4	Effect of applied bias on adhesive and friction forces .....	176
8.5	Summary .....	190

Conclusions.....	191
Conclusions.....	197
Outlook .....	201
References.....	203
Nomenclature.....	214
Biography.....	217

*Human beings, who are almost unique in having the ability to learn from the experience of others, are also remarkable for their apparent disinclination to do so.*

*Douglas Adams  
1952 – 2001, English writer and dramatist  
in “Last Chance to See”*

## List of papers

The presented thesis is based on the following international reviewed journal papers

1. **Zaghloul, U.**, G.J. Papaioannou, B. Bhushan, H. Wang , F. Coccetti, P. Pons, and R. Plana (2011), "Effect of deposition gas ratio, RF power and substrate temperature on the charging/discharging processes in PECVD silicon nitride films for electrostatic NEMS/MEMS reliability using atomic force microscopy," *IEEE/ASME J. Microelectromechanical Systems* (in press).
2. **Zaghloul, U.**, B. Bhushan, G.J. Papaioannou, F. Coccetti, P. Pons, and R. Plana (2011), "Nanotribology-based novel characterization techniques for the dielectric charging failure mechanism in electrostatically actuated NEMS/MEMS devices using force-distance curve measurements," *J. Colloid and Interface Science*, doi:10.1016/j.jcis.2011.08.005 (in press).
3. **Zaghloul, U.**, G.J. Papaioannou, B. Bhushan, F. Coccetti, P. Pons, and R. Plana (2011), “On the reliability of electrostatic NEMS/MEMS devices: Review of present knowledge on the dielectric charging and stiction failure mechanisms and novel characterization methodologies,” *Microelectron. Reliab.* **51**, 1810-1818 (**Invited paper**).
4. **Zaghloul, U.**, B. Bhushan, F. Coccetti, P. Pons, and R. Plana (2011), "Kelvin probe force microscopy-based characterization techniques applied for electrostatic MEMS/NEMS devices and bare dielectric films to investigate the dielectric and substrate charging phenomena,” *J. Vac. Sci. Technol. A* **29**, Art.# 051101. (**The 3<sup>rd</sup> most downloaded article in JVST**).

5. **Zaghoul, U.**, B. Bhushan, P. Pons, G.J. Papaioannou, F. Coccetti, and R. Plana (2011), "Nanoscale characterization of different stiction mechanisms in electrostatically driven MEMS devices based on adhesion and friction measurements", *J. Colloid Interface Sci.* **358**, 1-13. **(Selected for the cover page of the journal)**
6. **Zaghoul, U.**, G.J. Papaioannou, H. Wang, B. Bhushan, F. Coccetti, P. Pons, and R. Plana (2011), "Nanoscale characterization of the dielectric charging phenomenon in PECVD silicon nitride thin films with various interfacial structures based on Kelvin probe force microscopy," *Nanotechnology* **22**, Art. # 205708.
7. **Zaghoul, U.**, G. Papaioannou, B. Bhushan, F. Coccetti, P. Pons, and R. Plana (2011), "New insights into reliability of electrostatic capacitive RF MEMS switches," *Int. J. of Microwave and Wireless Technologies*, doi:10.1017/S1759078711000766.
8. **Zaghoul, U.**, B. Bhushan, P. Pons, G. Papaioannou, F. Coccetti and R. Plana (2011), "On the Influence of Environment Gases, Relative Humidity and Gas Purification on Dielectric Charging/Discharging processes in Electrostatically Driven MEMS/NEMS Devices," *Nanotechnology* **22**, Art.# 035705.
9. **Zaghoul, U.**, M. Koutsourelis, H. Wang, F. Coccetti, G. Papaioannou, P. Pons and R. Plana (2010), " Assessment of dielectric charging in electrostatically driven MEMS devices: A comparison of available characterization techniques," *Microelectron. Reliab.* **50**, 1615-1620.
10. **Zaghoul, U.**, G. J. Papaioannou, F. Coccetti, P. Pons and R. Plana (2010), "A systematic reliability investigation of the dielectric charging process in electrostatically actuated MEMS based on Kelvin probe force microscopy " *J. Micromech. Microeng.* **20**, Art.# 064016.
11. **Zaghoul, U.**, G. Papaioannou, F. Coccetti, P. Pons and R. Plana (2009), "Dielectric charging in silicon nitride films for MEMS capacitive switches: Effect of film thickness and deposition conditions," *Microelectron. Reliab.* **49**, 1309-1314.

Also, the work has been presented in the following international reviewed conferences

12. **Zaghloul, U.** (2011), "Dielectric charging phenomenon in electrostatically driven MEMS/NEMS devices: Nanoscale and macroscale characterization using novel assessment methodologies," *the 22<sup>nd</sup> European Symposium on Reliability of Electron Devices, Failure Physics and Analysis (ESREF 2011)*, October 3-7, Bordeaux - France. **(Invited paper)**
13. **Zaghloul, U., B. Bhushan, P. Pons, G. Papaioannou, F. Coccetti, and R. Plana** (2011), "Nanoscale characterization of different stiction mechanisms in electrostatic RF-MEMS switches", *Proc. of the 41<sup>st</sup> European Microwave Conference*, October 9-14, Manchester, UK, pp. 478- 481.
14. **Zaghloul, U., B. Bhushan, P. Pons, G. Papaioannou, F. Coccetti, and R. Plana** (2011), "Different Stiction Mechanisms In Electrostatic MEMS Devices: Nanoscale Characterization Based On Adhesion And Friction Measurements," *the 16<sup>th</sup> Int. Conf. on Solid-State Sensors, Actuators and Microsystems (TRANSDUCERS 2011)*, IEEE, New York.
15. **Zaghloul, U., B. Bhushan, P. Pons, G. Papaioannou, F. Coccetti, and R. Plana**, (2010) "On the Impact of Relative Humidity and Environment Gases on Dielectric Charging Process in Capacitive RF MEMS Switches Based on Kelvin Probe Force Microscopy," *AVS 57<sup>th</sup> Int. Symposium & Exhibition (MEMS and NEMS)*.
16. **Zaghloul, U., M. Koutsourelis, H. Wang, F. Coccetti, G. Papaioannou, P. Pons, and R. Plana** (2010), "Assessment of dielectric charging in electrostatically actuated MEMS devices: A comparison of available characterization techniques," *21<sup>st</sup> European Symposium on Reliability of Electron Devices, Failure Physics and Analysis (ESREF 2010)*.
17. **Zaghloul, U., F. Coccetti, G. Papaioannou, P. Pons and R. Plana** (2010), "A novel low cost failure analysis technique for dielectric charging phenomenon in electrostatically actuated MEMS devices," *Proc. of the 2010 IEEE Int. Reliability Physics Symp.*, pp. 237-245, IEEE, New York.
18. **Zaghloul, U., G. Papaioannou, F. Coccetti, P. Pons and R. Plana** (2009), "Effect of Humidity on Dielectric Charging Process in Electrostatic Capacitive RF MEMS Switches Based on Kelvin Probe Force Microscopy Surface Potential Measurements," *Microelectromechanical*

*Systems-Materials and Devices III, MRS Proc.* Vol. 1222, (eds. J. Bagdahn, N. Sheppard, K. Turner and S. Vengallatore), pp. 39-44, Material Research Society(MRS), Pennsylvania.

19. **Zaghoul, U.**, G. Papaioannou, F. Coccetti, P. Pons, and R. Plana (2009), "Dielectric charging in silicon nitride films for MEMS capacitive switches: effect of film thickness and deposition conditions," *Proc. of the 20<sup>th</sup> European Symposium on Reliability of Electron Devices, Failure Physics and Analysis (ESREF 2009)*, pp. 1309-1314.
20. **Zaghoul, U.**, G. Papaioannou, F. Coccetti, P. Pons, and R. Plana (2009), "Investigation of Dielectric Charging in Low Frequency PECVD Silicon Nitride Films for MEMS Capacitive Switches," *Proc. of the 10<sup>th</sup> Int. Symposium on RF MEMS and RF Microsystems (MEMSWAVE 2009)*, pp. 97-100.
21. **Zaghoul, U.**, A. Belarni, F. Coccetti, G. Papaioannou, L. Bouscayrol, P. Pons and R. Plana (2009), "A comprehensive study for dielectric charging process in silicon nitride films for RF MEMS switches using Kelvin probe microscopy," *Proc. of the 15<sup>th</sup> Int. Conf. on Solid-State Sensors, Actuators and Microsystems (TRANSDUCERS 2009)*, pp. 789-793, IEEE, New York.
22. **Zaghoul, U.**, A. Abelarni, F. Coccetti, G. Papaioannou, R. Plana and P. Pons (2008), "Charging processes in silicon nitride films for RF-MEMS capacitive switches: The effect of deposition method and film thickness," *Microelectromechanical Systems-Materials and Devices II, MRS Proc.* Vol. 1139, (eds. S. M. Spearing, S. Vengallatore, N. Sheppard and J. Bagdahn), pp. 141-146, Material Research Society (MRS), Pennsylvania.



*The purpose of learning is growth, and our minds, unlike our bodies, can continue growing as we continue to live.*

*Mortimer Adler  
1902 – 2001, American Philosopher and author*

## **1 Thesis organisation**

A general introduction to MEMS/NEMS reliability and a comprehensive overview of the available knowledge related to the reliability of electrostatic capacitive MEMS switches with main focus on the dielectric charging are presented in chapter 2. This includes the basic polarization/charging mechanisms in dielectrics, various dielectric materials used in electrostatic MEMS and their related charging mechanisms, and the available characterization methods. A review of the state-of-the-art knowledge for the influence of several factors on the reliability of MEMS switches is then discussed and concluded with the motivation behind this thesis.

In chapter 3, the investigated samples and the employed characterization techniques are described. Various novel characterization techniques are proposed. The investigated assessment methods are based on Kelvin probe force microscopy (KPFM), force-distance curve (FDC), and discharge current transients (DCT). The theory behind each technique as well as its procedure is discussed, and an example of results is presented. Since these techniques were applied to study the charging in a large variety of samples including bare dielectric films, MIM capacitors, and electrostatic MEMS switches, the layer structure of the investigated samples is also discussed in this chapter. The parameters used for the physical material characterization methods (XPS and FT-IR) are also presented. In spite of the various electrical characterization techniques reported to study the dielectric charging in electrostatic MEMS, there has been no correlation between them. Chapter 4 is dedicated mainly to address this point where a link between assessment methods that use MIM capacitors and MEMS switches is made. In addition, a correlation between the results of the proposed characterization methods explained in chapter 3 is discussed.

The influence of various parameters on the charging/discharging processes is discussed in chapter 5. This includes the impact of dielectric film thickness, dielectric deposition conditions, and under layers. The impact of the electrical stress field intensity, duration, and polarity used to charge the dielectric films are also explained. Three electrical characterizations methods were employed to study these parameters. A further study of the dependence of the electrical properties of  $\text{SiN}_x$  on the material deposition conditions and consequently on stoichiometry is presented in chapter 6. The influence of each PECVD deposition parameter on the dielectric charging of  $\text{SiN}_x$  films is investigated separately. For these experiments,  $\text{SiN}_x$  films were deposited using different gas ratio, RF power, and substrate temperature. In addition, XPS and FT-IR were employed, and an attempt to correlate between the chemical and electrical properties of  $\text{SiN}_x$  films is made in chapter 5 and 6.

Chapter 7 investigates the influence of environment medium and relative humidity on the charging/discharging processes in  $\text{SiN}_x$  films. Surface potential measurements were performed on the nanoscale under different relative humidity levels in both air and nitrogen environments. In addition, the influence of oxygen gas as well as hydrocarbon contaminants is discussed. On the other hand, different stiction mechanisms in electrostatic MEMS switches are presented in chapter 8. In these devices stiction can be caused by two main mechanisms: dielectric charging and meniscus formation resulting from the adsorbed water film between the switch bridge and the dielectric layer. The effect of each mechanism and their interaction were investigated on the nanoscale by measuring the adhesive and friction forces under different electrical stress conditions and relative humidity levels.

Finally, a conclusion of the study and an outlook for future work are presented. In this thesis, 'MEMS' is used as a generic name that also includes devices with nanometer-scale features, i.e 'NEMS'.

*The most exciting phrase to hear in science, the one that heralds new discoveries, is not “Eureka!” (“I found it!”) but “That's funny ...”*

*Isaac Asimov  
1920 – 1992, American author and professor*

## **2 Review of present knowledge**

### **2.1 Introduction**

This chapter provides an overview of the presently available knowledge related to the reliability of electrostatic capacitive MEMS switches with a main focus on the dielectric charging phenomenon. An introduction to the MEMS reliability field is presented first. This is followed by describing the main failure mechanisms and failure modes of MEMS switches with a brief discussion for some of them. The basic polarization/charging mechanisms in dielectrics are then explained and the various dielectric materials used in electrostatic MEMS as well as their related charging mechanisms are discussed. Next, the available assessment methods of the dielectric charging phenomenon are summarized focusing on advantages and limits of each technique. A review of the state-of-the-art knowledge related to the influence of various factors on the reliability of MEMS switches and the currently open issues are then discussed. Finally, the motivation behind this study is presented.

### **2.2 General introduction to MEMS Reliability**

MEMS/NEMS are integrated micro/nano devices or systems combining electrical and mechanical components and normally fabricated using Integrated Circuit (IC) compatible batch-processing techniques. Currently, there are numerous MEMS leading products in the market, for example accelerometers, gyroscopes, pressure sensors, silicon microphones, inkjet print heads, microfluidics for diagnostics and drug delivery. They offer considerable potential mostly due to small size, small weight, and low power consumption which enables a whole new line of

applications with compelling advantages in many related areas such as health care, wireless telecommunication, environmental monitoring, and a wide range of consumer electronics. In spite of that, MEMS technology is still considered in its juvenile age, similar to the IC technology 40 or 50 years ago, and several MEMS products are still prototypes. Several reliability concerns are the major hindering factors that prevent the commercialization and utilization of numerous MEMS devices [1].

Reliability can generally be defined as ‘the probability that an item will perform a required function under stated conditions for a stated period of time’ [2]. The term ‘probability’ points out that we deal with probabilistic models and statistical methods. Also, the term ‘required function’ indicates that we have well defined specifications of satisfactory operation, and therefore it includes the definition of failure. The ‘stated conditions’ term includes the total physical environment (electrical, mechanical, thermal, and environmental conditions). Finally, the term ‘stated period of time’ defines a concept of the required lifetime. When a failure occurs, i.e. the device does not perform anymore the required function during functional or reliability testing or in the field, a failure analysis (FA) is normally carried out to investigate and determine the cause. FA can involve electrical testing, fail-site isolation, deprocessing, defect characterization and corrective actions [3]. There is often confusion on the terminology used for failure analysis where four terms are used inconsistently: ‘*failure mode*’, ‘*failure defect*’, ‘*failure mechanism*’, and ‘*failure cause*’ [4]. The ‘*failure mode*’ is what is first identified, i.e. measured or observed as a deviating or failing behaviour with respect to the specs. For example, a shift in the C-V characteristics of a MEMS switch is a failure mode. The ‘*failure defect*’ is what is observed after identifying the failure mode, and in some cases no failure defect is seen. A stuck of a MEMS cantilever to the substrate is an example of a failure defect. The ‘*failure mechanism*’ is the physics and/or chemistry causing the failure, for example, charging, creep, fatigue, etc. Finally, the ‘*failure cause*’ is what is causing the failure mechanism, for example, the relative humidity causing capillary stiction.

For conventional microelectronic devices, for example ICs, there is a large knowledge available on the reliability testing and failure analysis. The key failure modes are well identified, and the reliability test methodologies are available and described in standards such as IEC [5] or MIL [6]. Though a considerable portion of this knowledge could be applied to MEMS, there are numerous key issues which are unique to MEMS and stand against that. For example, the

reliability issues related to the mechanical part of MEMS structures and to the particular packaging prototype, and deal with failures such as creep, fatigue, fracture, wear, stiction, outgassing, hermeticity, etc occurs only in MEMS and has no equivalent reliability concerns in conventional microelectronics. In addition, MEMS devices have a large variety of different applications involving interfacing with various kinds of signals (electrical, optical, chemical, fluidic, pressure, acceleration, etc). For these reasons, the involved reliability tests of MEMS are typically defined on an application-specific basis, and there are not much generic test methods or standardization.

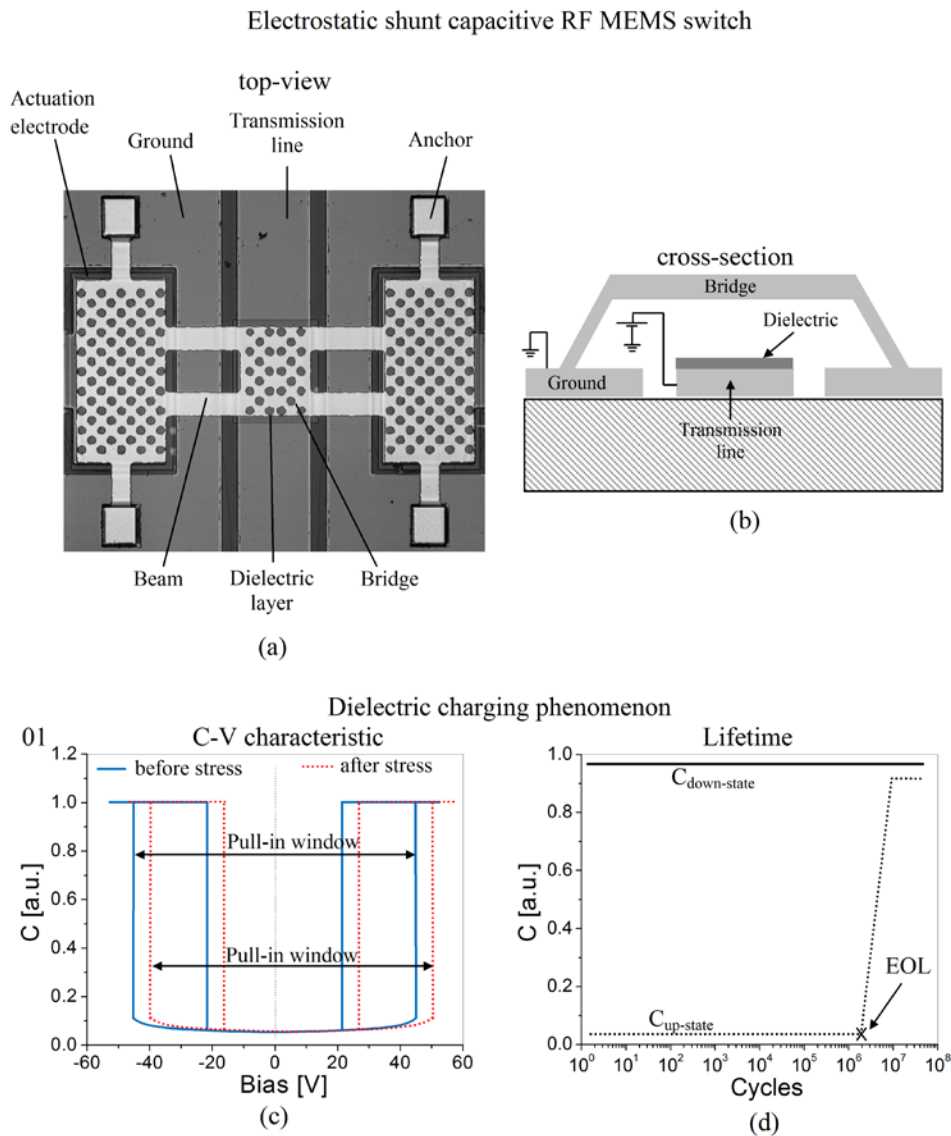


Figure 2.1. Dielectric charging in electrostatic MEMS switches: (a) a magnified image of a finished switch from LAAS - CNRS [15], (b) a vertical cross-section; (c) a shift in C-V characteristic and (d) a lifetime test result.

Using techniques like failure mode and effects analysis (FMEA) helps to assess the reliability in all development stages of a MEMS device. Basically, FMEA is defined as ‘a systematic and structured study of the potential failures that might occur in any part of the MEMS to determine the probable effect of each on all other parts of the system and on probable operational success, with the aim of improvement in the design, product and process development’. Therefore, it involves brainstorming of potential failure modes, identifying suspected root causes, assigning levels of risk, and following through with corrective and protective actions [7]. FMEA starts with identifying the failure modes, defects, mechanisms and causes and estimating their severity (S), occurrence (O) and detectability (D) for a specific MEMS device and for a certain application in a certain environment. The latter three parameters are given weighting points between for example 1 and 10, where  $S = 1$  means that this failure mechanism does not cause any damage to the MEMS, while  $S = 10$  indicates that it causes an immediate irremediable death of the device [4]. Also,  $O = 1$  means that the failure is very unlikely to occur, while  $O = 10$  indicates the very high probability for its occurrence.  $D = 1$  means that the defect is detectable, while  $D = 10$  points out that that defect detection is almost impossible. This is followed by determining a risk priority number ( $RPN = S \times O \times D$ ) for each failure mechanism. Thus, the higher the RPN is, the more critical is the failure mechanism.

### **2.3 Reliability of electrostatic MEMS switches**

MEMS switches are devices which use mechanical movement to achieve a short circuit or an open circuit in the transmission line at radio frequency (RF) to millimeter-wave frequencies [8, 9]. Due to their exceptional properties, which are high operating frequency range, wide bandwidth, high isolation, low insertion loss and low power consumption, RF-MEMS switches are considered as a strong competitor to solid state devices such as PIN (P-type, Intrinsic material, N-type) diodes and field effect transistor (FET) switches [10, 11]. These unique characteristics make MEMS switches ideal candidates for incorporation into passive circuits, such as phase shifters or tunable filters, for implementation in many terrestrial and space applications including portable telecommunication, wireless computer networks, reconfigurable antennas and others [12]. There are two main types of RF-MEMS switches: capacitive switches and DC-contact switches. The capacitive MEMS switch like the one shown in **Fig. 2.1a, b** is characterized by the capacitance ratio between the up-state (open circuit) and down-state (short-circuit) positions of the movable electrode (bridge), and it can be operated at a higher frequency

range than the DC-contact one [13, 14, 15]. The DC-contact switch has small up-state capacitances, and in the down-state it becomes a series resistor [16]. For both types of switches a mechanical movement for the suspended electrode towards or far from the signal transmission line is required to achieve the switching function. The forces required for this movement can be obtained using electrostatic, magnetostatic, piezoelectric, or thermal designs. To date, only electrostatic-type switches were demonstrated at 0.1-100 GHz with high reliability and/or wafer-scale manufacturing techniques.

In spite of the mentioned advantages for RF-MEMS switches, their commercialization is still hindered due to several reliability concerns. Up to now, only DC-contact switches are commercially available on a very limited scale. For both types of MEMS switches a number of different failures can occur during the exploitation of the device. Some of these reliability issues are the creep resulting from high temperature used during the packaging process [17], outgassing of the packaging material [18] and adhesion or commonly referred to as stiction due to dielectric charging [19] and/or the presence of condensed water vapor from the environment [20]. In DC-contact switches, the main failure is due to the degradation of the ohmic contacts with repeated actuations [21], while for electrostatic capacitive switches the main failure is due to the dielectric charging of the switch insulating film [8, 22].

An example of an FMEA study performed for electrostatic capacitive MEMS switches is presented in **Table 2.1** [4, 23]. The failure mechanisms are ranked in the table based on the RPN numbers where the failure mechanism with the highest RPN (i.e. the most critical) is listed first. The first three failure mechanisms are briefly discussed in this section. The dielectric charging of the insulating film is the first ranked failure mechanism, and therefore it has been intensively studied during the last two decades [14, 19, 24, 25, 26, 27], and it is the main focus of our thesis. The failure defect of this mechanism is a non-permanent stiction of the suspended electrode (bridge) to the dielectric. It is not permanent since the injected charges are removed from the dielectric film after a certain time. The associated failure mode is a shift of the C–V characteristic of the switch [19, 28] with a constant pull-in window evolving the same way as shown in **Fig. 2.1c.**, or narrowing of the C–V characteristic [29, 30, 31]. A typical lifetime experiment involves stressing the RF-MEMS switch with unipolar actuation cycles with the up and down-state capacitances monitored during cycling. Due to charge build-up in the dielectric during the lifetime test, high adhesion or stiction occurs between the bridge and the dielectric.

## LIST OF PAPERS

This is detected through the reduction in the measured up-state capacitance and is used to determine end-of-life (EOL) of the switch as shown in **Fig. 2.1d**. Therefore, the failure mode of the dielectric charging mechanism can also be a nonfunctional device. There are several different failure causes behind this mechanism. First, the charging during the down-state position due to the high electric field applied to the thin insulating film. The charging due to radiation (ex. for MEMS switches in space applications), air-gap breakdown, and electron emission are other failure causes for this mechanism.

Table 2.1 FMEA study of electrostatic capacitive MEMS switches, the RPN of each failure mechanism is not included.

	Failure mechanism	Failure defect	Failure mode	Failure cause
1	Dielectric charging of the insulator	Non-permanent stiction	-Drift in C-V, $V_{pi}$ , $V_{po}$ -Dead device	<ul style="list-style-type: none"> <li>• Electric field charge</li> <li>• Radiation</li> <li>• Air-gap breakdown</li> <li>• Electron emission</li> </ul>
2	T-induced elastic deformation of the bridge	Non-permanent deformation of the bridge (restored when T-source is removed), possibly stiction	-Drift in C-V, $V_{pi}$ , $V_{po}$ -Dead device	<ul style="list-style-type: none"> <li>• Environment T</li> <li>• Different CTE</li> <li>• Power RF signal induced T</li> <li>• Non uniform T</li> </ul>
3	Plastic deformation of the bridge	Permanent deformation, possibly stiction	-Drift in C-V, $V_{pi}$ , $V_{po}$ -Dead device	<ul style="list-style-type: none"> <li>• Creep</li> <li>• Thermal induced charges in material properties (for <math>T &gt; T_c</math>)</li> </ul>
4	Structural Short (electrical and non-electrical connections)	Particles, shorted metals, contamination, remains of sacrificial layer, stuck bridge	Anomalous or dead device	<ul style="list-style-type: none"> <li>• Contamination, particles, remaining sacrificial layer</li> <li>• Wear particles</li> <li>• Fracture</li> <li>• Lorenz forces</li> <li>• Shock</li> </ul>
5	Capillary Forces	Stiction	Dead device	Humidity (Package leaks)
6	Fusing	Opens, roughness increase	Dead device	High RF power pulses, ESD
7	Fracture	Broken bridges or hinges	Dead device	<ul style="list-style-type: none"> <li>• Fatigue</li> <li>• Brittle materials and shock</li> <li>• High local stresses and shock</li> </ul>
8	Dielectric breakdown	Dead device, possibly stiction	Short between the bridge and the actuation electrodes	<ul style="list-style-type: none"> <li>• ESD</li> <li>• Excessive charging of the insulator</li> </ul>
9	Corrosion	Dendrites formation, oxidation, changes in	-Drift in C-V, $V_{pi}$ , $V_{po}$	<ul style="list-style-type: none"> <li>• Humidity, enhanced by bias</li> </ul>

		color	-Dead device	<ul style="list-style-type: none"> <li>Corrosive gases induced chemical reaction (ex. oxidation)</li> </ul>
10	Wear Friction Fretting corrosion	Surface modifications, debris, stiction	-Drift in C-V, $V_{pi}$ , $V_{po}$ -Dead device	Rough Surfaces in sliding contact
11	Creep	Deformation of the bridge in time	-Drift in C-V, $V_{pi}$ , $V_{po}$ -Dead device	High metal stress and high temperature, creep sensitive
12	Equivalent DC voltage	Self biasing stiction	-Drift in C-V, $V_{pi}$ , $V_{po}$ -Dead device	High RF power including spontaneous collapsing or stiction of mobile part
13	Lorenz forces	Self biasing stiction	Anomalous switching behavior	<ul style="list-style-type: none"> <li>High RF power in two adjacent lines</li> <li>External magnetic field</li> </ul>
14	Whisker formation	Bumps in metal, holes in insulator on top of metal layers, etc	Anomalous down capacitance	High compressive stress in metal resulting in grains extrusions, might be enhanced
15	Fatigue	Broken bridges and hinges, cracks, microcracks	Shifts in electrical and mechanical properties	<ul style="list-style-type: none"> <li>Large local stress variations due to motion of parts</li> <li>Enhanced probability of cracks</li> </ul>
16	Electromigration	Cracks, opens, thickness changes in metal lines	Increase of resistance, opens, shorts	High current density
17	Van der Waals forces	Stiction	Dead device	Smooth and flat surfaces in close contact

The temperature (T) induced elastic deformation of the bridge is the second ranked failure mechanism in **Table 2.1**. The failure defect of this mechanism is a non-permanent deformation of the bridge if it is restored after removing the T-source. If the deformation is so large that the deformed bridge touches the dielectric or the cap of the package, the failure defect might be also stiction. The failure mode of this mechanism is a drift of C-V characteristic and changes in the pull-in and pull-out voltages, or a nonfunctional device similar to the dielectric charging failure mechanism. There are different possible failure causes for the elastic deformation. One is the change in the environmental temperature which causes a deformation of the bridge either because of an expansion or because of a difference in thermal expansion coefficient (CTE) between the materials used for the bridge. Another possible cause is the non-uniform temperature in the bridge caused by the power of the RF signal. The Third failure mechanism listed in **Table 2.1** is the plastic deformation of the bridge. The failure defect is a

permanent deformation of the bridge, and also a possible stiction if the deformation is too large. The failure mode is similar to the one of the first and second failure mechanisms, but is in this case irremediable. Actually, the device is not necessary to be malfunction, but its electrical parameters will show a permanent drift. Possible failure causes are creep in the metal layer of the bridge and temperature-induced changes in the material properties while the latter could results during the device packaging.

## 2.4 Dielectric polarization/charging

The basic polarization/charging mechanisms in dielectrics are presented in order to obtain a better insight on the effect of ionic or covalent bonds as well as different conduction mechanisms which occur in MEMS dielectrics.

### 2.4.1 Polarization/Charging mechanisms

The polarization of a solid dielectric submitted to an external electric field occurs through a number of mechanisms involving microscopic or macroscopic charge displacement. These mechanisms could be divided according to the time scale of polarization build-up in two categories, the instantaneous and the delayed time dependent polarization. The time dependent polarization mechanisms [32, 33, 34], which are responsible for the dielectric charging phenomena, are characterized by a time constants that may be as low as  $10^{-12}$  s or as large as years. In the latter, no relaxation could be observed under normal experiment time windows. These mechanisms are called slow and include dipolar, space charge, and interfacial polarization. **Figure 2.2** presents a summary of these polarization mechanisms which could take place in contact as well as contactless scenarios. In contactless charging (**Fig. 2.2a**), the time varying electric field can interact with the dielectric material under two processes: dipolar polarization (reorientation of defects having an electric dipole moment), and space charge polarization (arising from redistribution of preexisting and/or field generated charge carriers). In contact charging (**Fig. 2.2b**), charges are injected into the dielectric film through various charge injection mechanisms that will be described in section 2.4.2.

The dipolar or orientational polarization (**Fig. 2.2c**) occurs in materials containing permanent molecular or ionic dipoles. The time required for this process can vary between picoseconds to even years depending on the frictional resistance of the medium. The dipolar polarization of inorganic crystals may be caused by structural properties of the crystal lattice or it

may be due to lattice imperfection or doping. The structural interpretation of the dielectric processes occurring in many polar materials is usually approached by assuming impaired motions or limited jumps of permanent electric dipoles. In molecular compounds for example, relaxation can be considered as arising from hindered rotation of the molecule as a whole, of small units of the molecule or some flexible group around its bond to the main chain. On the other hand, relaxation is mainly associated with ionic jumps between neighboring sites in ionic crystals.

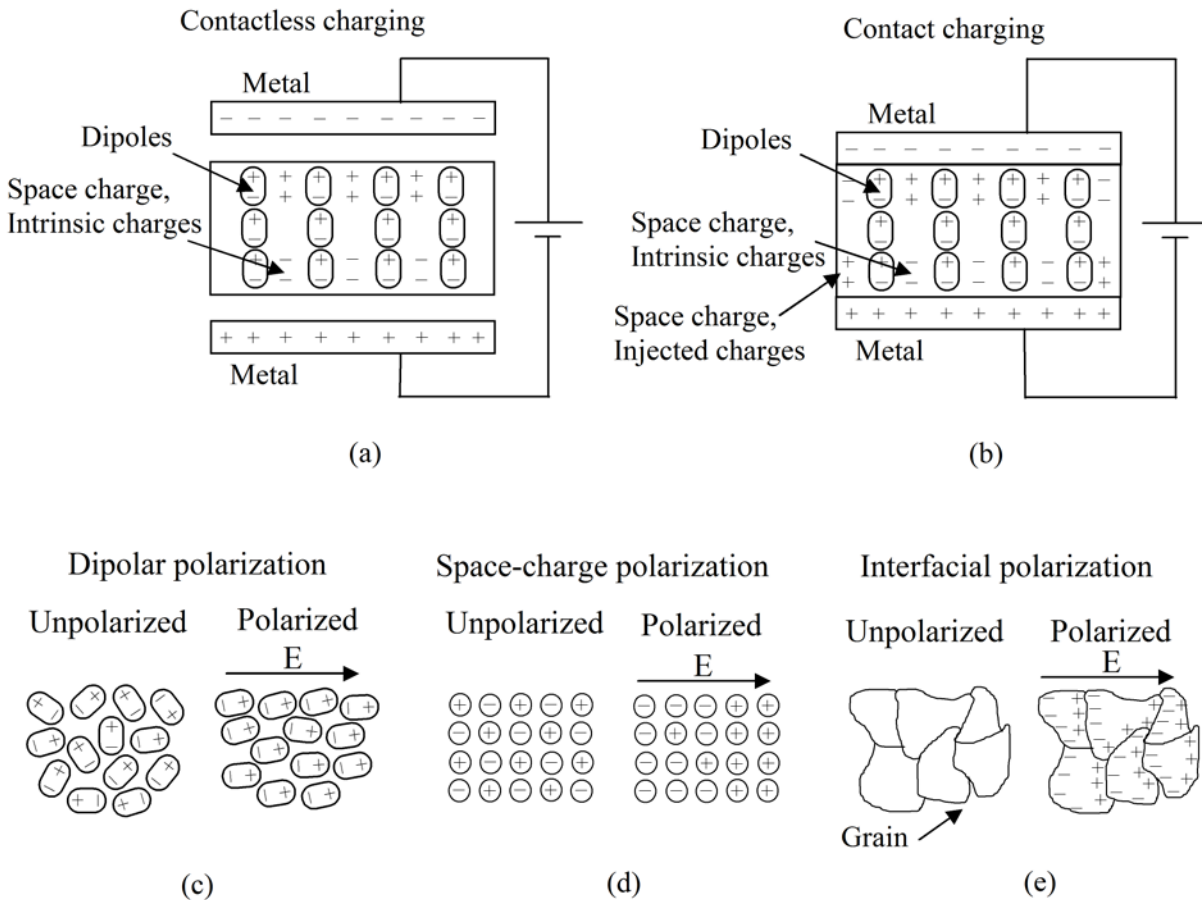


Figure 2.2. Different polarization mechanisms: (a) polarization under contactless and (b) under contact charging; (c) dipolar, (d) space-charge, and (e) interfacial polarization.

The space charge or translational polarization (**Fig. 2.2d**) is observed in materials containing intrinsic free charges such as ions or electrons or both. It arises from macroscopic charge transfer towards the electrodes that may act as total or partial barriers. Moreover, the charging of space-charge electrets may be achieved by injecting charge carriers. Other methods include the generation of carriers within the dielectric by light, radiation or heat and

simultaneous charge separation by a field. The space charge polarization causes the material to be spatially not neutral, hence is a much more complex phenomenon than the dipolar polarization. Dipolar and space charge polarizations often coexist and the electric field and polarization are averaged over the dielectric film thickness. In addition, the simultaneous displacement of free charges and dipoles during the polarization process may lead to a particular situation where the internal electric field is nearly zero, so that no preferred orientation of dipoles occurs.

The interfacial polarization (**Fig. 2.2e**), referred also as Maxwell-Wagner-Sillars (MWS) polarization, is a characteristic of systems with heterogeneous structure. It results from the formation of charged layers at the interfaces due to unequal conduction currents within the various phases. In structurally heterogeneous materials, such as complicated mixtures or semi-crystalline products, it can be expected that field-induced ionic polarization will obey more closely an interfacial model of the MWS type than a space-charge model of the barrier type. The electric field can achieve a migration charge by (a) bulk transport of charge carriers within the higher conductivity phase, and (b) surface migration of charge carriers. As a consequence surfaces, grain boundaries, and interphase boundaries may charge. Charges “blocked” at the interface between two phases with different conductivity give a contribution to the net polarization of the body exposed to the electric field.

#### 2.4.2 *Charge injection mechanisms*

The conduction mechanisms in dielectrics are divided in two categories; the steady state and transient current [34]. The steady state does not contribute to dielectric charging while the transient current does. In electrostatic MEMS switches the dielectric films are usually a few hundred nm thick and because of the high fields ( $\sim 10^6$  V/cm) applied across these films during actuation, conduction is typically nonohmic and dominated by transport via traps in the dielectric and by charge injection and tunneling. In order to describe the charge injection mechanisms in MEMS, the leakage current models from metal-insulator-metal (MIM) capacitors reported in [35] could be employed. By analyzing leakage current transients in MIM, the dielectric charging can be monitored and then linked to MEMS reliability [36, 37]. However, there has been no direct evidence of relation between the dielectric film DC leakage current and the dielectric charging, except the fact that the leakage current masks the slow charging and discharging

processes [36]. The main electronic processes that were identified to take place in MEMS switches are the Poole-Frenkel (PF) and the Trap Assisted Tunneling (TAT) conduction.

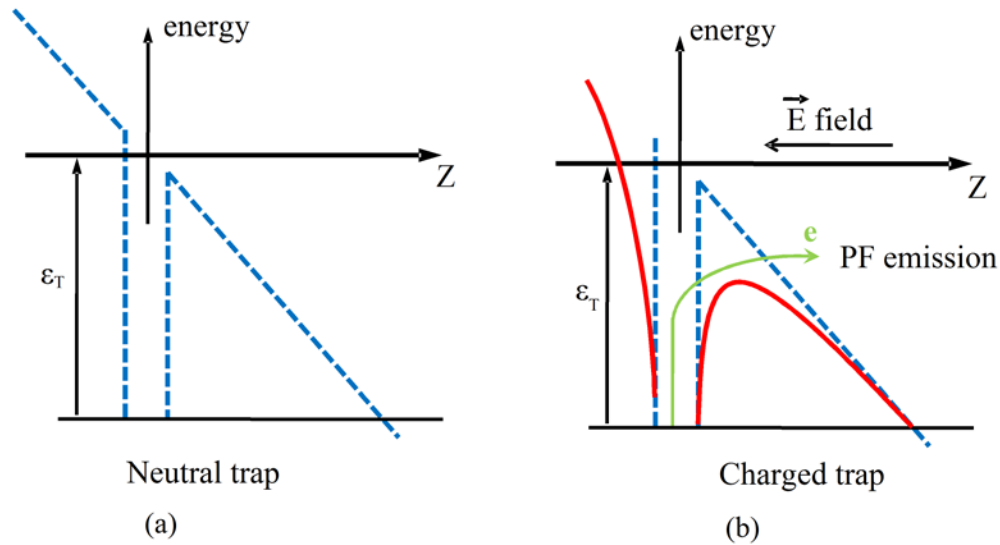


Figure 2.3. Poole-Frenkel conduction: energy level diagram for (a) a neutral, and (b) a charged trap.

#### 2.4.2.1 Poole-Frenkel (PF) process

The classical Poole-Frenkel (PF) effect is the thermal emission of charge carriers from Coulombic (i.e., charged) traps in the bulk of a dielectric or semiconductor, enhanced by the application of an electric field [38, 39]. An illustration for this mechanism is shown in **Fig. 2.3**. The Energy level diagram for a neutral trap is shown in **Fig. 2.3a**. When an electric field is applied, the barrier height is reduced on one side of the trap, thereby increases the probability of the electron escaping from the trap (**Fig. 2.3b**). As the field increases, the potential barrier further decreases, making it easier for the electron to vacate the trap by thermal emission and enter the quasi-conduction band of the host material. The quasi-conduction band edge is the energy at which the electron is just free from the influence of the positive nucleus. The term “quasi-conduction band” is often used when discussing amorphous solids, which have no real band structure. For the PF emission process to occur, the trap must be neutral when filled with an electron, and positively charged when the electron is emitted, making it a Coulombic attractive trap. A first-order model for the current due to the PF effect was developed by Frenkel assuming that the potentials do not overlap, which is valid only if the impurity density is low. Although in amorphous materials the impurities density is usually relatively high, for the purpose of simplicity this model is used where the current due to PF emission is given by

$$J_{PF} = N\mu E \exp\left[-\frac{(\varphi - \beta_{PF} E^{1/2})}{KT}\right] \quad (2.1)$$

where  $J$  is the current density,  $N$  is the density of trapping sites,  $\mu$  is the effective carrier mobility,  $E$  is the electric field,  $\varphi$  is the zero-field trap depth, and  $\beta_{PF}$  is the PF coefficient.

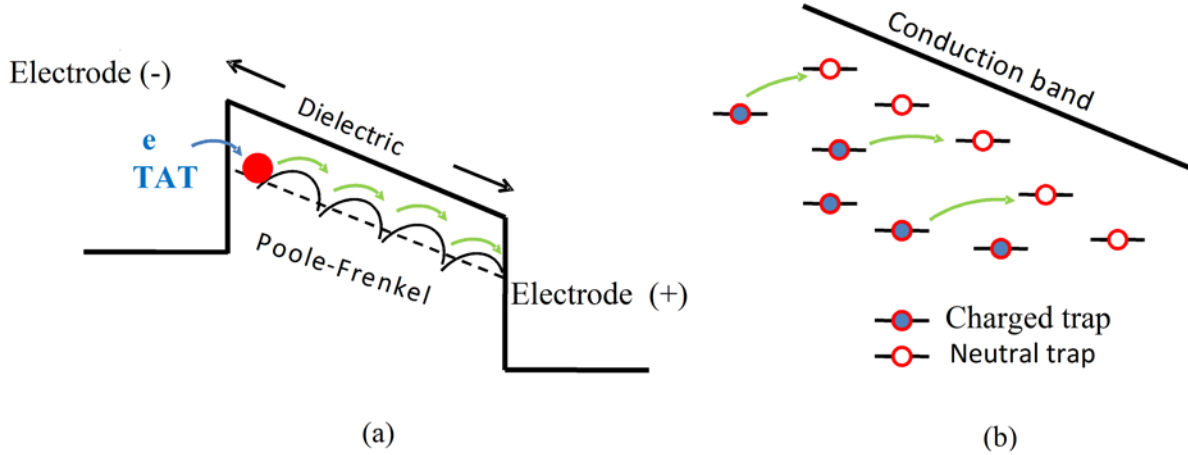


Figure 2.4. Illustration of the combined TAT and PF effects: (a) energy level diagram illustrating tunneled electrons from the electrode to the dielectric, and (b) excitation of tunneled electrons to the conduction band by PF.

#### 2.4.2.2 Trap Assisted Tunneling (TAT)

Trap assisted tunneling (TAT) is determined by the spatial and energetic distribution of trap states, the offset between the Fermi energy of the electrode and the conduction band of the dielectric and the lower limit of the tunneling relaxation times [40]. It has been widely investigated in thin dielectric films applicable to MOS capacitors and memory devices [41]. Defects in the dielectric layer give rise to tunneling processes based on two or more steps. **Figure 2.4** illustrates the combined contribution of both TAT and PF in MIM capacitors. Tunneled electrons from the MIM electrode to unoccupied defect or trap states in the dielectric close to the electrode-dielectric interface is shown in **Fig. 2.4a**. These electrons must be further excited to the conduction band again by the PF mechanism (**Fig. 2.4b**). Various models were reported to describe TAT process. A simple model applicable to MEMS switches which relates tunneling current density with the trap energy level is given by:

$$J_{TAT} \cong \exp\left[-\frac{4\sqrt{2qm_e}}{3\hbar E} \Phi_t^{3/2}\right] \quad (2.2)$$

where  $q$  is the electronic charge,  $m_e$  is the electron effective mass,  $\hbar$  is Planck's constant,  $E$  is the electric field, and  $\Phi_t$  is determined from the slope of " $\ln J_{TAT}$  versus  $1/E$ ".

## 2.5 Investigated dielectric materials in electrostatic MEMS

Several dielectric materials were investigated in electrostatic MEMS switches on the way to solving the dielectric charging problem. This includes SiO<sub>2</sub> [42], Si<sub>3</sub>N<sub>4</sub> [43, 44], AlN [45, 46, 47], Al<sub>2</sub>O<sub>3</sub> [48], Ta<sub>2</sub>O<sub>5</sub> [45, 49], and HfO<sub>2</sub> [50, 51].

SiO<sub>2</sub> and Si<sub>3</sub>N<sub>4</sub> are the most intensively investigated dielectric materials for electrostatic MEMS switches. In spite of the extensive knowledge gathered on their electrical properties and stemmed from the semiconductor technology, a comprehensive understanding of the charging phenomenon of these materials implemented in electrostatic MEMS switches is still missing. This is attributed to the deposition of dielectric films on rough metal surfaces and at low temperatures ( $\leq 300$  °C) which are normally required by the fabrication technology of MEMS switches. The underlying metal roughness influences the dielectric film surface morphology. Also, the low temperature deposition results in a considerable deviation of material stoichiometry, and leads to SiO<sub>x</sub> and SiN<sub>x</sub> films with  $x < 2$  and  $x < 1.33$ , respectively. Additionally, the low temperature gives rise to the formation of silicon nanoclusters and/or nanocrystals in both materials which are expected to lead to a random distribution of dipolar polarization as well as interfacial polarization. In SiO<sub>x</sub> the stored charge density was reported to be thermally activated, with activation energies of 0.35 eV and 0.30 eV [56]. Also, the time constants were found to be temperature independent. On the other hand, in SiN<sub>x</sub>, it was shown that the stored charge increases with the film thickness and the deposition temperature [52]. The "holes injection" introduces metastable traps [53, 54] which affect the charge transport in the dielectric film [55], and give rise to asymmetrical current-voltage characteristics in MIM capacitors with electrode-dielectric symmetry [32].

There is a little known on the influence of other investigated dielectric materials on MEMS reliability. Ta<sub>2</sub>O<sub>5</sub> and HfO<sub>2</sub> were used for MEMS switches due to their high dielectric constant (see **Table 2.2**). Both materials exhibit ionic conduction and in the case of Ta<sub>2</sub>O<sub>5</sub> it was reported that under high electric field space charge arises due to formation of anodic-cathodic vacancy pair [57]. In addition, isothermal current transients in chemical vapor deposited material revealed that protons are incorporated in the structure and the current transient arises from proton displacement [58]. In the case of HfO<sub>2</sub> material, it was shown that hole trapping produces stable

charge [59]. The trapped charge density was found to be strongly sensitive to the deposition methods and the work-function of the gate electrodes. In thin layers ( $\leq 10$  nm), it was shown that charge trapping follows a logarithmic dependence on time [60].

The charging behavior of  $\text{Al}_2\text{O}_3$  and  $\text{AlN}$  materials has not been deeply investigated. The O–Al bonds in  $\text{Al}_2\text{O}_3$  compound exhibit highly ionic nature. Experimental  $I(t)$  curves have shown that the ‘quasi’ steady-state current is reached for time ranging from 104 to 105 s [61]. The transient current was reported to consist of two components. The first component arises from the polarization of dipoles in the dielectric which dominate at short time, whereas the second one was reported to correspond to the carriers transport mechanism. On the other hand,  $\text{AlN}$  piezoelectric material was recently employed in MEMS switches [62]. Reliability measurements have shown that under low pull-in voltage or certain polarity the device degradation may be extremely low. Assessment of MIM capacitors with crystalline  $\text{AlN}$  dielectric has indicated that this behavior is attributed to the presence of a spontaneous polarization arising from dislocations that may induce a surface charge in the order of  $c.\text{cx}10^{-7}\text{Ccm}^{-2}$ , which is much smaller than the theoretically predicted spontaneous polarization [47].

**Table 2.2** summarizes the charging mechanisms which exist in the dielectric materials employed in electrostatic MEMS switches [63]. The space charge polarization due to presence of free charges or injected charges as well as the dipolar polarization constitutes the major charging mechanisms in all aforementioned dielectric films. The dielectric constant for each material is also presented in the table since it resembles an important selection criterion for MEMS dielectrics in addition to the material charging behavior. The investigated dielectric material in this thesis is plasma-enhanced chemical vapor deposition (PECVD)  $\text{SiN}_x$ .

Table 2.2. charging mechanisms and dielectric constants for dielectric materials used in MEMS capacitive switches, adapted from [63]. ‘\*’ indicates polarization due to deviation from stoichiometric materials.

Dielectric material	Space charge	Dipolar	Ionic	Dielectric constant
$\text{Si}_3\text{N}_4$	x	x*	-	6-7.5
$\text{SiO}_2$	x	x*	-	3-4.5
$\text{Ta}_2\text{O}_5$	x	x	x	~100
$\text{HfO}_2$	x	x	x	11-12
$\text{Al}_2\text{O}_3$	x	x	x	8-9
$\text{AlN}$	x	x	x	10-12

## 2.6 Available characterization techniques for the dielectric charging

Due to the complexity of dielectric charging phenomenon, it cannot be investigated through a simple assessment method, and hence various characterization techniques are required. For this reason, the charging was studied through numerous methods which are based on the actual MEMS switches, or metal-insulator-metal (MIM) capacitors, or bare dielectric films using Kelvin probe force microscopy (KPFM). In this section, the most important employed assessment methods are presented.

### 2.6.1 MEMS-based characterization methods

Several characterization methods were reported to study dielectric charging using the actual MEMS switches. Among those, the basic assessment methods rely on monitoring the shift of bias for minimum capacitance,  $V_{\min}$ , or pull-in and pull-out voltages of the C-V characteristic of a MEMS switch. The shift in  $V_{\min}$  method is based on the fact that when the switch dielectric is charged, the C-V characteristic below pull-in is asymmetrical. The unique advantage of  $V_{\min}$  based methodology is that the shift is a quantity that accurately provides information on the dielectric charging and does not depend on the mechanical parameters of the switch metal bridge (see **Fig. 2.1b**). For this reason, it has been widely used [19, 64] to assess the charging due to cycling and ESD stress at room as well as at elevated temperatures. Yet, the charge calculated through this method is obtained under low electric field conditions. Since the performance of a capacitive MEMS switch is determined by the shift of pull-in and pull-out voltages which occur under high electric fields, the importance of  $V_{\min}$ -based characterization technique is limited. This further explains why the influence of dielectric charging on the shift of pull-in and pull-out voltages and the evolution of their windows under electrical stress has been the most intensively investigated method to study charging in electrostatic MEMS switches.

Monitoring the switch-ON and switch-OFF transients or discharge current transients is another method to study the dielectric charging in MEMS switches [44, 65, 66]. In this technique, the dielectric charging and discharging kinetics and the mechanisms that contribute to them could be investigated. The modification of the electrostatic force between the switch bridge and the dielectric film by trapped charges resembles the concept behind this method. This effect is emphasized by the fact that in a real MEMS switch the surfaces of the switch bridge and the dielectric film are not perfectly flat during contact. So, the charge injection occurs through

asperities and the surface roughness. In the case of discharge currents, the C-V characteristic is required in order to determine the charge sign. On the other hand, the presence of thermally activated mechanisms in dielectrics requires characterizing MEMS switches under different temperatures.

### 2.6.2 *MIM-based characterization methods*

Although MIM capacitors do not substitute MEMS switches in the ‘up’ and ‘down’ states, they were proved to be valuable test structures for studying the electrical properties of dielectric materials. The dielectric charging in MIM capacitors were investigated through two experimental methods; the charge/discharge current transients (C/DCT) and the thermally stimulated depolarization currents (TSDC). Both methods are based on the application of an electric field for a long time so that to produce saturation of dipole orientation and trapping of injected charges. In the C/DCT method, the charging and discharging currents of a MIM capacitor are measured. The TSDC provides a complete picture of the temperature-dependent relaxations, and allows the parameters of activation energy,  $E_A$ , and relaxation time,  $\tau_0$ , to be obtained from a single measurement.

The C/DCT method was extensively applied to study dielectric charging in  $\text{SiO}_2$  [28] and  $\text{Si}_3\text{N}_4$  [37, 67, 68] films. In all cases, the results revealed that both the charging and discharging transients are multi exponential with temperature independent relaxation time constants. Also, the presence of thermally activated mechanisms in  $\text{SiN}_x$  was reported based on the C/DCT measurements. The decay was fitted using the stretched exponential law and the Arrhenius plot of relaxation time allowed the calculation of  $E_A$  and  $\tau_0$  at room temperature [67]. On the other hand, the advantages of employing the TSDC method are twofold. First, the measured TSDC current at different temperature is analyzed and leads to the different involved charging mechanism for which  $E_A$  and  $\tau_0$  can be determined. A direct example for that was reported by Papandreou et al. [69] where the relaxation times in  $\text{SiN}_x$  were found to be distributed around specific activation energies with values of 0.17 eV, 0.35 eV and 0.55 eV. The other important benefit is that the TSDC method could measure a wide range of relaxation times which exists in amorphous dielectric films where the relaxation times are normally distributed over several decades.

The abovementioned assessment methods applied for either actual MEMS switches or MIM capacitors, although extremely useful, lead to results that depend strongly on the nature of

the device under test. Thus, in MIM capacitors the discharge takes place under a short circuit condition and the trapped charges are collected by the injecting electrodes. On the contrary, in MEMS the injected charges are collected only by the bottom electrode while the top electrode, the bridge, is in the up-state (see **Fig. 2.1b**). Additionally, MEMS failure mechanisms are often related to multiphysics phenomena. For example, **Table 2.1** highlights that several failure mechanisms rather than the dielectric charging results in a shift of the C-V characteristics, and pull-in and pull-out voltages. This includes the elastic and plastic deformation of the bridge, corrosion, wear, friction, fretting corrosion, and creep failure mechanisms. Therefore, the characterization techniques which make use of the actual MEMS switches cannot study separately the dielectric charging phenomenon since other failure mechanisms contribute to the measurements. Besides, these methods are quite expensive and time consuming since the fabrication of the complete MEMS devices, including many levels of photolithography, is required.

### 2.6.3 *KPFM-based characterization*

More recently, KPFM-based characterization was employed to study the dielectric charging in MEMS switches and proved to be a promising methodology. In MEMS switch (**Fig. 2.1b**), due to the roughness of the metal layer under the dielectric film, the roughness of the bridge, and the surface micromachining process normally used to fabricate the device, the contact between the dielectric/bridge surfaces during the down-state occurs at numerous asperities as described in **Fig. 2.5**. The concept behind the KPFM-based characterization is using the AFM tip to simulate one of these asperities as shown in **Fig. 2.5**. In this technique, charges are injected first over bare dielectric films using a biased atomic force microscope (AFM) tip, and then the induced surface potential is measured using KPFM. The evolution of the injected charges by the AFM tip showed that the charges do not redistribute across the dielectric surface during charge dissipation, and the decay of the charge was attributed to transport and trapping into the bulk of the dielectric [70]. Moreover, the decay time constant extracted from KPFM surface potential decay was reported to depend on the dielectric material and practically not affected by the tip potential [71]. KPFM was also used to monitor the discharging process for a charged dielectric film implemented in electrostatic MEMS switch [72].

There are several advantages for the KPFM-based assessment methods. First, it efficiently simulates the charging through asperities and the charge collection through the bottom

electrode of MEMS switches providing qualitative information on dielectric free surface charge distribution and decay [70, 71, 73, 74, 75, 76]. Second, the KPFM-based technique allows studying the dielectric charging physics separately, and hence building a comprehensive understanding of the charging phenomenon without interferences with other failure mechanisms. Finally, it represents a low cost and quite fast solution compared to the currently available assessment methods since the required samples for this approach are bare dielectric films, hence no photolithography steps are required during the sample preparation [76].

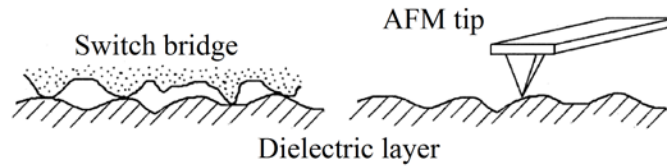


Figure 2.5. Multi-asperity contacts at the interface between the switch bridge and the dielectric film, and the usage of AFM tip to simulate a single asperity.

In spite of the abovementioned advantages, the KPFM based characterization suffers from several weaknesses. First, the AFM tip simulates charging through only a single asperity, while in MEMS switch charging takes place through thousands or millions of asperities simultaneously. Also, the published work related to dielectric charging assessment using KPFM was performed in ambient air, and hence the effect of relative humidity has not been addressed. Moreover, the used samples have not been thermally treated before the KPFM experiments. Jacobs et al. reported that at low humidity ( $\approx 10\%$ ) trapped surface charges could be detected in the KPFM measurements while such charging effects become less prominent at high humidity levels ( $\approx 80\%$ ) [77]. In addition, the adsorbed water layer on the sample surface is considered to shield the surface potential [78]. The removal of the water-related layer from both surfaces of the sample and the AFM tip was found to be very important to improve the reliability of KPFM measurements [79]. For these reasons, the available results from KPFM characterization related to the charging phenomenon have to be considered carefully since their experimental conditions have not been addressed properly. In addition, there has been no report on the dielectric charging under different electric fields comparable to the existing ones in driving MEMS switches using KPFM.

As concluded from the abovementioned discussion, each assessment method provides partial information about the charging phenomenon and has its own advantages and limitations.

The other critical issue is that there has been no correlation between the results from these assessment methods. Thus, the methods associated to MIM capacitors (C/DCT and TSDC) have been considered as efficient tools to assess the bulk properties of the dielectric films, which provide limited information and therefore being not appropriate to simulate MEMS. Also, there has been no link between the reported data from KPFM on the level of a single asperity and the measurement results of actual MEMS switches. In view of the aforesaid unique advantages of KPFM-based characterization, it becomes essential to investigate deeply and properly such nanoscale assessment methods. Additionally, a correlation between these nanoscale characterization results and the measurements from actual MEMS and MIM devices turns out to be vital for a comprehensive understanding of the charging phenomenon.

## **2.7 State-of-the-art knowledge and open issues**

As explained in section 2.3, the reliability of electrostatic capacitive MEMS switches is determined by several failure modes which originate from different mechanisms. In this section, we shall review the state-of-the-art knowledge related to the influence of several parameters on the reliability of these devices and the open issues which will be investigated in this thesis.

### *2.7.1 Effect of dielectric deposition conditions on charging*

Significant research was performed to identify the dependence of dielectric charging on material stoichiometry and its relation to the deposition parameters especially for PECVD  $\text{SiN}_x$  films. The distribution of relaxation times was studied by TSDC method in MIM capacitors with  $\text{SiN}_x$  films deposited with high frequency (13.6 MHz), low frequency (380 KHz) and mixed frequency (13.6 MHz + 380 KHz) deposition recipes [69]. More silicon rich  $\text{SiN}_x$  films were reported to have faster charge decay [68]. The stored charge was found to increase with increasing  $\text{SiN}_x$  deposition temperature [52, 80], a behavior which was attributed to increasing the nitrogen content in the  $\text{SiN}_x$  material with the temperature [80]. High deposition temperature was reported also to reduce the hydrogen concentration and particularly decrease N–H bonds compared to Si–H bonds films [81]. The charging of  $\text{SiN}_x$  was reported to increase when the silicon content increases in spite of the increasing leakage current [82]. The impact of surface and bulk leakage currents on the chemical modification of the dielectric film surface and charge accumulation were discussed by Shea et al. [83]. In spite of all of these efforts, the dependence of the dielectric charging in  $\text{SiN}_x$  films on material stoichiometry, which affect the concentration

of bulk and interface traps as well as the concentration of dipoles and charge accumulation, and its relation to the deposition parameters have not not fully understood.

### 2.7.2 *Effect of substrate charging*

Substrate charging was reported recently as a possible failure mechanism which affects the reliability and limits the lifetime of electrostatic capacitive MEMS switches [84]. Switches fabricated on different substrates were found to exhibit different lifetimes. Also, MEMS switches stressed using voltage levels below pull-in were reported to pull-in due to charging of the substrate. In MEMS switches fabricated on silicon substrates for example, charge injection has different scenarios: charging of the dielectric material deposited over the metallic transmission line (**Fig. 2.1b**), and charging of dielectric deposited directly over the silicon substrate in the coplanar wave guide (CPW) slots. In the latter, which is responsible for what is called substrate charging, the formation of the space charge region in the silicon substrate is expected to highly influence the charging/discharging processes. The substrate charging was investigated in [84] through ‘minimizing’ the former charging scenario (the dielectric film over the transmission line) which clearly indicates the contribution of the interposer dielectric charging to the substrate charging measurements. Therefore, to study the substrate charging phenomenon accurately, the charging of the interposer dielectric layer must be ‘completely’ avoided, which is not possible using the available characterization techniques of the actual MEMS device.

### 2.7.3 *Effect of packaging environment*

It is obvious that the packaging process and packaging environment could have a large impact on the functionality and reliability of MEMS switches. In spite of that very few works have addressed these issues. This includes performing lifetime measurements for MEMS switches from different origins and with different insulator materials ( $\text{SiO}_2$ ,  $\text{Ta}_2\text{O}_5$  and  $\text{SiN}_x$ ) in normal lab-air and nitrogen gas under the same actuation conditions [66]. For the three switches, the lifetime was found to be a factor of about 100 longer in nitrogen than in air. These effects were attributed to the higher humidity of air and its influence on charge trapping in the dielectric film. However, this explanation has to be taken carefully since changing the environment from air to nitrogen in the mentioned experiments employs two different parameters, which are the environment relative humidity and environment gas. For a proper analysis, the influence of each parameter should be addressed separately. On the other hand, for different types of unpackaged

[85] and packaged [86] capacitive MEMS switches tested under different humidity levels, it was found that bulk charging dominates in dry air, while surface charging increases rapidly with increasing humidity. Also, under comparable humidity levels and electric fields, unpackaged or improperly packaged switches employing SiO<sub>2</sub> were reported to be less susceptible to surface charging than switches made of SiN<sub>x</sub> [87]. This work, though useful, was based on measuring the shift in pull-in voltage with time under different humidity levels with its drawbacks mentioned in section 2.6, and it didn't lead to a full understanding of the impact of humidity on the charging/discharging processes in MEMS switches.

#### *2.7.4 Effect of tribological phenomena*

Tribological phenomena such as adhesion and friction are crucial in MEMS/NEMS devices requiring relative motion [20]. Due to the scale down with size in these devices, surface forces such as adhesion, friction, meniscus forces, viscous drag forces, and surface tension that are proportional to area become hundreds of times larger than the forces proportional to the volume, such as inertial and electromagnetic forces [88, 89, 90]. In addition, since MEMS are designed for small tolerances, physical contact becomes more likely, which makes them particularly vulnerable to adhesion between adjacent components. Since the start-up forces and torques involved in MEMS operation available to overcome retarding forces are relatively small, the increase in resistive forces such as adhesion and friction becomes a serious tribological concern. Several studies revealed the profound influence of adhesion and friction on the performance and reliability of MEMS [20, 91]. Also, various lubricant films were introduced to reduce adhesion and friction in these devices. Adhesion and friction measurements performed on self-assembled monolayers (SAMs) and on perfluoropolyether (PFPE) films showed that these films are potential candidate lubricants for MEMS devices [92, 93, 94]. Thus, these films could be used also as anti-adhesion coatings for MEMS in different environments. In addition, the adsorption of water molecules leading to the formation of meniscus and its change during sliding, and change in surface chemistry properties were reported to play a big role on the friction, adhesion, and durability of the interfacial films [94]. Finally, adhesive force and coefficient of friction were found to be dependent on the relative humidity [20, 95].

Electrostatic MEMS switches represent an example of MEMS devices with critical tribological concerns. The operation of the switch is based on the contact between two surfaces: the movable bridge and the dielectric film (see **Fig. 2.1b**), which are full of asperities as

described in **Fig. 2.5**. Since capillary condensation of water vapor from the environment results in the formation of meniscus bridges between contacting and near-contacting asperities of two surfaces in close proximity to each other [20], an intrinsic attractive force occurs which may lead to high adhesion and stiction between the two surfaces. Therefore, the adhesion or stiction between the switch bridge and the dielectric film could be also affected by meniscus formation. Consequently, micro/nanotribological studies are needed to develop a fundamental understanding of the interfacial phenomena between the two contacting surfaces of the switch. Similar to the concept behind using KPFM to study the dielectric charging phenomenon on the nanoscale, investigating a single asperity contact in studies of the fundamental tribological properties of both surfaces becomes essential.

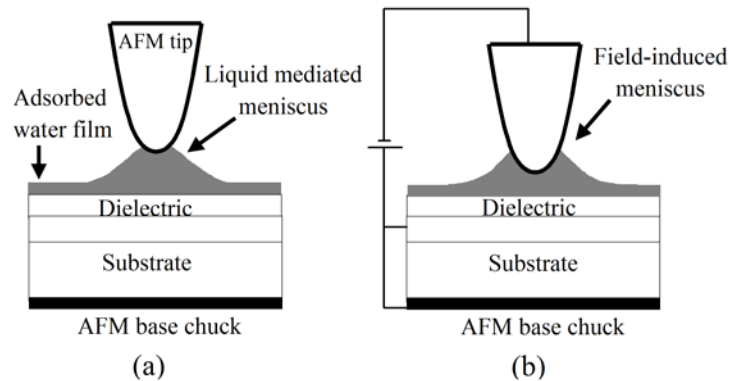


Figure 2.6. (a) Formation of liquid mediated meniscus when AFM tip comes in contact with the adsorbed water layer over the dielectric surface, and (b) the field-induced meniscus formed when electric field is applied between the tip and the sample.

A single asperity at the switch bridge-dielectric interface could be simulated using an AFM tip in contact with the dielectric layer (see **Fig. 2.5**). When the tip comes in contact with the adsorbed water film, a liquid mediated meniscus is formed between both surfaces as described in **Fig. 2.6a**. Moreover, when an electric field is applied between the AFM tip and the sample surface, a field-induced water meniscus is formed [96, 97, 98] as shown in **Fig. 2.6b**. A model that predicts the existence of a threshold field strength for the formation of a meniscus under a given tip-sample distance is presented in [97]. The lateral and vertical dimensions of field-induced meniscus was determined by Calleja et al. [96], and it was found that the meniscus size increases with increasing strength and duration of the voltage pulse. Menisci with diameters in the range of 20-80 nm were observed under different tip bias amplitudes and bias durations.

Based on these reported data, the applied bias used to actuate electrostatic MEMS switches and the resulting dielectric charging are expected to affect the meniscus formation at the switch bridge-dielectric interface, hence affecting the adhesion or stiction in these devices. The individual impact of the two stiction mechanisms (charging induced and meniscus force induced) and their multiphysics interaction under different electrical stress conditions and relative humidity levels have not been studied before. Also, the impact of the dielectric charging on the friction force between the switch bridge and the dielectric material, though expected, has not been investigated. Due to this multiphysics coupling between the dielectric charging and tribological phenomena, novel characterization tools which could address this interaction and provide a comprehensive understanding of the interfacial phenomena in electrostatic MEMS switches becomes necessary.

In conclusion, the reliability of electrostatic capacitive MEMS switches is determined by numerous factors. Several failure mechanisms are related to the charging phenomenon including the influence of field-induced meniscus, substrate, and packaging environment. In addition to the significant gap of information related to these effects, there are many open issues which are not fully understood related to the dielectric charging itself, for example the influence of dielectric deposition conditions and the working conditions of MEMS.

### **2.8 Summary and motivation**

A comprehensive overview of the current knowledge on the reliability of electrostatic MEMS switches has been presented. More attention has been paid to the charging related failure mechanisms describing the basic polarization/charging mechanisms in dielectrics, different dielectric materials used in MEMS, and the available characterization methods. The recent knowledge on the influence of various factors on the reliability of MEMS switches including the substrate charging and the tribological phenomena as well as numerous open issues have been discussed. There are key messages that could be concluded from the aforementioned discussion. First, the charging and the interfacial tribological phenomena in electrostatic MEMS and their related failure mechanisms are not entirely understood indicating that there are plenty of open issues to be investigated. Second, the presently available characterization techniques, though important, are not adequate to provide a comprehensive understanding of these reliability concerns. Finally, the nanoscale characterization techniques, for example KPFM, although providing unique information, have not been properly employed.

The motivation behind this thesis is to address the abovementioned weaknesses through introducing novel characterization methodologies for the charging and tribological phenomena, and then employing these methods to study several open issues. Two different categories of nanoscale and macroscale characterization techniques have been proposed based on Kelvin probe force microscopy (KPFM) and, for the first time, force-distance curve (FDC) measurements. In addition to the KPFM and FDC based assessment methods, the charge/discharge current transient (C/DCT) and thermally stimulated depolarization currents (TSDC) have been used to study the charging phenomena. The results from the proposed characterization methods have been correlated and linked to the data from other characterization techniques applied for MEMS switches or MIM capacitors. Using the proposed assessment methods as well as the conventional characterization techniques, the influence of various technological, environmental, and operational parameters on the charging/discharging processes has been investigated. This includes the effect of dielectric film thickness, dielectric deposition conditions, substrate charging, relative humidity, environment gases, stress electric field intensity, and stress duration. On the other hand, tribological phenomena (ex. adhesion and friction) have been studied under different relative humidity levels and electrical stress conditions to evaluate their influence on the reliability of MEMS switches. The multiphysics coupling between these tribological phenomena and the charging failure mechanism has been also investigated. The proposed characterization techniques in this thesis, though have been employed to investigate the reliability of electrostatic MEMS switches, could be extended to cover other electrostatic MEMS/NEMS devices.

*Do not be too timid and squeamish about your actions. All life is an experiment. The more experiments you make the better. What if they are a little course, and you may get your coat soiled or torn? What if you do fail, and get fairly rolled in the dirt once or twice. Up again, you shall never be so afraid of a tumble.*

*Ralph Waldo Emerson  
1803 – 1882, American philosopher, essayist, and poet*

### **3 Experimental context**

#### **3.1 Introduction**

In this chapter, the investigated samples and the employed characterization techniques are presented. Three electrical assessment methods were used to study the charging phenomenon in PECVD silicon nitride films which are based on KPFM, FDC, and DCT measurements. They were applied to study the charging in a large variety of samples with different layer structures including bare dielectric films, MIM capacitors, and electrostatic capacitive MEMS switches. Moreover, X-ray photoelectron spectroscopy (XPS) and Fourier transform infra-red spectroscopy (FT-IR) physical characterization techniques were used to determine the compositions and chemical bonds, respectively, of the investigated SiN<sub>x</sub> films.

The chapter is organized as follows. First, the layer structure of samples and the used deposition conditions of SiN<sub>x</sub> films are described. This is followed by discussing the theory, procedure, and an example of the results of the employed electrical characterization techniques. Finally, the physical material characterization methods are presented.

#### **3.2 Investigated samples**

Three different categories of PECVD SiN<sub>x</sub> samples were investigated. The first sample group consists of bare SiN<sub>x</sub> thin films deposited over planar substrates. The second and third sample groups are MIM capacitors and electrostatic capacitive MEMS switches, respectively, which implement the same SiN<sub>x</sub> films as dielectric layers.

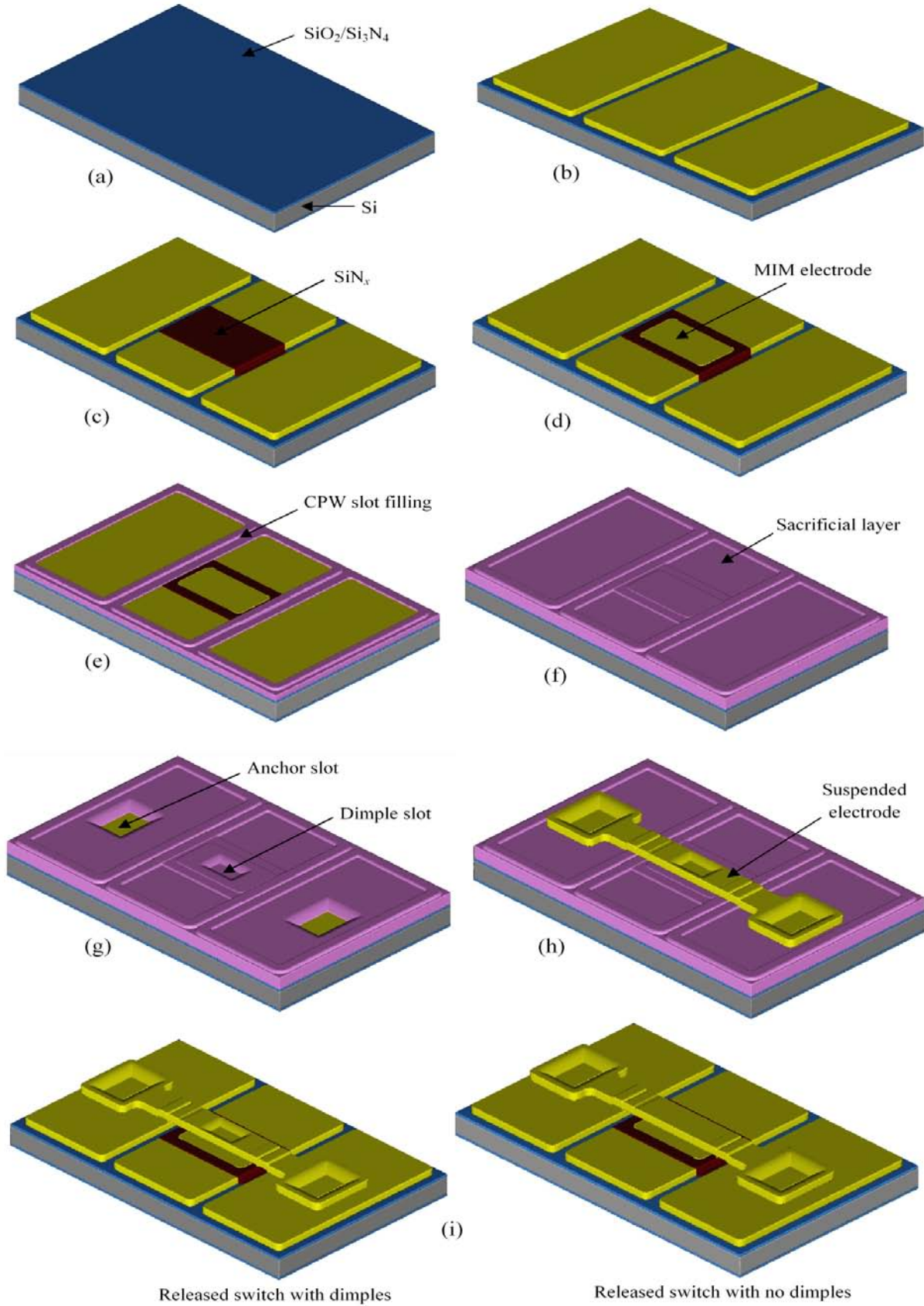


Figure 3.1 (a - i)

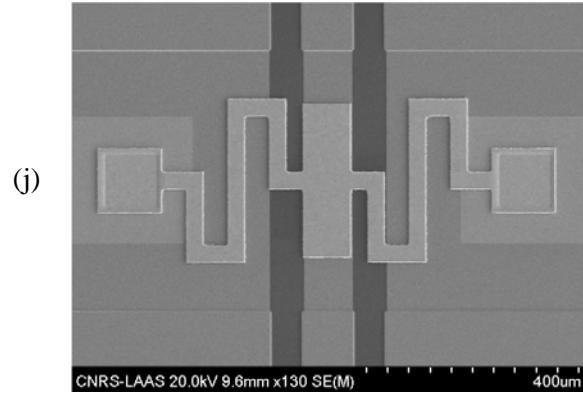


Figure 3.1. The fabrication process flow of electrostatic MEMS switches used in this study and an example of a finished device.

Electrostatic capacitive MEMS switches, the third group of samples, are normally fabricated using a relatively straightforward process. Two well known approaches are usually used to fabricate such devices [8]. The first one is to fabricate MEMS switches directly on the microwave substrate [99, 100] using surface micromachining process [101]. Another possibility is to fabricate MEMS switches on a low resistivity silicon substrate using standard high-temperature poly-silicon and Low pressure chemical vapor deposition (LPCVD) processing, and then transfer them to the carrier microwave substrate using substrate dissolution techniques [102, 103]. In both approaches, the critical step is the development of a low-stress thin film process for the movable electrode material (see **Fig. 2.1b**). The suspended electrode must have a low biaxial residual stress and a low stress gradient in the vertical direction. Otherwise, it will bow up or down by several micrometers, which results in a very large change in the actuation voltage and may render the switch unusable. The MEMS switches used in this study were fabricated on silicon substrates using the first approach and the employed process flow is described in **Fig. 3.1**. The process starts with cleaning high resistivity Si wafers using the RCA method. This is followed by thermally growing a 200 nm-thick dry SiO<sub>2</sub> layer and depositing a 200 nm-thick LPCVD Si<sub>3</sub>N<sub>4</sub> film to provide an electrical isolation from the substrate (**Fig. 3.1a**). The following are the major steps in the fabrication process flow:

- (a) *Coplanar wave guide (CPW)*: A Ti/Au (50 nm/200 nm) seed layer is evaporated and a photoresist mould is patterned to define the CPW lines. Next, a 2.5  $\mu\text{m}$  Au is electrochemically deposited and the photoresist mould is removed. A 50 nm Ti layer is then evaporated over the electroplated Au layer to provide a proper adhesion with the dielectric

film which will be deposited later. Then, the Ti/Au/Ti layers are chemically etched to define the CPW lines (**Fig. 3.1b**).

- (b) *Dielectric layer*: A PECVD SiN<sub>x</sub> layer is deposited and patterned using reactive ion etching (RIE) to form the switch dielectric layer (**Fig. 3.1c**).
- (c) *MIM capacitor*: This step is optional and is used to fabricate MIM capacitors in the same process along with MEMS switches. This is made by evaporating and patterning a Ti/Au (50 nm/ 200 nm) layer over the SiN<sub>x</sub> film to define the MIM top electrode (**Fig. 3.1d**). This floating metal layer can be implemented in MEMS switches as well in order to increase the C<sub>on</sub>/C<sub>off</sub> ratio.
- (d) *CPW slot filling*: A 2.5 μm layer of PMGI SF15 (polydimethylglutarimide) polyimide or AZ1529 photoresist layer is spun coated over the wafer and pre-baked. This dumpy layer is intended to fill the gaps in the CPW slots to improve the suspended electrode planarity and smoothness. After photolithography, this layer is etched and hard-baked (**Fig. 3.1e**).
- (e) *Sacrificial layer*: Another 2.5 μm PMGI or AZ1529 layer is spun coated and pre-baked to form the sacrificial layer (**Fig. 3.1f**). Then, the openings for both anchors and dimples (optional) are defined in this layer by photolithography (**Fig. 3.1g**). Next, the sacrificial layer is hard-baked at higher temperature than the vitreous transition to promote the spreading. For PMGI, a chemical mechanical polishing (CMP) step can be performed before hard-baking in order to improve the planarity.
- (f) *Suspended electrode*: A 100 nm Au seed layer is evaporated. Then, a 2 μm electrochemically-deposited Au layer is deposited over the sacrificial layer and is patterned by chemical etching to define the suspended electrode (**Fig. 3.1h**).
- (g) *Releasing the movable electrode*: The final step in the process is to remove the sacrificial layer by wet etching. Then, the suspended electrode is released using the CO<sub>2</sub> supercritical dryer (**Fig. 3.1i**).

An example of finished capacitive MEMS switch fabricated in LAAS –CNRS using this process is presented in **Fig. 3.1j**. Also, more details about the employed fabrication process flow and optimization can be found in [104]. The used electrostatic MEMS switches in this study were unpackaged. In view of the aforesaid fabrication steps, it is obvious that developing a reliable technological process for realizing these devices is a big challenge that requires tremendous amount of research work. This includes determining the optimum deposition

conditions of the dielectric film, selecting the substrate and underlying metal layers, and specifying the packaging environment and prototype, which lead to MEMS switches with reduced charging, hence with better reliability. These concerns will be investigated in details in this thesis.

A cross section of an electrostatic capacitive MEMS switch fabricated on Si substrate is presented in **Fig. 3.2a**. It is evident from the figure that there are two different charging scenarios in these devices where the dielectric layer is deposited over the metallic transmission line and extends directly over the Si substrate in the CPW slots. In order to investigate these two

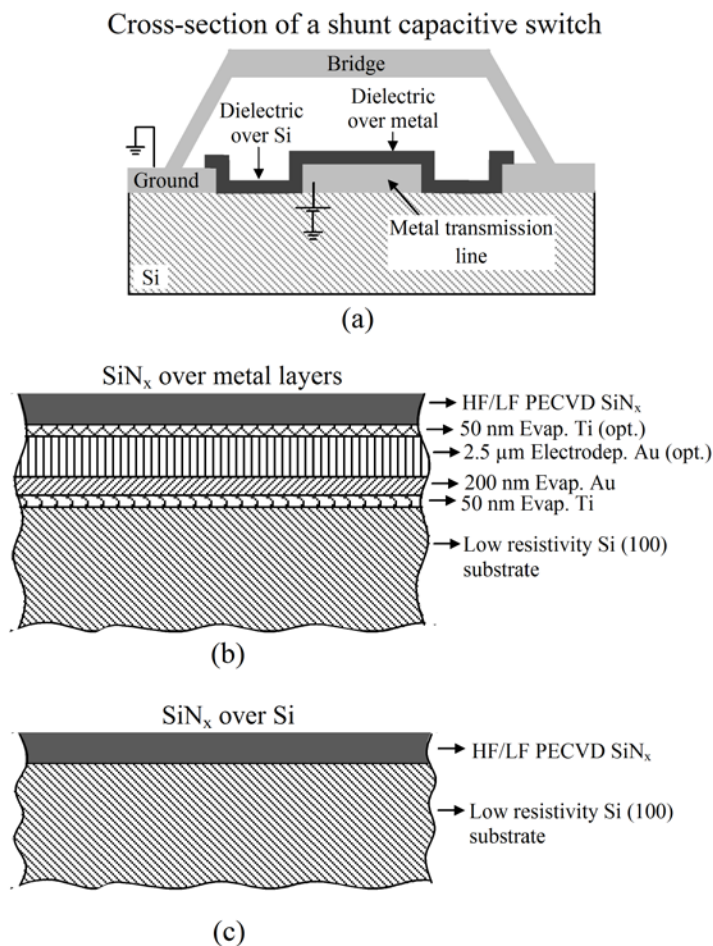


Figure 3.2. (a) Vertical cross section of a capacitive MEMS switch fabricated on silicon substrate; and the layer structure of the investigated bare dielectric samples (b)  $\text{SiN}_x$  over metal, and (c) over silicon.

scenarios, the first group of samples (bare dielectrics) includes  $\text{SiN}_x$  films deposited over metal layers (**Fig. 3.2b**) and directly over Si substrates (**Fig. 3.2c**). In both cases, the  $\text{SiN}_x$  films were deposited with different thicknesses in order to study the effect of dielectric film thickness on charging. The details of the layer structure for the first sample group are presented in **Table 3.1**. The impact of the metal layer over which the dielectric is deposited has also been investigated through depositing  $\text{SiN}_x$  films on evaporated gold (Evap Au), evaporated titanium (Evap Ti), and electrochemically-deposited gold (ECD Au) layers (**Fig. 3.2b**). These are the different metal layers used in the fabrication process flow described in **Fig. 3.1**. In addition, the

influence of the underneath metal layer roughness on the charging process was studied through the Evap Au and ECD Au samples which have an average roughness of 1.6 nm and 6.3 nm, respectively.

The deposition of the  $\text{SiN}_x$  films was carried out using a PECVD reactor (STS, Multiplex Pro-CVD). For this reactor, a pair of 8" size upper and bottom electrodes made of stainless steel is used within the deposition chamber that is kept at high vacuum during the deposition process. During the deposition process, silane ( $\text{SiH}_4$ ) and ammonia ( $\text{NH}_3$ ) are used as the reactive species, while nitrogen ( $\text{N}_2$ ) is used as a dilution gas. The main feature of this deposition system is its duality of RF operation modes, namely low frequency (LF) at 380 KHz and high frequency (HF) at 13.56 MHz. Also, the operating power can be adjusted to range from 0 to 1000 W in the LF mode and from 0 to 600 W in the HF mode. Other features of the system include the pressure ranging from 0 to 2000 mTorr;  $\text{SiH}_4$  flow rates ranging from 0 to 500 sccm;  $\text{NH}_3$  flow rates ranging from 0 to 360 sccm and  $\text{N}_2$  flow rates varying from 0 to 5000 sccm. In order to study the influence of the dielectric deposition conditions on the charging phenomenon, various  $\text{SiN}_x$  deposition parameters were used. **Table 3.2** shows the parameters of the two deposition recipes extensively used in this study (LF and HF) which were employed to deposit the  $\text{SiN}_x$  films with different thicknesses over different substrates shown in **Table 3.1**. As shown from the table, the two recipes doesn't have only different deposition RF mode, but also dissimilar gas flow rate, RF power, and chamber pressure.  $\text{SiN}_x$  films were also deposited using different deposition conditions by changing individually the reactive gas ratio ( $\text{SiH}_4/\text{NH}_3$ ), RF power, and substrate temperature, as will be discussed in chapter 6.

Table 3.1. The layer structure of bare  $\text{SiN}_x$  samples. The samples' names are designated as follows: the used deposition recipe (HF or LF) followed by the layer under the dielectric film, ex: HF-Evap Au means HF  $\text{SiN}_x$  deposited over evaporated gold.

Sample designation	HF-Evap Au	HF-Si	HF-ECD Au	HF-Evap Ti	LF-Evap Au	LF-Si	LF-ECD Au	LF-Evap Ti
$\text{SiN}_x$ (nm) HF/LF PECVD	100, 200, 300, 400	100,200, 300, 400	200, 300	200, 300	100, 200, 300, 400	100,200, 300, 400	200, 300	200, 300
Ti (nm) Evaporated	-	-	-	<b>50</b>	-	-	-	<b>50</b>
Au ( $\mu\text{m}$ ) Electrodeposited	-	-	<b>2.5</b>	-	-	-	<b>2.5</b>	-
Au (nm) Evaporated	<b>200</b>	-	200	200	<b>200</b>	-	200	200
Ti (nm) Evaporated	50	-	50	50	50	-	50	50
Low resistivity Si (100) ( $\mu\text{m}$ )	500	<b>500</b>	500	500	500	<b>500</b>	500	500

Table 3.2. PECVD deposition parameters for the HF and LF deposition recipes.

Parameter		High Frequency (HF)	Low Frequency (LF)
Gas flow rate (sccm)	SiH <sub>4</sub>	18	21
	NH <sub>3</sub>	40	15
	N <sub>2</sub>	1200	1960
Radio frequency (RF) power (W)		20	185
Chamber pressure (mTorr)		1000	650
Radio frequency mode		13.56 MHz	380 kHz
Substrate temperature (°C)		200	200

The second sample group consists of circular MIM capacitors of 500  $\mu\text{m}$  diameter. Similar to the bare dielectric samples, MIM capacitors with SiN<sub>x</sub> films which have different thicknesses and deposited using both HF and LF recipes were investigated. The layer structure of the used MIM capacitors is presented in **Table 3.3**, and it shows that the SiN<sub>x</sub>/metal interface for top and bottom electrodes is asymmetric.

Table 3.3. The layer structure of the investigated MIM capacitors.

	Sample designation	MIM-HF	MIM-LF
Top Electrode	Evaporated Au (nm)	800	800
	Evaporated Ti (nm)	100	100
Dielectric	PECVD SiN <sub>x</sub> (nm)	100, 200, 300, 400	100, 200, 300, 400
Bottom Electrode	Evaporated Au (nm)	500	500
	Evaporated Ti (nm)	100	100
Substrate	Low resistivity Si (100) ( $\mu\text{m}$ )	500	500

### 3.3 KPFM-based characterization

In this section, the theory behind surface potential measurements using KPFM is presented first. This is followed by discussing the procedure of different KPFM-based characterization techniques employed to study the charging phenomenon. The critical KPFM measurement parameters and their optimization are also discussed.

#### 3.3.1 KPFM theory

A block diagram of the KPFM surface potential measurement system is shown in **Fig. 3.3a**. There are three spectral components for the electrostatic force between the AFM tip and the sample surface that exist at DC,  $\omega$  and  $2\omega$ , and are given by [105, 106, 107]

$$\left. \begin{aligned}
 F_{DC} &= -\frac{1}{2} \frac{dC}{dz} ((\Delta\Phi - U_{DC})^2 + \frac{1}{2} U_{AC}^2) \\
 F_{\omega} &= -\frac{dC}{dz} (\Delta\Phi - U_{DC}) U_{AC} \sin(\omega t) \\
 F_{2\omega} &= \frac{1}{4} \frac{dC}{dz} U_{AC}^2 \cos(2\omega t)
 \end{aligned} \right\} \quad (3.1)$$

where  $\omega$  is the mechanical resonance frequency of the AFM tip,  $C$  is the capacitance between the tip and the sample surface,  $z$  is the tip-sample separation,  $\Delta\Phi$  is the contact potential difference between the tip and the sample materials,  $U_{DC}$  is the applied DC voltage to the AFM tip from the KPFM feedback loop, and  $U_{AC}$  is the voltage amplitude of the sinusoidal signal applied from the oscillator to drive the AFM tip at or very close to  $\omega$  during the surface potential measurements. Since the cantilever responds only to forces at or very close to its resonance frequency, the DC and  $F_{2\omega}$  force components do not cause any significant oscillation of the cantilever, and  $F_{\omega}$  becomes the dominant one. The main goal of the KPFM feedback loop is to adjust the potential of the tip,  $U_{DC}$ , until the term  $\Delta\Phi - U_{DC}$  becomes 0, at which point the cantilever oscillation amplitude should be zero ( $F_{\omega} = 0$ ). At this point, the measured tip potential,  $U_{tip}$ , which corresponds to the contact potential difference between the tip and the sample,  $\Delta\Phi$ , is equal to the sample surface potential, and is used to generate a potential map for the sample surface. The presence of the induced charges on a charged dielectric surface produces an additional electrostatic force which contributes to the total electrostatic force between the AFM tip and the sample surface. In other words, the trapped charge alters the contact potential difference between the tip and the dielectric materials,  $\Delta\Phi$ , and therefore could be determined by the local measured tip potential,  $U_{DC}$ .

The KPFM surface potential measurements are normally performed using the lift-mode (**Fig. 3.3b**). In this mode, the surface topography and the potential signals are subsequently recorded over the sample surface. First the surface topography is acquired in tapping mode along a single line profile (1 in **Fig. 3.3b**) [108]. Next, the mechanical excitation of the cantilever is turned off and the tip ascends to a fixed distance from the sample surface  $H$  (2 in **Fig. 3.3b**). Finally, a second scan is executed along the same line following the same topographic profile recording local variations in the surface potential (3 in **Fig. 3.3b**). In this study, conductive scanning capacitance microscopy-Platinum Iridium Tapping (SCM-PIT) AFM tips from

NanoWorld<sup>®</sup> were used for the KPFM measurements. These tips are Antimony n-doped Si, coated with platinum/iridium to provide high conductivity, and have a typical tip radius of less than 25 nm. The metallic coating as well as the low spring constant ( $K = 1-5$  N/m) and the low resonance frequency ( $f_o = 60-100$  KHz) of these tips make them well suited for sensitive surface potential measurements.

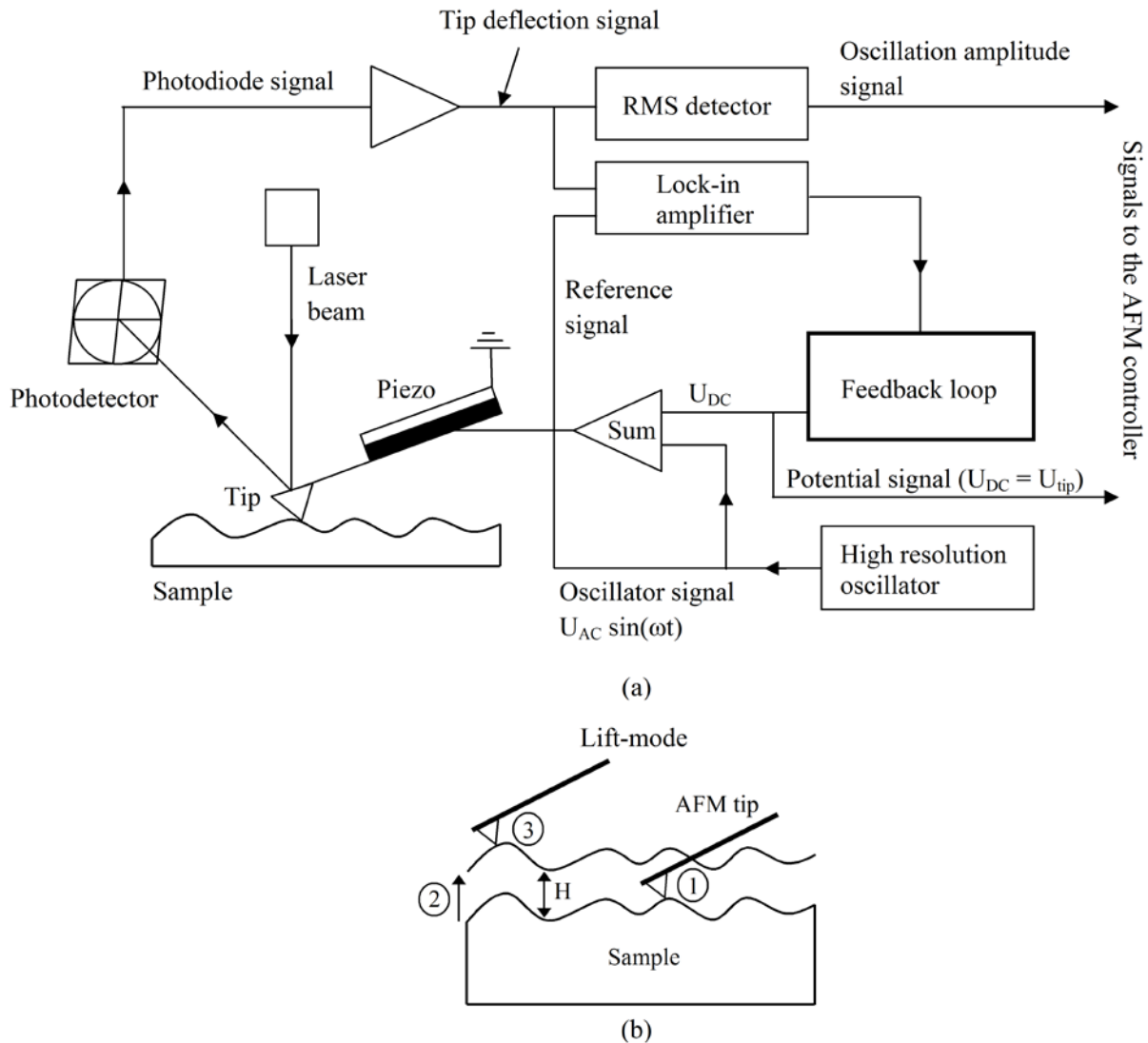


Figure 3.3. Procedure of KPFM surface potential measurements: (a) a block diagram, (b) the lift-mode.

Three different characterization methodologies based on KPFM surface potential measurements have been introduced to study the charging phenomena. This includes the application of KPFM to investigate the charging in bare dielectric thin films (KPFM-TF), MIM capacitors (KPFM-MIM), and MEMS switches (KPFM-MEMS).

### 3.3.2 KPFM-TF technique

The KPFM-TF characterization method is used to study the charging in bare  $\text{SiN}_x$  thin films (TF) deposited over planar substrates which are described in **Fig. 3.2b, c** and **Table 3.1**. The procedure of this assessment method constitutes two consecutive steps as shown in **Fig. 3.4**. First, charges are injected in single points over the  $\text{SiN}_x$  surface by applying voltage pulses of defined amplitude,  $U_p$ , and duration,  $T_p$ , to the AFM tip during scanning the sample surface in tapping mode (**Fig. 3.4a**). In this mode, the oscillating tip alternately contacts the sample surface and lifts off, generally at the cantilever resonance frequency using a piezoelectric actuator. As the oscillating cantilever begins to intermittently contact the surface, the oscillation amplitude is reduced due to energy loss caused by the tip contacting the surface. The pulse duration,  $T_p$ , is selected to be much longer than the tapping period of the cantilever in order to ensure that the tip will touch the sample surface several times during each pulse. The tapping mode was used for charge injection since it is the most reliable mode for obtaining reproducible KPFM results. Charge injection in contact mode often led to a damaged tip shape which affects the KPFM measurements negatively. After completing the charge injection, KPFM surface potential measurement is performed using the lift-mode as explained above. For all KPFM-TF experiments, the time interval between the end of charge injection step and the beginning of surface potential measurements is fixed to be 30 s.

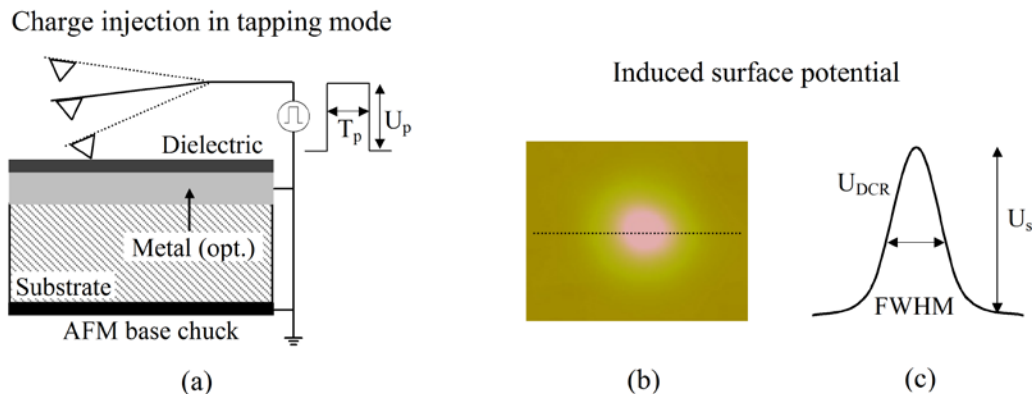


Figure 3.4. Dielectric charging assessment using KPFM-TF technique: (a) charge injection in tapping mode, (b) resulting surface potential map from a single injected point, and (c) the extracted relative potential profile represented by  $U_s$  and FWHM.

For each injected position over the dielectric surface, the measured surface potential,  $U_{DC}$ , has a maximum at the position which was directly under the AFM tip apex during the

charge injection step, and it decreases gradually at the edges of injected position as shown in **Fig. 3.4b, c**. The peak value of the induced surface potential is located in the KPFM map, and a horizontal cross section is taken at this position resulting in the absolute surface potential profile. In order to eliminate the impact of the tip material, the background surface potential of the  $\text{SiN}_x$  film was measured first before performing the charge injection step. Then, the background potential was subtracted from the absolute potential profile resulting in the relative surface potential profile,  $U_{\text{DCR}}$  (**Fig. 3.4c**) which is a direct indication of the injected charge density in the dielectric film. Therefore, the analysis of KPFM-TF results is performed using the surface potential peak amplitude,  $U_s$ , full width at half maximum (FWHM), and the integral of the relative potential profile (**Fig. 3.4c**). For better accuracy, each KPFM-TF measurement was performed three times, and a statistical evaluation was made by averaging over these three measurements. The evolution of  $U_s$  and FWHM with time were also monitored and analyzed in order to study the discharging process in dielectric films.

An example of KPFM-TF surface potential maps measured for charges injected under different pulse amplitude,  $U_p$ , using positive and negative voltage is presented in **Fig. 3.5a, b**, respectively. The figure also shows the potential maps obtained at different time points after the charge injection step for studying the charge relaxation. The decay of the measured surface potential with time due to charge collection is obvious from the figure. **Fig. 3.5c** presents the resulting potential profile for charges injected under different pulse amplitude,  $U_p$ . It is clear from the figure that  $U_s$ , FWHM (**Fig. 3.5d**) and consequently the potential profile integral (**Fig. 3.5e**) increases remarkably with increasing the applied pulse amplitude.

### 3.3.3 KPFM measurement parameters

During surface topography scan, the AFM tip is held grounded. So, attractive Coulomb forces arise between the tip and the sample due to the induced surface potential over the dielectric surface resulting from the charging step. These electrostatic forces result in a damping of the tip oscillation amplitude, and cause the controller to retract the tip far from the surface, resulting in an apparently higher topography [109, 110]. In other words, the controller cannot discriminate between electrostatic and van der Waals forces, and therefore the electrostatic forces could cause errors in surface topography imaging. In spite that tapping mode, which operates in the repulsive force regime, is less sensitive to electrostatic forces, topography errors will exist when electrostatic forces exceed the average tip-sample interaction forces. Since the

KPFM measurements are performed in lift-mode (see **Fig. 3.3b**) and the surface potential is determined based on the surface topography measured in the first scan pass, any fault in the topography scan will lead to an erroneous KPFM surface potential signals. In addition, due to the increased tip sample separation done by the controller as a result of the electrostatic forces, the lateral resolution of KPFM surface potential is degraded.

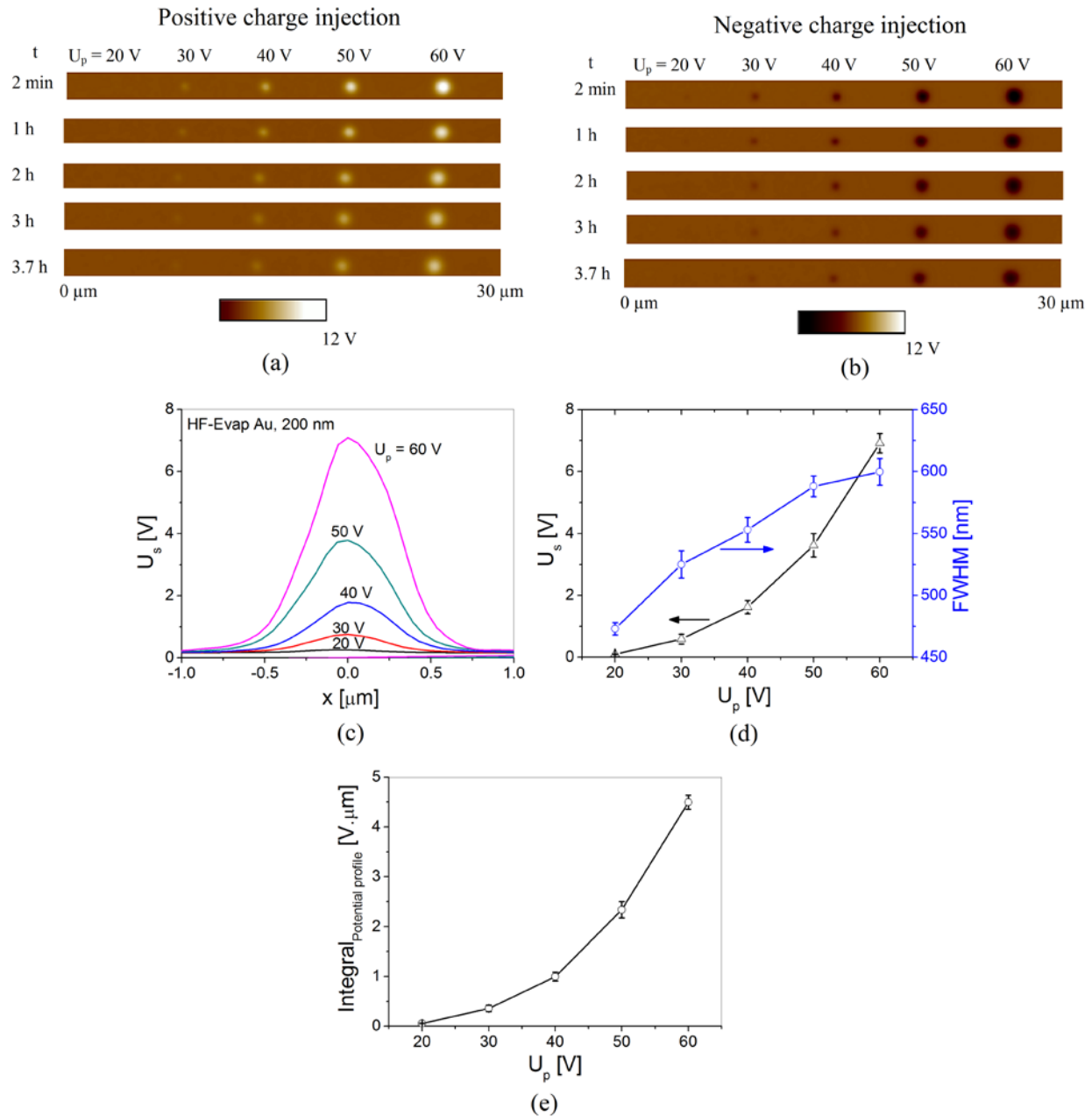


Figure 3.5. An example of KPFM-TF results for charges injected using different  $U_p$ : surface potential maps obtained at different time points after charge injection for (a) positive and (b) negative charge injection; (c) the potential profiles for positive charge injection at  $t = 0$ , (d) the corresponding  $U_s$ , FWHM, and (e) potential profile integral.

In this study, charges were injected using relatively high voltage levels, comparable to the large actuation voltage normally used to drive MEMS switches. This often results in relatively large induced surface potential which shown to affect the surface topography scan remarkably, resulting in an erroneous topography signal and degrading the lateral resolution. In order to overcome this issue, the feed-forward compensation technique proposed by Ziegler et al. [111] was employed in our KPFM measurements. In this technique, during the topography scan the AFM tip is biased with the surface potential recorded in the previous KPFM scan line in order to minimize electrostatic forces. An example of the surface potential and topography maps measured for charges injected under positive and negative voltage are presented in **Fig. 3.6**. Thanks to the employed feed-forward method, the injected charge in the  $\text{SiN}_x$  film has no effect on the topography maps.

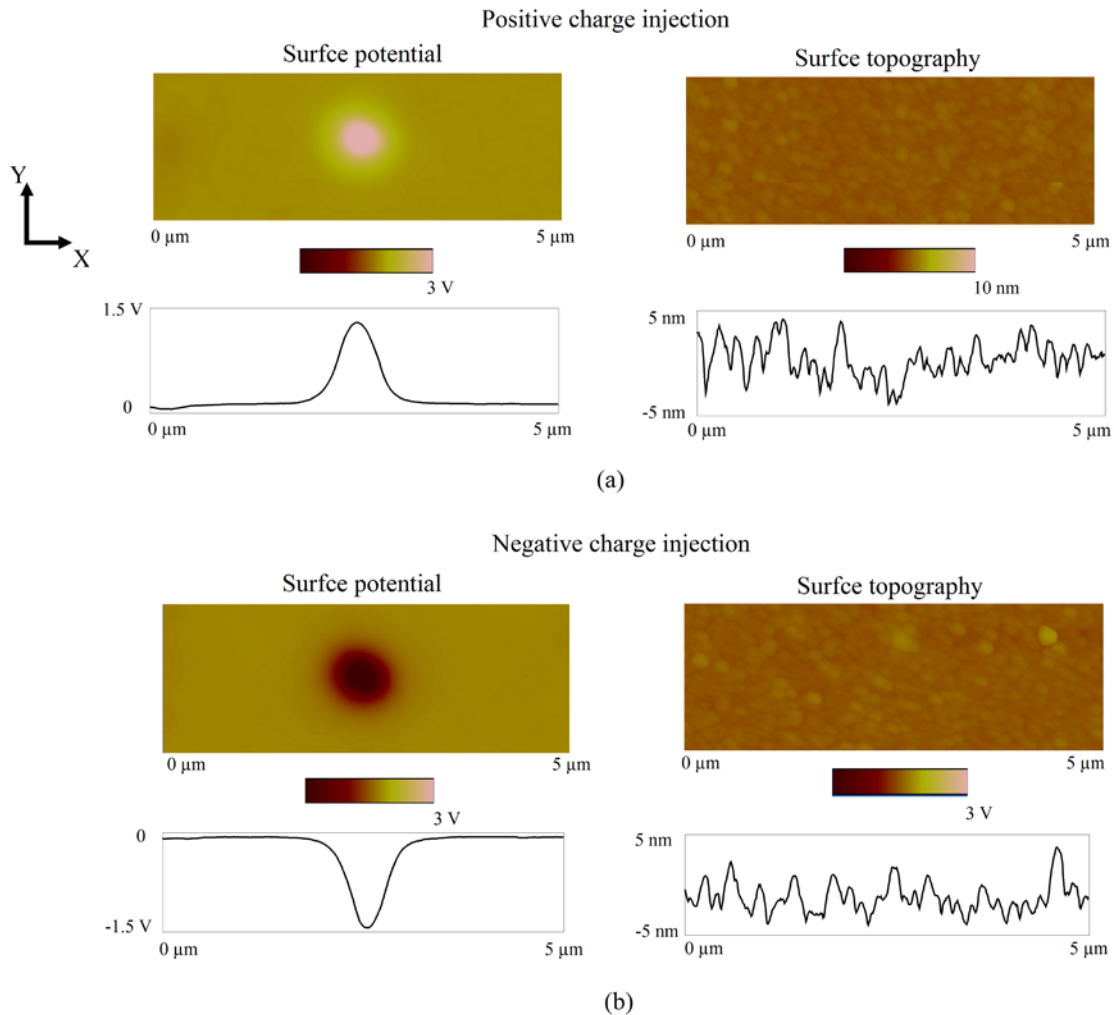


Figure 3.6. The induced surface potential and surface topography measured after charge injection for (a) positive and (b) negative charge injection while employing the feed-forward method.

One important parameter which can be controlled during the surface potential scanning is the lift scan height,  $H$  (**Fig. 3.3b**) which controls the separation between the tip and sample surface. The smaller the value of  $H$  is, the better the lateral resolution and the signal to noise ratio of the scanned potential. However, as the separation between the tip and the sample surface becomes smaller, the surface topography artifacts tend to be more pronounced in the measured potential data. Basically, the lower limit of  $H$  is determined by the sample roughness, scan speed, and tip oscillation amplitude used during the tuning step, etc. In order to investigate the impact of  $H$  on our KPFM measurements, charges were injected on the  $\text{SiN}_x$  surface and the induced surface potential maps were obtained at different tip-sample separations. **Figure 3.7a** presents the potential maps measured at the center of the injected charge position under different  $H$ . The relative surface potential profile and the peak potential amplitude,  $U_s$ , for different  $H$  are plotted in **Fig. 3.7b, c**, respectively. It is evident from the figures that the measured surface potential decreases as  $H$  increases, and this effect is more pronounced at smaller tip-sample separations. **Figure 3.7b** shows also that the noise in KPFM potential signal increases as  $H$  decreases due to the more prominent effect of topography artifacts.

The variation in KPFM surface potential with tip sample-separation could be understood considering the electrostatic force acting between the tip and the sample surface with  $n$  inhomogeneous regions, which is given by [112]

$$F_\omega = \sum_{i=1}^n -\frac{\partial C_i}{\partial z} (\Delta\Phi - U_{DC}) U_{AC} \sin(\omega t) \quad (3.2)$$

where  $\partial C_i/\partial z$  is the derivative of the capacitance between the tip and the area of the sample surface with the potential  $\Delta\Phi_i$ . The capacitance between the tip and the sample and its derivative depend on the tip shape, the tip-sample separation and the position of the tip over various regions on the sample surface. Thus, for a homogeneous sample the measured surface potential is independent of the tip-sample separation and the tip shape. In contrast, for an inhomogeneous sample the measured potential is averaged over all existing potentials  $\Delta\Phi_i$  on the surface, with the capacitance derivatives being the weighting factors [112, 113]. In our experiments, the sample surface is inhomogeneous due to the charge injection in single points over the dielectric surface. The measured surface potential is averaged over the injected/non-injected areas on the  $\text{SiN}_x$  surface, and therefore is affected by the tip-sample separation. As the tip goes far from the

sample surface ( $H$  increases),  $\partial C_i/\partial z$  decreases resulting in reducing the measured surface potential as obtained in **Fig. 3.7b, c**.

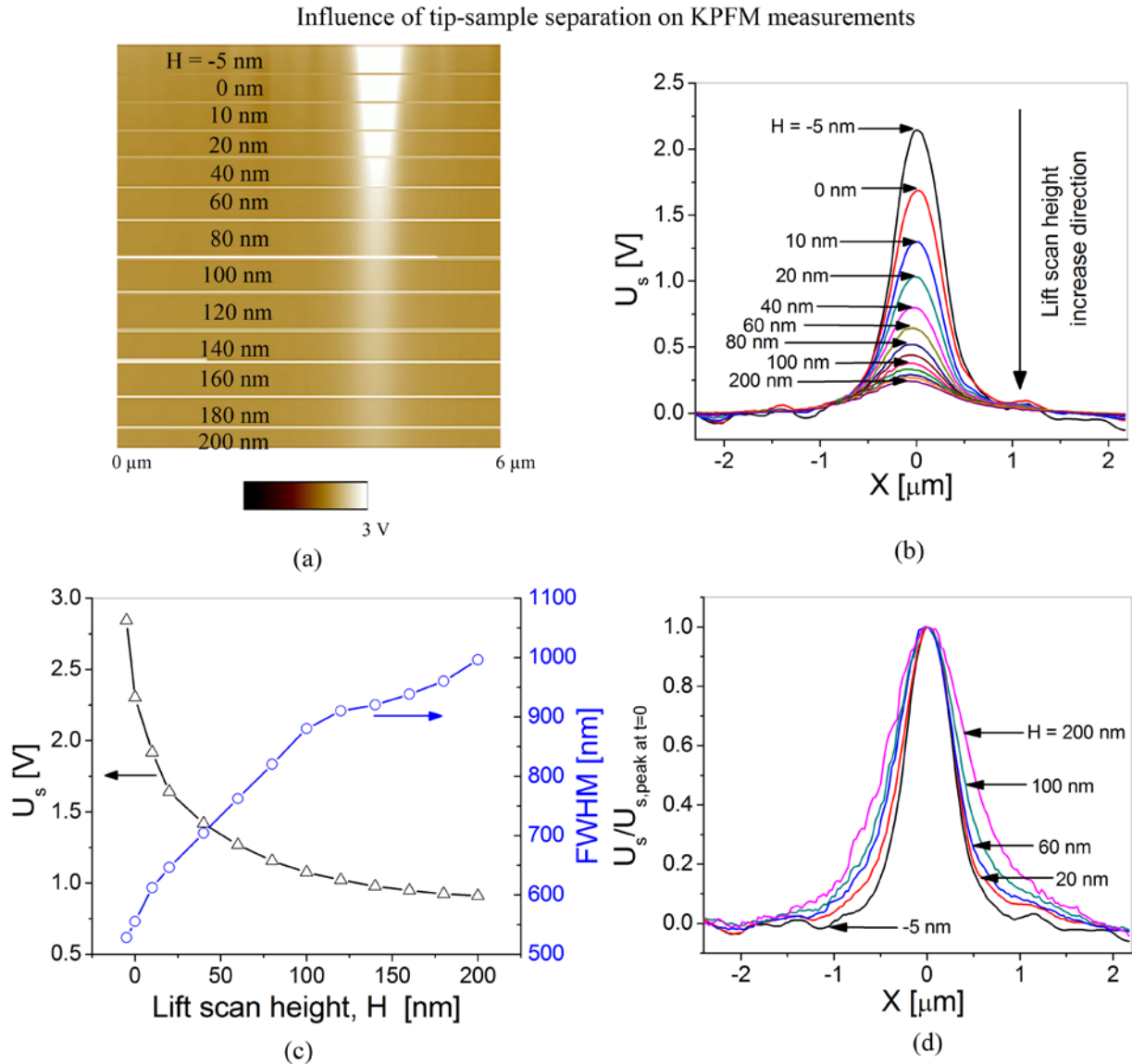


Figure 3.7. The influence of lift scan height,  $H$ , on the KPFM potential signal: (a) surface potential maps obtained at different  $H$ , (b) the corresponding potential profiles, (c) extracted  $U_s$  and FWHM versus  $H$ , and (d) normalized potential profiles.

In order to investigate the impact of tip-sample separation on the KPFM potential lateral resolution, the normalized surface potential at different  $H$  is plotted in **Fig. 3.7d**. Also, the FWHM of the normalized surface potential is plotted versus  $H$  in **Fig. 3.7c**. Obviously, the FWHM increases as the tip travels far from the sample surface and hence the lateral resolution is degraded. The surface potential changes gradually at the edges of injected charge due to the

averaging of the measured signal over injected/non-injected areas, which possibly results from the long-range electrostatic interaction between the tip and the sample [112, 113]. This averaging is expected to be extended to include larger areas on the sample surface as the tip-sample increases. Therefore, the transition from the non-injected area to the injected area will be less sharp and so the FWHM will increase as  $H$  increases. For our KPFM experiments, the optimized value of  $H$  which minimizes the influence of surface topography artifacts and at the same time provides an acceptable lateral potential resolution was found to be 20 nm.

In addition to optimizing the tip-sample separation, the sensitivity and stability of KPFM potential measurements were enhanced by fine tuning the feedback system (**Fig. 3.3a**). For example, the ‘drive phase’ which is the phase difference between the reference signal of the lock-in section and the deflection signal of the cantilever was optimized using the scheme presented in [77]. Other optimized parameters include the free oscillating tip amplitude and the gain of the feedback loop, etc. Here it should be mentioned that the measured surface potential varies from one tip to another due to the differences in geometry and intrinsic characteristics of each tip. Moreover, the AFM tip shape changes with continuous measurements which affects the measured potential signal. Since KPFM was used in this study to investigate the charging in different  $\text{SiN}_x$  samples, the influence of degrading the tip shape and switching from one tip to another on the measurements had to be considered carefully. The used tips were calibrated continuously before each experiment by measuring the KPFM potential against a reference sample.

#### 3.3.4 KPFM-MEMS, KPFM-MIM characterization techniques

Although the KPFM-TF characterization method simulates efficiently the charging and discharging scenarios in electrostatic MEMS switches, it suffers from some drawbacks. First, the charge injection using the AFM tip in single points simulates a single asperity only where in MEMS switches charging takes place through thousands or may be millions of asperities simultaneously due to the roughness of both the dielectric film and the switch bridge (see **Fig. 2.5**). Second, the charge injection in single points results in inhomogeneous sample surface and therefore the measured KPFM potential is an average value as explained earlier, and hence it does not reflect accurately the real induced surface potential. Finally, due to the influence of the dielectric charging on surface topography measurements, additional techniques are required to

avoid erroneous KPFM signals [111] as explained in section 3.3.3, leading to more complex measurements.

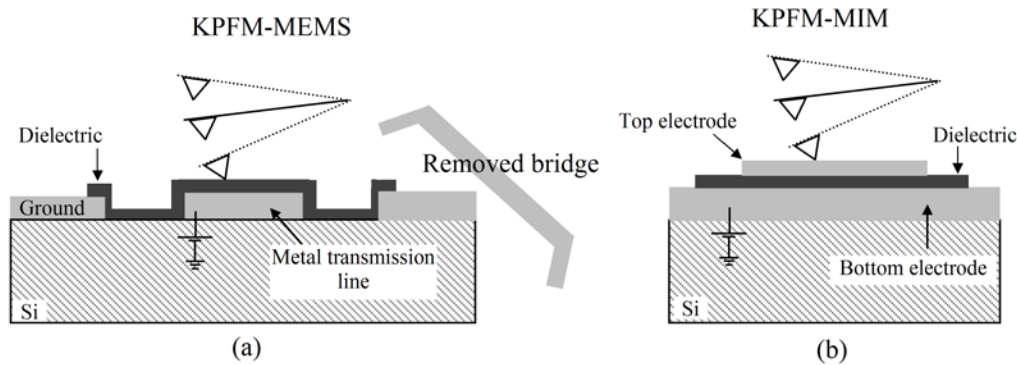


Figure 3.8. Generic cartoons describing the procedure of (a) KPFM-MEMS, and (b) KPFM-MIM characterization techniques.

In order to overcome the aforesaid drawbacks, other KPFM-based characterization techniques have been proposed in this study. The first technique (KPFM-MEMS) makes use of KPFM to study the discharging process on a microscopic scale for a charged dielectric film implemented in MEMS switch. The switch is actuated first using the desired stress voltage and duration to charge the  $\text{SiN}_x$  film. Next, the switch suspended electrode is mechanically removed, and KPFM is used to monitor the induced surface potential over the charged dielectric with time (**Fig. 3.8a**). The second technique (KPFM-MIM), is proposed for the first time in this study and is used to study the discharging process in MIM capacitors. Similar to KPFM-MEMS, the  $\text{SiN}_x$  film is charged first by electrically stressing the MIM capacitor. Then, the surface potential of the top MIM electrode, which reflects the potential of the charged  $\text{SiN}_x$  film, is measured with time using KPFM (**Fig. 3.8b**). Since the MIM top electrode has a homogeneous surface potential, the measured KPFM signal is independent of aforementioned tip related issues (i.e. the tip shape, tip-sample separation, tip position over the sample, etc). Moreover, the measured KPFM-MIM potential is closer to the real surface potential of the charged dielectric compared to KPFM-TF, since it is averaged over an equipotential surface. Finally, the impact of the dielectric charging on surface topography which usually exists in the KPFM-TF method can be completely eliminated using the KPFM-MIM technique. The MIM capacitor can be stressed using any homemade flexible probes in order to avoid any scratch or stress over the electrode surface. Then, the KPFM surface potential can be measured over any area of the MIM top electrode.

Hence, the additional techniques employed to reduce the effect of charging on topography like the one presented in [111] are not anymore required.

### 3.4 FDC-based characterization

In this section, the concept behind using FDC measurements to study the dielectric charging is discussed. Then, the procedure of various FDC-based characterization techniques is described.

#### 3.4.1 Induced adhesive force and surface potential measurements using FDC

An example of the force-distance curve for the investigated  $\text{SiN}_x$  samples is presented in **Fig. 3.9a**. The force-distance measurement starts at a large separation from the sample surface (point A) where there is no deflection of the cantilever. As the piezo moves towards the sample, a sudden mechanical instability occurs between point B and point C, and the tip jumps into contact with the adsorbed water film and wicks up around it to form a meniscus. The cantilever bends downwards because of the attractive meniscus force acting on the tip. As the piezo further approaches the  $\text{SiN}_x$  surface, the deflection of the cantilever increases while the tip travels in the water film and eventually contacts the underlying  $\text{SiN}_x$  surface at point C, and then the cantilever starts to bend upwards. Once the piezo reaches the end of its designated ramp size at point D, it is retracted to its starting position. The tip goes beyond zero deflection (point E) and enters the adhesion region. At point E, the elastic force of the cantilever becomes equivalent to the adhesive force, causing the cantilever to snap back to point F. The adhesive force, which is the force needed to pull the tip away from the sample, can be calculated from FDC by multiplying the vertical distance between E and F with the stiffness of the cantilever,  $k$ , as given by [20].

$$F_{adh} = (F - E)k \quad (3.3)$$

When voltage is applied between the AFM tip and the sample, the cantilever deflection increases due to the increase in the attractive electrostatic force as shown in **Fig. 3.9b**. The difference between the points E and F increases too with increasing the applied voltage as shown from the figure, and according to Eq. 3.3 this leads to an increase in the adhesive force between the AFM tip and the sample. A similar response exists when measuring the adhesive force between the AFM tip and a charged  $\text{SiN}_x$  film. Due to trapped charges in a charged dielectric, the induced surface potential over the dielectric results in increasing the voltage difference between the tip and the dielectric, leading to larger adhesive force. Basically, this is the principle behind

which the FDC measurements were employed to study the dielectric charging phenomenon. The force-volume method was used in order to map the adhesive force between the sample and the tip in three dimensions. A single force-distance curve records the force imposed on the tip as it approaches and retracts from a point on the sample surface, as explained in **Fig. 3.9a**. Force-volume imaging associates each (X, Y) position with a force-distance curve in Z. For each sample, the force-volume method was used to obtain adhesive force maps over a selected dielectric area. The adhesive force for each position in the map is then calculated from the obtained force-distance curves using Eq. 3.3. This is followed by a statistical evaluation for each map by averaging over all the measured positions.

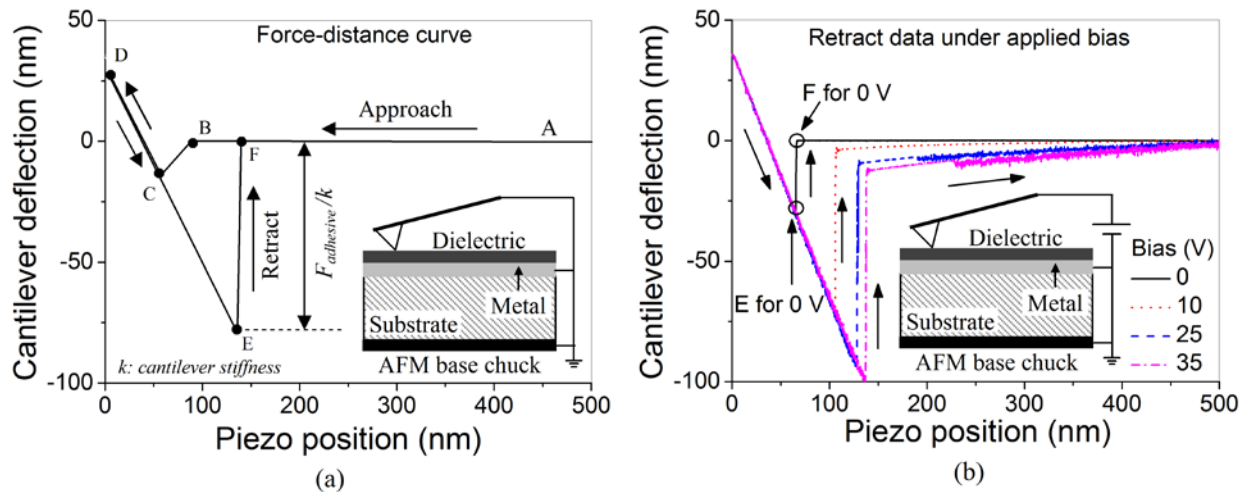


Figure 3.9. Dielectric charging characterization based on FDC measurements: (b) An example of a force-distance curve for the investigated  $\text{SiN}_x$  samples, and (c) the retract data of force-distance curve at different voltage levels between the AFM tip and the sample.

A novel methodology which is based also on the FDC measurements has been proposed to measure the induced surface potential over the charged  $\text{SiN}_x$  films. As shown from **Fig. 3.9b**, when a voltage difference exists between the AFM tip and the sample, the cantilever does not return directly to its original position, and instead its return path has an intermediate stag. Based on that, for charged dielectric films an external voltage is applied to the AFM tip and is modified gradually in order to set off the induced surface potential over the dielectric surface. When the applied bias equals the induced surface potential over the dielectric film, force distance curve returns to its original shape and the intermediate stages shown in **Fig. 3.9b** disappears. At that point, the external applied voltage is equal in amplitude and opposite in sign to the induced surface potential over the dielectric surface. The FDC measurements were performed using

highly doped Si tips, FORTA-10 (resistivity 0.01-0.025 ohm/cm, tip radius < 10 nm, spring constant 1.2-6.4 N/m). The tips were calibrated before each experiment by measuring the adhesive force for a reference sample.

### 3.4.2 FDC-based different characterization techniques

Three FDC-based characterization techniques have been proposed in this study for the first time [114]. The first technique applies the FDC methodology to study the charging in bare SiN<sub>x</sub> thin films (FDC-TF) described in **Fig. 3.2b, c** and **Table 3.1**, similar to the KPFM-TF method. The second and third techniques apply the FDC method to study the dielectric charging in SiN<sub>x</sub> films implemented in MIM capacitors (FDC-MIM) and MEMS switches (FDC-MEMS), similar to KPFM-MIM and KPFM-MEMS methods, respectively. In the FDC-TF technique, the charging of the SiN<sub>x</sub> film is performed through scanning the SiN<sub>x</sub> surface in contact mode using the force-volume method while a voltage difference is applied between the tip and the Au layer underneath the SiN<sub>x</sub> film (**see subfigure in Fig. 3.9b**). The charge build-up with time in the dielectric film is studied through performing multiple scans over the same dielectric area (10 μm X 10 μm) while the adhesive force maps were continuously measured using the force-volume method. After completing the charging experiment, the voltage difference between the AFM tip and the sample was removed. Also, the Au layer underneath the SiN<sub>x</sub> film was grounded to provide a path for the charge collection, similar to the charge collection process by the transmission line in MEMS switches. Then, the discharging process was investigated by using the force-volume method to map the adhesive force between the AFM and the SiN<sub>x</sub> film continuously with time over the same charged SiN<sub>x</sub> area. The observation time window for both the charging and discharging experiments was 1 hour each.

An example of the obtained adhesive force maps using the FDC-TF technique after charging the SiN<sub>x</sub> film using a single scan is shown in **Fig. 3.10a**. The figure highlights that the adhesive force in the charged area is much larger compared to the non-charged area over the dielectric surface. Charge injection over the dielectric surface results in a large induced surface potential that causes a considerable voltage difference between the AFM tip and the SiN<sub>x</sub> sample. Consequently, the electrostatic attractive force between the AFM tip and the dielectric surface will increase, causing the net adhesive force to be larger than the non-charged areas. The adhesive force maps obtained from charge injection using different applied electric field is presented in **Fig. 3.10b**, while the measured surface potential using the FDC method and the

measured adhesive force for these maps are presented in **Fig. 3.10c**. It is clear from the figures that the measured surface potential and adhesive force increase with the electric field applied during the charging step due to larger injected charge density in the dielectric film.

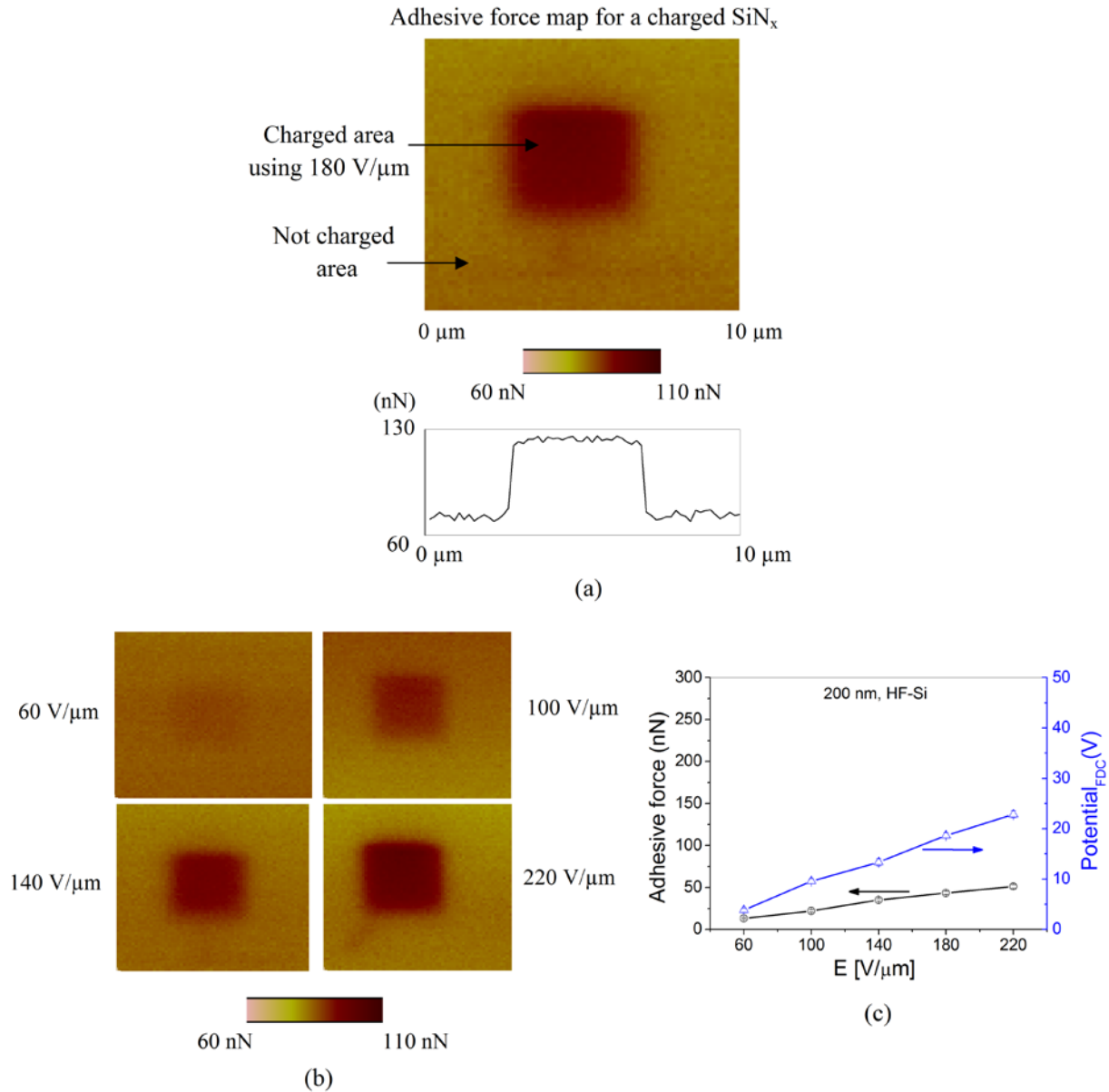


Figure 3.10. (a) An example of adhesive force maps measured by FDC-TF for HF-Si  $\text{SiN}_x$  film charged using  $E = 180 \text{ V}/\mu\text{m}$ ; (b) the adhesive force maps for the same film charged using different electric field, and (c) the corresponding induced adhesive force and surface potential.

In the FDC-MIM, both the charge build-up with time as well as the discharging process of  $\text{SiN}_x$  films implemented in MIM capacitor were studied. Force-volume method was used to map the adhesive force between the AFM tip and MIM top electrode continuously with time

during both the charging and discharging experiments. Similar to the FDC-TF, the charging experiment is performed first while the AFM tip is biased. Then, the voltage difference between the AFM tip and the MIM bottom electrode is removed, and then the discharging adhesive force is measured continuously with time. As with the FDC-TF method, the bottom MIM electrode is kept grounded during the discharging process. In the FDC-MEMS technique, the adhesive force between the AFM tip and a charged  $\text{SiN}_x$  film implemented as the dielectric layer in a capacitive MEMS switch is monitored with time, similar to the KPFM-MEMS method.

Before charging the  $\text{SiN}_x$  films in the abovementioned FDC-based characterization techniques, the adhesive force map was first measured between the AFM tip and the  $\text{SiN}_x$  surface in the case of FDC-TF and FDC-MEMS, and between the AFM tip and the MIM top electrode in the FDC-MIM method. This adhesive force represents the adhesion due to meniscus formation, and is subtracted from the resulting induced adhesive force from the charge injection experiments. Therefore, the adhesive force data presented in this thesis related to the study of the dielectric charging phenomenon represents mainly the induced attractive force between the AFM tip and the sample surface that results from trapped charges in the dielectric film. In chapter 8, the FDC will be used also to investigate different stiction mechanisms where the presented data of adhesive force represents different sources of attractive forces.

The dielectric charging assessment based on FDC has several advantages over KPFM-based methods. First, FDC takes into account the influence of meniscus formation between the AFM tip and the dielectric surface (see **Fig. 2.6a**) which cannot be measured using KPFM. As will be explained in chapter 8, the meniscus formation resulting from the adsorbed water film between the MEMS switch bridge and the dielectric layer and its related electric field-induced meniscus (**Fig. 2.6b**) constitutes major force components which contribute heavily to the final measured adhesive force especially at larger relative humidity levels. Second, the potential levels which can be measured using FDC is much larger compared to KPFM. These higher surface potential levels often exists over charged MEMS dielectrics due to the large actuation voltage used to actuate MEMS switches, and are usually larger than the maximum potential which could be measured by KPFM. With the tips used in FDC measurements, the best obtained accuracy of this technique was around 1.2 V, much larger compared to KPFM where the accuracy is in the range of few mV. Yet, it is believed that the accuracy the surface potential measured by FDC can be significantly improved by using AFM tips with much smaller stiffness. Finally, the FDC can

measure the surface potential accurately at larger relative humidity levels while KPFM cannot due to the potential shielding effect [78]. In this study, both KPFM and FDC measurements were performed using a commercial AFM from Bruker (MultiMode<sup>TM</sup> with NanoScope® IIIa controller and Extender<sup>TM</sup> Electronics Module).

### 3.4.3 Environment control system

The relative humidity has a very high influence on charging/discharging processes in SiN<sub>x</sub> dielectric films as will be explained in chapter 7. Also, the removal of the water-related layer from both surfaces of the sample and the AFM tip was reported to be very important for improving the reliability of the KPFM measurements [79]. In addition, larger humidity levels and thicker adsorbed water film over the sample surface results in larger adhesive force between the AFM tip and the sample as will be discussed in chapter 8. This adhesive force increases remarkably when voltage is applied between the tip and the sample due to the formation of electric field induced meniscus (see **Fig. 2.6b**). For these reasons, both the SiN<sub>x</sub> samples and the AFM tips went through two cycles of heating (150 °C) and cooling steps under vacuum before each measurement in order to avoid the influence of humidity and the adsorbed water film over the dielectric surface on both KPFM and FDC measurements. In order to avoid tip crash due to thermal expansion, the AFM tips were fixed close to the hot sample stage without contact and were radiatively heated. Moreover, the KPFM and FDC measurements were performed in a controlled environment chamber under dry air flow (relative humidity ≈ 0.02%) except for the experiments conducted to study the influence of environment parameters on both charging and stiction which are presented in chapter 7 and 8.

The environment control system used in this study is shown in **Fig. 3.11**. The AFM was enclosed in a Plexiglas chamber with two inlet feed pipes: one for dry gas and another for moist gas. These two inlets carried the required environment gas and were mixed together inside the AFM chamber in order to obtain the desired relative humidity. The lab-air or nitrogen lines used were connected to the inlet of the system. Dry gas was obtained by passing the gas through a line purifier containing a desiccant while humid gas was obtained by bubbling air through water. The relative humidity in the controlled chamber was monitored with a humidity sensor. This sensor was connected to a microcontroller which controls solenoid valves in order to adjust the ratio between dry and humid gas to reach the desired humidity and maintain it at a constant level during the experiment. The environment control system includes also two types of gas purifiers



$$I_{dis}(t) = -\frac{dP(t)}{dt} = \frac{P(t)}{\tau} \quad (3.4)$$

where  $P(t)$  is the buildup of polarization during a time  $t$  after the application of an electric field and  $\tau$  the process time constant. In both cases, the polarization and depolarization, the current flowing through the external circuit consists of several components including the polarization or depolarization current, the absorption current and, in the case of polarization, the dielectric conduction current [37, 68].

A typical result for the decay of the measured current transients in MIM capacitors with HF SiN<sub>x</sub> films stressed using positive bias is presented in **Fig. 3.12** [37]. In these measurements, the charging and discharging current transients were recorded with Keithley 4200 Semiconductor Characterization System for 1000 s each. As shown from the figure, the dielectric charging and discharging currents in principle are not equal due to the presence of external electric field during charging and the internal one during discharging. For this reason the charging current may be masked by high leakage currents.

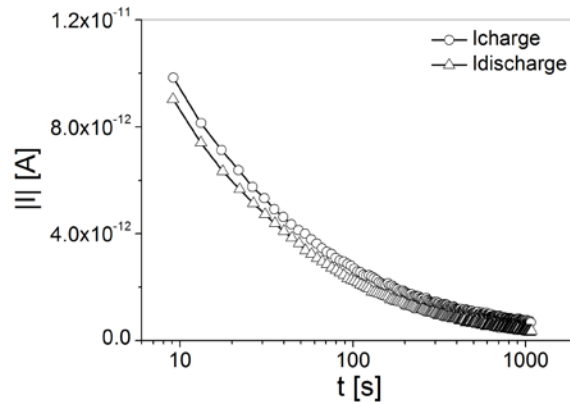


Figure 3.12. The Absolute value of charging and discharging current transients measured using the C/DCT method at  $E=140$  V/ $\mu\text{m}$  for HF SiN<sub>x</sub>.

### 3.5.2 Thermally Stimulated Depolarization Current (TSDC)

The TSDC technique is used as an efficient tool for the investigation of dipolar and DC relaxation phenomena observed by heating a variety of materials over a wide temperature range after polarization by an electrostatic field at a polarization temperature,  $T_p$ . The observed phenomena occur due to the orientation sensitivity of bond dipoles and charges (electrons and ions) to the external electrostatic field. During temperature scan, the current density produced by

the progressive decrease in polarization in the course of a TSDC experiment, where time and temperature are simultaneously varied, is approximated by [32, 33]

$$J_D(T) \approx \frac{P_s(T_p)}{\tau_0} \cdot \exp\left(-\frac{E}{kT}\right) \cdot \exp\left[-\frac{1}{\gamma\tau_0} \cdot \frac{kT^2}{E} \exp\left(-\frac{E}{kT}\right)\right] \quad (3.5)$$

where  $\tau_0^{-1}$  is the attempt escape frequency related to lattice,  $P_s$  is the steady state polarization,  $E$  is the activation energy of the contributing polarization mechanism,  $\gamma$  is the heating rate and

$$\tau(T) = \tau_0 \cdot \exp\left(\frac{E}{kT}\right) \quad (3.6)$$

is the thermally activated relaxation time for each contributing mechanism with a corresponding activation energy  $E$  and  $\tau_0$ . The electric charge,  $Q$ , produced during the depolarization (heating) stage in a TSDC experiment reduced to the sample-electrode surface area can be estimated by the integration over the TSDC spectrum (from  $T_0$  to  $T_f$ ):

$$Q = \gamma^{-1} \int_{T_0}^{T_f} I(T) \cdot dt \quad (3.7)$$

which is proportional to the dielectric film polarization.

### 3.6 Physical material characterization

In order to further study the investigated  $\text{SiN}_x$  films, two physical material characterization techniques were used; Fourier transform Infra-Red spectroscopy (FT-IR) and (X-ray photoelectron spectroscopy) XPS. FT-IR spectroscopy was performed to provide information about the chemical bonds of the dielectric film and their variations. The infrared spectra were acquired in the  $400 - 4000 \text{ cm}^{-1}$  range with a BIORAD FTS60A spectrometer with the samples under nitrogen flow to avoid the effect of humidity and ambient. The reflection and transmission modes were employed for  $\text{SiN}_x$  layers deposited on metal and silicon, respectively. The XPS experiments were used in order to provide information about the different chemical bonds and valence state in the  $\text{SiN}_x$  surface, and then in depth through sputtering. A VG ESCALAB 220-iXL spectrometer was used to perform the XPS measurements. The deposited  $\text{SiN}_x$  layers were excited by  $\text{MgK}\alpha$  (1253.6 eV), and the kinetic energies of the electrons emitted were collected at a constant energy resolution of 1 eV. The energy step used to record the spectra was 0.2 eV. Since the  $\text{SiN}_x$  films are rather nonconductive, electron compensation was used

during the measurement. Here it should be pointed out that the XPS measurement is not sensitive to hydrogen or helium.

### **3.7 Summary**

The investigated samples in this study have been presented. Also, the employed electrical and physical characterization techniques have been described. In the next chapter, the correlation between the results from these techniques is discussed.

*We learn more by looking for the answer to a question and not finding it than we do from learning the answer itself.*

*Lloyd Alexander  
1924 – 2007, American Author*

*The important thing is not to stop questioning. Curiosity has its own reason for existing.*

*Albert Einstein  
1879 – 1955, German-born American Physicist  
Nobel Prize for Physics in 1921*

## **4 Correlation and comparison between electrical characterization techniques**

### **4.1 Introduction**

The advantages and limitations of the available electrical characterization techniques reported to study the dielectric charging phenomenon have been explained in chapter 2. Moreover, chapter 3 presents the theory and procedure of the novel nanoscale characterization techniques proposed in this thesis based on KPFM and FDC. This chapter presents the results of these novel characterization techniques and discusses their correlation. It also discusses the correlation between the results from the conventional assessment methods described in chapter 3. For the first time, the KPFM and FDC based characterization methods were used to create a link between the results from the C/DCT and TSDC techniques applicable to MIM and the results from MEMS switches.

First, the results from C/DCT method are presented. Then, the results from KPFM- based characterization techniques are discussed and correlated to the C/DCT and TSDC measurements. This is followed by presenting the FDC-based characterization results and comparing them to other used methods.

### **4.2 DCT-based assessment methods**

In C/DCT experiments, the transient charging and discharging currents are measured in the external circuit of MIM capacitors as described in section 3.5.1. A typical result for the decay of current transients in MIM capacitors with HF SiN<sub>x</sub> films stressed using positive voltage is presented in **Fig. 4.1a, b**. The figures show the decay of the charging (**Fig. 4.1a**) and discharging

**(Fig. 4.1b)** current transients measured under different applied electric field intensities. The measured charging/discharging currents at the beginning of the observation time window (at  $t \approx 0$  s) increases with the electric field applied during the charging experiment. This indicates that the injected charge density in the  $\text{SiN}_x$  film increases with the applied electric field. Assuming that the charging and discharging processes decay according to the stretched exponential law:

$$\sigma(t) = \sigma_0 \exp\left[-\left(\frac{t}{\tau}\right)^\beta\right] + \sigma_{bg} \quad (4.1)$$

where  $\sigma_{bg}$  is the background charge per unit area,  $\tau$  is the process time constant and  $\beta$  ( $0 \leq \beta \leq 1$ ) is the stretch factor, the transient charging and discharging currents will decay as [37]

$$J(t) = \sigma_0 \frac{\beta}{\tau} \left(\frac{t}{\tau}\right)^{\beta-1} \exp\left[-\left(\frac{t}{\tau}\right)^\beta\right] \quad (4.2)$$

The stretched exponential relaxation fits many relaxation processes in disordered and quenched electronic and molecular systems. For electronic relaxation, the appearance of the stretched exponential is often described in the context of dispersive transport, where  $\beta$  is treated as an adjustable parameter, but in almost all cases it is generally assumed that no microscopic meaning can be assigned to it. Besides, modeling of possible interactions suggested that the values of  $\beta \approx \frac{3}{5}$  and  $\beta \approx \frac{3}{7}$  can be applied for short-range and long-range Coulomb forces, respectively, as originally observed in [115, 116] for the decay of residual charge on a Leyden jar.

As can be noticed from **Fig. 4.1a, b**, the decay of the charging and discharging currents are best fitted with Eq. 4.2 for the whole applied electric field series. For a given applied electric field, the charging and discharging currents in principle are not equal as explained in chapter 3 (see **Fig. 3.12**). This suggests a different mechanism for charging and discharging processes since the latter is performed in the presence of internal electric fields that vary with time. Moreover, the charging current is often masked by leakage currents, which depend on the applied electric field and temperature, and have been found to affect the fitting process resulting in significant fitting parameters dispersion. That is why the fitting results for C/DCT experiments presented in this thesis depend mainly on the discharging current transients. **Fig. 4.1c** presents the calculated decay time constant,  $\tau$ , and the stretch factor,  $\beta$ , from fitting the discharging current transients with Eq. 4.2 as a function of the electric field intensity for MIM capacitors with HF  $\text{SiN}_x$ . It is

obvious that the decay time constant increases while the stretch factor slightly decreases with increasing the electric field intensity.

Furthermore, **Fig. 4.1d** plots the stored charge versus temperature calculated from the TSDC method explained in section 3.5.2 for the same MIM sample. It is evident that the calculated stored charges at room temperature from C/DCT and TSDC are almost similar. For example, the stored charge at room temperature for HF SiN<sub>x</sub> with 200 nm thickness under an electric field of 20 V/μm for C/DCT and TSDC, are 1.6x10<sup>-10</sup> C and 1.05x10<sup>-10</sup> C, respectively.

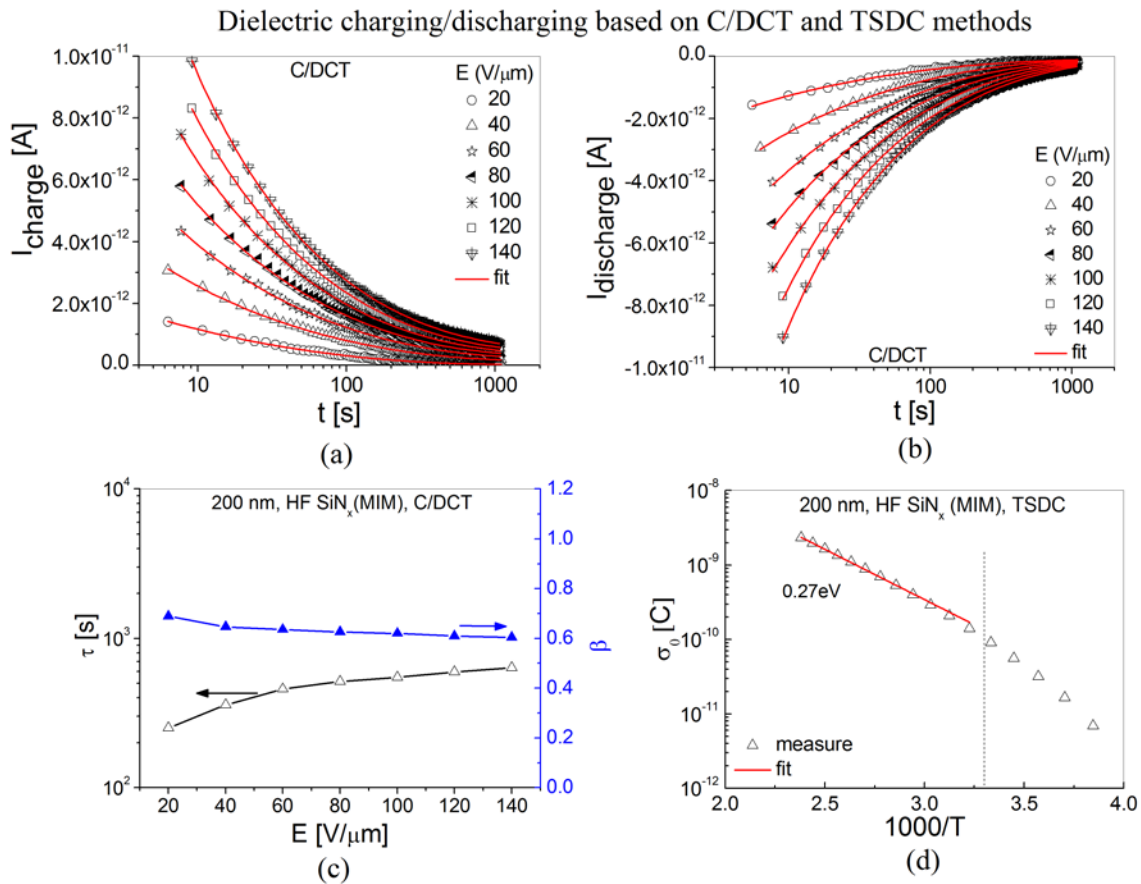


Figure 4.1. Dielectric charging/discharging based on the C/DCT and TSDC methods: (a) charging current transient decay, (b) discharging current transient decay, (c) the calculated decay time constant and stretch factor; and (d) the measured charge,  $\sigma_0$ , versus temperature.

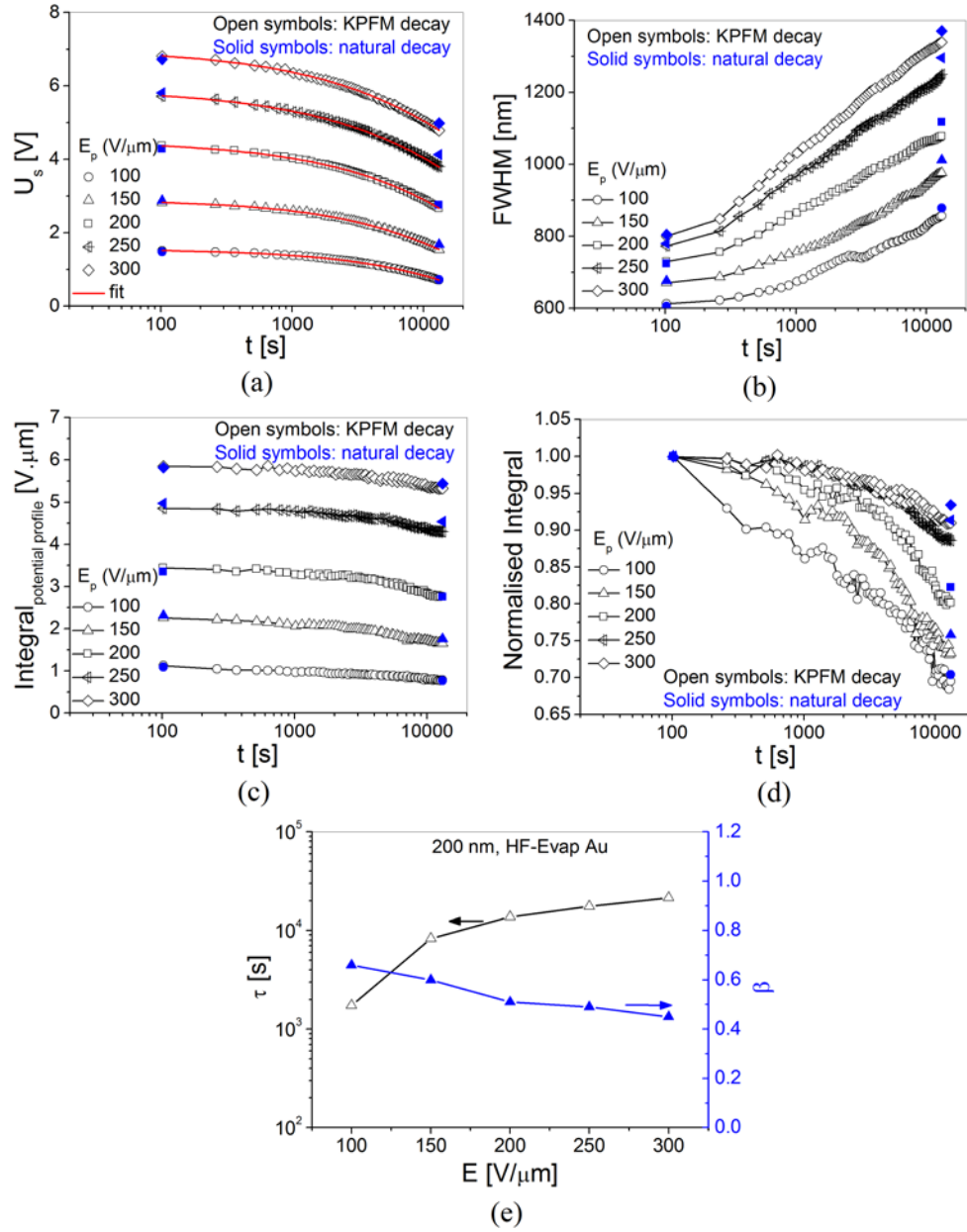


Figure 4.2. Time evolution of KPFM surface potential represented by (a) surface potential amplitude,  $U_s$ , (b) potential distribution, FWHM, (c) absolute and (d) normalized potential profile integral; and (e) the decay time constant and stretch factor. The influence of the AFM tip on the measured KPFM potential is also plotted in the figure.

### 4.3 KPFM-based characterization and correlation to DCT

This section discusses, for the first time, the correlation between the results from the KPFM and DCT based characterization techniques described in sections 3.3 and 3.5, respectively. First, an example of the results obtained from the KPFM-TF method is presented highlighting the effect of the AFM tip on the charge injection/collection processes. This is

followed by discussing the correlation between the KPFM-MEMS, KPFM-MIM, C/DCT, and TSDC characterization methods.

#### 4.3.1 KPFM-TF: example of results and the influence of the AFM tip

**Figure 4.2** presents an example of the surface potential decay with time measured using the KPFM-TF method described in section 3.3.1 for charges which were injected in separate points over HF-Evap Au SiN<sub>x</sub> sample using different pulse amplitudes,  $U_p$ . As shown from the figure, the surface potential amplitude,  $U_s$ , decreases (**Fig. 4.2a**) while the potential distribution, FWHM, increases (**Fig. 4.2b**) with time. The integral of the corresponding potential profile for these data, which is a direct indication of the trapped charge density in the dielectric film, is plotted in **Fig. 4.2c**. The figure shows that the potential profile integral measured at the beginning of observation time window increases with the pulse amplitude,  $U_p$ . This indicates that the injected charge density in the SiN<sub>x</sub> film increases with the electric field applied during the charging step. **Figure 4.2c** shows also that the measured charge density decreases with time, indicating that trapped charges are being collected or removed.

In the lift mode used to perform the KPFM measurements (**Fig. 3.3b**), the AFM tip is held to ground during topography imaging in the first pass while its potential is updated continuously by the KPFM feedback loop during surface potential measurement in the second pass. Therefore, the grounded AFM in the first pass and the biased tip in the second pass could contribute to the charge collection and injection processes, respectively. In order to quantify this contribution, the results from two experiments ('KPFM decay' and 'natural decay') used to monitor the discharging process were compared. In the first experiment (KPFM decay), the dielectric surface was scanned continuously with time just after completing the charge injection step. The second experiment (natural decay) is similar to the one described in [111]. In this experiment, charges were injected over the SiN<sub>x</sub> using the same charge injection parameters used in the 'KPFM decay' experiment. Then, instead of scanning the dielectric surface continuously with time as done for the 'KPFM decay' experiment, the surface potential was measured at two time points only: directly after the charge injection step and then at the end of the observation time window (after 3.5 hours). During this period the AFM tip was disengaged far from the sample surface in order to avoid affecting the charge injection or collection. The resulting  $U_s$ , FWHM, and potential profile integral of these experiments are plotted in **Fig. 4.2 a, b, and c**, respectively. Also, the

normalized values of the potential profile integral to the initial values at  $t = 0$  s for both experiments are plotted in **Fig. 4.2d**.

Comparing the results from both experiments reveals that the measured  $U_s$ , FWHM, and potential profile integral in the ‘natural decay’ experiment is slightly larger than their corresponding values in the ‘KPFM decay’ experiment, and this could be observed for charges injected under different pulse amplitude. For example, for charges injected under  $U_p = 40$  V, the potential profile integral (**Fig. 4.2d**) measured at the end of the observation time window for the ‘natural decay’ and ‘KPFM decay’ experiments is 82% and 80%, respectively, from their initial values. This indicates that the grounded AFM tip used during measuring surface topography in the first pass of lift mode and/or the different updated tip potential applied during determining the surface potential in the second pass have a negligible effect on the charge collection and injection processes, respectively. In other words, the charge transfer between dielectric film and the AFM tip is minimal. Based on that, studying the discharging process in electrostatic MEMS switches by monitoring the evolution of KPFM surface potential with time is a very efficient methodology. It simulates to a great extent the charge collection scenario which takes places in MEMS switches where the injected charge is collected by the transmission line when the switch bridge is in the up-state position (see **Fig. 3.2a**).

Furthermore, **Fig. 4.2a** highlights that the decay of the surface potential peak amplitude,  $U_s$ , follows the stretched exponential law given by [76]

$$U_s(t) = U_0 \exp \left[ - \left( \frac{t}{\tau} \right)^\beta \right] \quad (4.3)$$

and this could be observed for charges which were injected under different electric field. The decay time constant,  $\tau$ , and stretch factor,  $\beta$ , calculated from surface potential decay measurements are shown in **Fig. 4.2e**. The decay time constant increases while the stretch factor decreases with increasing the applied electric field, similar to what is observed from the C/DTC measurements (**Fig. 4.1c**).

#### 4.3.2 Correlation between KPFM and DCT based methods

The aim of this section is to reveal the common features and main differences between the KPFM and DCT based characterization methods.

#### 4.3.2.1 Experimental

Four different characterization methods (KPFM-MEMS, KPFM-MIM, DCT, and TSDC) were used to monitor the discharging process in the same  $\text{SiN}_x$  film. The procedures of these techniques have been explained in details in chapter 3. The dielectric materials used were  $\text{SiN}_x$  films with 500 nm thickness deposited using the high frequency (HF) recipe presented in **Table 3.2**. The investigated samples included circular MIM capacitors of 500  $\mu\text{m}$  diameter and electrostatic MEMS capacitive switches, both employing the same  $\text{SiN}_x$  film. For the C/DCT method, an electric field was applied to MIM capacitor for a specific time followed by measuring the discharge current transients [37]. Keithley 4200 Semiconductor Characterization System was used to record the discharge current. In the TSDC experiment, the discharge current of MIM capacitor was measured under simultaneous temperature scan using Keithley 6487 picoampere-meter in the range of 200K to 450K [69]. KPFM was used to measure the surface potential decay of charged  $\text{SiN}_x$  films implemented in MEMS switch using the KPFM-MEMS method and in MIM capacitor using the KPFM-MIM technique. For all techniques, the same electrical stress conditions were applied for charging the  $\text{SiN}_x$  film (10 V for 15 min). Also, the decay of both surface potential or discharge current transients was monitored for a fixed observation time window (20000 s).

For the KPFM-MEMS experiment, a capacitive MEMS switch with lateral actuation electrodes was used [15]. The lateral actuation topology allows charging the  $\text{SiN}_x$  film with a smaller stress voltage than the actual pull-in voltage of the electrostatic actuators. After completing the charging step and the removal of the switch suspended electrode, the whole area of the charged dielectric surface was scanned first (100  $\mu\text{m}$  x 100  $\mu\text{m}$ ) in order to localize the hot spots with the maximum induced potential [72, 117]. Then, a smaller area (5  $\mu\text{m}$  x 5  $\mu\text{m}$ ) which exists within one of these hot spots was scanned with time. During the surface potential measurements, the transmission line was connected to the AFM chuck which was grounded. This is to provide a path for the injected charges in the  $\text{SiN}_x$  film to be released as occurs in MEMS switches during the up-state. The KPFM-MEMS measurements were performed in a controlled environment chamber with a very low relative humidity (RH0.02%). For the KPFM -MIM experiment, MIM capacitor was electrically stressed first. Then, the surface potential of the top electrode, which reflects the potential of the  $\text{SiN}_x$  film, was measured with time. Similar to

KPFM-MEMS, during surface potential measurement the bottom electrode of MIM capacitor was grounded.

#### 4.3.2.2 KPFM-MEMS and KPFM-MIM results

The surface potential decay measured by KPFM-MEMS and KPFM-MIM techniques is shown in **Fig. 4.3a, b**, respectively. As the charge injection in MEMS switches is not uniform due to roughness and topography of both the bridge and the dielectric film, the surface potential decay was analyzed in two different positions over the  $\text{SiN}_x$  surface within the scanned area. The selected two positions are the ones with the minimum (position 1) and maximum (position 2) surface potential as highlighted in **Fig. 4.3a**. On the contrary, the charge injection is uniform in case of the MIM capacitor and the surface potential is the same all over the top metal electrode. The surface potential decay for both KPFM-MEMS and KPFM-MIM follows accurately the stretched exponential function (Eq. 4.3), through the whole observation time window as shown from **Fig. 4.3a, b**. Comparing the fitting results in **Fig. 4.3a** and **Fig. 4.3b**, it is obvious that the stretched exponential law gives very similar values for the decay time constant,  $\tau$ , and stretch factor,  $\beta$ , for both techniques, in spite of the mentioned difference between charge injection in MIM and MEMS. This indicates that the decay of MIM and MEMS surface potential measured by KPFM arises from charge collection by the bottom electrode through the same mechanisms. In consequence, MIM capacitors and MEMS switches can lead to the same conclusions regarding the electrical properties of the dielectric film when assessed properly using KPFM.

#### 4.3.2.3 C/DCT results

The discharge current transient resulting from the C/DCT method is presented in **Fig. 4.3c**. The results from two different fitting equations which are the stretched exponential equation (Eq. 4.3) and the Debye law ( $\beta = 1$ ) are shown in the figure. Similar time constants are obtained from the C/DCT decay using both equations. However, when using the Debye law the fitting fails to provide adequate information in the short time range while the stretched exponential law fits very well for both short and long time range. Moreover, the fitting although greatly improved when the number of contributing Debye mechanisms increases, does not lead to a concrete conclusion because a continuous distribution of defects is expected for an amorphous material such as the  $\text{SiN}_x$  films used in MEMS. In contrast, the stretched exponential equation revealed that the decay time constant increases with the charging electric field intensity (**Fig. 4.1c**).

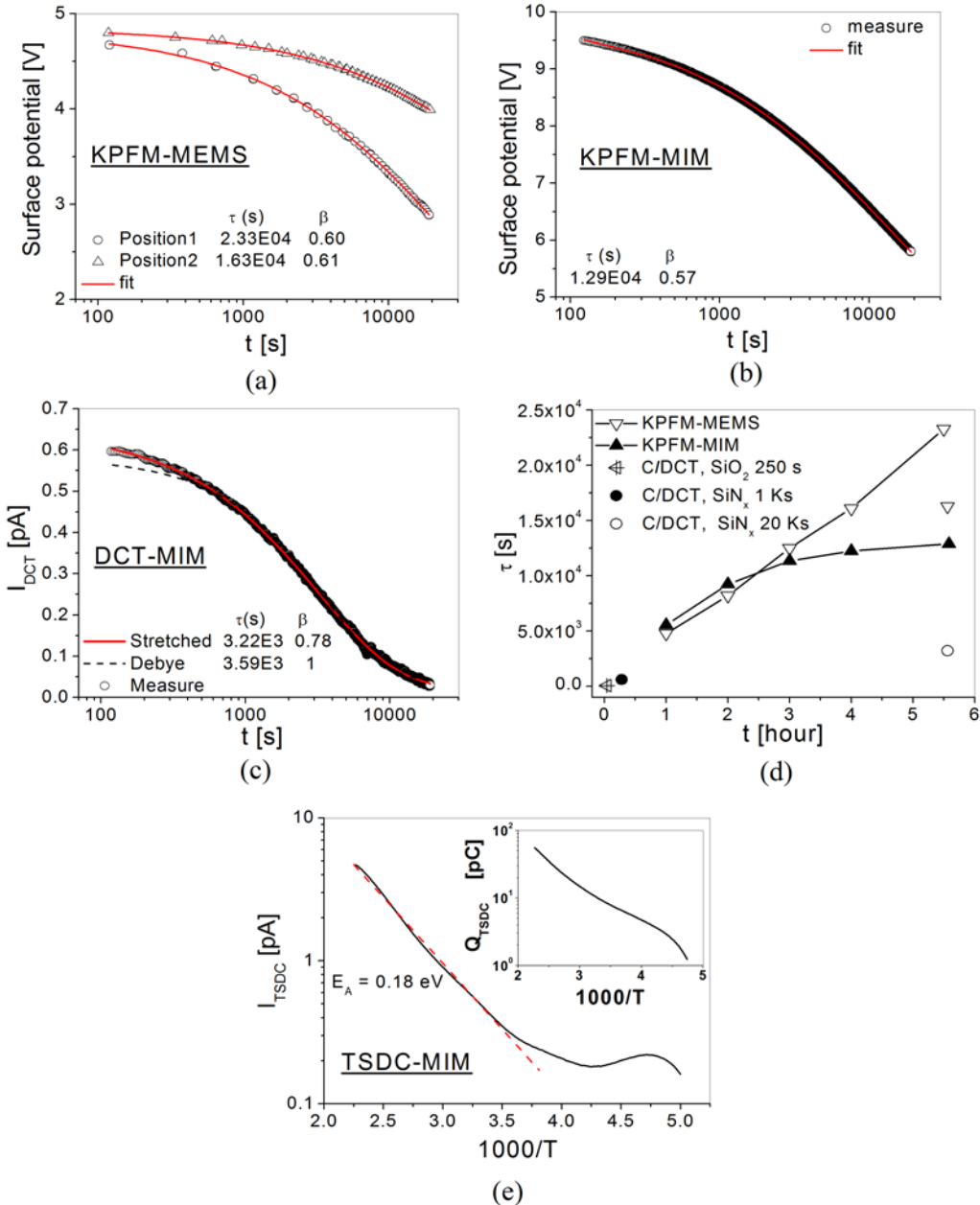


Figure 4.3. Correlation between KPFM and DCT characterization methods: surface potential decay measured by (a) the KPFM-MEMS technique, (b) the KPFM-MIM method; (c) discharge current transient measured by the C/DCT method; (d) the decay time constants versus the observation time window for different assessment methods, and (e) the TSDC spectra.

A close comparison of the decay data obtained from KPFM (**Fig. 4.3a, b**) and C/DCT (**Fig. 4.3c**) reveals that the C/DCT method provides always smaller decay time constants with respect to the KPFM based techniques. Similar observation could be drawn from the comparison between **Fig. 4.1c** (C/DCT) and **Fig. 4.2e** (KPFM-TF). This difference obviously arises from the

difference in charge collection mechanisms in both methods, the collection by the injecting electrode in C/DCT and the opposite electrodes in the KPFM based methods. Thus, in MEMS switches, so does in the KPFM-MIM and KPFM-MEMS, the discharge occurs through currents crossing the dielectric film. This discharge current is expected to be much smaller than the one measured in C/DCT method because of the successive trapping and emission of charges and the charge percolation due to potential fluctuation caused by inhomogeneities in the nonstoichiometric material, i.e. in PECVD SiN<sub>x</sub> [118] or SiO<sub>2</sub> [119, 120]. Here we should like to define the term ‘*percolation*’ which is a standard model for disordered systems and its applications include the transport in amorphous and porous media (ex. amorphous SiN<sub>x</sub>). The percolation theory, an extensive mathematical model of percolation, has brought new understanding to a wide range of topics in physics, materials science, etc.

**Fig. 4.3d** shows the decay time constants extracted for different observation time windows from KPFM-MEMS, KPFM-MIM and C/DCT decay. The figure includes also the C/DCT relaxation times reported in other studies for SiO<sub>2</sub> [28] and SiN<sub>x</sub> [37] films implemented in MIM capacitors. It is obvious from the figure that the decay time constant increases as the observation time window increases for both KPFM-MEMS and KPFM-MIM. Also, from C/DCT experiments the decay time constant is 3.2E03 s for an observation time window of around 20000 sec. When the observation window is reduced to 1000 s, the decay time constant decreases to approximately 100 s only, under the same stress conditions. The figure also highlights that for the C/DCT method the decay time constant calculated for SiO<sub>2</sub> [28] for an observation window of 250 s is smaller than the calculated value for SiN<sub>x</sub> with longer observation time windows. This can lead us to the conclusion that for both KPFM and C/DCT characterization methods, the calculated discharge time constants are practically determined by the observation time window.

#### 4.3.2.4 TSDC results

**Figure 4.3e** presents the TSDC spectra for the investigated SiN<sub>x</sub> sample. As seen from the figure, the TSDC spectra shows in most cases a peak that is detected in the low temperature regime followed by a continuous one arising from a continuous distribution of charging centers [52, 80]. The continuous increase of TSDC current with increasing temperature exhibiting thermal activation,  $I(T) \propto \exp\left(-\frac{\alpha E}{kT}\right)$ , where  $\alpha$  is related to the fractional dimension, was attributed to power-law relation and attributed to a Fractal distribution of charge trapping centers.

The continuous spectrum is observed because the current in the power-law scheme is determined by the peak maxima of the Debye sub processes that become active in a certain temperature window [121, 122]. Finally, it is evident from **Fig. 4.3e** that the TSDC spectrum shows the envelope of the measured current peaks.

The TSDC method provides indirectly information on dipoles and trapping centers relaxation time constants. The linear temperature ramp in TSDC allows the scan of both a very wide range of time constants through equation 3.6 and simultaneously a scan of dielectric film band gap through equation 3.5 For  $\text{SiN}_x$  material, it was reported that charging arises from continuous distribution of time constants around specific activation energies [69]. Taking this into account, it could be concluded that the TSDC spectrum in **Fig. 4.3e** arises from a continuous distribution of time constants too. This is supported by the data presented for both KPFM-MEMS and C/DCT where the calculated time constant is found to increase with the observation time window (**Fig. 4.3d**). Finally the electric charge  $Q$  produced during the depolarization stage can be calculated through equation 3.7 (see inset of **Fig. 4.3e**). This makes TSDC method a complementary tool for both the C/DCT and KPFM based characterization techniques.

In conclusion, the C/DCT and KPFM assessment methods reveal that both the injected charge density and the discharge time constants increase with the applied electric field. The application of KPFM method in MIM capacitors leads to decay time constants similar to the ones obtained from direct charge injection in MEMS insulating films. In consequence, MIM capacitors and MEMS can lead to similar conclusions regarding the electrical properties of MEMS dielectric films when assessed properly using KPFM. Due to processes involved on the collection of injected charges, which is the collection by the injecting electrodes, the C/DCT method reveals always shorter relaxation times. In contrast in KPFM method, hence in MEMS, the injected charges are always collected by the opposite electrodes and due to successive charge trapping and emission as well as percolation the process relaxation time is always larger. In both methods due to the complexity of involved mechanisms, the calculated time constants are determined by the time window of experiment. Finally, the TSDC method could be considered as a complementary technique to the KPFM and C/DCT based characterization techniques since it allows the evaluation of time constant dispersion over a wide range of values simultaneously with the distribution of centers in the material energy gap.

#### **4.4 FDC-based characterization techniques**

In this section, the charging/discharging processes in SiN<sub>x</sub> films are investigated using the FDC-based characterization techniques described in section 3.4. Also, the results from FDC are correlated to the C/DCT and KPFM methods. The main advantages of the FDC-based techniques are twofold. First, it takes into account the meniscus force between the MEMS switch movable electrode and the dielectric surface which cannot be measured by KPFM. Second, the FDC-based methods could measure the real surface potential with larger amplitudes which are comparable to the induced potential levels over MEMS dielectrics due to the large actuation voltage normally used to drive these devices. KPFM can't measure such higher surface potential amplitudes, and also provides an averaged potential value for inhomogeneous charged films induced by nonuniform charging in MEMS.

##### *4.4.1 Experimental*

Three FDC-based characterization techniques were proposed. The first technique applies the FDC methodology to study the charging in bare SiN<sub>x</sub> thin films (FDC-TF) shown in **Fig. 3.2a, b** and **Table 3.1**, similar to the KPFM-TF method. The second and third techniques employ the FDC to study the dielectric charging in SiN<sub>x</sub> films implemented in MIM capacitors (FDC-MIM) and MEMS switches (FDC-MEMS), respectively. For the three techniques, a modified force-volume method was used during the discharging experiment in order to minimize the charge collection by the grounded AFM tip. The investigated MIM capacitors in the FDC-MIM technique were circular with 500 μm diameter, and implementing HF SiN<sub>x</sub> films with 200 nm thickness. Also, the used MEMS switches in the FDC-MEMS method had a HF SiN<sub>x</sub> film with 230 nm thickness and were fabricated using the process described in **Fig. 3.1**. First, the switch was actuated through the central transmission line using 44 V for 15 min in order to charge the SiN<sub>x</sub> film. Next, the switch movable electrode was mechanically removed, and the force-volume technique was used to map the adhesive force decay between the tip and the charged SiN<sub>x</sub> film with time.

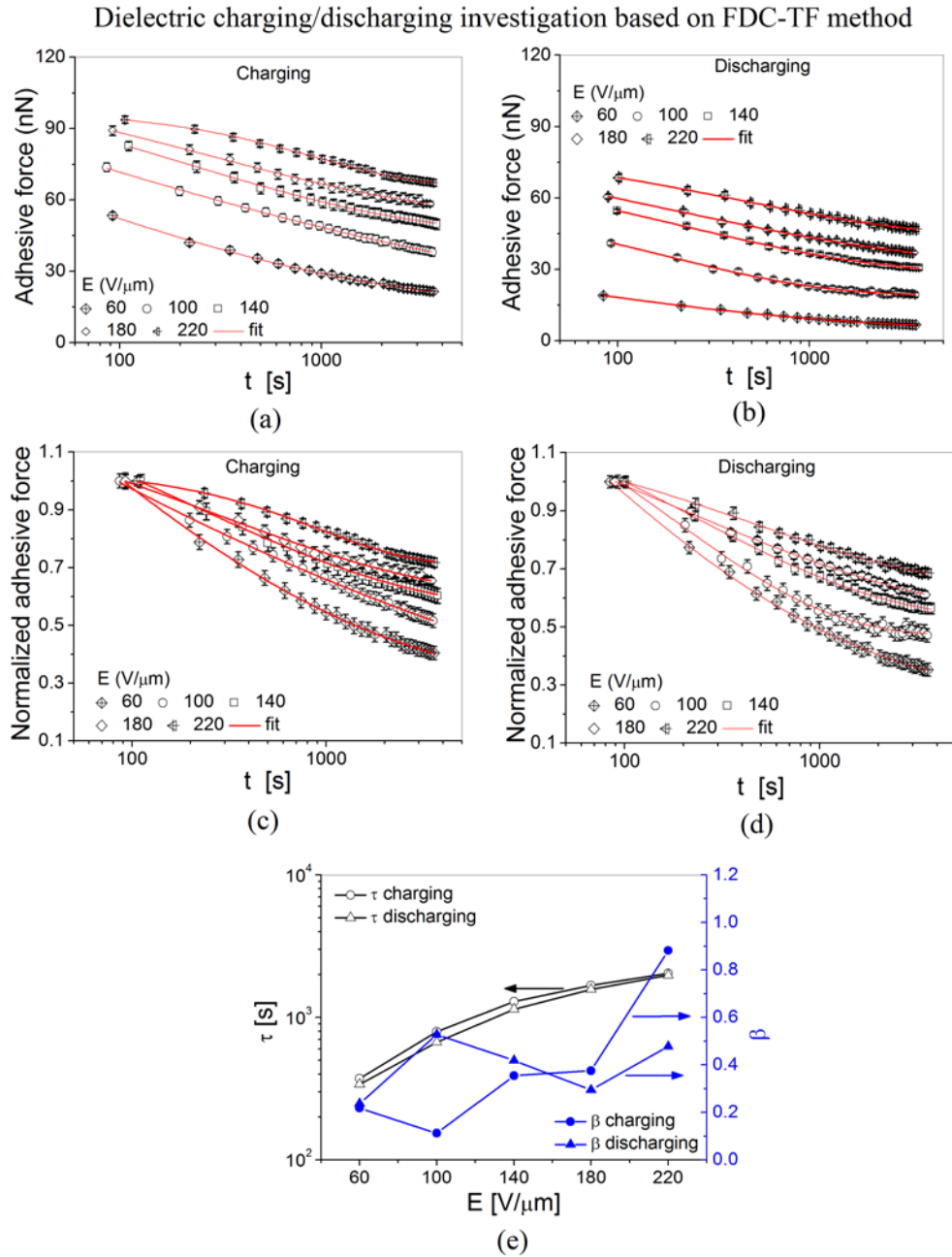


Figure 4.4. Dielectric charging/discharging for the HF-Evap Au SiN<sub>x</sub> sample with 200 nm thickness based on FDC-TF technique: (a) charging and (b) discharging adhesive force decay with time; (c) normalized charging and (d) discharging adhesive force decay to their initial values at  $t = 0$  s, and (e) the decay time constant and stretch factor.

#### 4.4.2 FDC-TF results

The evolution of the induced adhesive force with time during the dielectric charging and discharging processes as extracted from the FDC-TF technique is shown in **Fig 4.4a, b** [114]. The charging adhesive force (**Fig. 4.4a**) is the force measured between the AFM tip and the SiN<sub>x</sub>

sample while the tip bias was kept applied continuously with time. The discharging adhesive force (**Fig. 4.4b**) is the force measured after removing the applied bias at the end of the charging experiment. The figure highlights that the measured adhesive force shows a gradual decay with time for both charging and discharging experiments, and this has been observed for charges which were injected using different bias. The charging adhesive force decays with time due to charge build-up inside the dielectric film which results in reducing the voltage difference between the AFM tip and the SiN<sub>x</sub> sample. This in sequence leads to a smaller attractive electrostatic force between the AFM tip and the sample and results in the measured adhesive force decay. Due to the charge collection process during the discharging experiment, the voltage difference between the grounded AFM tip and the sample is reduced too leading to the decay of discharging adhesive force with time as shown in **Fig. 4.4b**. Thus, based on the FDC-TF technique the charge build-up in the dielectric film as well as the charge collection process can be studied. This resembles a major advantage over KPFM-based characterization which cannot investigate the charge build-up with time during the charging of the dielectric film. The normalized adhesive force to the maximum measured value at  $t = 0$  for both the charging and discharging data is shown in **Fig. 4.4c, d**, respectively. It is evident from the figures that the charge injection/collection processes becomes slower with increasing the applied electric field intensity,  $E$ , during the charging experiment.

The adhesive force decay with time follows accurately the square of the stretched exponential equation [114]

$$F_{adh}(t) = F_0 \left( \exp \left[ - \left( \frac{t}{\tau} \right)^\beta \right] \right)^2 \quad (4.4)$$

and this has been observed for different applied electric fields. Since the KPFM surface potential decay fits properly with the stretched exponential law (Eq. 4.3), it is concluded that the measured adhesive force between the AFM tip and the SiN<sub>x</sub> surface resembles mainly the attractive electrostatic force. The decay time constant,  $\tau$ , and stretch factor,  $\beta$ , calculated from the time evolution of charging/discharging adhesive forces is plotted in **Fig. 4.4e**. The figure shows that the decay time constant,  $\tau$ , for both charging/discharging adhesive force increases with the applied electric field, similar to what has been concluded from C/DC and KPFM-TF techniques. No consistent trend has been found for the stretch factor versus the electric field as shown in the figure.

The FDC-TF is close in principle to the C/DCT method presented in section 4.2. The charging adhesive force measured by the FDC-TF technique (**Fig. 4.4a**) is equivalent to the charging current obtained from the C/DCT method (**Fig. 4.1a**). Similarly, the discharging adhesive force measured by the FDC-TF (**Fig. 4.4b**) is equivalent to the discharging current measured by the C/DCT method (**Fig. 4.1b**). Comparing **Fig. 4.4a, b** with **Fig. 4.1a, b**, it is clear that the charging/discharging processes measured by FDC-TF technique is much slower compared to C/DCT method. For example, for  $E = 140 \text{ V}/\mu\text{m}$  the charging/discharging adhesive forces drop to around 60% from their initial values at  $t = 0 \text{ s}$  after an observation time window of 1 hour, while the charging/discharging currents drop to around 10% from their initial values at  $t = 0 \text{ s}$  after only 15 min. This is also evident from the decay time constant for both techniques, where the time constant for C/DCT (**Fig. 4.1c**) is much smaller compared to FDC-TF (**Fig. 4.4e**). Moreover, the variation in the stretch factor with the electric field is much smaller in the C/DCT compared to FDC-TF.

The charging in C/DCT is much faster than FDC-TF for two main reasons. First, the electrical stress applied to MIM capacitors during the charging experiment in C/DCT is continuous with time, while for FDC-TF the electrical stress is discontinuous for each charged  $\text{SiN}_x$  position due to the employed force-volume method. This discontinuous charging leads to longer required stress time in order to reach the saturation in FDC-TF compared to C/DCT since the injected charge is collected during the intervals between discontinuous charging. Second, in spite of the longer observation time window used in the FDC-TF charging experiment (1 hour) compared to the C/DCT (15 min), the effective electrical stress time in the FDC-TF is much smaller compared to the C/DCT due to the force-volume method. During the whole observation time window for the FDC-TF charging experiment, the AFM tip comes in contact with each position over the  $\text{SiN}_x$  surface for only 27 times, each for less than 1 s, while in the C/DCT the charge injection takes place during the whole experiment time. On the other hand, the longer relaxation time for FDC-TF compared to C/DCT is attributed to the difference in charge collection mechanisms between both techniques. As explained, in C/DCT the charge is collected by the injecting electrodes. In contrast, in FDC-TF the discharging process takes place through charges crossing the dielectric film that are collected by the bottom electrode, similar to the discharging process in KPFM and in MEMS switches. This similarity in charge collection

mechanisms between the FDC-TF technique and MEMS switches resembles a very important advantage for FDC over the C/DCT technique.

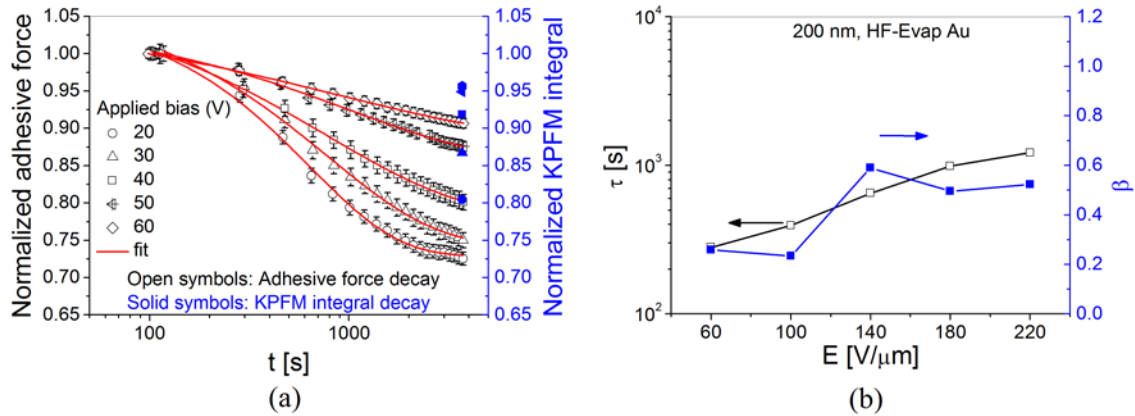


Figure 4.5. An example of adhesive force decay with time measured using the FDC-TF technique: (a) normalized adhesive force decay, and the corresponding values of KPFM potential profile integral, (b) the calculated decay time constant and stretch factor.

In principle, the charge collection process in KPFM-TF and FDC-TF methods are identical. **Fig. 4.5a** shows the normalized adhesive force decay measured by FDC-TF method for charges which were injected using the same electric fields and over the same  $\text{SiN}_x$  sample used in **Fig. 4.2** (KPFM-TF). In this experiment, the charging of  $\text{SiN}_x$  film was performed through a single scan with the biased AFM tip similar to charge injection in KPFM-TF, and then the induced adhesive force is monitored with time. For the sake of comparison with KPFM-TF decay, the corresponding values of KPFM potential profile integral from **Fig. 4.2d** after a time period of 1 hour from the charging step are plotted also in **Fig. 4.5a**. Though the comparison between decay data from both techniques (KPFM and FDC) is difficult considering that the measured physical quantity is different in both techniques, **Fig. 4.5a** shows a good correlation between the normalized data obtained from both measurements. The calculated decay time constant and stretch factor from FDC-TF is plotted in **Fig. 4.5b**. Comparing the decay time constant from FDC-TF (**Fig. 4.5b**) to KPFM-TF (**Fig. 4.2e**) reveals that the relaxation time is shorter for FDC-TF. This doesn't indicate a faster charge collection process in FDC-TF compared to KPFM-TF since both methods show a comparable decay as shown in **Fig. 4.5a**. The observed difference in the time constant calculated from both techniques is attributed mainly to the different observation time window used for both experiments (3.5 hours for KPFM-TF and 1

hour for FDC-TF). As explained earlier the relaxation time increases with the observation time window (**Fig. 4.3d**).

#### 4.4.3 FDC-MIM results

Though the FDC-TF method simulates efficiently the charge injection and discharging in MEMS switches, it suffers from two main drawbacks. First, in FDC-TF, similar to KPFM-TF, the AFM tip simulates only a single asperity while in MEMS switches charge injection takes place through thousands or maybe millions of asperities simultaneously. Second, due to the employed force-volume method, the FDC-TF technique requires a quite long observation time window in order to study the charging process resulting from fairly comparable electrical stress time compared to the normal actuation time in real MEMS devices. In order to overcome these issues and better approach the charging/discharging scenarios of MEMS switches, the FDC-MIM technique is developed to study charging/discharging processes in  $\text{SiN}_x$  films implemented in MIM capacitors [114]. During the charging process, the AFM tip contacts the MIM top electrode periodically at a relatively fast rate. Electrically stressing the MIM capacitor leads to charge injection in the whole MIM area simultaneously, similar to charging the whole dielectric film in MEMS switches. Also, the relatively fast contacting rate provides quite short intervals between consecutive contacting, and hence results in minimizing the charge collection between alternate charging time points. Finally, employing the MIM and the relatively fast contacting rate results in longer electrical stress times compared to FDC-TF for the same observation time window. After completing the charging step, the electric field is removed, and the induced adhesive force is measured over MIM top electrode with time. For the FDC-MIM method, MIM capacitors with the same  $\text{SiN}_x$  films used in section 4.4.2 (FDC-TF) were used.

An example of the induced adhesive force evolution with time as measured by FDC-MIM for charging and discharging experiments is presented in **Figs. 4.6a, b**, respectively. The voltage difference between the AFM tip and the MIM top electrode, which is determined by the potential of the MIM electrode, results in the measured induced adhesive force. Since the potential of the MIM electrode reflects the trapped charge in the  $\text{SiN}_x$  film, the measured force over the MIM electrode is a direct indication of the trapped charges in the dielectric film. Similar to the FDC-TF technique, the adhesive force evolution with time measured by FDC-MIM fits well with Eq. 4.4. The calculated decay time constant,  $\tau$ , and stretch factor,  $\beta$ , for charging/discharging decay is presented in **Fig. 4.6c**. Once again, the decay time constant is found to increase with the electric

field intensity,  $E$ , in agreement with the FDC-TF, C/DCT, and KPFM assessment methods. Furthermore, no consistent trend is found for the stretch factor versus the electric field as observed from the FDC-TF technique.

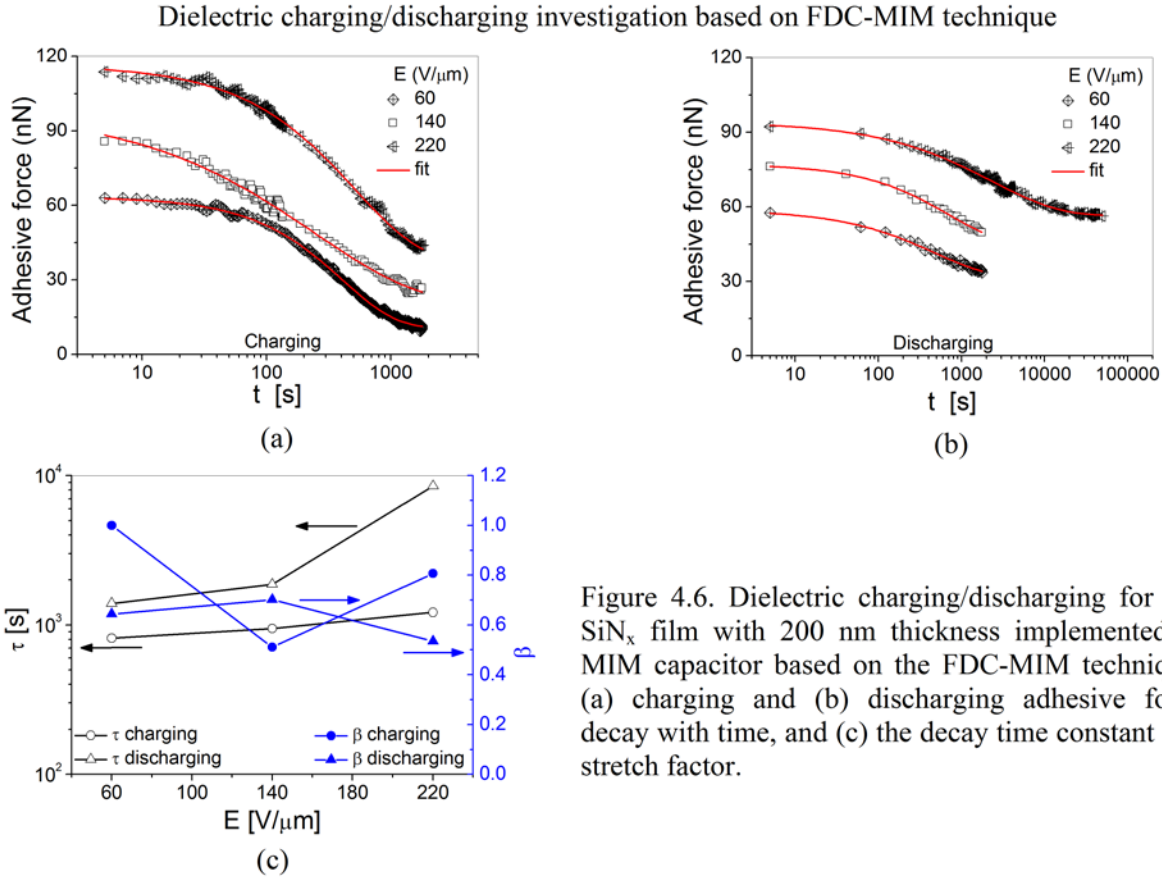


Figure 4.6. Dielectric charging/discharging for HF  $\text{SiN}_x$  film with 200 nm thickness implemented in MIM capacitor based on the FDC-MIM technique: (a) charging and (b) discharging adhesive force decay with time, and (c) the decay time constant and stretch factor.

Comparing the charging adhesive force measured by FDC-MIM (**Fig. 4.6a**) to the one from FDC-TF (**Fig. 4.5a, c**) and C/DCT methods (**Fig. 4.1a, b**), it is obvious that the charge injection process almost approaches saturation after only 30 min stress time in FDC-MIM, similar to the C/DCT experiment which reaches saturation after only 15 min, while the saturation point is still very far in FDC-TF even after 1 hour of charge injection. This is evident also from the calculated values of the decay time constant,  $\tau$ , for the three techniques. The charging decay time constant from the FDC-MIM technique (**Fig. 4.6c**) is generally smaller compared to the FDC-TF method (**Fig. 4.4e**), and it further approaches the decay time constant calculated from the C/DCT technique (**Fig. 4.1c**). The shorter time constant calculated for FDC-MIM compared to FDC-TF is attributed mainly to the longer effective electrical stress in the FDC-MIM time due to employing MIM capacitors as well as minimizing the charge collection between alternate

charging time points. Comparing **Fig. 4.6b** with **Fig. 4.4b, d**, it is clear that the discharging process in FDC-MIM is longer compared to the FDC-TF method. This is evident from the longer time constant calculated from FDC-MIM (**Fig. 4.6c**) compared to FDC-TF (**Fig. 4.4e**) and is attributed to the longer electrical stress time in FDC-MIM compared to FDC-TF. As reported in [76, 117], longer charging duration leads to larger relaxation time constant.

The comparison between **Fig. 4.6b** and **Fig. 4.1b** reveals that the discharging process in FDC-MIM is much longer compared to the C/DCT experiment. For example, for  $E = 220 \text{ v}/\mu\text{m}$ , the discharging adhesive force measured by FDC-MIM drops only to around 60% from its initial value at  $t = 0$  even after an observation time window of 10.6 hours, while from the C/DCT method the discharging current reaches almost 10% from its initial value after only 15 min for all investigated electric field. The longer decay time constant in FDC-MIM compared to C/DCT is also obvious comparing the discharging decay time constant for both techniques (**Fig. 4.6c, Fig 4.1c**) and is attributed mainly to the different charge collection mechanisms in both techniques as explained earlier.

#### 4.4.4 FDC-MEMS results

In the FDC-MEMS technique, the adhesive force evolution with time is measured over a charged  $\text{SiN}_x$  film implemented in a MEMS switch [114]. The results are compared to the adhesive force decay with time measured over the top electrode of a charged MIM capacitor implementing the same  $\text{SiN}_x$  film using the FDC-MIM technique. For both experiments, the MEMS switch and/or the MIM capacitor were continuously stressed first using the same conditions (44 V, 15 min). The  $\text{SiN}_x$  film implemented in the MIM capacitors and MEMS switches used in these experiments has 230 nm thickness and was deposited using the HF PECVD recipe in different fabrication run than the other samples investigated in this study. The results of these experiments are presented in **Fig. 4.7**. It is obvious from the figure that the adhesive force decay for both FDC-MEMS and FDC-MIM follows accurately Eq. 4.4 through the whole observation time window, similar to other FDC-based methods. Comparing the fitting results for the FDC-MEMS and FDC-MIM techniques reveals that the stretched exponential equation gives very similar values for the decay time constant and stretch factor for both techniques. This indicates that the discharging process in both techniques originates from charge collection by the bottom electrode through the same mechanisms. A similar conclusion has been drawn from the comparison between KPFM-MEMS and KPFM-MIM methods.

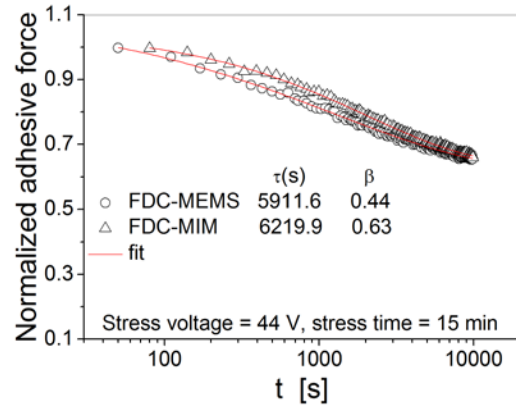


Figure 4.7. The normalized adhesive force decay with time measured by FDC-MEMS and FDC-MIM for the same HF SiN<sub>x</sub> films implemented in MEMS switches and MIM capacitors.

To sum up, three FDC-based novel characterization techniques have been introduced, correlated, and shown to be very powerful in studying the charging phenomenon in electrostatic MEMS. Both FDC-TF and FDC-MIM were used to study the charge build-up with time during the charging process as well as the charge collection during the discharging process. The FDC-TF technique simulates efficiently the charge injection and collection through a single asperity while the FDC-MIM methodology exhibits a considerable advantage over FDC-TF simulating the real scenarios of charging/discharging in MEMS switches. In both FDC-TF and FDC-MIM techniques, charge is collected by the bottom electrode similar to MEMS switches in the up-state, while for C/DCT the charge collection takes place through the injecting electrodes. This resembles a considerable advantage of the FDC-based characterization techniques over the C/DCT method, which always provides shorter relaxation times compared to MEMS. Finally, the FDC-MEMS and FDC-MIM lead to almost identical relaxation times indicating that the discharging process in both techniques arises from the same mechanisms.

#### 4.5 Summary

A complete package of novel characterization techniques based on KPFM and FDC measurements has been introduced and correlated. They were used to study the charging and discharging processes in bare dielectric films, MIM capacitors, and MEMS switches. The results from these techniques were correlated and compared to the C/DCT and TSDC measurements. The following are the main conclusions from this chapter:

- The C/DCT, KPFM, and FDC based characterization methods reveal larger injected charge density and longer decay time constants with increasing the charging electric field.

- MIM capacitors and MEMS switches lead to similar conclusions regarding the electrical properties of MEMS dielectrics when assessed using KPFM or FDC.
- KPFM-MIM and FDC-MIM can be applied as powerful characterization tools for the charging in MEMS (require MIM capacitors which have simpler structure than MEMS).
- FDC-TF and KPFM-TF simulate efficiently charge injection and collection through a single asperity (the AFM tip doesn't contribute to the charge injection/collection processes).
- FDC-TF and FDC-MIM can be used to study the charge build-up with time during the charging process which cannot be investigated using KPFM-based methods.
- The stretched exponential equation fits properly with the C/DCT charging/discharging current transients, KPFM surface potential decay, and FDC adhesive force decay. In all cases, the time constant increases with the experiment time window.
- In C/DCT, charge collection by the injecting electrodes reveals shorter relaxation times while in KPFM and FDC, charges are collected by the opposite electrodes, similar to MEMS switches, which results in longer relaxation times.
- The TSDC method allows determining the time constant dispersion over a wide range of values simultaneously with the distribution of centers in the material energy gap.

In conclusion, the integration between results from KPFM on the level of a single asperity, FDC on the level of multi asperity including the influence of meniscus formation, DCT for assessing the dielectric bulk properties represents a comprehensive characterization tool for a deeper understanding of the charging phenomenon in MEMS. In subsequent chapters, the characterization of numerous dielectric films is performed based mainly on the KPFM-TF and FDC-TF techniques. The C/DCT and TSDC methods were also used in some sections.

*Twenty years from now you will be more disappointed by the things you didn't do than by the ones you did. So throw off the bowlines, sail away from the safe harbor. Catch the trade winds in your sails. Explore. Dream. Discover.*

*Mark Twain  
1835 – 1910, American author and humorist*

## **5 Charging/discharging processes in SiN<sub>x</sub> films with various interfacial structures**

### **5.1 Introduction**

In this chapter, the influence of various key parameters on the dielectric charging/discharging processes is presented. This includes the effect of the dielectric film thickness, dielectric deposition conditions, and the physical layers under the dielectric films. Moreover, the impact of the bias amplitude, polarity, and duration applied to stress the dielectric films is discussed. Three electrical characterizations methods were employed to study these parameters (KPFM-TF, FDC-TF and C/DCT) that have been described in chapter 3, and the results from these techniques were correlated and compared. Furthermore, FT-IR and XPS were used to determine the chemical bonds and compositions, respectively, of the investigated SiN<sub>x</sub> films and their data were linked to the electrical characterization results.

The chapter is organized as follows. The investigated samples and the parameters of the used electrical characterization techniques are presented. Next, the influence of the dielectric film thickness and substrate are discussed. This is followed by presenting the impact of the charge injection conditions and the dielectric deposition parameters. A summary of the chapter is presented at the end.

### **5.2 Experimental**

Two different categories of SiN<sub>x</sub> samples were investigated. The first sample group consists of bare SiN<sub>x</sub> films deposited over planar substrates, while the second sample group is

MIM capacitors with the same SiN<sub>x</sub> films. The layer structure for the first group of samples and the details of each layer are presented in **Fig. 3.2** and **Table 3.1**, respectively. SiN<sub>x</sub> films with different thicknesses were deposited over metal layers (**Fig. 3.2b**) and over silicon substrates (**Fig. 3.2c**) in order to study the effect of the dielectric thickness and substrate. This basically resembles various charging scenarios which take place in capacitive RF MEMS switches where the dielectric layer is deposited over a metal transmission line and extends in the coplanar wave guide (CPW) slot (see **Fig. 3.2a**). The impact of the metal layer over which the dielectric is deposited was also studied through depositing SiN<sub>x</sub> films on evaporated gold (Evap Au), evaporated titanium (Evap Ti), and electrochemically-deposited gold (ECD Au) layers (**Fig. 3.2b**). The SiN<sub>x</sub> films were deposited using two recipes: low frequency (LF) and high frequency (HF) that are described in **Table 3.2** in order to study the influence of the deposition parameters on the dielectric charging. The layer structure of the second group of samples (MIM capacitors) is presented in **Table 3.3**. Similar to the investigated bare dielectric films, MIM capacitors employing SiN<sub>x</sub> films with different thicknesses and deposited using both LF and HF deposition recipes were investigated.

The first sample group (bare dielectric films) was characterized using the KPFM-TF and FDC-TF assessment methods described in chapter 3. The KPFM-TF method (**Fig. 3.4**) was employed to investigate the charging/discharging processes for a single asperity where charges were injected in single points over the SiN<sub>x</sub> films using different pulse amplitudes, U<sub>p</sub>, and pulse duration, T<sub>p</sub>. The FDC-TF technique described in section 3.4.2 was used to study the charging/discharging processes and the influence of meniscus formation in selected bare SiN<sub>x</sub> films. In this technique, the charge injection was performed in areas over the SiN<sub>x</sub> surface rather than in single points as performed with the KPFM-TF method. Charge injection in areas resembles the real situation of MEMS switches where charging takes place in the whole dielectric area between the bridge and the dielectric film. This could not be performed using the KPFM-TF method due to the limited maximum potential which could be measured as explained in chapter 3. In the FDC-TF measurements, the charging of SiN<sub>x</sub> films was performed through a single scan over a selected area of the dielectric surface (10 μm X 10 μm) using different voltage amplitudes. After completing the charge injection step, the discharging process was studied through monitoring the decay of induced surface potential and induced adhesive force with time using KPFM and FDC, respectively. The observation time window for the decay experiments

was 3.5 hours and 1 hour for the KPFM and the FDC measurements, respectively. Also, the time interval between the end of the charge injection step and the beginning of the KPFM or FDC measurement was 30 s. In order to avoid the influence of humidity and the adsorbed water film over the dielectric surface on both KPFM and FDC measurements as well as on the charging/discharging processes, the SiN<sub>x</sub> samples and the AFM tip went through two cycles of heating (150 °C) and cooling steps under vacuum. In addition, both KPFM and FDC measurements were performed under dry air flow (relative humidity ≈ 0.02%) using the controlled environment AFM chamber presented in **Fig. 3.11**.

On the other hand, the second sample group (MIM capacitors) was characterized using the C/DCT method presented in section 3.5.1 where MIM capacitors were stressed under different electric field intensities. The observation time window for the C/DCT experiments measurements was 1000 s for each charging and discharging measurement. Finally, the results obtained from the KPFM, FDC, and C/DCT were correlated and linked to the FT-IR and XPS data.

### **5.3 Influence of SiN<sub>x</sub> film thickness**

In this section, the results from the electrical characterization techniques (KPFM-TF, FDC-TF, and C/DCT) are presented first. This is followed by presenting the influence of SiN<sub>x</sub> film thickness on material stoichiometry based on FT-IR and XPS data. The explanation of the electrical characterization results and their correlation with the dielectric material stoichiometry are then discussed.

#### *5.3.1 KPFM results*

**Figure 5.1** depicts the measured KPFM-TF surface potential amplitude,  $U_s$ , FWHM, and potential profile integral as a function of the applied electric field intensity,  $E$ , for HF-Evap Au and LF-Evap Au samples with different film thicknesses. It is evident from the figure that for each film thickness, increasing the electric field,  $E$ , applied during the charge injection results in higher  $U_s$ , FWHM, and consequently larger potential profile integral. Since the potential profile integral is a direct indication of the injected charge density in the dielectric film, it is concluded that higher electric field leads to larger trapped charges in the dielectric film. It is also clear that the measured  $U_s$ , FWHM, and potential profile integral are larger for thicker dielectric films when the same electric field is applied during the charge injection step. This further indicates that

thicker dielectric films have larger injected charge density compared to thinner ones for the same applied electric field [123]. These remarks have been made for both positive and negative charge injection and for both HF and LF  $\text{SiN}_x$  films, deposited over metal layers or directly over Si substrates.

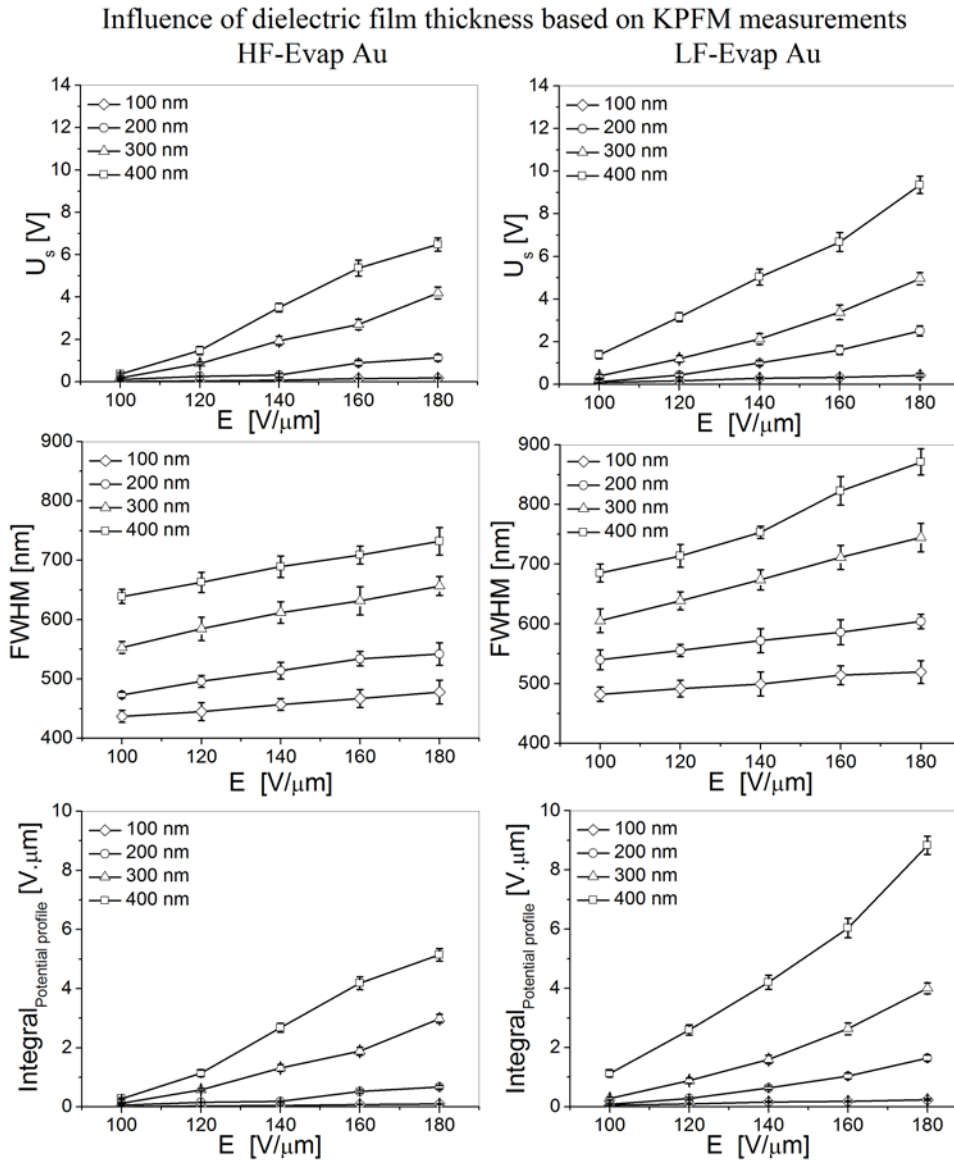


Figure 5.1. The influence of the  $\text{SiN}_x$  film thickness on the induced surface potential amplitude,  $U_s$ , potential distribution, FWHM, and potential profile integral as measured by KPFM for HF-Evap Au (left) and LF-Evap Au (right) samples, for injected charges using different electric field ( $T_p = 1$  s).

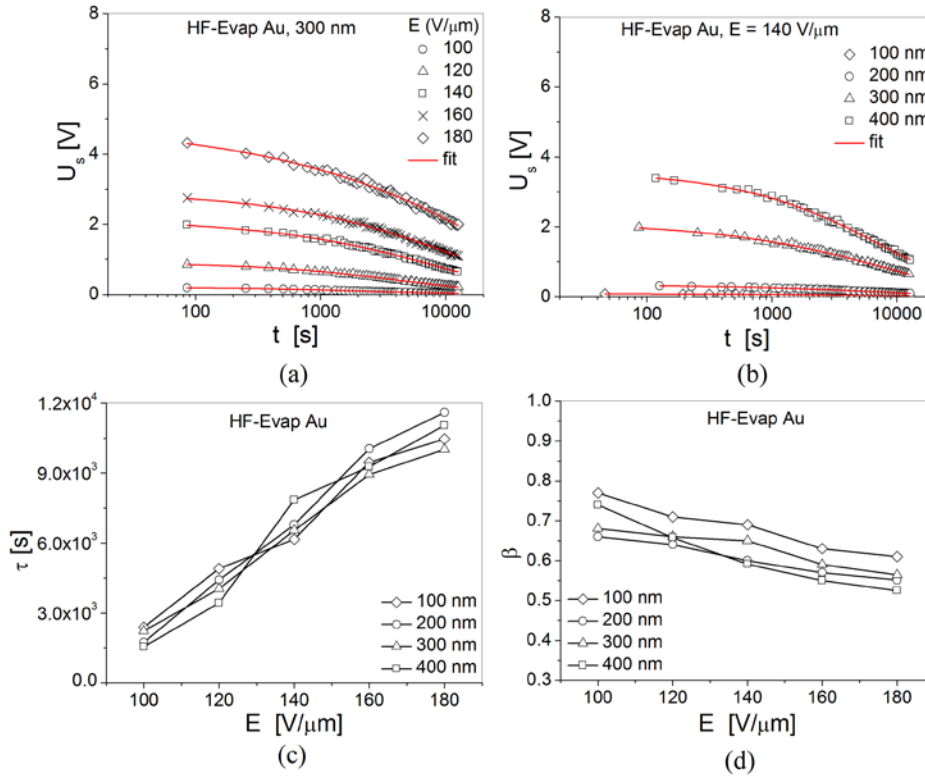
Surface potential decay,  $\tau$ , and  $\beta$  for different dielectric thicknesses based on KPFM measurements

Figure 5.2. The influence of the SiN<sub>x</sub> film thickness on the discharging process as measured by KPFM: surface potential decay with time for (a) HF-Evap Au sample with 300 nm film thickness under different electric field and (b) HF-Evap Au samples with different film thicknesses under the same electric field (140 V/ $\mu$ m); (c) the calculated decay time constant,  $\tau$ , and (d) stretch factor,  $\beta$ , for HF-Evap Au samples with different film thicknesses, ( $T_p = 1$  s).

An example for the surface potential decay with time is presented in **Fig. 5.2a, b**. The potential decay for HF-Evap Au samples with 300 nm thickness, for charges which were injected under different electric field intensities,  $E$ , is shown in **Fig. 5.2a**. Also, the surface potential evolution with time for HF-Evap Au samples with different film thicknesses for the same applied electric field intensity is presented in **Fig. 5.2b**. For all potential decay experiments, the charge evolution was monitored for a fixed time window of 3.5 hours. Since a charge trapped near the surface will be monitored by KPFM, the potential decay arises from charge collection or transport to sites far from dielectric surface. As shown from **Figs. 5.2a, b**, the surface potential decay follows the stretched exponential law (Eq. 4.3) as explained in chapter 4. This has been observed for charges which were injected under different electric field, different charge injection duration,  $T_p$ , both bias polarities, and for all SiN<sub>x</sub> samples investigated in this study. The decay

time constant,  $\tau$ , and stretch factor,  $\beta$ , calculated from fitting the KPFM surface potential decay with Eq. 4.3 for the HF-Evap Au samples with different thicknesses are shown in **Fig. 5.2c**. For all film thicknesses, the decay time constant,  $\tau$ , increases while the stretch factor,  $\beta$ , decreases with increasing the applied electric field. The figure also shows that for a given electric field the impact of the dielectric film thickness on the decay time constant,  $\tau$ , and stretch factor,  $\beta$ , is very small and does not constitute a clear trend. These remarks have been also made for the LF-Evap Au, HF-Si and LF-Si samples, with different film thicknesses.

### 5.3.2 FDC results

**Figure 5.3** presents the influence of dielectric film thickness on the charging/discharging processes as measured by the FDC-TF method. For all investigated  $\text{SiN}_x$  samples, it is found that increasing the electric field applied during the charging step leads to larger induced surface potential (**Fig. 5.3a**) and higher adhesive force (**Fig. 5.3b**). This indicates larger injected charge density in the  $\text{SiN}_x$  films with higher applied electric field. **Figure 5.3a, b** shows also that the induced surface potential as well as the induced adhesive force increases considerably with increasing the dielectric film thickness for the same applied electric field. An example of the evolution of the measured adhesive force with time for  $\text{SiN}_x$  samples with different thicknesses charged using the same electric field (140 V/ $\mu\text{m}$ ) is presented in **Fig. 5.3c**. It is found that the decay of the adhesive force with time fits very well with the square of the stretched exponential equation (Eq. 4.4) as explained in chapter 4, and this has been observed for all investigated  $\text{SiN}_x$  samples in this study. For each film thickness, charge injection using larger electric field results in increasing the decay time constant as shown in **Fig. 5.3d**. In addition, **Fig. 5.3c** highlights that the  $\text{SiN}_x$  films with different thicknesses exhibits similar discharging behavior and have quite similar decay time constants when stressed with the same electric field (**Fig. 5.3d**). These observations regarding the induced surface potential, induced adhesive force, and discharging process have been observed for both  $\text{SiN}_x$  films deposited over evaporated Au layers (HF-Evap Au) and over Si substrate (HF-Si) as shown from the figure.

The comparison between **Fig. 5.3a, b** and **Fig. 5.1** reveals that the KPFM-TF measurements performed on the scale of a single asperity and the FDC-TF characterization on the scale of multi asperity lead to the same conclusion regarding the influence of the dielectric film thickness on the charging process. The higher levels of induced surface potential measured by the FDC method (**Fig. 5.3a**) indicates clearly the importance of employing such assessment

methodology compared to KPFM for characterizing the dielectric films used in MEMS. Also, the comparison between **Fig. 5.3d** and **Fig. 5.2c** leads to a similar conclusion regarding the influence of film thickness on the discharging process. The shorter decay time constant calculated from the adhesive force decay (**Fig. 5.3d**) compared to the time constant calculated from KPFM surface potential decay (**Fig. 5.2c**) is attributed mainly to the different observation time window used for both experiments (3.5 hours for KPFM and 1 hour for FDC) as explained in chapter 4.

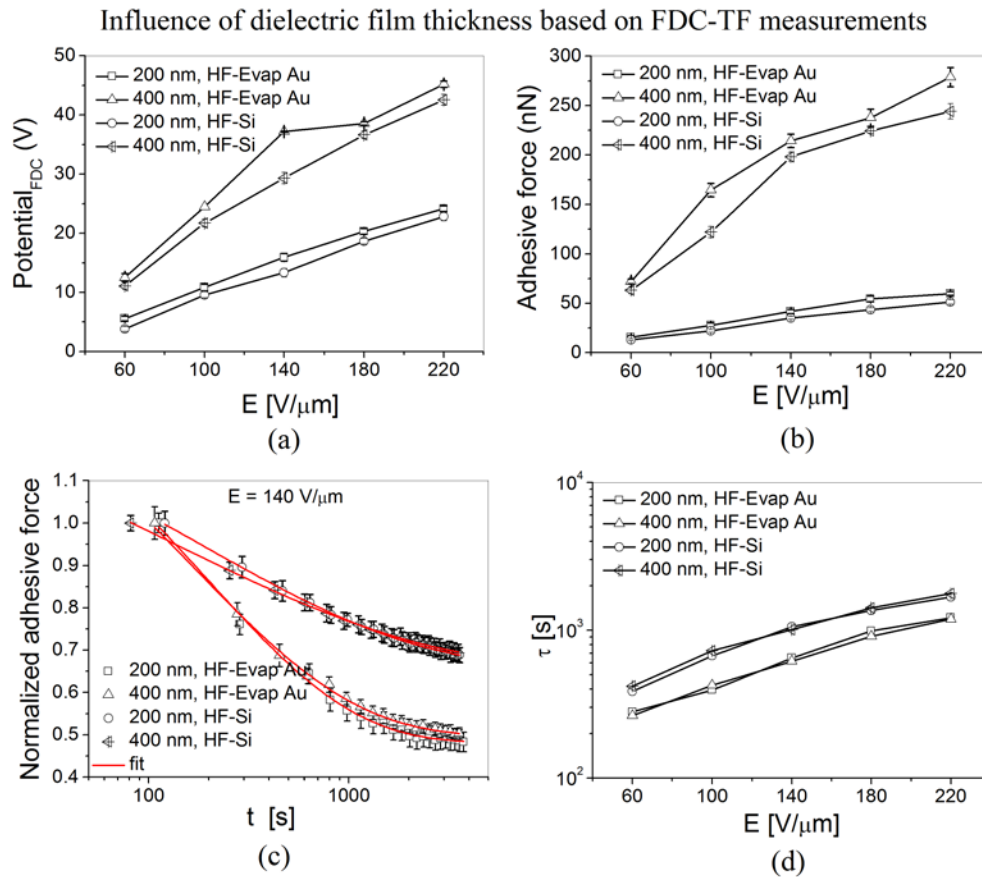


Figure 5.3. The influence of dielectric film thickness as measured by the FDC-TF technique for charges which were injected using different electric field: (a) the induced surface potential, (b) the induced adhesive force, (c) an example of the adhesive force decay with time for different samples for charges injected using  $E = 140 \text{ V}/\mu\text{m}$ , and (d) the calculated decay time constant from the adhesive force decay.

### 5.3.3 C/DCT results

The MIM capacitors described in **Table 3.3** were characterized using the C/DCT technique (see section 3.5.1) and an example of the results is shown in **Fig. 5.4**. The measured charge in the external MIM circuit,  $\sigma_0$ , as a function of applied electric field intensity,  $E$ , for LF

SiN<sub>x</sub> films with different thicknesses is plotted in **Fig. 5.4a**. For a given film thickness, the measured charge,  $\sigma_0$ , which is a direct indication of the measured discharge current amplitude, increases with the applied electric field. In addition, for the same electric field larger current amplitudes and hence larger charges,  $\sigma_0$ , are measured for thicker dielectric films compared to thinner ones. In C/DCT the measured discharge current transients are performed in the presence of internal electric fields generated by trapped charge gradients. As the injected charge density in the dielectric film increases, the charge gradient increases too, leading to a higher internal electric field. This in sequence results in larger measured discharge current transients and hence larger measured charge,  $\sigma_0$ , in the external circuit. Based on this analysis the injected charge density increases with the applied electric field for a given film thickness. Furthermore, when the same electric field is applied, thicker dielectrics have larger injected charge density than thinner ones.

Influence of dielectric film thickness based on C/DCT measurements

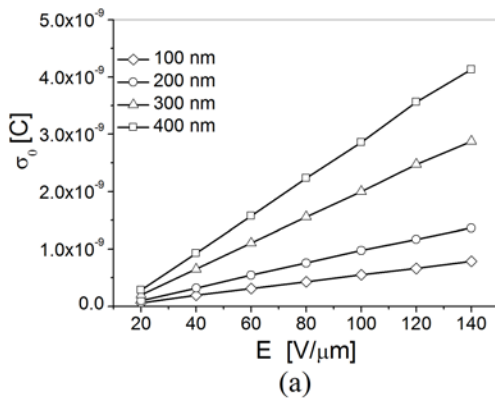
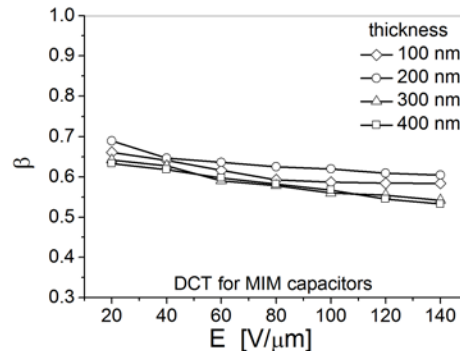
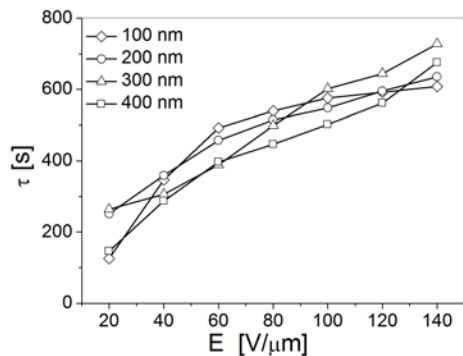


Figure 5.4. The influence of dielectric thickness as measured using the C/DCT method: (a) the measured charge,  $\sigma_0$ , for LF SiN<sub>x</sub> samples, (b) the decay time constant,  $\tau$ , and stretch factor,  $\beta$ , for HF SiN<sub>x</sub>.



(b)

Comparing **Fig. 5.4a**, **Fig. 5.3a** and **Fig. 5.1**, it is obvious that the results from the C/DCT measurements agree quite well with FDC-TF and KPFM-TF. As presented earlier, KPFM and

FDC measurements shows that as the applied electric field and/or dielectric thickness increases, the induced surface potential increases too indicating larger injected charge density. This is supported by the increase in the measured stored charge,  $\sigma_0$ , using the C/DCT methodology for higher electric field and/or dielectric film thickness. In KPFM and FDC experiments, the measured surface potential just after completing the charge injection step (at  $t = 0$  s) represents the induced potential caused mainly by surface charges rather than bulk charges. This is primarily due to electric field screening by surface charges. In the C/DCT method, the measured current transients at  $t = 0$  are caused mainly through collecting charges which are very close from the injecting MIM electrodes rather than charges trapped in the dielectric bulk. This similarity between KPFM, FDC and C/DCT measurements explains the agreement in the results related to the charging process obtained from these techniques.

The decay of charging/discharging current transients follows a modified version of the stretched exponential law (Eq. 4.2), and this has been observed for all  $\text{SiN}_x$  films charged using different electric field and measured by the C/DCT method. The decay time constant,  $\tau$ , and stretch factor,  $\beta$ , calculated from fitting the decay of the discharge current with Eq. 4.2 for HF  $\text{SiN}_x$  films with different thicknesses are shown in **Fig. 5.4b**. It is obvious that the decay time constant increases with the electric field, similar to what has been observed from both KPFM and FDC. Moreover, the stretch factor decreases with the electric field similar to KPFM. Comparing the values of the decay time constant,  $\tau$ , calculated from KPFM (**Fig. 5.2c**), FDC (**Fig. 5.3d**) and C/DCT (**Fig. 5.4b**) reveals that the decay time constant is much longer for KPFM and FDC compared to the C/DCT. This is attributed to the different processes involved in the collection of injected charges. The charge collection by the injecting electrodes which occurs in the C/DCT method always reveals shorter relaxation times. In contrast, in the KPFM or FDC method the injected charges are always collected by the opposite electrodes, and due to successive charge trapping and emission as well as percolation, the process relaxation time is always longer as explained in chapter 4. Here it is important to mention that the results related to the charging process presented in **Fig. 5.1** (KPFM), **Fig. 5.3a, b** (FDC), and **Fig. 5.4a** (C/DCT) are obtained just after completing the charge injection step (at  $t = 0$ ). Therefore, the mentioned difference in the charge collection process between these techniques does not affect the charging measurements. This further explains the agreement between KPFM, FDC and C/DCT results related to the charging process.

To sum up, the results from the three employed electrical characterization techniques (KPFM-TF, FDC-TF, and C/DCT) show a very good agreement, and leads to similar conclusions regarding the influence of the dielectric film thickness on both charging/discharging processes. For each film thickness, the injected charge density as well as the decay time constant increases remarkably with the applied electric field. The injected charge density is found to be higher for thicker dielectric films compared to thinner ones when the same electric field is applied during the charging step. Finally, SiN<sub>x</sub> films with different thicknesses show a similar discharging behavior when stressed with the same electric field intensity.

#### *5.3.4 Influence on material stoichiometry*

The XPS results for HF and LF SiN<sub>x</sub> samples are summarized in **Table 5.1** and **Table 5.2**, respectively. It is evident from **Table 5.1** that both the surface and the bulk of the HF samples with different film thicknesses and different substrates are all silicon rich (N/Si ratio is in the range of 0.56 to 0.73) with almost consistent concentrations for different elements. The natural contamination in the layers surface by carbon and oxygen is present, especially the 300 nm HF-Evap Au sample with a higher carbon contamination (23.1%) in its surface compared to other samples. Furthermore, there is concentration difference in the N/Si ratio between the surface and the bulk of all samples, while the N/Si ratio in the bulk represents the true composition of the dielectric film. **Table 5.2** shows also that the surface and the bulk of the LF samples with different film thicknesses and different substrates are all silicon rich (N/Si is in the range of 0.56 to 0.85) with consistent concentrations for different elements. The difference in the N/Si ratio between the surface and bulk composition for LF SiN<sub>x</sub> samples is also present. Here it should be emphasized that in all investigated SiN<sub>x</sub> films, there are unknown hydrogen concentrations, which could play an important role in the material properties, and consequently could contribute to the charge trapping behavior.

Table 5.1. Surface and bulk quantification by XPS (% atomic) for the HF SiN<sub>x</sub> samples (source ray Al or Mg monochromator, E<sub>p</sub> = 20 eV, correction Scofield).

Sample	thickness (nm)	Type	C	O	N	Si	N/Si
			at %				
HF-Evap Au	100	Surface	8.6	23.6	27.6	40.2	0.69
HF-Evap Au	100	<b>Bulk</b>	-	-	42	58	<b>0.72</b>
HF-Evap Au	200	Surface	6.6	24.0	29.2	40.1	0.73
HF-Evap Au	200	<b>Bulk</b>	-	-	41	59	<b>0.69</b>
HF-Evap Au	300	Surface	23.1	25.9	18.3	32.6	0.56
HF-Evap Au	300	<b>Bulk</b>	-	-	40	60	<b>0.67</b>
HF-Evap Au	400	Surface	7.8	30.2	23.6	38.4	0.61
HF-Si	100	Surface	9	29.2	23.9	37.8	0.63
HF-Si	100	<b>Bulk</b>	-	-	41.5	58.5	<b>0.71</b>
HF-Si	200	Surface	16.1	31.9	18.1	33.9	0.53
HF-Si	200	<b>Bulk</b>	-	-	41	59	<b>0.70</b>
HF-Si	300	Surface	12	31.7	21.7	34.6	0.63
HF-Si	300	<b>Bulk</b>	-	-	41.8	58.2	<b>0.72</b>
HF-Si	400	Surface	13.8	28.6	21.4	36.0	0.59
HF-Si	400	<b>Bulk</b>	-	-	41.5	58.5	<b>0.71</b>

Table 5.2. Surface and bulk quantification by XPS (% atomic) for the LF SiN<sub>x</sub> samples.

Sample	Thickness (nm)	Type	C	O	N	Si	N/Si
			at %				
LF-Evap Au	100	Surface	10	30.8	25	34.2	0.73
LF-Evap Au	100	<b>Bulk</b>	-	-	46	54	<b>0.85</b>
LF-Evap Au	200	Surface	10	28.8	26	35.2	0.74
LF-Evap Au	200	<b>Bulk</b>	-	-	45	55	<b>0.82</b>
LF-Evap Au	300	Surface	10.6	27.4	26.4	35.6	0.74
LF-Evap Au	300	<b>Bulk</b>	-	-	43.5	56.5	<b>0.77</b>
LF-Evap Au	400	Surface	9.8	28.1	26.1	35.9	0.73
LF-Evap Ti	200	Surface	10	30.9	24.2	34.9	0.69
LF-Evap Ti	200	<b>Bulk</b>	-	-	45.4	55.6	<b>0.82</b>
LF-Si	100	Surface	11.9	37.7	18.6	31.8	0.58
LF-Si	100	<b>Bulk</b>	-	-	45	55	<b>0.81</b>
LF-Si	200	Surface	11.7	36.2	19.0	33.1	0.57
LF-Si	200	<b>Bulk</b>	-	-	44	56	<b>0.79</b>
LF-Si	300	Surface	10.5	37.5	19.4	32.6	0.60
LF-Si	300	<b>Bulk</b>	-	-	44.4	55.6	<b>0.80</b>
LF-Si	400	Surface	9.0	38.1	18.9	34.0	0.56
LF-Si	400	<b>Bulk</b>	-	-	45	55	<b>0.82</b>

The FT-IR spectra for HF-Evap Au, LF-Evap Au, and HF-Si samples with different thicknesses are presented in **Fig. 5.5a, b, c**, respectively. Also, **Table 5.3** presents the corresponding wavenumbers of different bonds for HF-Evap Au and LF-Evap Au films. Such FT-IR spectra reveal that there is a strong Si-H bond (at around 2150 cm<sup>-1</sup> for HF SiN<sub>x</sub> and at 2179 cm<sup>-1</sup> for LF SiN<sub>x</sub>) and N-H bond (at around 3356 cm<sup>-1</sup> and at 3346 cm<sup>-1</sup> for LF SiN<sub>x</sub>), independently of the dielectric film thickness and substrate. Since the hydrogen content in the

film will affect the silicon excess, a particular attention was paid to the Si–H and N–H bonds. The relative intensity of Si–H and N–H peaks extracted from FT-IR spectra for HF-Evap Au and LF-Evap Au materials are shown in **Table 5.4**, and the N–H / Si–H ratio is plotted in **Fig. 5.5d**. The N/Si ratio determined by XPS analysis (**Table 5.1, 5.2**) is also plotted in the figure. It is evident that the dielectric film thickness has a negligible influence on the N/Si and N–H/Si–H ratios. Similar remarks have been made for the HF-Si and LF-Si samples with different film thicknesses. This similarity in material stoichiometry was expected since those films with different thicknesses were deposited using the same deposition conditions but for different deposition durations.

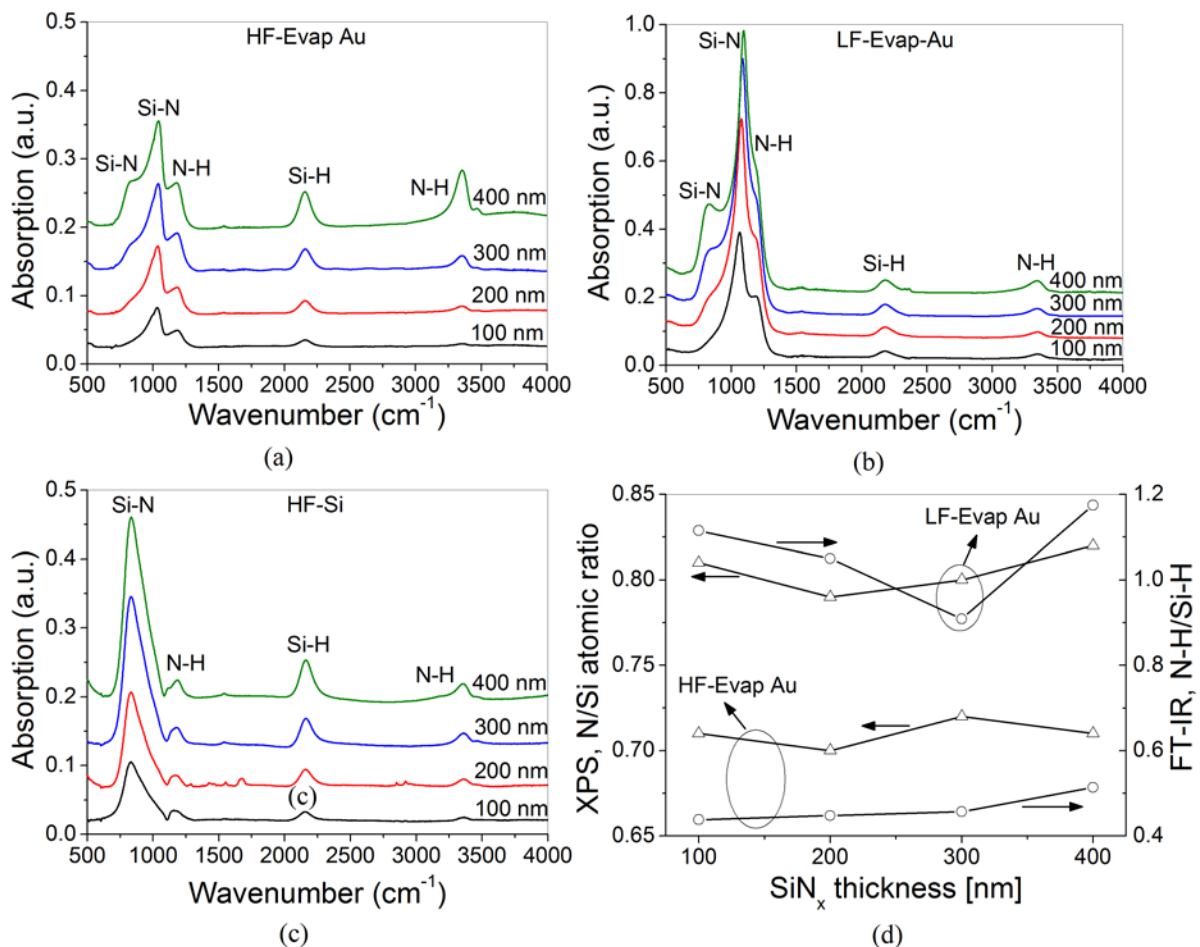


Figure 5.5. The material stoichiometry for SiN<sub>x</sub> films with different thicknesses: FT-IR reflection spectra at an angle of 70° for (a) HF-Evap Au samples and (b) LF-Evap Au samples; (c) FT-IR transmission spectra for HF-Si samples; and (d) the N/Si ratio from XPS and N-H/Si-H ratio from FT-IR as a function of the dielectric thickness for HF-Evap Au and LF-Evap Au samples.

Table 5.3. The FT-IR absorptions for HF-Evap Au and LF-Evap Au SiN<sub>x</sub> films with different thicknesses.

Sample	HF-Evap Au (Cm <sup>-1</sup> )					LF-Evap Au (Cm <sup>-1</sup> )				
	Si-N	Si-N	N-H	Si-H	N-H	Si-N	Si-N	N-H	Si-H	N-H
100		1038	1194	2149	3356		1064	1205	2176	3349
200	850	1039	1193	2150	3356	850	1078	1200	2181	3347
300	852	1040	1192	2150	3356	852	1071	1200.5	2181	3346
400	850	1043	1190	2151	3355	850	1080	1195	2179	3344

Table 5.4. The relative intensity of Si-H and N-H bonds extracted from FT-IR spectra and the N-H/Si-H ratio for HF-Evap Au and LF-Evap Au SiN<sub>x</sub> films with different thicknesses.

Sample	HF-Evap Au			LF-Evap Au		
	Si-H (2150 Cm <sup>-1</sup> )	N-H (3356 Cm <sup>-1</sup> )	N-H/ Si-H	Si-H (2179 Cm <sup>-1</sup> )	N-H (3346 Cm <sup>-1</sup> )	N-H/ Si-H
100	0.00776	0.00340	0.43814	0.01019	0.01136	1.11514
200	0.01899	0.00850	0.44760	0.01220	0.01281	1.04985
300	0.03500	0.01600	0.45714	0.02090	0.01876	0.89773
400	0.05660	0.02906	0.51351	0.04450	0.05226	1.17447

### 5.3.5 Discussion

The injected charge density is known to increase with the applied electric field intensity [35]. This agrees with the presented electrical characterization results for each SiN<sub>x</sub> thickness where the potential profile integral from KPFM, the induced surface potential and adhesive force from FDC, and the measured charge from C/DCT are found to increase with the applied electric field. There are three main factors that determine the amount of the trapped charges in SiN<sub>x</sub> films with different thicknesses, which are the electric field intensity, electrical stress duration, and the material trap density which is directly determined by material stoichiometry. As presented, both FT-IR and XPS measurements lead to the conclusion that the influence of the dielectric film thickness on SiN<sub>x</sub> material stoichiometry is negligible, and this has been observed for HF and LF SiN<sub>x</sub> films independently of the substrate. Therefore, for given electrical stress duration the main dominant parameter in determining the injected charge density in SiN<sub>x</sub> films with different thicknesses is the applied electric field intensity. The increase in the injected charge density with the dielectric film thickness for a given applied electric field cannot be explained by the contribution of the dipole orientation solely. This is because dipolar polarization will lead to the formation of a bound surface charge which is independent of the dielectric thickness. In contrast, the space charge polarization gives rise to a distribution of charges which leads to a non neutral bulk, and depending on the material properties will lead to a macroscopic charging that may depend on the film thickness [37, 52]. According to this we are led to the conclusion that in HF and LF SiN<sub>x</sub> materials the space charge polarization induced by trapped charge, constitutes the dominant charging mechanism.

The increase of decay time constant,  $\tau$ , with the electric field intensity as measured by KPFM (**Fig. 5.2c**), FDC (**Fig. 5.3d**), and C/DCT (**Fig. 5.4b**) is attributed mainly to the lowering of potential barrier for charge emission from band gap states due to the Poole–Frenkel (PF) effect explained in section 2.4.2. The classical PF equation is given by Eq. 2.1. From this equation, the decrease in the traps potential barrier given by  $\sqrt{\frac{qE}{\pi\epsilon}}$  [124] is the same for all traps.

Therefore, for shallow states the decrease of the potential barrier is expected to be more efficient in terms of the required energy for charge emission from these states compared to deeper ones. Since the discharging process is monitored in a predetermined time window (3.5 hours for KPFM, 1 hour for FDC, and 15 min for C/DCT), the apparent relaxation time will be determined by the states which exhibit relaxation times comparable to this time window [125]. According to that when the applied electric field intensity increases, charges from shallower states will be more easily released, leaving charges trapped in deeper ones. Since the latter are characterized by larger relaxation times, it becomes clear that the decay time constant,  $\tau$ , will increase with increasing the electric field intensity. Another contribution to the increase of the decay time constant with the electric field intensity arises from the tunneled electrons from the MIM electrode and/or the metal coated AFM tip to the traps nearby the electrode through the Trap Assisted Tunneling (TAT) explained in chapter 2. These electrons must be further excited to the conduction band again (PF) leaving the ones in deeper traps to hop to next trap sites to reach the anode when the insulator is thick enough as described in **Fig. 2.4** [126].

The stretch factor,  $\beta$ , is found to slightly decrease with the electric field intensity as obtained from KPFM (**Fig. 5.2c**) and C/DCT (**Fig. 5.4b**), while the FDC measurements does not lead to a consistent trend for the stretch factor as a function of the electric field. Generally speaking, the decreases of the stretch factor points out that the discharge process deviates from the simple exponential law (where  $\beta = 1$ ), and hence the charge collection mechanism becomes more complex. During the charging process, the combined contribution of the PF and TAT effects is expected to lead to a more complex process as the applied electric field intensity increases. In the case of discharge, the charge collection is performed in the presence of internal electric fields generated by charge gradients. Then, the charge collection process is also expected to follow a more complex process since that shallow states were previously emptied by the

charging under high electric field intensities. Based on this analysis, the value of the stretch factor,  $\beta$ , is expected to decrease as the applied electric field intensity increases.

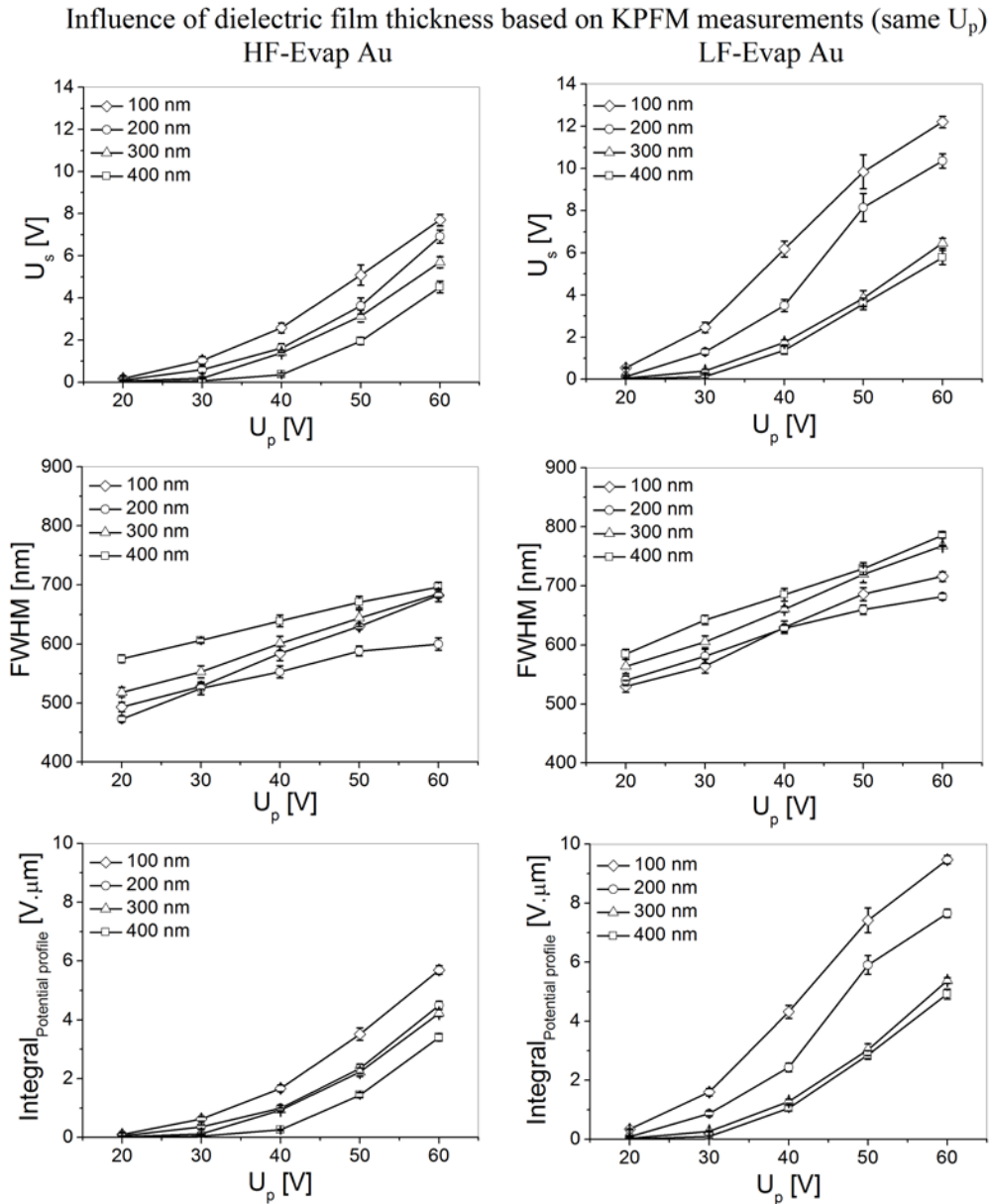


Figure 5.6. The KPFM surface potential amplitude,  $U_s$ , distribution, FWHM, and potential profile integral for HF-Evap Au (left) and LF-Evap Au (right) samples with different film thicknesses, for charges injected using different  $U_p$  ( $T_p = 1$  s).

For MEMS capacitive switches, the applied actuation voltage does not vary a lot with the dielectric film thickness. This further indicates that the employed thinner dielectric films are normally exposed to higher electric field intensities compared to thicker ones. Therefore, the

influence of the dielectric film thickness should be assessed using the same applied voltage rather than the same electric field. **Figure 5.6** depicts the KPFM surface potential amplitude,  $U_s$ , FWHM, and potential profile integral as a function of the applied pulse amplitude,  $U_p$ , for the HF-Evap Au (left) and LF-Evap Au (right) samples with different film thicknesses. For a given pulse amplitude,  $U_p$ , a smaller surface potential amplitude,  $U_s$ , is measured for thicker dielectric films compared to thinner ones. Yet, the FWHM does not show a consistent trend as a function of the film thicknesses for a given pulse amplitude,  $U_p$ . The potential profile integral is also presented in the figure and shows that the injected charge density is higher in thinner dielectric films compared to thicker ones, for a given pulse amplitude. This could be observed for both HF and LF  $\text{SiN}_x$  films, deposited over metal layers or directly over Si.

The decay of KPFM surface potential for bare  $\text{SiN}_x$  samples with different film thicknesses stressed with the same pulse amplitude,  $U_p$ , was also investigated. The decay time constant,  $\tau$ , and stretch factor,  $\beta$ , calculated from fitting the surface potential decay with Eq. 4.3 as a function of the dielectric film thickness for the HF-Evap Au samples are plotted in **Fig. 5.7**. For a given film thickness, the decay time constant,  $\tau$ , increases while the stretch factor,  $\beta$ , decreases with increasing the applied pulse amplitude,  $U_p$ , due to increasing the electric field intensity as explained earlier. For a given pulse amplitude,  $U_p$ , thinner dielectric films have longer decay time constant,  $\tau$ , and smaller stretch factor,  $\beta$ , compared to thicker ones. The electric field intensity is larger for thinner dielectric films compared to thicker ones, for a given pulse amplitude,  $U_p$ . Therefore, the influence of reducing the film thickness is equivalent to increasing the electric field intensity, and in sequence the PF effect and TAT will be more pronounced leading to longer decay time constant,  $\tau$ , and smaller stretch factor,  $\beta$ , as explained earlier. Finally, similar trends for both the decay time constant,  $\tau$ , and the stretch factor,  $\beta$ , under different applied pulse amplitude,  $U_p$ , have been observed for the LF-Evap Au samples with different film thicknesses.

In view of the above analysis, thicker  $\text{SiN}_x$  films that have smaller injected charge density (hence smaller trapped charge) and shorter decay time constant (hence faster charge decay) for charges injected using the same voltage are more robust compared to thinner films to reduce the dielectric charging phenomenon. Consequently, MEMS switches employing thicker  $\text{SiN}_x$  dielectric films will have less dielectric charging and therefore longer lifetime compared to switches employing thinner films, for the same actuation voltage. Certainly, a very high

dielectric thickness cannot be used for electrostatic capacitive MEMS switches which operate mainly based on the high capacitance ratio between the “on” and “off” states ( $C_{on}/C_{off}$ ). As the dielectric thickness increases,  $C_{on}/C_{off}$  decreases which degrades the RF performance of the device. Therefore, for capacitive MEMS switches the selection of the dielectric thickness should be a compromise between the dielectric charging phenomenon and the device RF performance. Additionally, in order to further minimize the dielectric charging, it is recommended to actuate the switch using a smaller voltage. As concluded from KPFM, FDC, and C/DCT measurements, stressing the dielectric film with a smaller electric field results in smaller injected charge density and faster charge collection process. This conclusion agrees with the measurement results of capacitive MEMS switches where increasing the applied stress voltage was reported to accelerate dielectric charging and hence increase the actuation voltage shift [56, 127], and finally results in shortening the switch life time [21].

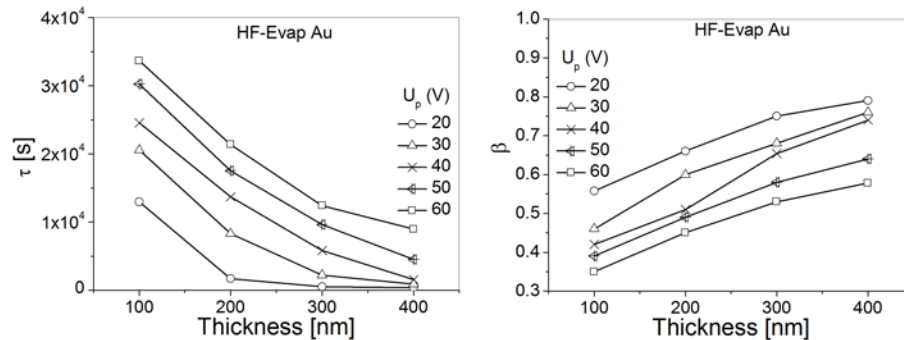


Figure 5.7. The decay time constant,  $\tau$ , and stretch factor,  $\beta$ , calculated from KPFM surface potential decay for HF-Evap Au samples with different film thicknesses, for charges injected using different  $U_p$  ( $T_p = 1$  s).

## 5.4 Influence of substrate and underlying metal layers

In this section, the difference in charging/discharging processes between  $\text{SiN}_x$  films deposited over metal layers and over Si substrates is presented first. This is followed by discussing the effect of the metal layer under the  $\text{SiN}_x$  film.

### 5.4.1 $\text{SiN}_x$ over silicon substrate versus $\text{SiN}_x$ over Au

Recently, charging related lifetime tests of capacitive RF MEMS switches showed that substrate charging can highly affect the reliability of these devices [84]. Due to this phenomenon, MEMS switches fabricated on different substrates were found to exhibit different lifetimes, and

also the influence of environmental conditions on the lifetime was found to depend on the substrate type. In order to accurately study the impact of the substrate charging in MEMS switches, the charging of the interposer dielectric layer should be completely avoided which is not possible using the characterization techniques of the actual MEMS devices as explained in chapter 2. There are two charge injection scenarios in MEMS switches fabricated over Si substrates (**Fig. 3.2a**): charging of the dielectric material deposited over the metallic transmission line (**Fig. 3.2b**), and charging of dielectric deposited directly over the Si substrate (**Fig. 3.2c**). In the latter, the formation of space charge region in the Si substrate is expected to highly influence the charging/discharging processes. Thanks to the unique advantage of the nanoscale characterization based on KPFM-TF and FDC-TF, it is possible to study each of the two mentioned charging scenarios separately, and hence the influence of the substrate charging could be addressed properly.

#### 5.4.2 KPFM and FDC results

**Figure 5.8** shows the KPFM-TF measured surface potential amplitude,  $U_s$ , FWHM, and potential profile integral for the HF  $\text{SiN}_x$  (left) and LF  $\text{SiN}_x$  (right) films deposited over evaporated Au and Si substrates, with different film thicknesses. For a given film thickness, it could be seen from the figure that the induced surface potential amplitude,  $U_s$ , FWHM, and the potential profile integral are higher for HF-Evap Au samples compared to HF-Si, for the same applied electric field intensity,  $E$ . Similar observations exist for the LF  $\text{SiN}_x$  material with different film thicknesses. In other words, the injected charge density in the  $\text{SiN}_x$  films deposited over metal layers is larger compared to the  $\text{SiN}_x$  material deposited over Si substrates. During the charging process, the contact between the biased AFM tip and the  $\text{SiN}_x$  sample resembles a point contact MIS capacitor for the  $\text{SiN}_x$  films deposited directly over Si, while it forms a point contact MIM capacitor for the  $\text{SiN}_x$  layers deposited over Au layers.

The surface potential decay with time for the  $\text{SiN}_x$  films deposited over evaporated Au layers and over Si substrates were also studied and an example of the obtained results is shown in **Fig. 5.9a**. The figure presents the normalized surface potential decay for HF-Evap Au and HF-Si samples with different film thicknesses, for charges which were injected under the same electric field intensity ( $E = 140 \text{ V}/\mu\text{m}$ ). For a given electric field intensity, the surface potential decay for HF-Evap Au samples is faster compared to the HF-Si samples, and this could be observed for all investigated film thicknesses. Similar remarks have been drawn for the LF-Evap

Au compared to LF-Si samples. The decay time constant,  $\tau$ , and the stretch factor,  $\beta$ , calculated from fitting the KPFM surface potential decay with Eq. 4.3 for HF-Evap Au, HF-Si, LF-Evap Au and LF-Si are presented in **Fig. 5.9b**. For both HF and LF  $\text{SiN}_x$  samples, the decay time constant,  $\tau$ , is longer for  $\text{SiN}_x$  samples deposited over Si compared to  $\text{SiN}_x$  samples deposited over Au. This has been observed for all investigated dielectric film thicknesses as shown in the figure. Regarding the values of the stretch factor,  $\beta$ , no clear difference exists between the  $\text{SiN}_x$  samples deposited over Si and over Au, and this remark has been obtained for all film thicknesses and for both HF and LF  $\text{SiN}_x$  samples.

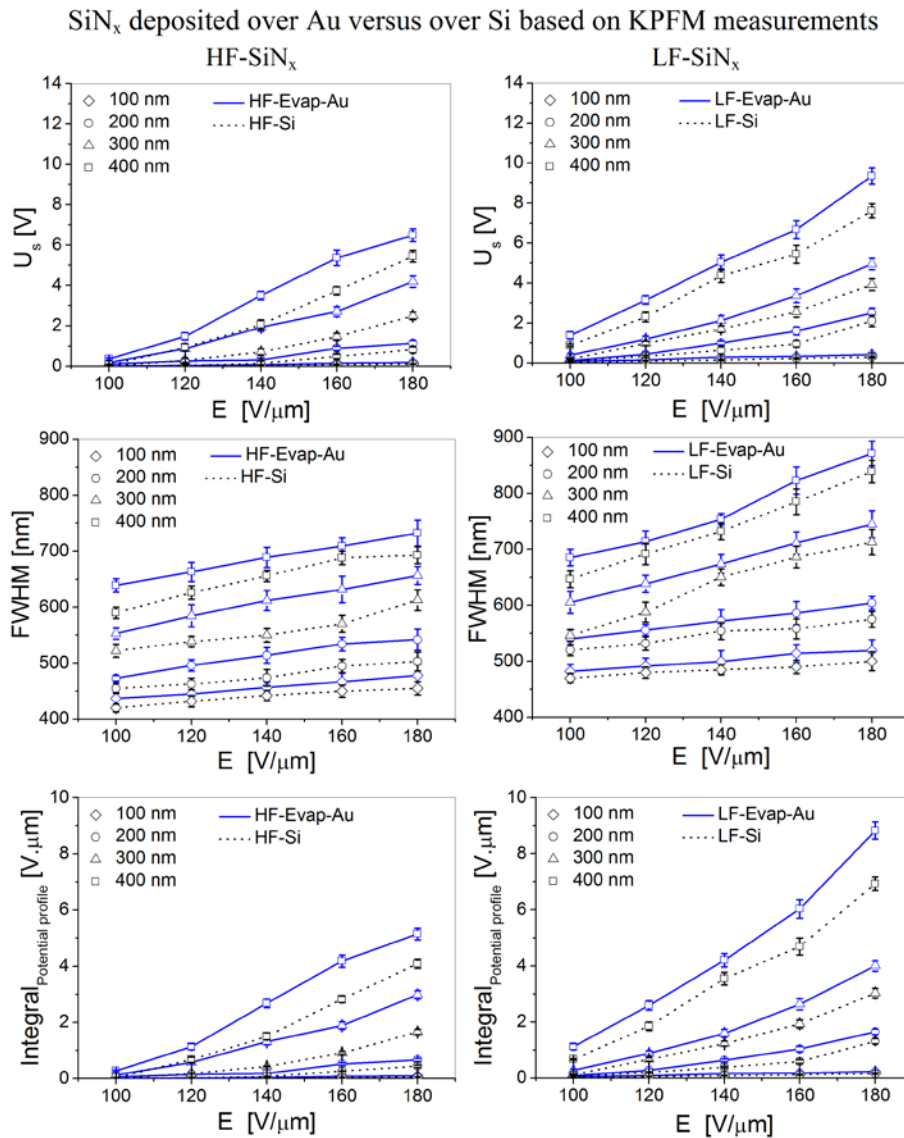
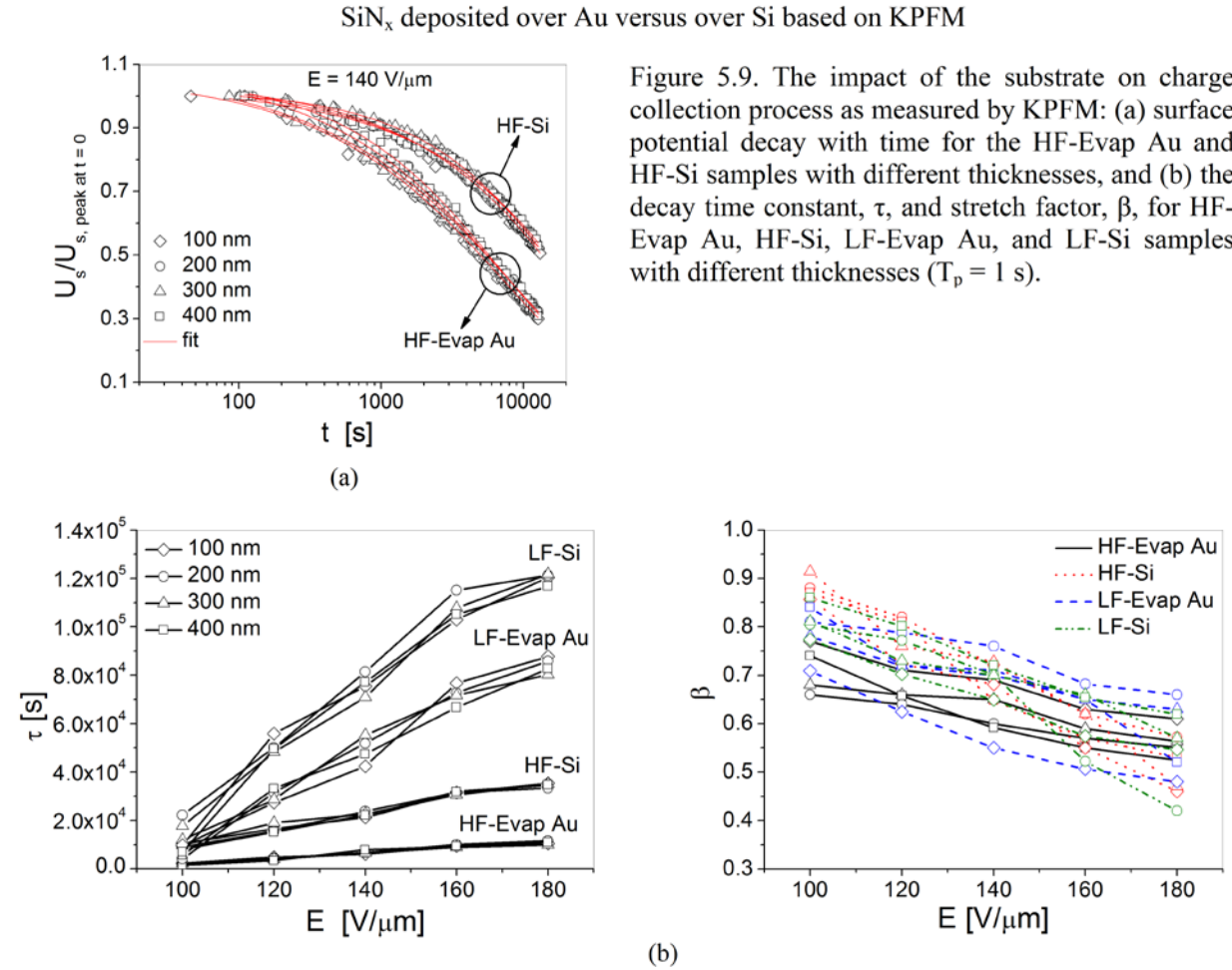


Figure 5.8. The KPFM surface potential amplitude,  $U_s$ , distribution, FWHM, and potential profile integral for  $\text{SiN}_x$  films deposited with different film thicknesses over evaporated Au and over silicon using HF (left) and LF (right) recipes ( $T_p = 1$  s).



The FDC-TF characterization results for HF-SiN<sub>x</sub> films deposited over Au versus over Si are plotted in **Figure 5.3**. **Figure 5.3a, b** show that the HF-Evap Au samples have relatively larger induced surface potential and adhesive force compared to HF-Si samples, for the same applied electric field. This indicates that the injected charge density is larger in HF-Evap Au compared to HF-Si SiN<sub>x</sub> samples. Also, **Figure 5.3c, d** highlights that the charge collection process is remarkably faster, and hence the decay time constant is much smaller in HF-Evap Au samples compared to HF-Si films, for charges injected using the same electric field. This has been observed for the investigated film thicknesses using the FDC-TF method (200 nm and 400 nm) as observed from the figure. The decay time constant plotted in **Fig. 5.3d** was calculated from fitting the adhesive force decay with Eq. 4.4.

In conclusion, the KPFM and FDC characterization results reveal that the injected charge density is smaller and the charge collection process is remarkably faster in HF-Evap Au SiN<sub>x</sub>

films compared to HF-Si samples for injected charges using the same electric field. Thus, the charging/discharging processes in  $\text{SiN}_x$  films deposited over Si substrates are directly affected by the space charge region at the dielectric-semiconductor interface.

### 5.4.3 Discussion

Comparing the FT-IR spectra of HF-Evap Au (**Fig. 5.5a**) with HF-Si (**Fig. 5.5c**) shows that both samples have almost the same bonds. In addition, **Table 5.1** shows that the difference in N/Si ratio between HF-Evap Au and HF-Si samples is negligible. Similar remarks have been made comparing the FT-IR spectra and XPS data of LF-Evap Au with LF-Si (**Table 5.2**). Thus, the  $\text{SiN}_x$  films deposited over Au layers and over Si substrates have the same material stoichiometry and the influence of the substrate on the dielectric composition is negligible. Basically, this was expected since for each dielectric thickness,  $\text{SiN}_x$  films were deposited over Si and over Au during the same deposition run. Therefore, the injected charge density in  $\text{SiN}_x$  films deposited over both substrates is determined mainly by the electric field intensity. When  $\text{SiN}_x$  films are deposited directly over Si, the formation of depletion layer in Si substrates and the higher dielectric constant of Si material result in increasing the effective thickness of the dielectric film. Consequently, the effective electric field intensity,  $E$ , will be smaller for  $\text{SiN}_x$  films deposited directly over Si compared to  $\text{SiN}_x$  deposited over Au. Since the injected charge density in the dielectric film follows the electric field intensity and distribution existing during the charging step, it becomes obvious that the charge density will be smaller in the  $\text{SiN}_x$  films deposited over Si compared to over Au. In sequence, the induced surface potential measured by KPFM and FDC are smaller in  $\text{SiN}_x$  films deposited over Si compared to over Au.

The longer decay time constant,  $\tau$ , obtained for the  $\text{SiN}_x$  samples deposited over Si compared to over Au could be attributed to numerous reasons. First, the charge collection by the semiconductor substrate in  $\text{SiN}_x$  films deposited over Si is directly affected by the presence and width of the depletion region. No such effect occurs in  $\text{SiN}_x$  films deposited over metal layers. Second, in the  $\text{SiN}_x$  films deposited over Si the presence of interface states and the Maxwell Wagner Sillars (MWS) effect due to discontinuity of dielectric constants and conductivities at the Si/ $\text{SiN}_x$  interface give rise to the generation of interfacial charges. These will introduce a discontinuity of the electric field intensity which is expected to affect the surface potential decay. In addition, during the discharge process in  $\text{SiN}_x$  films deposited over Si, the semiconductor surface potential will decrease too leading to a shift of the Fermi level across the band gap at the

semiconductor-insulator interface and changing the occupancy of the interface states hence the interface charges. Finally, the effective thickness of the dielectric film is larger and hence the effective electric field is smaller in the case of  $\text{SiN}_x$  films deposited over Si due to the presence of the semiconductor space charge region. As explained earlier, the charging under smaller electric field leads to smaller charge gradients and gives rise to longer discharge time constant,  $\tau$ . Based on this analysis, it becomes clear that the relaxation time,  $\tau$ , is expected to be longer in the  $\text{SiN}_x$  films deposited over Si substrates compared to over Au layers. In MEMS switches where the  $\text{SiN}_x$  dielectric film is normally deposited over  $\text{SiO}_2$  layer in the CPW slot, the MWS effect becomes more significant. The charge accumulated at the interface of the two dielectrics is responsible for the "substrate charging" phenomenon reported in [84].

#### *5.4.4 Influence of underlying metal layer*

Depending on the desired operating frequency range of RF MEMS capacitive switches, the thickness of the transmission line which carries the RF signal is determined. For low frequency applications, thicker metal transmission lines in the range of 2  $\mu\text{m}$  is required, while for higher frequency applications thinner metal layers in the range of 500 nm would be sufficient. Normally, thicker transmission lines are fabricated using electrochemical deposition, while thinner ones are fabricated using a simple evaporation process. Since the dielectric film is deposited over these different types of metal layers, the impact of these layers on the charging/discharging process needs to be explored. In order to study that,  $\text{SiN}_x$  films were deposited on evaporated gold (Evap Au), electrochemically-deposited gold (ECD Au), evaporated titanium (Evap Ti) layers (see **Fig. 3.2b** and **Table 3.1**). The ECD Au and Evap Ti layers were investigated since they are normally used in actual RF MEMS switches as described in the fabrication process of MEMS switches (see **Fig. 3.1**). The ECD Au is required for RF MEMS switches operating at lower frequency while the Ti layer is used as an adhesion layer between the transmission line and the dielectric film. In addition, the influence of the underneath metal layer roughness on the charging process was studied through the Evap Au and ECD Au samples which have, for example, an average roughness of 1.6 nm and 6.3 nm, respectively, for the LF  $\text{SiN}_x$  films.

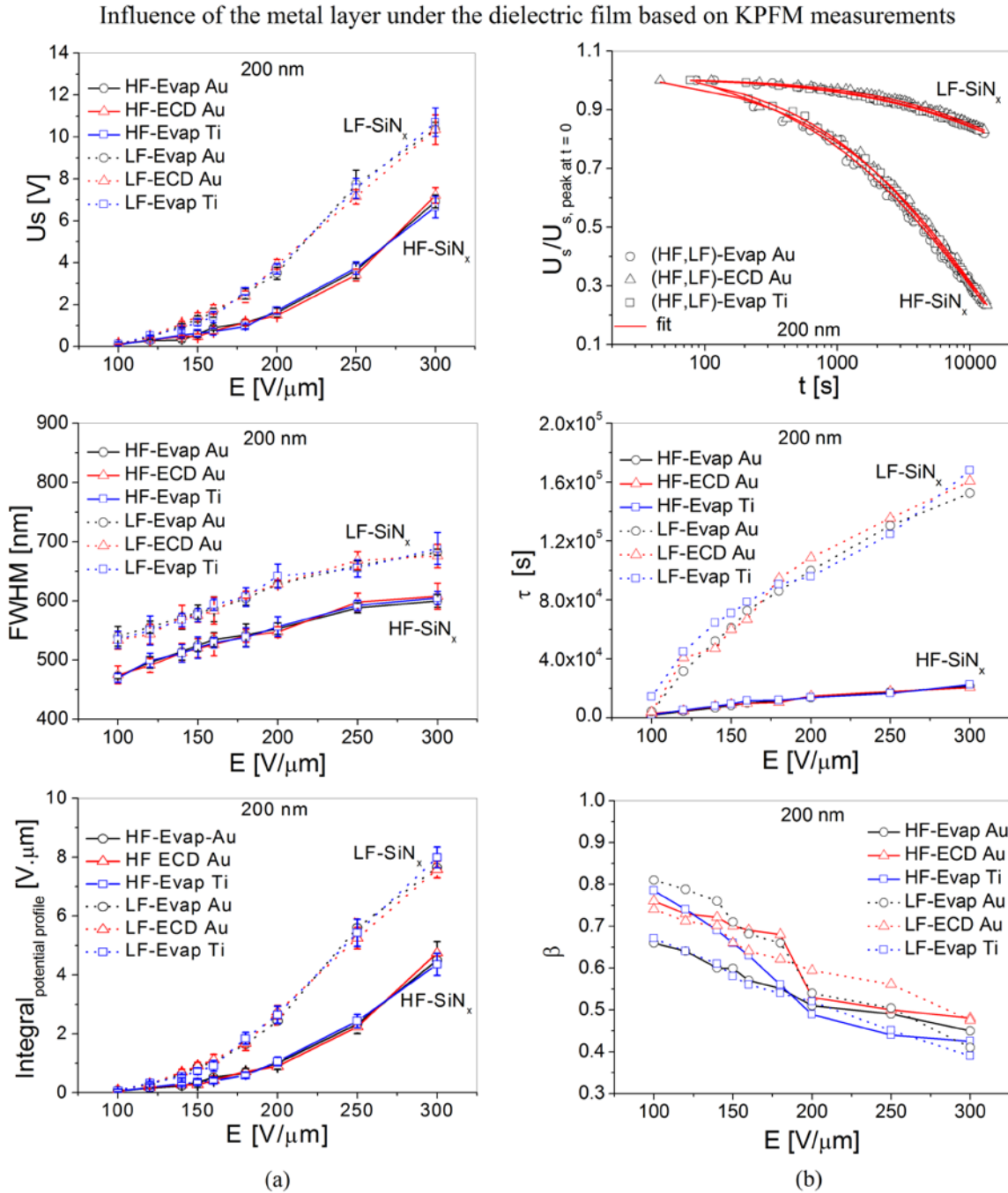


Figure 5.10. The effect of the metal layer under the SiN<sub>x</sub> film on the charging/discharging processes as measured by KPFM: (a) surface potential amplitude,  $U_s$ , distribution, FWHM, potential profile integral for HF-Evap Au, HF-ECD Au, HF-Evap Ti, LF-Evap Au, LF-ECD Au and LF-Evap Ti samples with 200 nm film thicknesses, and (b) the surface potential decay and the decay time constant,  $\tau$ , and stretch factor,  $\beta$ , for the mentioned samples ( $T_p = 1$  s).

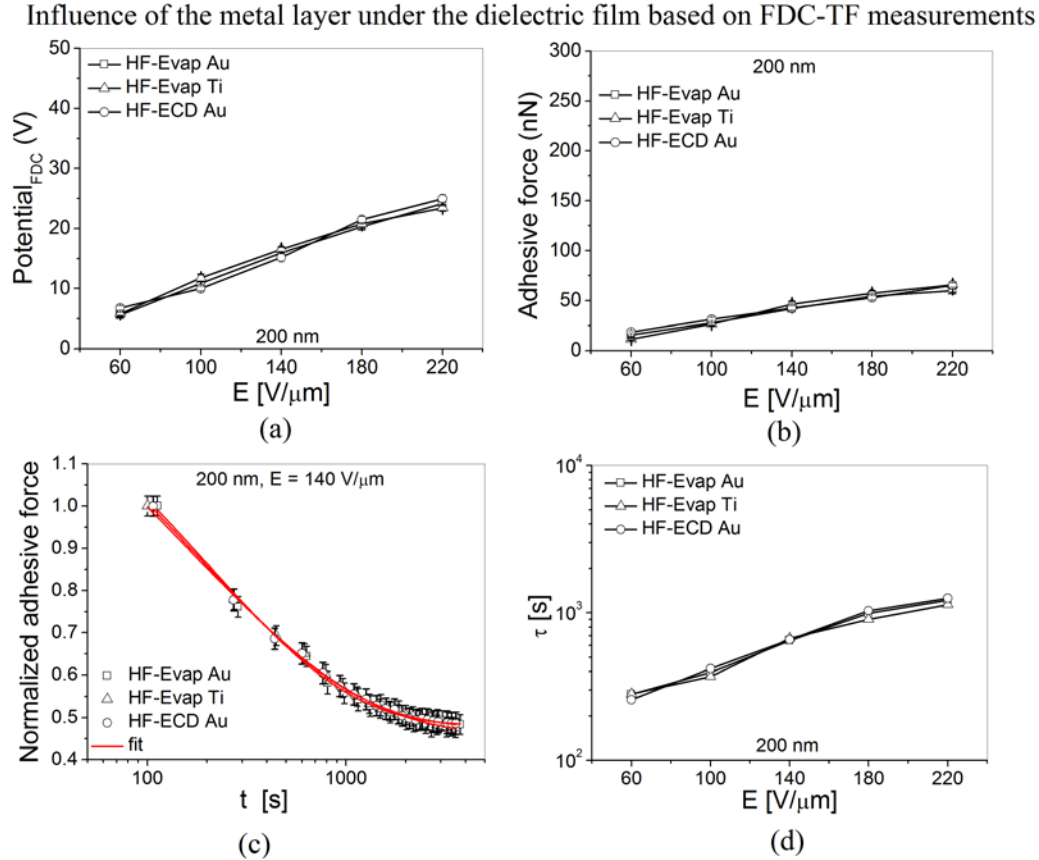


Figure 5.11. The effect of the metal layer under the SiN<sub>x</sub> film as measured by the FDC-TF technique for charges injected using different electric field: (a) the induced surface potential, (b) the induced adhesive force, (c) an example of adhesive force decay with time for different samples for charges injected using E = 140 V/μm, and (d) the calculated decay time constant from adhesive force decay.

#### 5.4.5 KPFM and FDC results

**Figure 5.10a** presents the KPFM induced surface potential amplitude,  $U_s$ , FWHM, and potential profile integral for the SiN<sub>x</sub> samples with 200 nm thickness deposited over different metallic layer. It is obvious from the figure that HF-Evap Au, HF-ECD, and HF-Evap Ti samples have almost the same  $U_s$ , FWHM, and potential profile integral under different applied electric field intensities, E. Similar observation could be drawn from the figure for the LF-Evap Au, LF-ECD Au and LF-Evap Ti samples. The normalized KPFM surface potential decay with time for SiN<sub>x</sub> films deposited over different metal layers is shown in **Fig. 5.10b**. Also, the decay time constant,  $\tau$ , and stretch factor,  $\beta$ , calculated from fitting the surface potential decay with Eq. 4.3 are plotted in the figure. The decay time constant,  $\tau$ , is almost identical and the stretch factor,  $\beta$ , shows a comparable values for the HF-Evap Au, HF-ECD and HF-Evap Ti sample. This could

be observed also for the LF SiN<sub>x</sub> samples. The same remarks regarding the charging (**Fig. 5.10a**) and discharging (**Fig. 5.10b**) processes have been made for negative charge injection as well as for the 300 nm SiN<sub>x</sub> sample deposited over different metal layers. On the other hand, the influence of metal layer on the charging/discharging processes as measured by the FDC-TF technique is shown in **Fig. 5.11**. The difference in the induced surface potential (**Fig. 5.11a**), induced adhesive force (**Fig. 5.11b**), adhesive force decay (**Fig. 5.11c**), and the decay time constant (**Fig. 5.11d**) between different samples is negligible. This is clearly observed for both HF and LF SiN<sub>x</sub> films for charges which were injected under different electric fields. The decay time constant plotted in **Fig. 5.11d** was calculated from fitting the adhesive force decay with Eq. 4.4.

In summary, the KPFM and FDC characterization lead to the conclusion that the influence of underlying metal layers over which the SiN<sub>x</sub> is deposited on the charging/discharging processes is negligible.

#### 5.4.6 Discussion

The investigated HF SiN<sub>x</sub> films over different metal layers were deposited at the same time. Also, the LF SiN<sub>x</sub> films over different metal layers were deposited during the same run. This indicates that the material stoichiometry for SiN<sub>x</sub> films deposited over different metals tend to be identical. **Figure 5.12c** shows an example of the obtained FT-IR spectra for LF-Evap Au and LF-Evap Ti SiN<sub>x</sub> films with 200 nm thickness, and it highlights that the spectra for both samples are identical. In addition, the XPS data presented in **Table 5.2** shows that the N/Si ratio for LF-Evap Au and LF-Evap Ti is the same (0.82). Similar observations have been obtained for the HF-SiN<sub>x</sub> samples. For example, from **Table 5.1** the Ni/Si ratio for the HF-Evap Au and HF-Evap Ti samples is 0.74 and 0.69, respectively, whose difference could be neglected. This similar material stoichiometry for SiN<sub>x</sub> samples deposited over different metal layers could explain why the underlying metal layer doesn't affect both the charging/discharging processes as obtained by KPFM and FDC measurements. Moreover, this further points out that the work function as well as the roughness of the underlying metal layer has a minimal effect on the charging/discharging processes. The same charge density is injected in the SiN<sub>x</sub> film independently of the fabrication process used to create the underneath metal layers and/or the metal work function and roughness. Also, for the SiN<sub>x</sub> films deposited over the investigated metal layers the trapped charges will be collected through the same discharging mechanisms.

Under any conditions, the underlying metal layers will act as a sink and the charge will be collected by these electrodes using the same mechanisms.

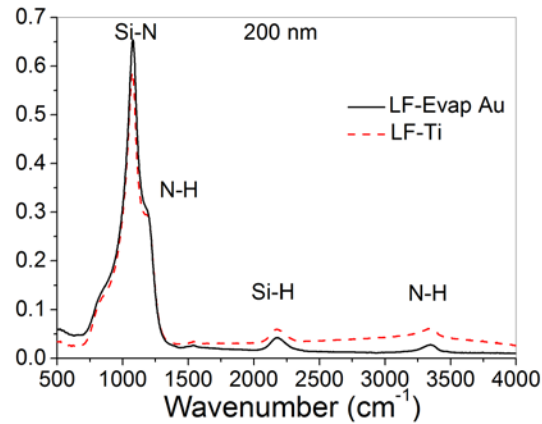


Figure 5.12. Reflection FT-IR spectra for LF-Evap Au and LF-Evap Ti  $\text{SiN}_x$  samples.

## 5.5 Influence of bias polarity

In  $\text{SiN}_x$  material, it was reported that “holes injection” introduces metastable traps [53, 54]. These metastable defects affect the charge transport in the dielectric [55], and give rise to asymmetrical current-voltage characteristic in MIM capacitors with electrode material symmetry [32]. In this section, the influence of the stress bias polarity on both charging/discharging as measured by KPFM and FDC is presented.

### 5.5.1 KPFM and FDC results

**Figure 5.13** presents the KPFM surface potential amplitude,  $U_s$ , and FWHM for charges which were injected using positive and negative bias,  $U_p$ , for HF-Evap Au  $\text{SiN}_x$  samples (left) and HF-Si (right) with different film thicknesses. It is obvious from the figure that the measured  $U_s$  and FWHM are asymmetric when positive or negative  $U_p$  is applied. For the HF-Evap Au samples, negative charge injection results in larger induced surface potential,  $U_s$ , and less confined potential distribution (larger FWHM), for a given film thickness and when the same electric field is applied during the charging step. This has been observed for all investigated film thicknesses. Similar observations could be drawn for the HF-Si  $\text{SiN}_x$  samples with different film thicknesses (**Fig. 5.13 right**) and with more significant difference between the negative and positive charge injection compared to the HF-Evap Au samples. These observations indicate that the injected charge density in the  $\text{SiN}_x$  films for negative charge injection is larger compared to

the positive charging. These remarks have been also made for LF-Evap Au and LF-Si samples, and for all investigated film thicknesses.

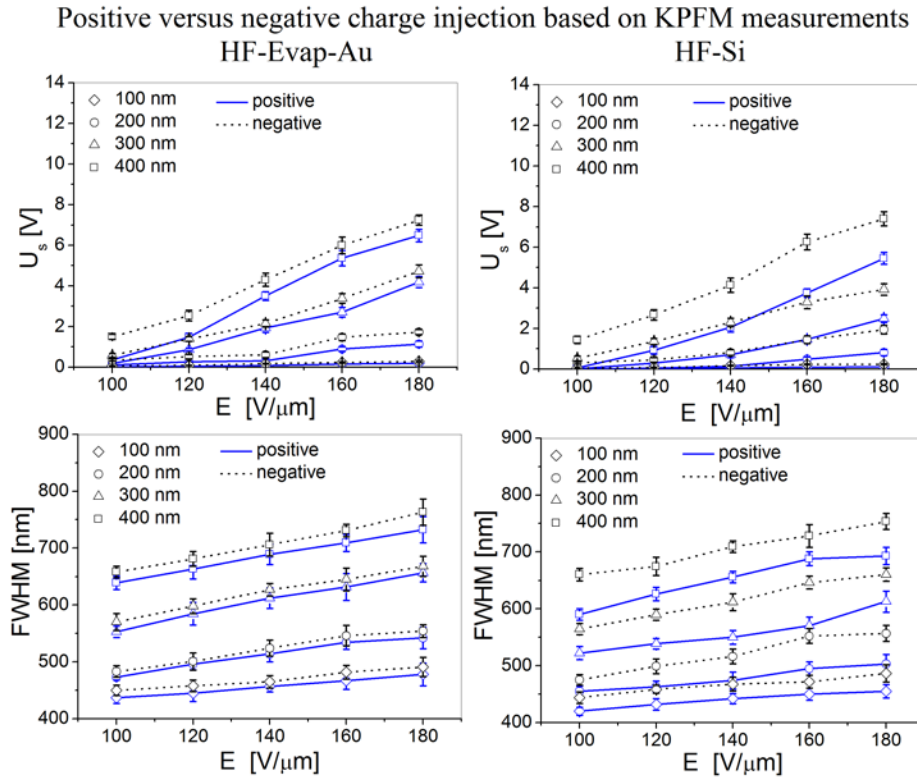


Figure 5.13. The influence of bias polarity on dielectric charging as measured by KPFM for HF-Evap Au (left) and HF-Si (right) samples with different film thicknesses ( $T_p = 1$  s).

The influence of the bias polarity on the discharging process was also studied through monitoring the KPFM surface potential decay with time. **Figure 5.14a** shows an example of these results for the HF-Evap Au (left) and LF-Evap Au (right) samples with 200 nm film thickness for charges which were injected under different electric field intensities,  $E$ . The decay time constant,  $\tau$ , and stretch factor,  $\beta$ , calculated from fitting the surface potential decay with Eq. 4.3 for the mentioned experiments are plotted in **Fig. 5.14b**. It could be seen from figures that charge decay is faster (smaller  $\tau$ ) for positive charge injection compared to negative for both HF and LF  $\text{SiN}_x$  films. **Figure 5.14b** also highlights that there is no clear effect of the bias polarity on the stretch factor,  $\beta$ , for both HF and LF samples. Similar trends for the difference between positive and negative charge injection in the decay time constant,  $\tau$ , and the stretch factor,  $\beta$ , have been obtained for the  $\text{SiN}_x$  films deposited over Si substrates.

Surface potential decay,  $\tau$ , and  $\beta$  for positive and negative charge injection based on KPFM measurements

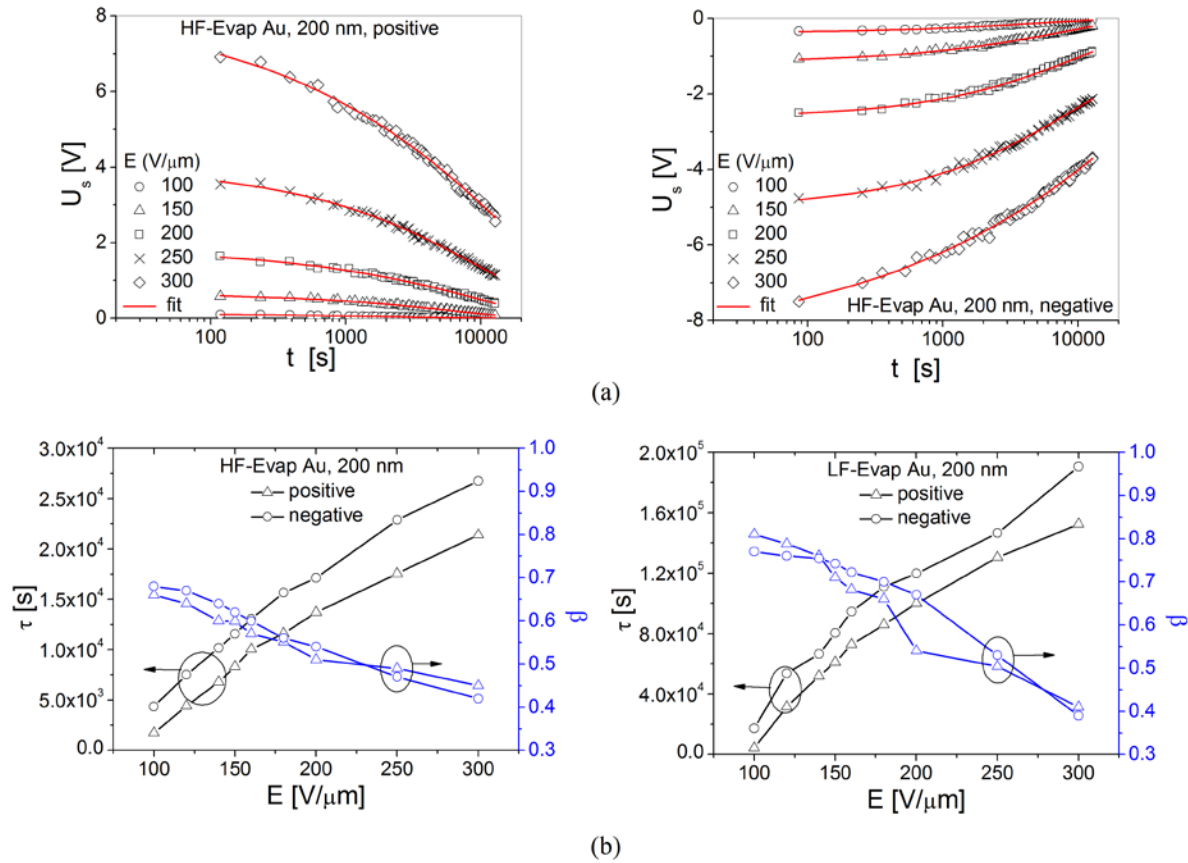


Figure 5.14. The influence of bias polarity on charge collection process as measured by KPFM: (a) surface potential decay for the HF-Evap Au sample with 200 nm film thickness for positive (left) and (negative) charge injection, and (b) the decay time constant,  $\tau$ , and stretch factor,  $\beta$ , for both bias polarities under different electric field ( $T_p = 1$  s).

The influence of the charging bias polarity on the charging/discharging processes as measured by the FDC-TF characterization method is presented in **Fig. 5.15**. The induced surface potential (**Fig. 5.15a**) and consequently the induced adhesive force (**Fig. 5.15b**) are larger for negative charge injection compared to positive one. This could be observed for LF-Evap Au and LF-Si samples with the latter being highly affected by the stress polarity. It could be seen also from **Fig. 5.15c, d** that the negative charge injection results in relatively longer relaxation process for both LF-Evap Au and LF-Si. The decay time constant plotted in **Fig. 5.15d** was calculated from fitting the adhesive force decay with Eq. 4.4. Here it should be highlighted that similar results were obtained from the measured capacitance transient response of capacitive MEMS switches stressed using both positive and negative stress bias [44]. In the mentioned work, the decay time constant for negative bias stress was found to be larger than the time

constant for positive stress, under different temperature in the range of 300–440 K. In conclusion, both KPFM and FDC reveal that negative charge injection for HF and LF  $\text{SiN}_x$  results in larger injected charge density and relatively longer charge collection process compared to positive charging.

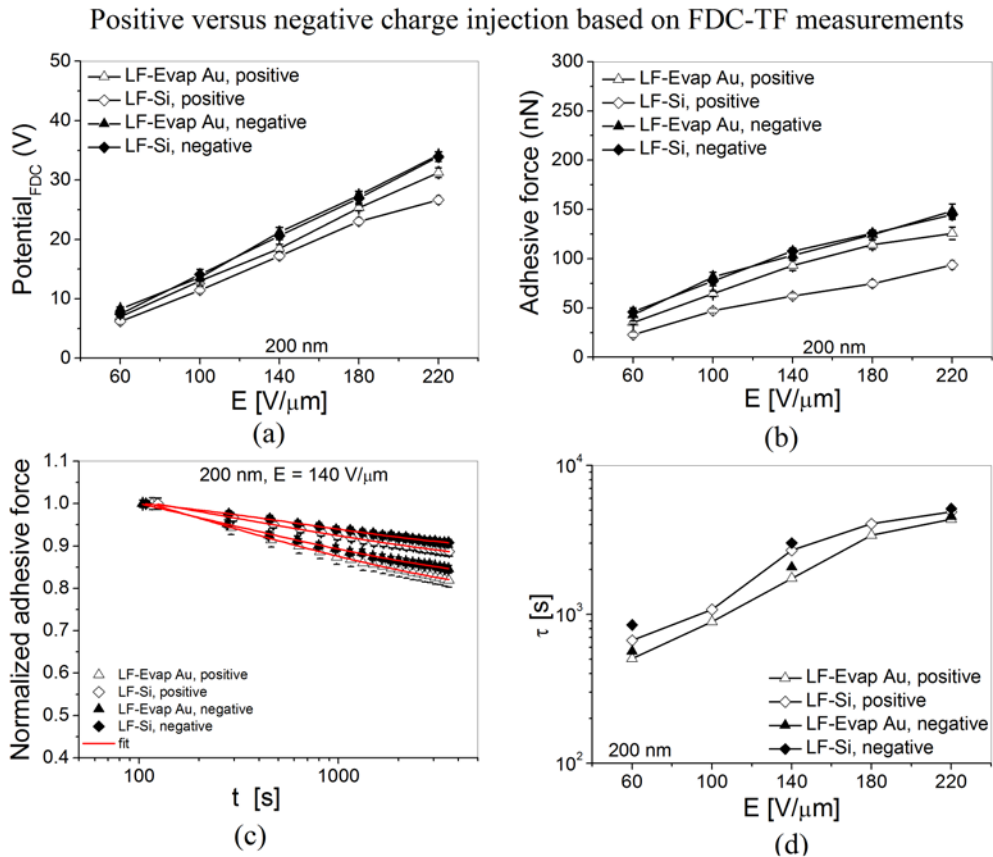


Figure 5.15. The influence of bias polarity on charge collection process as measured by FDC-TF method: (a) the induced surface potential for LF-Evap Au and LF-Si samples for positive and negative charge injection, (b) the induced adhesive force, (c) an example of adhesive force decay with time, and (d) the calculated decay time constant from the adhesive force decay.

### 5.5.2 Discussion

The larger difference in the injected charge density between positive and negative charge injection for the  $\text{SiN}_x$  samples deposited over Si compared to the ones deposited over Au is attributed to the space charge region which exists in the former samples in the case of no accumulation layer formation. This accumulation layer is formed only for either positive or negative charge injection based on the Si substrate doping type. Hence, for one bias polarity there will be a space charge region while for the opposite polarity there will be an accumulation

region. Therefore the effective dielectric film thickness will change considerably when changing the bias polarity for the  $\text{SiN}_x$  samples deposited over Si substrates. This large variation in the effective film thickness results in the considerable difference in the measured induced surface potential and adhesive force for the  $\text{SiN}_x$  samples deposited over Si compared to the films deposited over Au layers as presented in **Fig. 5.13**, and **Fig. 5.15**.

The asymmetry between positive and negative charge injection observed for both charging/discharging processes could be attributed to different penetration depths for positive and negative charge carriers in a dielectric film [128]. In the abovementioned  $\text{SiN}_x$  samples, the total amount of negative charge that can be stored is higher compared to positive charge, for the same applied electric field. Given that electrons are injected in the dielectric film, this disparity between positive and negative charge injection can be also attributed to the differences between the lower and the upper metal/silicon–dielectric interfaces. For one bias polarity, in KPFM electrons are injected by the metal layer coating of the used SCM-PIT AFM tips which is Pt/Ir, while for FDC the charge injection is performed through the employed FORTA-10 highly doped silicon tips. For the other polarity, electrons are injected by the bottom metal electrode in the case of  $\text{SiN}_x$  deposited over metal layer or directly through the Si substrates for  $\text{SiN}_x$  deposited over Si. Furthermore, the measured difference between positive and negative charge injection could be attributed to the silicon dangling bonds which appear to be a paramagnetic center in such silicon-rich  $\text{SiN}_x$  materials. The hole injection at this position of paramagnetic center generates a positively charged site, while the electron injection produces a doubly occupied nonbonding orbital which is negatively charged.

A comparison between the measured KPFM surface potential amplitude,  $U_s$ , and FWHM for HF-Evap Au and HF-Si samples for negative charge injection is presented in **Fig. 5.16**. The difference between the induced  $U_s$  and FWHM for negative charge injection for both HF-Evap Au and HF-Si samples is very small compared to positive charge injection (**Fig. 5.8**). This has been observed for all investigated film thicknesses as well as for LF  $\text{SiN}_x$  samples. It could be seen also from **Fig. 5.15a, b** that for negative charge injection, the induced surface potential as well as adhesive force measured by FDC is almost identical for LF-Evap Au and LF-Si, while for positive charge injection the measured potential and adhesive force for  $\text{SiN}_x$  films deposited over Au are larger compared to  $\text{SiN}_x$  over Si as presented in **Fig. 5.3a, b**. In conclusion, the difference in the injected charge density between  $\text{SiN}_x$  samples deposited over Au and over Si for

negative charge injection is negligible and is very small compared to positive charge injection. In the present study, P-type silicon substrates were used for the  $\text{SiN}_x$  films deposited directly over Si. Therefore, for positive charge injection the space charge region does exist and results in increasing the effective dielectric film thickness, which in sequence results in reducing the injected charge density. On the contrary, negative charge injection will form an accumulation layer just below the  $\text{SiN}_x$  dielectric film. Therefore, for negative charge injection the difference in the effective dielectric thickness between both  $\text{SiN}_x$  deposited over Au and over Si is expected to be very small. Excluding the influence of the interfacial charging which exists for  $\text{SiN}_x$  samples deposited over Si substrates, negative charge injection should result in almost the same injected charge density for both  $\text{SiN}_x$  samples deposited over Si and over Au layers as observed from our KPFM measurements.

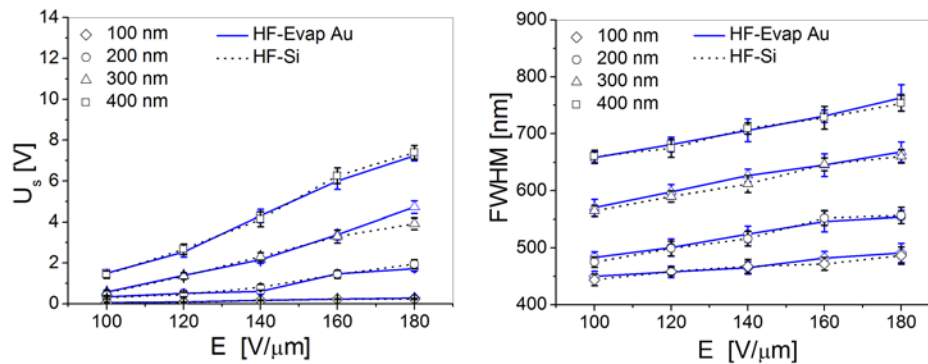


Figure 5.16. KPFM surface potential amplitude,  $U_s$ , distribution, FWHM, and potential profile integral under negative bias conditions for the HF-Evap Au and HF-Si samples ( $T_p = 1$  s).

Taking the effect of the bias polarity on  $\text{SiN}_x$  charging/discharging processes into account, we reach the fact that the injected charge density is larger and the charge relaxation time is longer when negative bias is used compared to positive bias for the same applied electric field. This could explain the shift and or narrowing of the C-V characteristics and the stiction observed for electrostatic capacitive MEMS switches in spite of using bipolar actuation signals. As reported in [129, 130], the shift in the actuation voltage for MEMS capacitive switches is considerably reduced when using a bipolar actuation signals. Yet, the same duty cycles were used for these bipolar actuation signals. The KPFM and FDC results reveal that the duty cycles of the bipolar actuation signal should not be the same and has to be engineered, since positive and negative charge injection affects the dielectric charging differently.

## 5.6 Impact of charge injection duration, $T_p$

In order to further study the impact of charge injection conditions on the dielectric charging/discharging processes, the induced KPFM-TF surface potential resulting from charges injected for different pulse duration,  $T_p$ , was investigated. **Figure 5.17a** shows an example of these results where the measured  $U_s$  is plotted as a function of the pulse duration,  $T_p$ , for HF-Evap Au samples with different film thicknesses under the same applied pulse amplitude,  $U_p$ . For a given film thickness, increasing  $T_p$  results in increasing the measured  $U_s$  as shown in the figure. Moreover, the measured FWHM is found to increase with  $T_p$ . This indicates that the injected charge density in the  $\text{SiN}_x$  film increases with increasing the applied pulse duration,  $T_p$ , and this has been observed for all investigated film thicknesses and for HF-Si, LF-Evap Au and LF-Si samples. Basically, this agrees with the measurement results obtained from the study of charging in dielectric less capacitive MEMS switches [131]. In the mentioned study, the drift in the pull-in voltage was found to be directly proportional to the duty cycle value of the periodic square signal stress that was used. In addition, initial modeling of dielectric charging showed that the amount of injected charge inside the dielectric layer increases with the charging time [132]. **Figure 5.17a** is plotted in log-log scale and the results are shown in **Fig. 5.17b**. The log-log plot is linear, and the increase in the induced surface potential,  $U_s$ , as a function of the charge injection duration,  $T_p$ , fits quite well with the Curie-Von Schweidler equation given by

$$U_s = A_0 T_p^n \quad (5.1)$$

that also agrees with the reported results in [131] where the shift in the pull-in voltage over time during lifetime assessment of MEMS switches was found to follow the same equation.

The influence of the pulse duration,  $T_p$ , on the charge collection process was also studied. Surface potential decay was monitored with time for charges which were injected under two different pulse durations ( $T_p = 1$  s and 1000 s) each for different pulse amplitude,  $U_p$ . As presented previously, the potential relaxation for charges injected for a short duration ( $T_p = 1$  s) follows the stretched exponential law (Eq. 4.3). This has been observed as well for the longer pulse duration ( $T_p = 1000$  s). **Figure 5.17c** presents the decay time constant,  $\tau$ , calculated from fitting the surface potential decay with Eq. 4.3 for the sample HF-Evap Au with 200 nm thickness, under the two investigated  $T_p$ . It is obvious from the figure that the decay time constant,  $\tau$ , increases with increasing  $U_p$ , for both  $T_p = 1$  s and 1000 s, which is attributed to the PF effect and TAT as explained earlier. For a given  $U_p$ , the decay time constant for  $T_p = 1000$  s

is larger compared to  $T_p = 1$  s. Since both the injected charge density as well as the charge relaxation time increase with the charge injection duration, it is recommended to actuate the capacitive MEMS switch for shorter durations in order to minimize the dielectric charging.

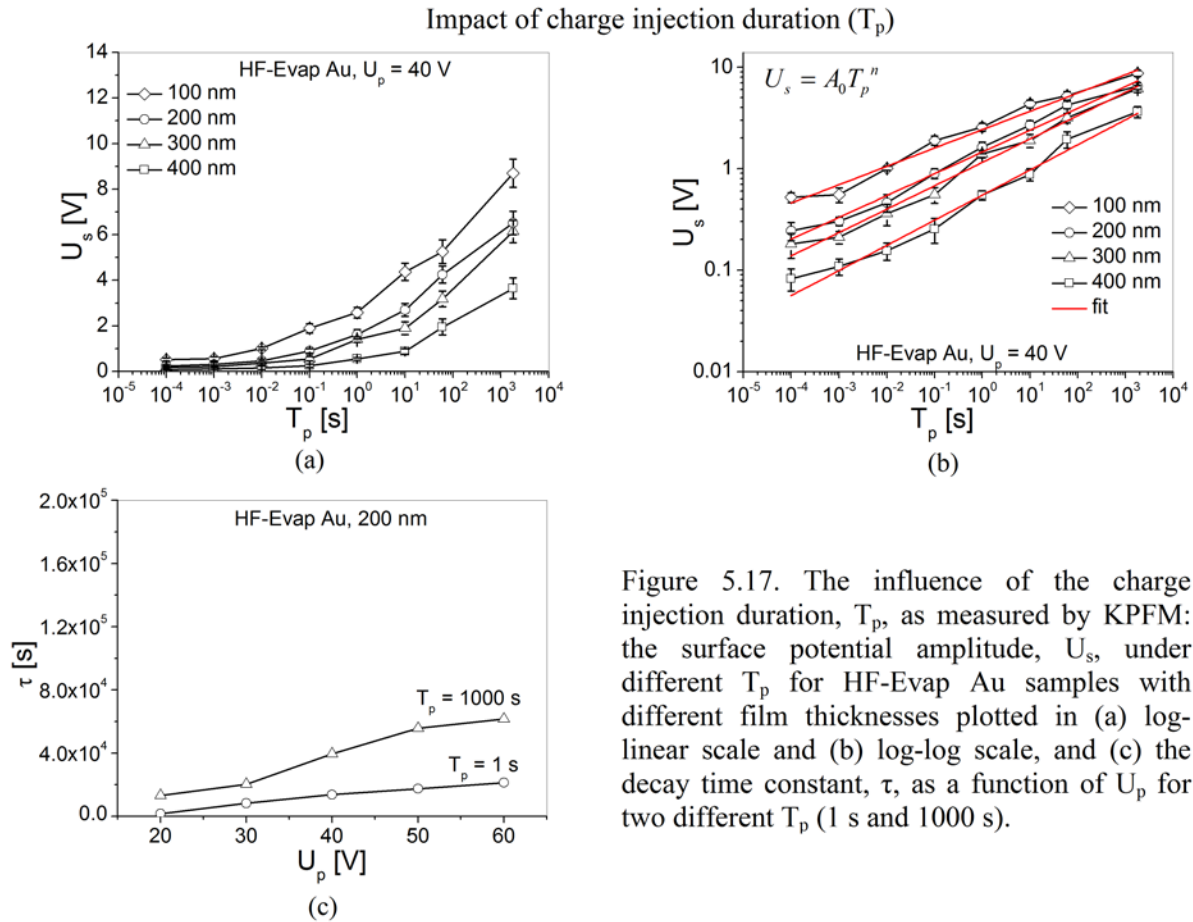


Figure 5.17. The influence of the charge injection duration,  $T_p$ , as measured by KPFM: the surface potential amplitude,  $U_s$ , under different  $T_p$  for HF-Evap Au samples with different film thicknesses plotted in (a) log-linear scale and (b) log-log scale, and (c) the decay time constant,  $\tau$ , as a function of  $U_p$  for two different  $T_p$  (1 s and 1000 s).

## 5.7 HF versus LF $\text{SiN}_x$

In this section, we discuss the difference in charging/discharging processes between  $\text{SiN}_x$  films deposited using the two PECVD deposition recipes; high frequency (HF), and low frequency (LF) presented in **Table 3.2**.

### 5.7.1 KPFM results

A comparison between the measured KPFM-TF surface potential amplitude,  $U_s$ , FWHM, and potential profile integral for HF and LF  $\text{SiN}_x$  films deposited over Au layers (left) and over Si substrates (right), for different film thicknesses is presented in **Fig. 5.18**. For a given film thickness, HF  $\text{SiN}_x$  has smaller  $U_s$  and FWHM compared to LF  $\text{SiN}_x$ , when the same electric

field intensity,  $E$ , is applied during the charge injection step. This has been observed for all investigated film thicknesses and for  $\text{SiN}_x$  films deposited over Au and Si substrates. The smaller  $U_s$ , FWHM, and potential profile integral for the HF  $\text{SiN}_x$  samples indicates that the injected charge density in this material is smaller compared to the LF material, for a given film thickness and when the same electric field intensity,  $E$ , is applied.

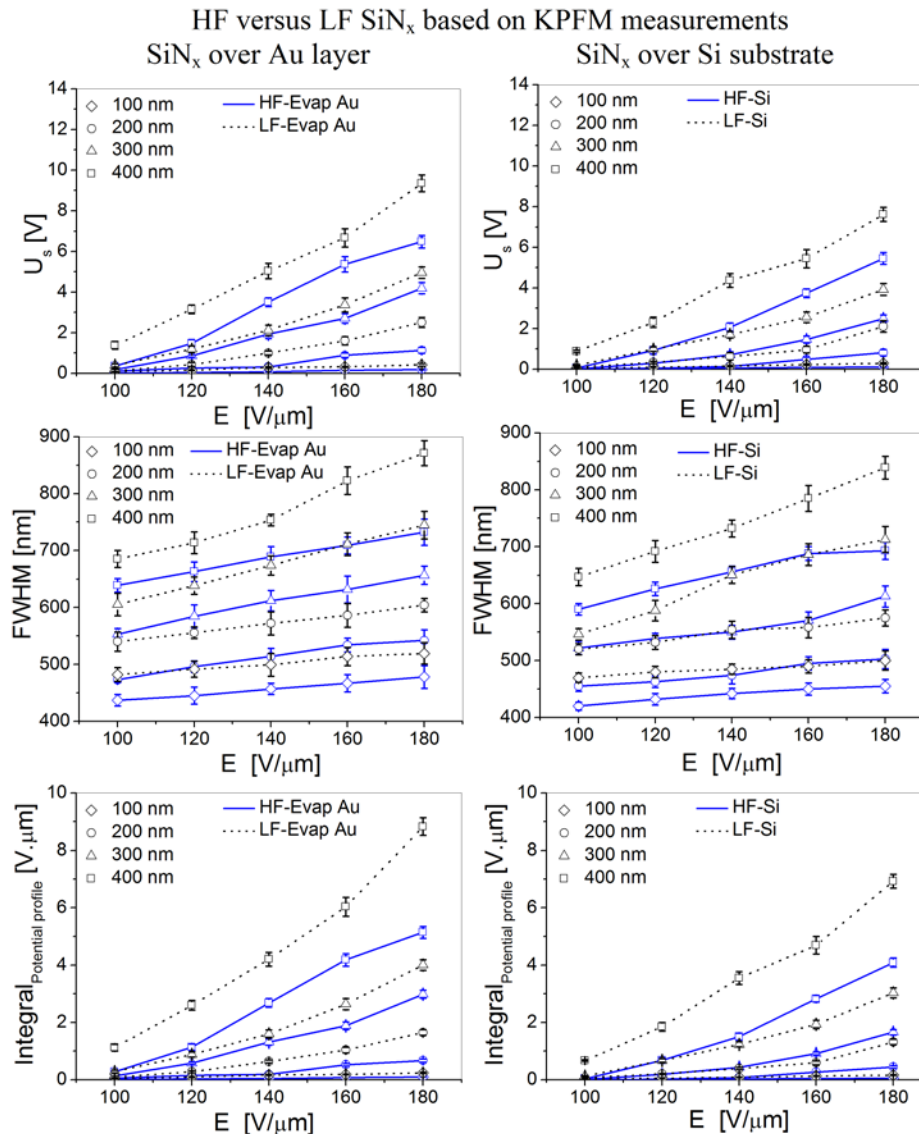


Figure 5.18. Charging in HF versus LF  $\text{SiN}_x$  as measured by KPFM: the measured surface potential amplitude,  $U_s$ , distribution, FWHM, potential profile integral for  $\text{SiN}_x$  films with different thicknesses deposited over evaporated Au layers (left) and over silicon ( $T_p = 1$  s).

. The surface potential decay for the  $\text{SiN}_x$  films deposited using the HF and LF recipes was also investigated. **Figure 5.19** shows an example of these results for a  $\text{SiN}_x$  film with 300

nm thickness deposited over evaporated Au layer. The figure clearly depicts that the surface potential decays faster for the HF  $\text{SiN}_x$  material compared to the LF one, for charges which were injected using the same electric field. In other words, the charge collection process is much faster in the HF material compared to the LF one. This is confirmed from the decay time constant,  $\tau$ , calculated from fitting the surface potential decay with Eq. 4.3 for both HF and LF films deposited over Au layers which are presented in **Fig. 5.9b**. The figure highlights also that the observed difference in the decay time constant,  $\tau$ , between the HF and LF  $\text{SiN}_x$  films deposited over Au layers exists for all investigated film thicknesses, and for the HF and LF  $\text{SiN}_x$  films deposited over Si substrates. Comparing the values of the decay time constant,  $\tau$ , for the HF-Evap Au, LF-Evap Au, HF-Si and LF-Si samples from **Fig. 5.9b**, it is clear that the impact of the material deposition conditions (whether HF or LF) on the charge collection process is more effective compared to the influence of the substrate layer (whether Au or Si). Finally, there is no clear effect of the dielectric deposition conditions on the stretch factor,  $\beta$ , as shown in the figure. This has been observed for dielectric films deposited over Au layers and over Si substrates.

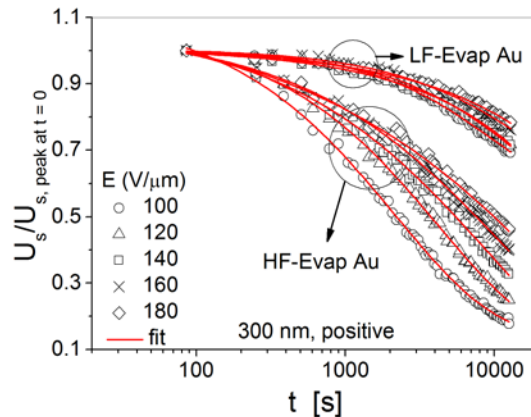


Figure 5.19. KPFM surface potential decay for the HF-Evap Au and LF-Evap Au samples with 300 nm film thicknesses, for charges injected under different electric field ( $T_p = 1$  s).

### 5.7.2 FDC results

The influence of the deposition conditions on the charging and discharging processes as extracted from the FDC-TF technique is presented in **Fig. 5.20**. The induced surface potential (**Fig. 5.20a**) and induced adhesive force (**Fig. 5.20b**) for HF-Evap Au samples is found to be smaller compared to the LF-Evap Au, for the same applied electric field. This indicates that the injected charge density is smaller in HF-Evap Au compared to LF-Evap Au. The difference

between LF and HF  $\text{SiN}_x$  is more pronounced in the discharging process as seen from **Fig. 5.20c**. For example, at  $E = 140 \text{ V}/\mu\text{m}$ , the induced adhesive force drops to 48% from its initial value at  $t = 0 \text{ s}$  for the HF-Evap Au compared to 88% in the case of LF-Evap Au. This considerable difference in the charge collection process is also evident from the decay time constant calculated from fitting the adhesive force decay with Eq. 4.4 for both materials (**Fig. 5.20d**). It is evident from the figure that the decay time constant is much smaller for the HF-Evap Au samples compared to the LF-Evap Au samples when stressed with the same electric field. In addition, the slope of increase in the decay time constant as a function of the applied electric field is much smaller in HF-Evap Au compared to LF-Evap Au samples. Similar remarks could be made comparing the difference between the HF-Si and LF-Si samples regarding the charging/discharging processes.

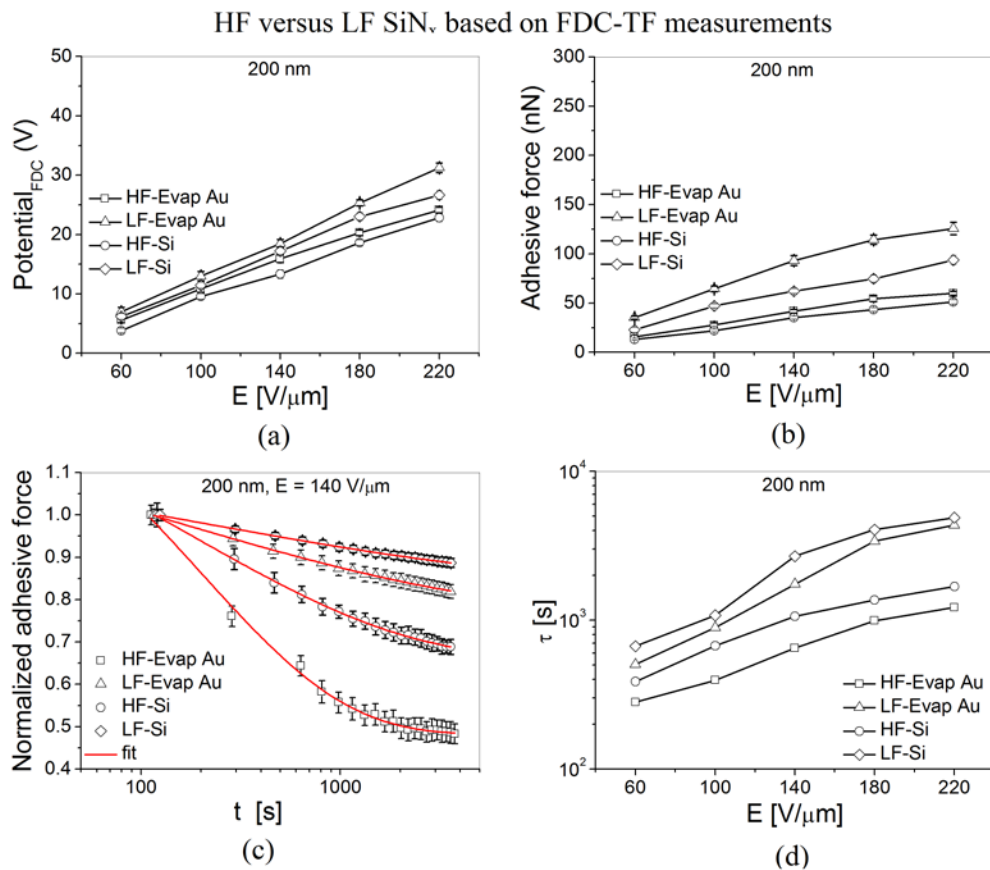


Figure 5.20. Charging/discharging processes in HF versus LF  $\text{SiN}_x$  as measured by the FDC-TF technique: (a) the induced surface potential, (b) the induced adhesive force, (c) an example of adhesive force decay with time for different samples for charges injected using  $E = 140 \text{ V}/\mu\text{m}$ , and (d) the calculated decay time constant from the adhesive force decay.

### 5.7.3 C/DCT results

**Figure 5.21a** shows the measured charge in the external circuits,  $\sigma_0$ , using the C/DCT technique for MIM capacitors which employs HF and LF SiN<sub>x</sub> dielectric films with 300 nm thickness. The measured charge,  $\sigma_0$ , for the LF SiN<sub>x</sub> material is larger compared to the HF one which indicates that the injected charge density in the LF SiN<sub>x</sub> material is larger compared to the HF material. This conclusion agrees well with both KPFM and FDC results. Hence, a very good correlation between the nanoscale characterization results and the device level measurements does exist. On the other side, the dependence of stored charge on electric field intensity was found to follow a Poole-Frenkel like law as shown in **5.21b**, and this has been observed for the LF and HF SiN<sub>x</sub> films and for the whole investigated thickness range under both bias polarities. From the figure, the stored charge values and the increase rates are not the same for LF and HF MIM capacitors with the same dielectric thickness. Basically, this can be related to the defect generation due to electron injection [53]. According to this the charge transport through traps in the band tails leads to a Poole–Frenkel like behavior. In such case, the increase of trap concentration reduces the value of the Poole–Frenkel factor,  $\beta_{PF}$ , of the classical Poole equation (Eq. 2.1).

The decay time constant and the stretch factor calculated from fitting the discharge current transients to Eq. 4.2 are shown in **Figs. 5.21c, d**, respectively. For both HF and LF SiN<sub>x</sub>, the decay time constant increases while stretch factor slightly decreases with the applied electric field intensity as shown earlier. As explained in chapter 4, in C/DCT method the injected charges are collected mainly by the injecting MIM electrodes, and not through charges crossing the dielectric film. Thus, the influence of the dielectric material itself on the discharging process cannot be assessed properly using the C/DCT method since the charges are collected mainly by the injecting electrodes. This explains the comparable decay time constants and stretch factor for HF and LF SiN<sub>x</sub> films with different thicknesses as shown in **Fig. 5.21c**. In spite of that, it could be seen from the figure that the decay time constant for LF SiN<sub>x</sub> is slightly larger compared to HF SiN<sub>x</sub> films for several electric fields and for different film thicknesses. The relatively smaller difference in the decay time constant between HF and LF SiN<sub>x</sub> could be also attributed to the smaller relaxation time obtained from C/DCT experiments as explained in chapter 4.

In conclusion, the KPFM, FDC and C/DCT measurements reveal that for the same applied electric field the injected charge density in HF SiN<sub>x</sub> films is higher compared to the LF

samples. Regarding the discharging process, both KPFM and FDC leads to similar conclusions that the charge collection process is much faster for the HF material compared to the LF SiN<sub>x</sub>. In contrast, the C/DCT method reveals a relatively smaller difference in the relaxation time between both materials due to charge collection by the injecting MIM electrodes. Considering the similarity between KPFM, FDC, and MEMS switches regarding the discharging process where the charge is collected mainly by bottom electrode as presented in chapter 4, we are led to the conclusion that the C/DCT measurements are not proper for studying the discharging process in MEMS. However, the importance of employing MIM capacitors in understanding the discharging process in MEMS based on the novel proposed characterization techniques such as KPFM-MIM and FDC-MIM described in chapter 4 is obvious.

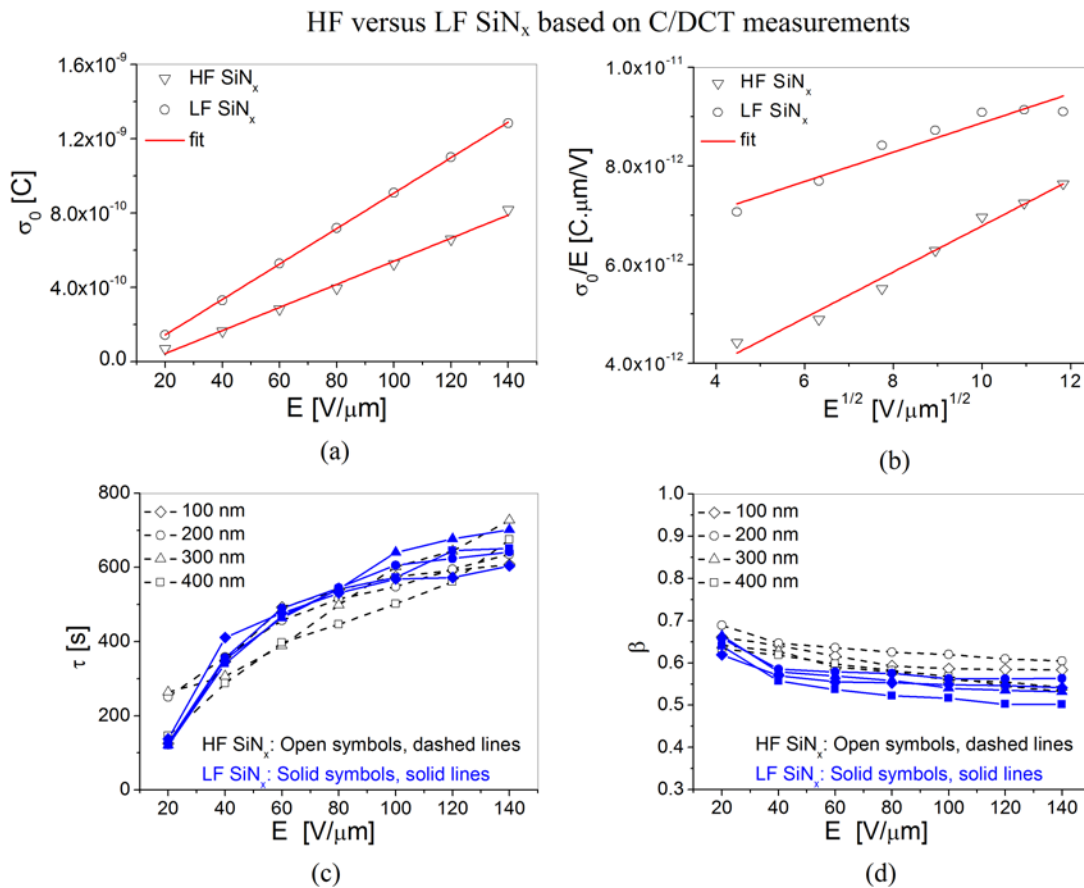


Figure 5.21. Charging/discharging processes in HF versus LF SiN<sub>x</sub> as measured by the C/DCT method: (a) the measured charge,  $\sigma_0$ , as a function of the electric field for MIM capacitors employing HF and LF SiN<sub>x</sub> films with 300 nm thickness, (b) Pool-Frenkel law dependence of the stored charge for LF and HF samples; (c) the decay time constant and (b) stretch factor calculated from discharging current transients.

#### 5.7.4 Influence on material stoichiometry

The FT-IR spectra for the HF-Evap Au and LF-Evap Au films with different thicknesses are shown in **Fig. 5.5a, b**, respectively, and some selected data were replotted in **Fig. 5.22a** for the sake of comparison between HF and LF SiN<sub>x</sub> films. The figure highlights that both materials have quite similar FT-IR spectra, and the Si-H and N-H bonds exist in all films. The N-H vibration at 1250 cm<sup>-1</sup> appears to be relatively weaker in HF SiN<sub>x</sub> compared to LF material, while the intensity of the transverse optical (TO) mode of Si-N band centered at 857 cm<sup>-1</sup> and its longitudinal optical (LO) mode at around 1030-1040 cm<sup>-1</sup> in LF SiN<sub>x</sub> samples is found to increase. Moreover, a shift to a lower wave number in Si-N bond of HF SiN<sub>x</sub> compared to LF films appears as shown from **Table 5.3**. A similar shift towards a lower wave number in Si-H stretching vibrations for HF films (at 2150 cm<sup>-1</sup>) could be observed compared to LF material (at 2179 cm<sup>-1</sup>). **Fig. 5.5d** highlights also that the N-H/Si-H ratio is smaller for HF SiN<sub>x</sub> compared to LF, indicating more Si-H molecules in the HF material. This is consistent with the corresponding decrease in N/Si ratio for the HF material (**Table 5.1**) compared to LF (**Table 5.2**) as obtained from XPS measurements, which might be an indication of the presence of a larger concentration of silicon clusters in the HF SiN<sub>x</sub> films. Furthermore, **Fig. 5.22b, c** presents an example of the XPS data for HF-Si and LF-Si samples. As seen from the depth profiles, the LF SiN<sub>x</sub> layer is more inhomogeneous compared to the HF film. The C and O contamination are also relatively larger in the HF material compared to the LF SiN<sub>x</sub>. These remarks have been also made from the comparison between the FT-IR spectra and XPS data of HF-Si and LF-Si films.

#### 5.7.5 Discussion

More silicon rich SiN<sub>x</sub> films have faster charge decay with time as reported in [68]. Since FT-IR and XPS data shows that the HF SiN<sub>x</sub> films are more silicon-rich than the LF ones, this could partially explain why the HF material exhibits faster charge decay when compared to the LF one. In other words, the small difference in the Ni/Si ratio between both materials cannot alone explain the large difference found with respect to the injected charge density and decay time constant,  $\tau$ , for both materials. Here it should be mentioned that the hydrogen contents in the investigated films, which could play a major role in the charge trapping process, has not been measured and is currently under investigation.

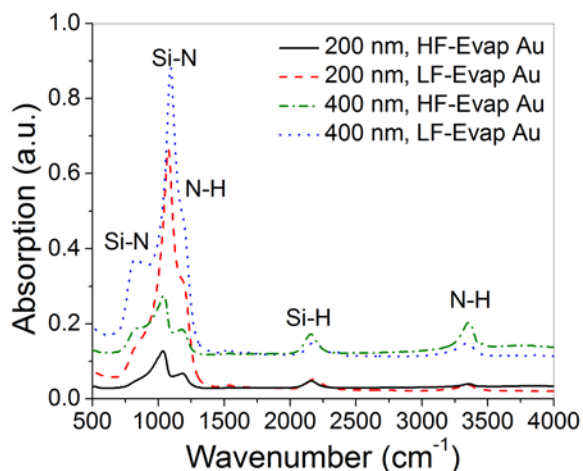
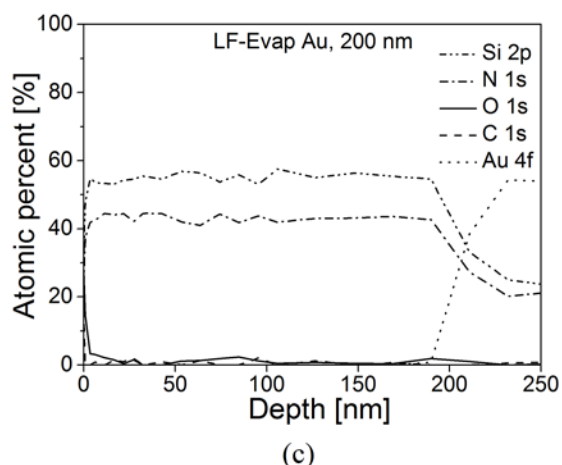
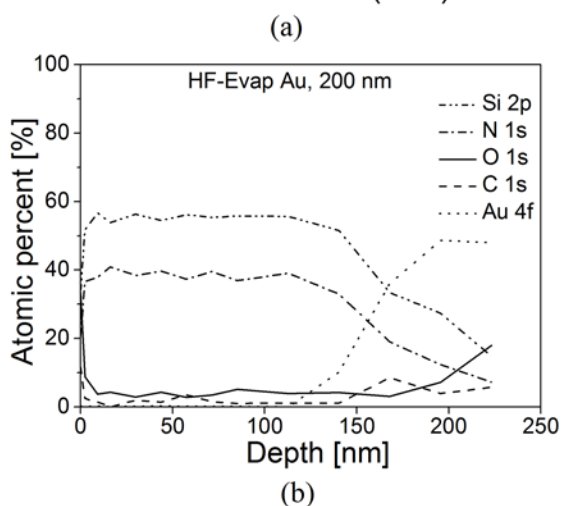


Figure 5.22. Difference in material stoichiometry between HF and LF  $\text{SiN}_x$ : (a) FT-IR spectra for HF-Evap Au and LF-Evap Au; XPS spectra for (b) HF-Evap Au and (c) LF-Evap Au samples with 200 nm thickness.



The density of defects is expected to be larger in the case of LF  $\text{SiN}_x$  material compared to the HF one due to the high RF power used during the LF film deposition (see **Table 3.2**). This difference in defects density and distribution in both materials affects the charge injection as well as the charge collection processes. In the case of  $\text{SiN}_x$  deposited directly over Si, the interface states are expected to be much higher in the LF material compared to the HF  $\text{SiN}_x$ . In addition, the high employed RF power results in a very high deposition rate for the LF material compared to the HF one. Therefore, the LF material is expected to suffer from larger disorder due to higher energy transfer to the Si and N atoms during the deposition process and the faster deposition rate. As shown in **Fig. 22b, c** the spatial distribution of layers in the nanoscale is different between both materials, and is more random in the LF  $\text{SiN}_x$  films. Moreover, the resistivity of both materials are different showing that the LF  $\text{SiN}_x$  material has smaller resistivity compared to the HF one, which might affect the charging and discharging processes [36]. All of these mentioned

differences between both materials could explain the larger injected charge density and the longer decay time constant,  $\tau$ , observed for the LF material compared to the HF material.

Based on these results, the KPFM, FDC, and C/DCT assessment technique reveals that the HF  $\text{SiN}_x$  material is more reliable with respect to the dielectric charging compared to the LF material. This is mainly due to the smaller injected charge density and faster charge decay in the case of the HF material compared to the LF  $\text{SiN}_x$ . Therefore, MEMS switches employing HF  $\text{SiN}_x$  as a dielectric layer are expected to have less dielectric charging, hence longer lifetimes compared to the switches employing the LF material. In the next chapter, an extended study for the influence of different deposition parameters on dielectric charging is presented.

In spite of the considerable differences between the KPFM and FDC based measurements, their results show a very good agreement and lead to similar conclusions regarding the influence of the dielectric film thickness, dielectric deposition conditions, the under layers, and the charge injection conditions on the dielectric charging/discharging processes. This is because the effect of meniscus force, which is considered the main difference between the FDC and KPFM, was minimized in the FDC experiments. This was done through dehydrating the  $\text{SiN}_x$  samples, and then by performing the FDC experiments at very low relative humidity [143].

An important issue that is worth mentioning here is the possible impact on the dielectric charging behavior due to the technological steps that follow the  $\text{SiN}_x$  deposition during the fabrication of real MEMS devices. For example, in MEMS switches the air gap is normally made by etching away a sacrificial layer which is deposited on top of the dielectric film as described in the fabrication process flow (see **Fig. 3.1**). As the etchant has to stop on the  $\text{SiN}_x$  film, it may affect the charging behavior of the dielectric material. The  $\text{SiN}_x$  samples which were characterized using KPFM-TF and FDC-TF techniques consist only of bare dielectric films deposited over planar substrates and did not go through any photolithography steps or further chemical treatments. Consequently, the possible impact of further chemical treatments on the  $\text{SiN}_x$  charging behavior has not been addressed in this thesis, and it requires further investigation. An initial estimation related to this effect could be extracted from our previous work [74] where KPFM was used to study the impact of the substrate over which  $\text{SiN}_x$  material is deposited on the dielectric charging. In the mentioned study, two groups of samples were explored. The first group of  $\text{SiN}_x$  films was implemented in real MEMS switches and hence was exposed to the

further technological steps while the second group of samples was not exposed to any chemical treatment after the dielectric deposition. The impact of the substrate on the charging/discharging behavior of both groups of samples was found to be the same. The only existing difference was related to the exact values of both decay time constant and stretch factor for both groups.

## **5.8 Summary**

The influence of various parameters on the dielectric charging/discharging processes was explored. This includes the effect of the dielectric film thickness, substrate, and dielectric deposition conditions (HF versus LF SiN<sub>x</sub>). The effect of the electrical stress parameters applied to charge the dielectric films which are the stress electric field, polarity, and duration were also studied. The electrical characterization was performed using the KPFM-TF, FDC-TF and C/DCT methods. FT-IR and XPS were used to study the chemical composition of SiN<sub>x</sub> films, and their data were correlated to the electrical characterization results. The main conclusive remarks from this chapter are the following:

- Charging the SiN<sub>x</sub> films using larger electric field or longer duration result in larger injected charge density and longer relaxation time (agrees with the reported data on MEMS switches).
- Increasing the dielectric film thickness leads to higher injected charge density and has no effect on the discharging process for a given stress electric field (FT-IR and XPS show comparable material stoichiometry for SiN<sub>x</sub> films with different thicknesses).
- Thicker SiN<sub>x</sub> films are preferred for MEMS switches with reduced charging (have smaller injected charge density and shorter decay time constant).
- FT-IR and XPS reveal similar material stoichiometry for SiN<sub>x</sub> films deposited over metal layers and over Si substrates.
- The SiN<sub>x</sub> films deposited over metal exhibit larger injected charge density and faster discharging process compared to SiN<sub>x</sub> over Si (due to the depletion region, interface states, and more pronounced MWS effect in SiN<sub>x</sub> over Si).
- The KPFM and FDC results explain the reported data on the considerable influence of the substrate charging on the shift in pull-in voltage and lifetime of MEMS switches.
- HF SiN<sub>x</sub> has smaller injected charge density and faster discharging process compared to LF SiN<sub>x</sub> (attributed to the more Si content, less density of defects, and less random spatial distribution in HF SiN<sub>x</sub> films).

- HF SiN<sub>x</sub> is more reliable for electrostatic MEMS with reduced charging compared to LF SiN<sub>x</sub>
- The work function and roughness of the underlying metal layer have no effect on the charging/discharging processes (similar electrical behavior and material stoichiometry for SiN<sub>x</sub> deposited over Evap. Au, Evap. Ti, and ECD Au).
- Negative charging of SiN<sub>x</sub> films leads to higher injected charge density and longer discharging process compared to positive charging.
- The obtained results from KPFM and FDC nanoscale characterization shows good correlation to C/DCT measurements applied for MIM capacitors.
- KPFM and FDC measurements leads to longer decay time constants compared to C/DCT due to the different charge collection process.

In conclusion, this chapter provides a deeper insight to the influence of various key parameters on the charging phenomenon using novel characterization methodologies that reveal proper explanations for the reported measurement results from actual MEMS devices.

*A science is any discipline in which the fool of this generation can go beyond the point reached by the genius of the last generation.*

*Max Gluckman  
1911 – 1975, South African and British social anthropologist  
in “Politics, Law and Ritual in Tribal Society”*

## **6 Influence of deposition reactive gas ratio, RF power and substrate temperature on charging/discharging processes in SiN<sub>x</sub> films**

### **6.1 Introduction**

The dependence of the electrical properties of SiN<sub>x</sub> on the deposition conditions used to prepare it and consequently on the material stoichiometry has not been fully understood as concluded from chapter 2. It has been partially addressed in chapter 5 where the charging in SiN<sub>x</sub> films deposited using two PECVD deposition recipes (HF, LF) was studied. The present chapter extends this work and introduces a detailed investigation of the influence of numerous PECVD deposition parameters on the dielectric charging in SiN<sub>x</sub> films. This includes the impact of the deposition reactive gas ratio, RF power, and substrate temperature. The charging/discharging processes were studied using the KPFM-TF and FDC-TF characterization methods explained in chapter 3. Moreover, XPS and FT-IR were employed to study the material stoichiometry of the investigated SiN<sub>x</sub> films. An attempt to correlate between the chemical and electrical properties of SiN<sub>x</sub> films was made.

The chapter is organized as follows. First, the investigated samples as well as the parameters of different used characterization techniques are presented. This is followed by discussing the influence of each deposition parameter. Finally, a summary of the study is presented.

## 6.2 Experimental

A generic layer structure of the samples investigated in this study is shown in **Fig. 3.2b**, and the details of each layer are presented in **Table 3.1**. HF-Evap Au samples which consist of HF SiN<sub>x</sub> films with 200 nm thickness deposited over Au/Ti (200 nm/50 nm) layers were used. The HF SiN<sub>x</sub> material was used in this work since it was concluded from chapter 5 that the HF material is more preferable for MEMS switches compared to the LF SiN<sub>x</sub> due to the smaller injected charge density and the faster discharging process in the HF material. During the deposition process silane (SiH<sub>4</sub>) and ammonia (NH<sub>3</sub>) were used as the reactive species, while nitrogen (N<sub>2</sub>) was used as a dilution gas. HF SiN<sub>x</sub> films were deposited using different deposition parameters by changing individually the reactive gas ratio (SiH<sub>4</sub>/NH<sub>3</sub>), RF power, and substrate temperature. The explored process parameters are the following: (1) gas ratios (SiH<sub>4</sub>/NH<sub>3</sub>) varying from 0.15 to 0.8; (2) RF power varying from 20 W to 100 W; and (3) substrate temperatures varying from 200 °C to 300 °C. **Table 6.1** lists the different deposition parameters which were investigated. The last sample in **Table 6.1** represents a reference sample and is common for the three changed deposition parameters. This reference sample was deposited using the default HF recipe presented in **Table 3.2**. All other SiN<sub>x</sub> films investigated in this chapter were deposited using the same N<sub>2</sub> flow and chamber pressure of the default HF recipe shown in **Table 3.2**.

Table 6.1: The investigated PECVD deposition parameters and a quantification of atomic concentration by XPS (% at) for the investigated HF SiN<sub>x</sub> films (source RX Mg, Ep=20 eV, correction Scofield).

SiH <sub>4</sub> / NH <sub>3</sub> gas ratio, r	RF power (W)	Substrate temperature (°C )	O at%	N at%	Si at%	N/Si
0.15	20	200	1.8	45	53.2	0.845
0.25	20	200	0.6	44.6	54.8	0.813
0.6	20	200	2.5	38.5	59.0	0.653
0.8	20	200	2.4	37.9	59.7	0.635
0.45	40	200	1.4	40.2	58.4	0.688
0.45	60	200	1.55	40.5	57.95	0.698
0.45	80	200	1.0	41.1	57.8	0.711
0.45	100	200	1.5	41.5	57	0.728
0.45	20	250	1.6	40.1	58.3	0.687
0.45	20	300	0.8	40.2	59.0	0.681
0.45 (reference)	20	200	-	41	59	0.694

The investigated deposition parameters were selected to either optimize the HF recipe for a minimal dielectric charging or to study the effect of a specific deposition parameter on the difference in the charging/discharging processes between HF and LF SiN<sub>x</sub>. The selected values of the SiH<sub>4</sub>/NH<sub>3</sub> ratio include larger (0.6, 0.8) and smaller (0.15, 0.25) gas ratios compared to the reference sample ( $r = 0.45$ ) in order to help predicting the charging behavior of SiN<sub>x</sub> for larger and smaller gas ratios around the reference value and hence to fine tune the dielectric film towards minimal charging. The highest investigated gas ratio (0.8) was selected to further approach the ratio used in the LF recipe (1.4). The values of the RF power were selected to increase from the 20 W used to deposit the reference sample (HF) to 100 W, which approaches the deposition RF power for the LF recipe (185 W), in order to understand influence of the RF power on the charging/discharging processes in HF and LF SiN<sub>x</sub> films. Finally, the substrate temperature was increased from 200 °C for the reference sample to 300 °C in order to study the influence of the hydrogen content in deposited SiN<sub>x</sub> films.

The KPFM and FDC based electrical assessment methods were used to study the dielectric charging for charges injected under different voltage amplitudes. KPFM was employed to investigate the charging/discharging processes for a single asperity. For this reason, the KPFM-TF method (**Fig. 3.4**) was used where charges were injected in single points over SiN<sub>x</sub> films. The charge injection duration,  $T_p$ , for the KPFM experiments was fixed to 1 s. In the FDC-TF measurements (see **Fig. 3.9**), the charging of the SiN<sub>x</sub> film was performed through a single scan over a selected area of the dielectric surface (10 μm X 10 μm). After completing the charge injection step, the discharging process was studied through monitoring the decay of induced surface potential and induced adhesive force with time using KPFM and FDC, respectively. The observation time window for the decay experiments was 3.5 hours and 1 hour for the KPFM and the FDC measurements, respectively. The time interval between the end of the charge injection step and the beginning of the KPFM or FDC measurement was 30 s. In order to avoid the influence of humidity and the adsorbed water film over the dielectric surface on both KPFM and FDC measurements as well as on the charging/discharging processes, the SiN<sub>x</sub> samples and the AFM tip went through two cycles of heating (150 °C) and cooling steps under vacuum. In addition, both KPFM and FDC measurements were performed under dry air flow (relative humidity ≈ 0.02%) using the controlled environment AFM chamber presented in **Fig. 3.11**.

### 6.3 Effect of reactive gas ratio

To study the influence of the reactive gas ratio, SiN<sub>x</sub> films were deposited using different SiH<sub>4</sub>/NH<sub>3</sub> while the deposition RF power and substrate temperature were kept constant as presented in **Table 6.1**. In this section the results obtained from KPFM-TF and FDC-TF measurements are presented first. This is followed by presenting the influence of the gas ratio on the material stoichiometry using the FT-IR and XPS data. Then, the electrical and chemical characterization results as well as their correlation are discussed.

#### 6.3.1 KPFM results

**Fig. 6.1** presents an example of the resulting KPFM-TF surface potential profiles for the SiN<sub>x</sub> films deposited using different gas ratios for charges injected under the same pulse amplitude ( $U_p = 40$  V). It is evident from the figure that the potential peak amplitude ( $U_s$ ), potential distribution (FWHM), and consequently the potential profile integral, which is a direct indication for the injected charge density inside the dielectric film, change remarkably with the deposition gas ratio. The influence of the gas ratio on the charging/discharging processes for charges injected using different pulse amplitudes,  $U_p$ , is presented in **Fig. 6.2**. It could be observed from **Fig. 6.2a** that the measured surface potential amplitude,  $U_s$ , decreases gradually when the gas ratio increases from 0.15 to 0.45, and this is followed by a sudden decrease to a very close value to 0 for both 0.6 and 0.8 gas ratios [133]. Also, the charge distribution represented by the FWHM decreases gradually as the gas ratio increases from 0.15 to 0.8 as

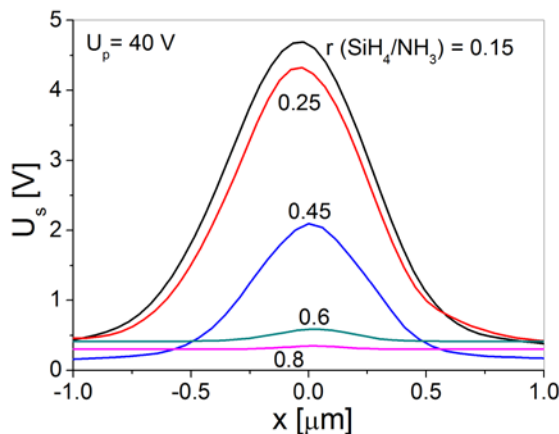


Figure 6.1. An example of KPFM induced surface potential profiles for SiN<sub>x</sub> films deposited using different gas ratio,  $r$ .

highlighted in **Fig. 6.2b**. The integral of the resulting potential profile (**Fig. 6.2c**) highlights clearly that the injected charge density decreases gradually as the gas ratio increases from 0.15 to 0.45 and then shows a very high drop when the gas ratio increases beyond 0.45. The similar trend between **Fig. 6.2c** and **Fig. 6.2a** for 0.6 and 0.8 gas ratios points out that the sudden decrease in the injected charge density is not attributed to a more confined charge distribution over the dielectric surface

since the FWHM shows a gradual decrease with a comparable rate for all gas ratios. This emphasizes the importance of KPFM-based characterization on the level of a single asperity in order to understand how the injected charge density changes from one sample to another.

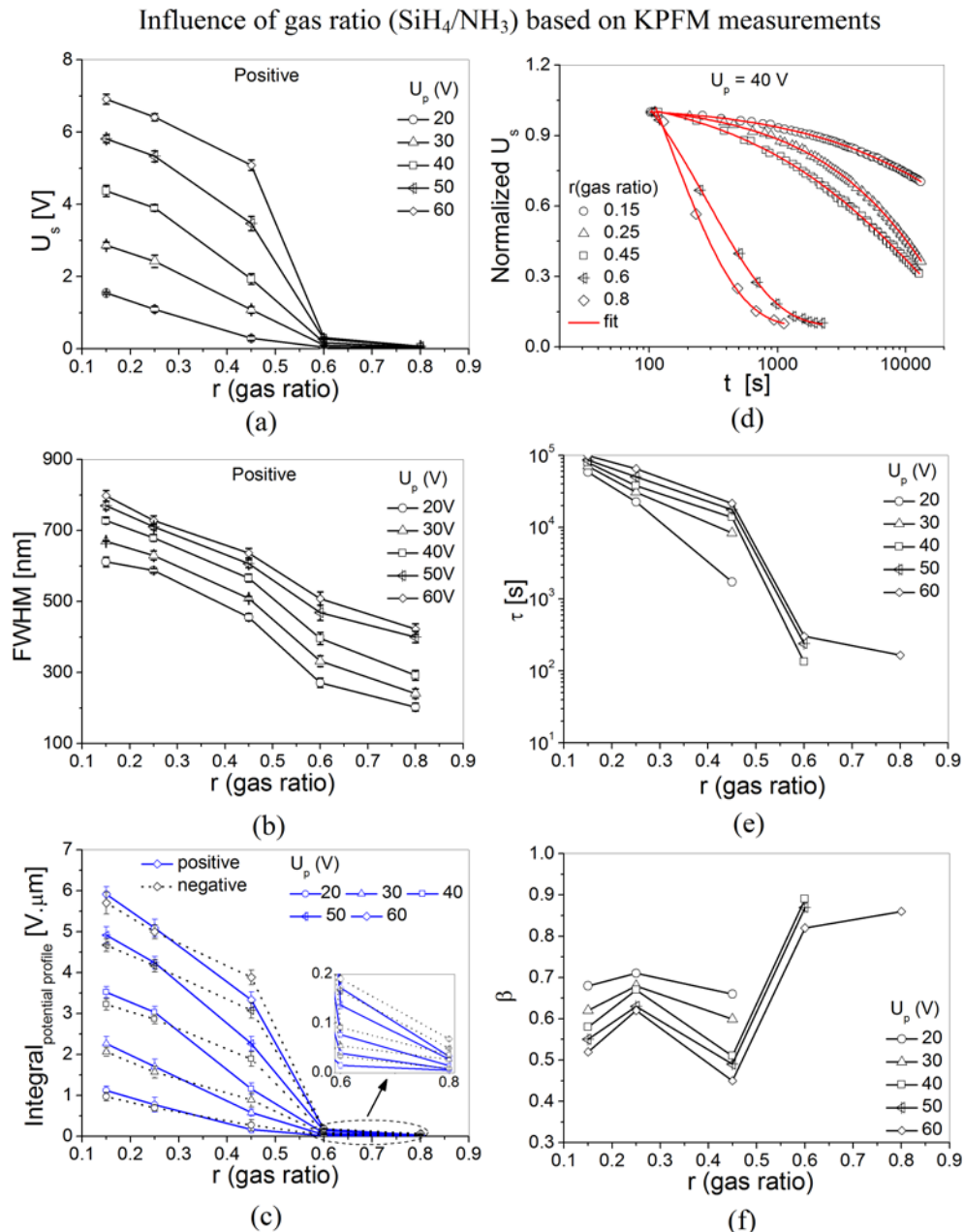


Figure 6.2. The influence of the reactive gas ratio,  $r$ , on the charging/discharging processes as extracted from the KPFM measurements for charges which were injected using different  $U_p$ : (a) surface potential amplitude,  $U_s$ , (b) potential distribution, FWHM, (c) potential profile integral for positive and negative charge injection, (d) an example of  $U_s$  decay with time for injected charges using the same  $U_p$ , (e) the decay time constant, and (f) stretch factor.

The asymmetry between positive and negative charge injection related to the injected charge density, though small, could be observed from **Fig. 6.2c**, and has been discussed in chapter 5. It could be seen also from **Fig. 6.2c** that changing the deposition gas ratio has a remarkable effect on the asymmetry between positive and negative charge injection. For example, for the 0.15 gas ratio the injected charge density for positive injection is relatively larger compared to negative charging, while for the 0.25 gas ratio the injected charge density using both bias polarities are comparable. Starting from the 0.45 gas ratio and up, the opposite trend could be observed showing that the injected charge density is larger for negative injection compared to positive. These remarks have been made for charges injected under different pulse amplitudes.

An example of the measured surface potential evolution with time for SiN<sub>x</sub> films deposited using different gas ratios is shown in **Fig. 6.2d**. The figure presents the normalized value of the surface potential with respect to the maximum U<sub>s</sub> measured directly after completing the charge injection step (at t = 0), and it highlights clearly that the surface potential decay becomes faster as the gas ratio increases. The sudden decrease in the relaxation time with increasing the gas ratio from 0.45 to 0.6 and 0.8 is also obvious from the figure. The surface potential decay with time is found to follow the stretched exponential law (Eq. 4.3:  $\exp[-(t/\tau)^\beta]$ ) [76, 116, 134, 135]. This has been observed for all investigated SiN<sub>x</sub> films deposited using different deposition parameters and for charges injected under different pulse amplitudes, U<sub>p</sub>. The decay time constant and stretch factor calculated from fitting the surface potential decay with Eq. 4.3 for the SiN<sub>x</sub> samples deposited with different gas ratios are shown in **Figs. 6.2e, f**, respectively. The y-axis of **Fig. 6.2e** is plotted in log scale, and it highlights clearly the huge variation in the decay time constant when changing the gas ratio. The time constant decreases gradually with increasing the gas ratio from 0.15 to 0.45 and then features a sudden decrease when the gas ratio reaches 0.6 and 0.8, which agrees with the potential decay data presented in **Fig. 6.2d**. No clear effect of the gas ratio on the stretch factor is found as shown in **Fig. 6.2f**. Also, the trend of the decay time constant and stretch factor versus the gas ratio is found to be similar for charges injected using different pulse amplitude, U<sub>p</sub>. Due to the fast charge collection process at higher gas ratios (0.6 and 0.8), the obtained data points for the surface potential evolution with time for several U<sub>p</sub> were not sufficient to fit with the stretched exponential equation. Finally, it could be observed that the decay time constant increases while the stretch

factor decreases with larger pulse amplitudes due to the combined contribution of Poole-Frenkel and Trap Assisted Tunneling effects as explained in chapter 5.

### 6.3.2 FDC results

The impact of the gas ratio on the charging/discharging processes based on FDC measurements is presented in **Fig. 6.3**. The correlation between the induced surface potential measured by FDC (**Fig. 6.3a**) and the induced adhesive force (**Fig. 6.3b**) as a function of the reactive gas ratio and/or the voltage applied during the charge injection is quite obvious. As the voltage applied during the SiN<sub>x</sub> charging increases, the induced surface potential as well as the induced adhesive force between the AFM tip and the dielectric surface increases too. Comparing **Figs. 6.3a, b** with **Fig. 6.2c**, it is obvious that the trend of the induced surface potential measured by FDC and the induced adhesive force as a function of the reactive gas ratio and the applied charging bias agrees quite well with the trend of KPFM potential profile integral. From **Fig. 6.3a**, the measured surface potential is relatively high especially for the 0.15 gas ratio. Such potential levels represent the real induced surface potential over SiN<sub>x</sub> films which are comparable to the induced potential over the dielectric films of MEMS switches, and cannot be measured by KPFM.

An example of the evolution of the measured adhesive force with time for SiN<sub>x</sub> samples deposited using different gas ratio is presented in **Fig. 6.3c**. It is found that the decay of the adhesive force with time fits well with the square of the stretched exponential equation (Eq. 4.4),  $(\exp[-(t/\tau)^\beta])^2$ , as shown in chapter 4. Also, the KPFM surface potential fits properly with the normal stretched exponential law (Eq. 4.3:  $\exp[-(t/\tau)^\beta]$ ). Since the electrostatic force between the AFM tip and the sample surface is proportional to the square of the voltage difference between both of them, the perfect fitting of the measured adhesive force with Eq. 4.4 confirms undoubtedly that the measured adhesive force between the AFM tip and the SiN<sub>x</sub> surface resembles mainly the attractive electrostatic force. The decay time constant calculated from fitting the adhesive force decay with Eq. 4.4 is shown in **Fig. 6.3d**. It is obvious from the figure that the trend of the decay time constant versus the reactive gas ratio agrees well with the trend obtained from the KPFM surface potential decay (**Fig. 6.2e**). This could be observed for charges injected using different voltage levels. The other interesting point here is that the decay time constant extracted from fitting the adhesive force evolution with time is found to increase with the voltage applied during charge injection, which agrees with what has been found from the

KPFM surface potential decay. The shorter decay time constant calculated from the adhesive force decay compared to the time constant calculated from KPFM surface potential decay is attributed mainly to the different observation time window used for both experiments (3.5 hours for KPFM and 1 hour for FDC). As reported in [125], the decay time constant increases remarkably as the observation time window increases.

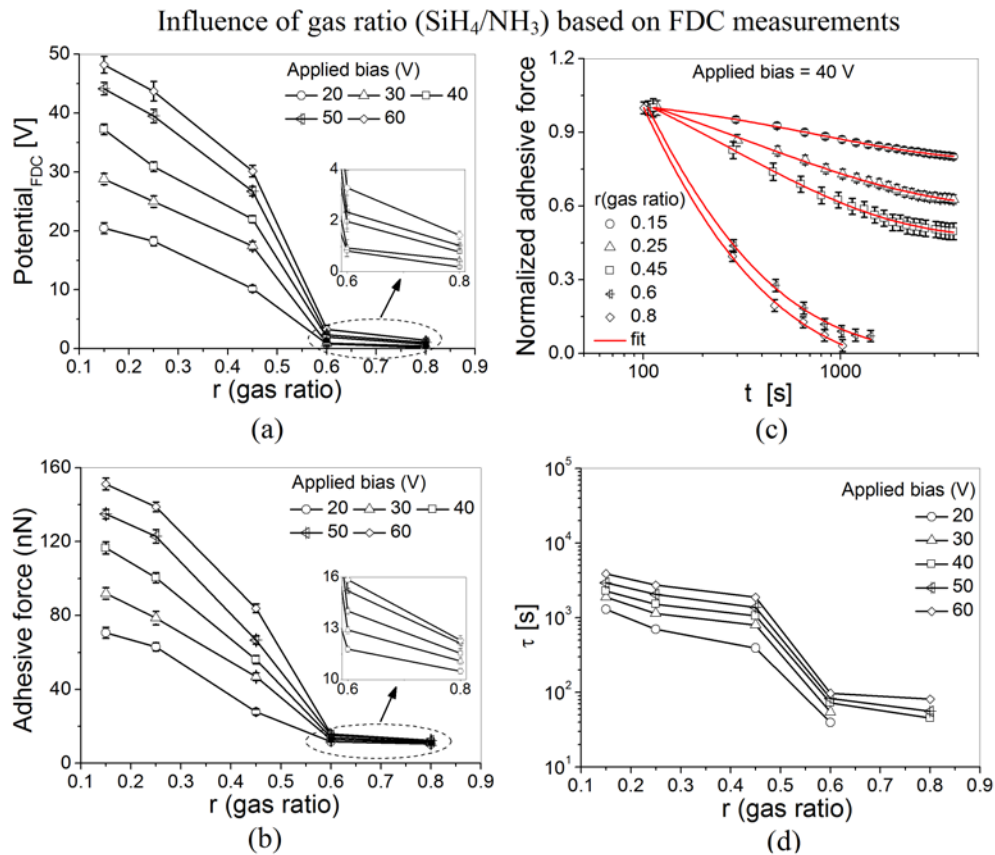


Figure 6.3. The impact of reactive gas ratio,  $r$ , on the charging/discharging processes as measured from the FDC measurements for charges which were injected using different voltage: (a) measured surface potential, (b) adhesive force, (c) an example of adhesive force decay with time for charges injected using the same voltage, and (d) the decay time constant.

In conclusion, the electrical characterization techniques using KPFM and FDC measurements lead to similar conclusions regarding the electrical properties of the  $\text{SiN}_x$  films deposited using different gas ratios. The injected charge density as well as the relaxation time decrease gradually when the gas ratio increases from 0.15 to 0.45, and then decrease sharply for the 0.6 and 0.8 gas ratios.

## 6.3.3 Influence on material stoichiometry

The FT-IR spectra for  $\text{SiN}_x$  films deposited using different gas ratios are presented in **Fig. 6.4a**. The change of Si–H (around  $2157\text{ cm}^{-1}$  at  $70^\circ$ ,  $2160\text{ cm}^{-1}$  at  $20^\circ$ ) and N–H (around  $3348\text{ cm}^{-1}$  at  $70^\circ$ ,  $3350\text{ cm}^{-1}$  at  $20^\circ$ ) extracted from FT-IR for different gas ratios is plotted in **Figure 6.4b**. The N/Si ratio determined by XPS analysis (**Table 6.1**) is also presented in the figure. In the as-deposited layers, the N/Si ratio (about 0.845 for  $r = 0.15$ , and 0.63 for  $r = 0.80$ ) decreases linearly with the gas ratio. Also, the relative intensity of Si–H versus N–H vibrations increases quite sharply with the gas ratio, indicating that the N–H molecules are being reduced. This is consistent with the corresponding reduced amount of nitrogen for the higher gas ratio as observed from XPS. Thus, the silicon content in  $\text{SiN}_x$  films increases with the gas ratio (i.e. with increasing the  $\text{SiH}_4$  gas flow).

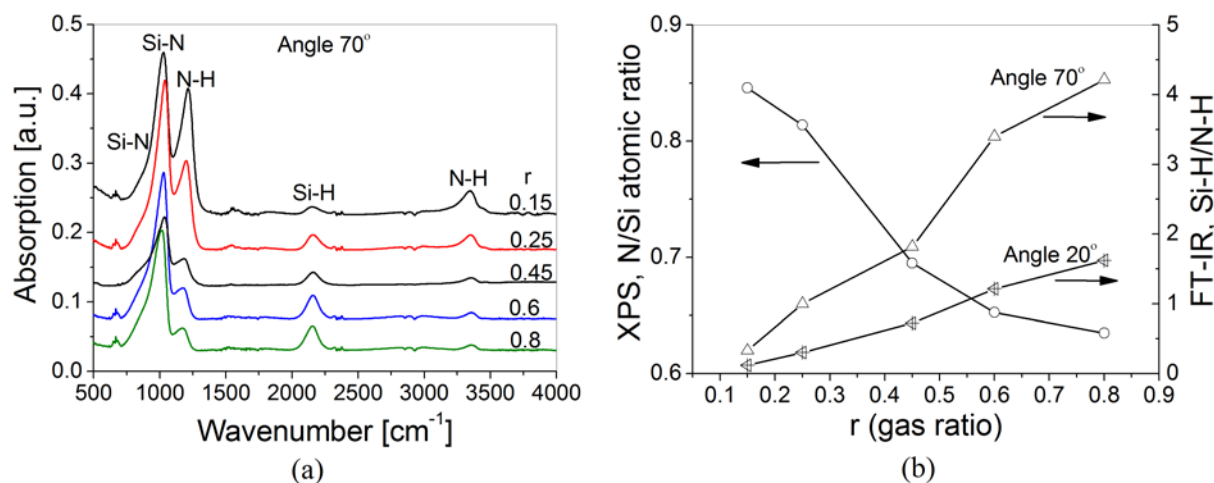


Figure 6.4. FT-IR and XPS data for  $\text{SiN}_x$  films deposited using different gas ratio,  $r$ : (a) FT-IR spectra at an angle of  $70^\circ$ , and (b) N/Si atomic ratio obtained from XPS analysis and the relative intensity Si–H (around  $2157\text{ cm}^{-1}$  at  $70^\circ$ ,  $2160\text{ cm}^{-1}$  at  $20^\circ$ ) versus N–H (around  $3348\text{ cm}^{-1}$  at  $70^\circ$ ,  $3350\text{ cm}^{-1}$  at  $20^\circ$ ) from FT-IR.

On the other hand, the observation of a strong increase of the Si–H relative intensity in the larger gas ratio suggests that Si atoms with more dangling bonds are present with large amounts in the matrix. As a consequence of the decreasing N/Si ratio (**Fig. 6.4b**), the absorption peak of Si–N vibrations tend to lie in the lower frequency from  $r = 0.15$  at longitudinal optical (LO) mode  $1029\text{ cm}^{-1}$ , to  $r = 0.8$  at  $1016\text{ cm}^{-1}$ . Meanwhile, the rocking mode =N–H (at  $1214\text{ cm}^{-1}$ ,  $1201\text{ cm}^{-1}$ ,  $1183\text{ cm}^{-1}$ ,  $1177\text{ cm}^{-1}$  for  $r = 0.15, 0.25, 0.6, 0.8$ , respectively) increases in the relative amplitude and shift to high frequency indicating that the involvement of more nitrogen in

the SiN<sub>x</sub> thin films as the gas ratio decreases. The trend described above is in agreement with the high frequency shift of SiN-H<sub>2</sub> bending mode at 1528 cm<sup>-1</sup> to 1553 cm<sup>-1</sup> with reduced gas ratio. The interesting point here is that the Si-H bond may have a slight shift to high frequency with more nitrogen backbond, while no such effect has been observed for the N-H bonds which are always in the same configuration, Si<sub>2</sub>N-H. The two large peaks of the LO mode and the transverse optical (TO) mode of Si-N stretching vibration could be observed, which are definitely related to the SiN<sub>x</sub> phonon spectra. Although in the present amorphous SiN<sub>x</sub> material the long range order no longer exists, the short-range may be similar to the crystalline part. At a high gas ratio, the nitrogen atoms are scarce and the vibration mode of the isolated Si-N<sub>x</sub> network is local, which is similar to the zone boundary mode of crystalline SiN<sub>x</sub>. When more nitrogen atoms are incorporated into the film as the gas ratio decreases, the Si-N<sub>x</sub> network become extended and similar to the zone center mode of Si<sub>3</sub>N<sub>4</sub>, and the high frequency shoulder appears.

#### 6.3.4 Discussion

Due to the trapped charges in the dielectric film, the electric field at the AFM tip/SiN<sub>x</sub> interface is reduced, and this further reduces the injection rate/efficiency. This is mainly because the injected charges in the dielectric film are most probably located very close to the injecting electrodes or the dielectric surface as reported in [132]. Furthermore, the charge injection rate is compensated by a charge redistribution rate, and the injected charge saturation is determined by the rate of charge injection and redistribution. Charge redistribution takes place through various mechanisms, i.e. Poole-Frenkel, hopping, leakage, etc. The magnitude of the injected charge density is obtained by the continuity equation of these two mechanisms during charging if no equilibrium is reached:  $\nabla J = \frac{d\rho}{dt} \neq 0$ , where  $J = J_{charge} - J_{discharge}$ , and  $\rho$  is the density of charge per unit volume. At saturation at any point, the total current from charge injection and redistribution is  $\nabla J = \frac{d\rho}{dt} = 0$ . This equilibrium is determined mainly by the charging electric field and charging time. It is also affected by the characteristics of the charge trapping centers and trapped charge redistribution which are dependent on the material stoichiometry.

The silicon content in the investigated SiN<sub>x</sub> films increases with the SiH<sub>4</sub>/NH<sub>3</sub> gas ratio as explained in section 6.3.3 (see **Fig. 6.4b**). Increasing the silicon content or equivalently

decreasing the nitrogen content in  $\text{SiN}_x$  films was reported to increase the leakage current as measured from current-voltage characteristics in MIM capacitors [82]. This is basically attributed to the formation of nanoclusters [118, 136, 137, 138] and traps which allow the charge transport through conductive percolation tunneling paths and hopping through defect states [139]. Increasing the silicon content also results in increasing the concentration of defects [82], and leads to a larger number of charge trapping centers [140]. This results in increasing the density of traps, as well as the probability of percolation and hopping. Therefore, charge redistribution paths increase and the redistribution becomes easier as the silicon content in the dielectric film increases. Consequently, the redistribution current will be larger and will lead to a smaller charge density at the dielectric surface. For this reason, the charge injection/redistribution equilibrium will be attained at a smaller surface charge density. For a smaller gas ratio (for example  $r = 0.15$ ) the silicon content is reduced and the material goes near to stoichiometry with less leakage and defect concentration. Thus, the charge redistribution paths will decrease, resulting in a smaller redistribution current and consequently larger charge density at the dielectric surface. Therefore, the equilibrium between charge injection/redistribution is obtained at a larger surface charge density.

The measured surface potential by KPFM and/or FDC measurements and consequently the induced adhesive force between the AFM tip and the dielectric film represents mainly the charge density at, or very close to, the dielectric surface. In view of the above analysis, for a small gas ratio ( $r = 0.15$ ) with less silicon content, the charge redistribution is small, and this results in a slow charge collection process by the bottom electrode. This explains the longer decay time constant in the case of a smaller gas ratio compared to a larger gas ratio (**Figs. 6.2e, 6.3d**) simply because the discharge rate depends on the discharge time constant. It also explains why the injected charge density, surface potential, and consequently the adhesive force between the AFM tip and the  $\text{SiN}_x$  surface are larger for smaller gas ratios compared to larger ones. Here it should be highlighted that the results obtained in this study from KPFM and FDC regarding the influence of the deposition gas ratio are in good agreement with data presented in [82]. In the mentioned study, the bias at which the measured TSDC current was zero in MIM capacitors implementing PECVD  $\text{SiN}_x$  films was found to decrease with decreasing the nitrogen content in the dielectric film, a behavior which was attributed to an increase in the leakage current. The KPFM and FDC results obtained in this study are also in good agreement with [140] where

increasing the gas ratio ( $\text{SiH}_4/\text{NH}_3$ ) was reported to result in increasing the leakage current density. Finally, it was reported that the  $\text{SiN}_x$  films with more silicon content exhibits a smaller injected charge density and a faster charge decay [135], which also agrees with the KPFM and FDC results presented in this study.

In summary, increasing the  $\text{SiH}_4/\text{NH}_3$  ratio results in increasing the silicon content in  $\text{SiN}_x$  films as obtained from XPS and FT-IR measurements, and consequently in increasing the charge redistribution passes, including leakage. This further leads to a faster discharging process and accordingly a smaller injected charge density in the dielectric material with increasing the gas ratio as measured by KPFM and FDC.

#### **6.4 Effect of RF power**

The influence of the deposition RF power was investigated through depositing  $\text{SiN}_x$  films using different RF power while the gas ratio (0.45) and substrate temperature (200 °C) were kept constant as shown in **Table 6.1**.

##### *6.4.1 KPFM results*

The influence of the deposition RF power on the charging and discharging processes as measured by KPFM is presented in **Fig. 6.5**. The measured surface potential,  $U_s$ , does not exhibit a clear trend as the RF power increases, and this could be observed for injected charges under different pulse amplitudes,  $U_p$ . A similar remark is made for the trend of the surface potential distribution, FWHM, versus RF power. Additionally, the trend of surface potential amplitude,  $U_s$ , and distribution, FWHM, as a function of the deposition RF power are not consistent together for some data points. For example,  $U_s$  decreases while FWHM increases when the RF power increases from 60 W to 80 W. An opposite trend for both  $U_s$  and FWHM could be observed with increasing the RF power from 80 W to 100 W. The opposite trend of  $U_s$  and FWHM highlights the importance of the KPFM-based characterization on the level of a single asperity. Based on the obtained data from this technique we could understand how the injected charge density changes, and whether this change is due to the potential distribution, FWHM, or amplitude,  $U_s$ , or both. The variation of both  $U_s$  and FWHM with RF power for the injected charges under different pulse amplitudes is smaller compared to their variation as a function of the gas ratio (**Fig. 6.2a, b**). This is more evident from the FWHM variation as a function of the gas ratio (**Fig. 6.2b**) and RF power (**Fig. 6.5b**).

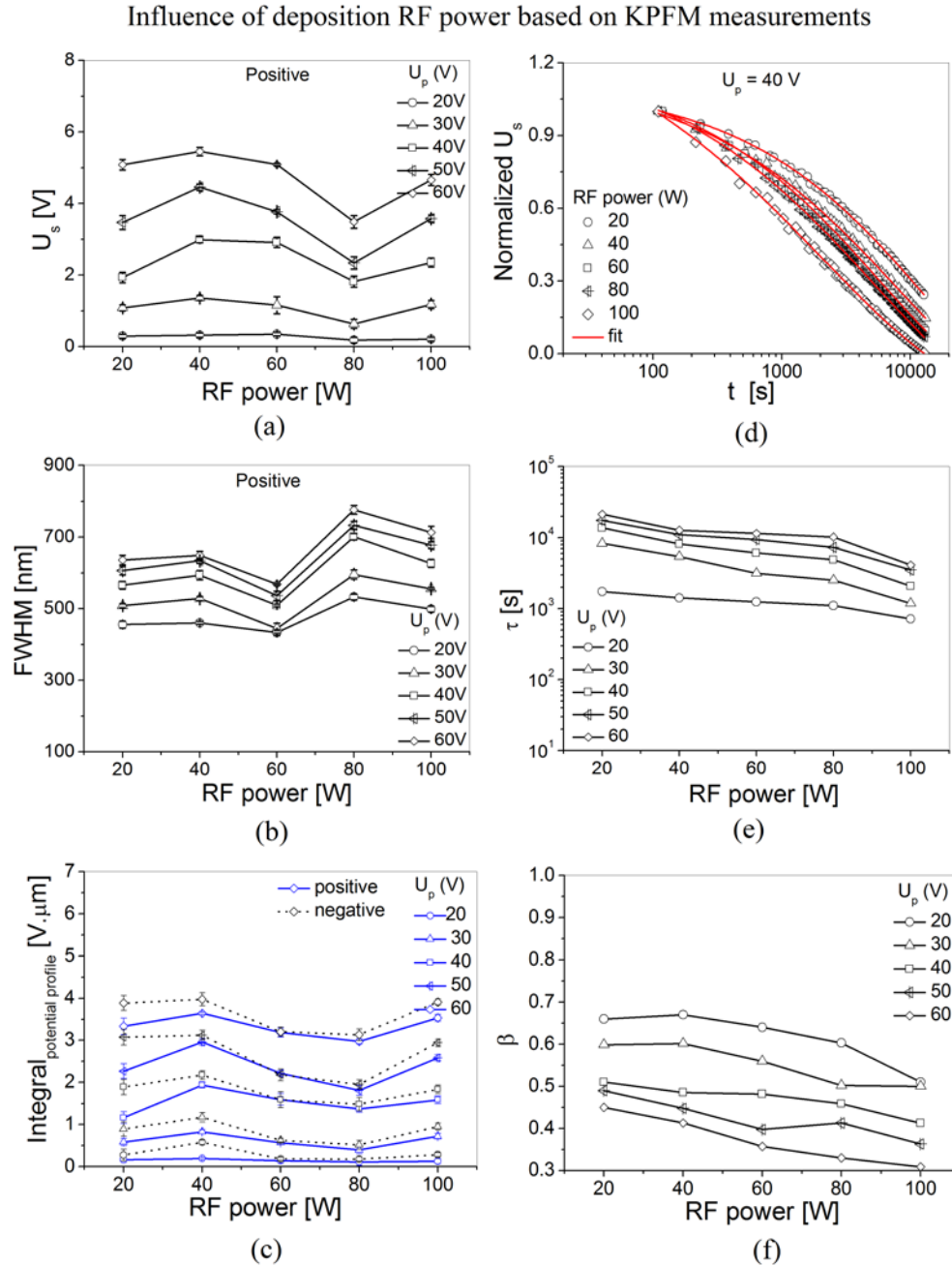


Figure 6.5. The effect of RF power on the charging/discharging processes as extracted from the KPFM measurements for charges which were injected using different  $U_p$ : (a) surface potential amplitude,  $U_s$ , (b) potential distribution, FWHM, (c) potential profile integral for positive and negative charge injection, (d) an example of  $U_s$  decay with time for injected charges using the same  $U_p$ , (e) the decay time constant, and (f) stretch factor.

The integral of the KPFM potential profile for different RF power is shown in **Fig. 6.5c**. The figure highlights that the injected charge density slightly increases when the RF power increases from 20 W to 40 W. The further increase in RF power leads to a slight decrease in the

injected charge density until the 80 W RF power is reached. The injected charge density increases once again when the RF power increases from 80 W to 100 W. The variation of the injected charge density with RF power is relatively small compared to its change versus the reactive gas ratio (**Fig. 6.2c**), and this has been observed for charges injected under different pulse amplitudes. **Figure 6.5c** shows also that the injected charge density for negative charge injection is relatively larger compared to positive charge injection for the whole investigated RF power values, except for the 60 W where positive and negative charge injection results in comparable injected charge densities. This has been observed also for injected charges using different pulse amplitude.

An example of the KPFM surface potential decay for SiN<sub>x</sub> films deposited using different RF power is presented in **Fig. 6.5d**. The figure points out that the charge collection process becomes relatively faster with increasing the deposition RF power. This is evident from the decay time constant calculated from fitting the surface potential decay with Eq. 4.3,  $\exp[-(t/\tau)^\beta]$ , as shown in **Fig. 6.5e**. Comparing **Fig. 6.5e** and **Fig. 6.2e**, it is concluded that the influence of the gas ratio on reducing the decay time constant is much larger compared to the impact of the deposition RF power. The stretch factor,  $\beta$ , shows also a decreasing trend as the deposition RF power increases as shown in **Fig. 6.5f**. In previous studies [37, 44, 117, 135],  $\beta$  was used as an index of charge collection complexity. The decrease of the stretch factor points out that the discharging process deviates from the simple exponential law (where  $\beta = 1$ ), and hence the charge collection mechanism becomes more complex as explained in chapter 5. **Figure 6.5e, f** show also that for each deposition RF power, the decay time constant increases while the stretch factor decreases when the pulse amplitude employed during the charge injection step increases which agrees with the results reported in [76, 117, 135].

#### 6.4.2 FDC results

**Figure 6.6** presents the influence of the deposition RF power on the charging/discharging processes in SiN<sub>x</sub> films as obtained from the FDC measurements. There is no clear trend for the measured FDC potential with RF power for the charges which were injected using different voltages as shown in **Fig. 6.6a**. This agrees well with the trend of the KPFM potential profile integral presented in **Fig. 6.5c**. Also, the variation of the measured FDC potential with the deposition RF power is relatively small compared to its change as a function of the reactive gas ratio (**Fig. 6.3a**). The almost horizontal fitting lines shown in **Fig. 6.6a** points out that the

investigated range of deposition RF power in this study has a minimal influence on the injected charge density. The measured adhesive force as a function of the deposition RF power is shown in **Fig. 6.6b**, and it also exhibits a very good correlation with the measured FDC potential for charges injected under different voltage amplitudes. Comparing **Fig. 6.3b** and **Fig. 6.6b**, it is obvious that the influence of the deposition RF power on the adhesive force between the AFM tip and the dielectric surface is relatively smaller compared to the effect of the gas ratio.

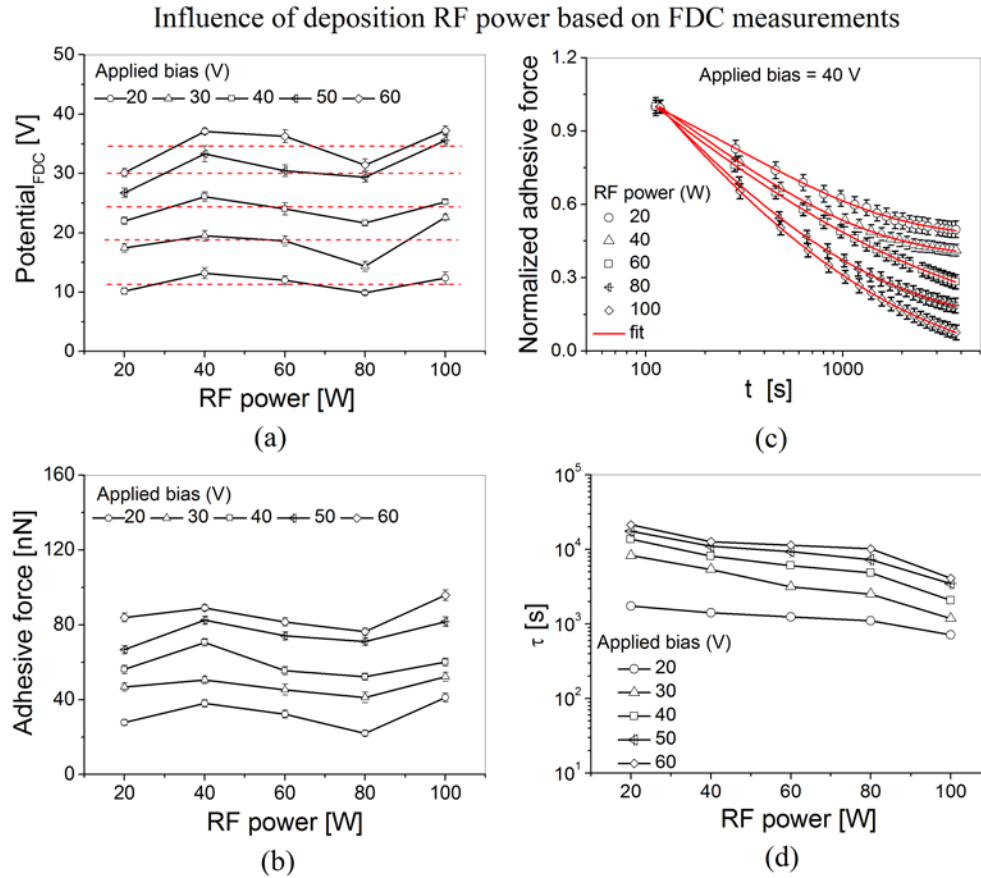


Figure 6.6. The influence of RF power on the charging/discharging processes as measured from the FDC measurements for charges which were injected using different voltage: (a) measured surface potential, (b) adhesive force, (c) an example of adhesive force decay with time for charges injected using the same voltage, and (d) the decay time constant.

An example of the adhesive force decay for  $\text{SiN}_x$  films deposited under different RF power is presented in **Fig. 6.6c**. It could be seen from the figure that the discharging process is slightly faster with a higher deposition RF power. This is evident from the decay time constant calculated from fitting the adhesive force decay with Eq. 4.4,  $(\exp[-(t/\tau)^\beta])^2$ , for  $\text{SiN}_x$  samples deposited using different RF power and charged under different voltage as shown in **Fig. 6.6d**.

Comparing **Fig. 6.6d** and **Fig. 6.3d**, it could be concluded that the influence of the reactive gas ratio on the discharging process is much larger than the impact of the deposition RF power. The correlation between the decay time constant calculated from the FDC adhesive force decay with time versus the deposition RF power (**Fig. 6.6d**) and the time constant extracted from the KPFM surface potential decay (**Fig. 6.5e**) is obvious.

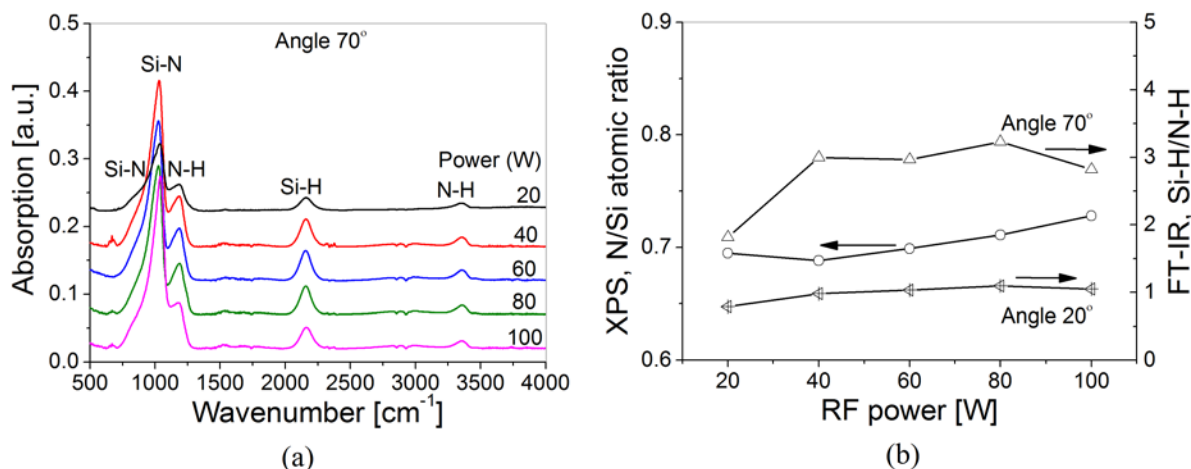


Figure 6.7. FT-IR and XPS data for  $\text{SiN}_x$  films deposited using different RF power: (a) FT-IR spectra for  $\text{SiN}_x$  films deposited using different RF power at an angle of  $70^\circ$ , and (b) N/ Si atomic ratio obtained from XPS analysis and the relative intensity Si–H (around  $2157\text{ cm}^{-1}$  at  $70^\circ$ ,  $2160\text{ cm}^{-1}$  at  $20^\circ$ ) versus N–H (around  $3348\text{ cm}^{-1}$  at  $70^\circ$ ,  $3350\text{ cm}^{-1}$  at  $20^\circ$ ) from FT-IR.

### 6.4.3 Influence on material stoichiometry

**Figure 6.7a** presents the FT-IR spectra for  $\text{SiN}_x$  films deposited using different RF power. Also, the Si-H/N-H ratio extracted from FT-IR and the N/Si atomic ratio from XPS are plotted in **Fig. 6.7b**. The XPS data show a relatively weak increase of the nitrogen content and a slight decrease of the silicon content when changing the RF power from 20 W to 40 W ( $\text{N/Si} \approx 0.694$ ). Increasing the deposition power beyond 40 W gives rise to a slight move up in N/Si atomic ratio till reaching 0.728 for the 100 W deposition power. On the other hand, there is an opposite trend in the relative intensity of Si–H (around  $2160\text{ cm}^{-1}$ ) versus N–H (around  $3330\text{ cm}^{-1}$ ) with plateau character. These behaviors correspond to the relatively reduced silicon content in the two power ends (20 W and 100 W). Indeed, the stoichiometric compositions of the layers are very close, as observed from the FT-IR spectra. The remarkable change occurs in the layers with the highest RF power 100 W, in which the LO mode shows a slight shift to high frequency (at

1036  $\text{cm}^{-1}$  for 40 W to 1048  $\text{cm}^{-1}$  for 100 W) and also relatively increased intensity considering the LO mode Si-N at 1048  $\text{cm}^{-1}$  versus the N-H rocking vibration at about 1185  $\text{cm}^{-1}$ .

#### 6.4.4 Discussion

The difference in the injected charge density and charge collection process obtained by KPFM and FDC results for  $\text{SiN}_x$  samples deposited using different RF power, though small, cannot be fully explained in view of the data obtained by FT-IR and XPS, which leads to the conclusion that the stoichiometric compositions of these films are quite similar [133]. However, it should be mentioned that the hydrogen content in the investigated films in this study was not quantified since the XPS measurement is not sensitive to hydrogen and helium. In addition, there is no report on the dependence of the dielectric charging in  $\text{SiN}_x$  films deposited using different RF power on the hydrogen content.

Increasing the RF power from 20 W to 40 W results in increasing the silicon content in the  $\text{SiN}_x$  film as shown from the variation in N/Si and Si-H/N-H (**Fig. 6.7b**). As explained earlier, increasing the silicon content results in increasing the density of defects and leads to faster charge collection process, and hence smaller decay time constants at the RF power of 40 W. With increasing the power to 60 W, the extra silicon tends to be bonded with a large number of hydrogen induced during gas reaction with more preferred formation of Si-H bonds. However, since higher RF power enhances the energy transfer to both silicon and nitrogen during the reaction, the change in Si-H/N-H ratio is kept relatively small as shown in **Fig. 6.7b**. This explains the relatively small drop in the injected charge density as well as the small reduction in decay time constant for the 60 W as measured by KPFM and FDC. Increasing the deposition power to 80 W results in enhancing the reactivity of silane and ammonia. This results in increasing slightly the nitrogen content in the  $\text{SiN}_x$  films and leads to more passivation by hydrogen as can be seen from **Fig. 6.7a** with the existence of  $=\text{N-H}_2$  around 1534  $\text{cm}^{-1}$ . Yet, this Si-rich  $\text{SiN}_x$  films is still composed of a large number of Si-H bonds, and thus tends to create a dynamic equilibrium between Si-H and N-H with less dangling bonds at almost constant Si-H/N-H as shown from **Fig. 6.7b**. This further results in slightly larger charge redistribution which explains the relatively smaller injected charge density and decay time constant at 80 W as obtained from KPFM and FDC data. **Figure 6.7** highlights that the highest investigated RF power (100 W) facilitates the formation of Si-N bonds with further increased nitrogen and reduced amount of Si-H and N-H bonds in the  $\text{SiN}_x$  films. The dangling bonds and defect density

tend to decrease for these more stoichiometric films, which lead to larger injected charge density as measured by KPFM and FDC. The shorter decay time constant at 100 W is still expected due to the contribution of higher spatial inhomogeneity as a result of the larger deposition rate accompanied with higher RF power.

On the other side, the density and distribution of defects in SiN<sub>x</sub> films is expected to be larger as the deposition RF power increases. Also, the higher the employed RF power is, the higher the deposition rate which possibly results in larger disorder due to higher energy transfer to silicon and nitrogen atoms during the deposition process [135]. The larger density of defects with the increased deposition power indicates that the charge redistribution paths are larger leading to higher redistribution currents. Consequently, this results in faster charge decay as the deposition RF power increases as obtained from KPFM and FDC. The injected charge density was expected to always increase as the RF power increases due to the higher density of defects which exists in SiN<sub>x</sub> films deposited at larger RF power. This has been observed only when the power changes from 20 W to 40 W and then from 80 W to 100 W as concluded from the KPFM (**Fig. 6.5c**) and FDC (**Fig. 6.6a, b**). Changing the RF power from 40 W to 80 W passing through 60 W shows a continuous and relatively small decrease in the injected charge density. The decreasing trend of the injected charge density with increasing the RF power from 40 W to 80 W could be also explained based on the equilibrium between charge injection and redistribution rates as explained in detail in section 6.3.4. Since the charge collection process becomes faster as the RF power increases indicating larger redistribution paths and consequently larger redistribution currents, the charge injection and redistribution equilibrium is attained at smaller surface charge density. This results in decreasing the measured KPFM potential and/or FDC adhesive force with increasing the RF power in this range. The variation in the injected charge density when changing the RF power from 20 W to 40 or from 80 W to 100 W does not follow this rule most probably due to a larger defect density as explained earlier.

**Table 3.2** shows that the LF deposition recipe has a larger RF power (185 W) and SiH<sub>4</sub>/NH<sub>3</sub> ratio ( $r = 1.4$ ) compared to the default HF recipe (20 W,  $r = 0.45$ ). In spite of that, the SiN<sub>x</sub> films deposited using the default HF recipe was found to have a smaller injected charge density and faster discharging process compared to the LF SiN<sub>x</sub> as explained in chapter 5. This should not cause any confusion with the conclusions drawn from sections 6.3 and 6.4 regarding the influence of the SiH<sub>4</sub>/NH<sub>3</sub> ratio or RF power on the charging/discharging processes since the

HF and LF deposition recipes have also a different frequency mode, N<sub>2</sub> gas flow, and pressure which were not investigated in the present study, in addition to the different SiH<sub>4</sub>/NH<sub>3</sub> ratio, and RF power. Furthermore, the HF and LF SiN<sub>x</sub> materials studied in chapter 5 were deposited using the conditions listed in **Table 3.2** which include a simultaneous change in all abovementioned depositions parameters, while in the present study only a single deposition parameter was varied at a time while all other parameters were kept fixed. Thus, no comparison could be made between the results presented in chapter 5 and the present chapter.

## 6.5 Effect of deposition temperature

To study the influence of deposition temperature, SiN<sub>x</sub> films were deposited using different substrate temperatures while the gas ratio (0.45) and RF power (20 W) were kept constant as presented in **Table 6.1**.

### 6.5.1 KPFM results

The KPFM results related to the charging/discharging processes in SiN<sub>x</sub> films deposited using different substrate temperatures is presented in **Fig. 6.8**. The surface potential amplitude, U<sub>s</sub>, distribution, FWHM, and the integral of potential profile slightly decrease with increasing the substrate temperature from 200 °C to 300 °C as shown in **Figs. 6.8a, b and c**, respectively. This indicates that the injected charge density slightly decreases as the substrate temperature increases in this investigated temperature range, and this could be observed for the charges injected under different pulse amplitude, U<sub>p</sub>. Comparing these results with the KPFM data extracted from the SiN<sub>x</sub> samples deposited using different gas ratios (**Fig. 6.2a, b and c**) leads to the conclusion that the influence of the substrate temperature on the charging process is much smaller compared to the effect of the reactive gas ratio. Finally, the difference in the injected charge density between the positive and negative charge injection is quite obvious for the SiN<sub>x</sub> films deposited at 200 °C, while this difference decreases considerably as the deposition temperature increases to 250 °C or 300 °C.

An example of the KPFM surface potential evolution with time for SiN<sub>x</sub> films deposited using different substrate temperatures is shown in **Fig. 6.8d**. It can be seen from the figure that the charge collection process becomes faster as the deposition temperature increases from 200 °C to 300 °C. This is also evident from the decay time constant values calculated from fitting the surface potential decay with Eq. 4.3,  $\exp[-(t/\tau)^\beta]$ , for charges injected using different pulse

amplitudes as shown in **Fig. 6.8e**. No clear trend is found for the stretch factor calculated for this set of samples as a function of the substrate temperature as presented in **Fig. 6.8f**. **Figure 6.8e, f** shows also that for each deposition temperature the decay time constant increases while the stretch factor decreases when the pulse amplitude employed during the charge injection step increases which agrees with the data reported in [117, 135]. Comparing the time constant calculated from KPFM surface potential decay for SiN<sub>x</sub> samples deposited using different gas ratio (**Fig. 6.2e**), RF power (**Fig. 6.5e**), and temperature (**Fig. 6.8e**), it could be concluded that the influence of the substrate temperature on the charge collection process is relatively larger than the effect of the RF power and much smaller compared to the influence of the gas ratio.

### 6.5.2 FDC results

The influence of the substrate temperature employed during the SiN<sub>x</sub> deposition on the charging/discharging processes as extracted from the FDC measurements is presented in **Fig. 6.9**. The measured FDC potential (**Fig. 6.9a**) and adhesive force (**Fig. 6.9b**) slightly decrease when the substrate temperature increases from 200 °C to 300 °C for charges injected using different voltages. The correlation between the FDC measured potential and adhesive force is also obvious from the figures. Moreover, the trend of both FDC potential and adhesive force versus the substrate temperature agree well with the trend of KPFM potential profile integral (**Fig. 6.8c**) indicating a relatively smaller injected charge density as the deposition temperature increases. Comparing the values of the FDC potential and adhesive force measured for SiN<sub>x</sub> samples deposited using different gas ratio (**Fig. 6.3a, b**) and substrate temperature (**Fig. 6.9a, b**) leads to the conclusion that the influence of the substrate temperature on the charging process is relatively small compared to the effect of the gas ratio, which is also concluded from KPFM.

An example of the measured adhesive force decay for SiN<sub>x</sub> films deposited using different substrate temperature is presented in **Fig. 6.9c**. The relaxation process becomes faster as the deposition temperature increases from 200 °C to 300 °C, as shown in the figure. The decay time constant calculated from fitting the adhesive force decay with Eq. 4.4,  $(\exp[-(t/\tau)^\beta])^2$ , for charges injected using different pulse amplitude is presented in **Fig. 6.9d**. The figure also highlights a faster charge collection process as the substrate temperature increases, which agrees well with the results obtained from KPFM measurements. Comparing the decay time constant calculated from adhesive force evolution with time for SiN<sub>x</sub> samples deposited using different gas ratio (**Fig. 6.3c**), RF power (**Fig. 6.6c**), and substrate temperature (**Fig. 6.9c**) leads to the

conclusion that the effect of the substrate temperature on the charge collection process is relatively larger than the effect of the RF power and much smaller compared to the influence of the gas ratio. This is similar to the conclusion drawn from the KPFM measurements.

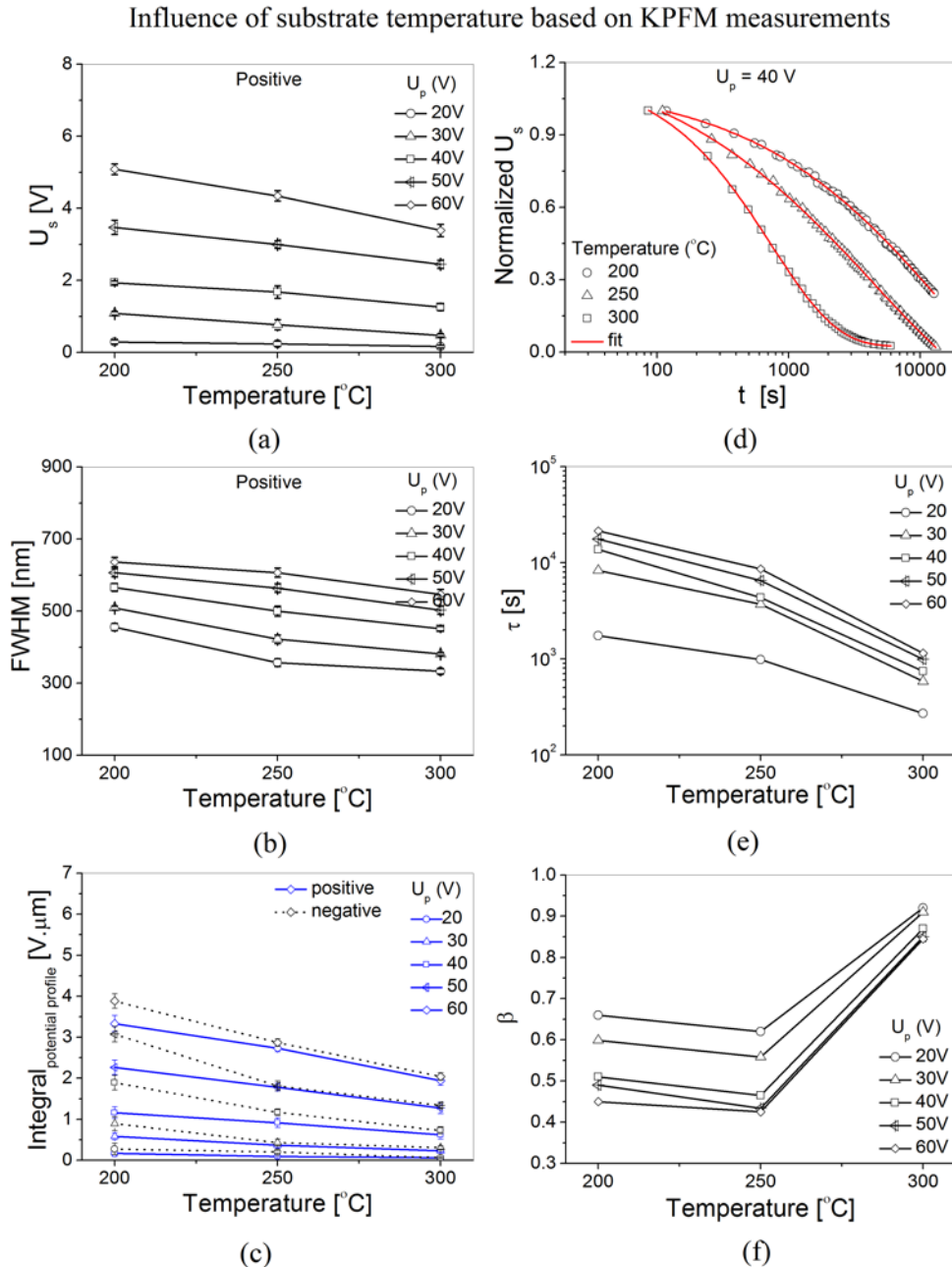


Figure 6.8. The effect of substrate temperature on the charging/discharging processes as extracted from the KPFM measurements for charges which were injected using different  $U_p$ : (a) surface potential amplitude,  $U_s$ , (b) potential distribution, FWHM, (c) potential profile integral for positive and negative charge injection, (d) an example of  $U_s$  decay with time for injected charges using the same  $U_p$ , (e) the decay time constant, and (f) stretch factor.

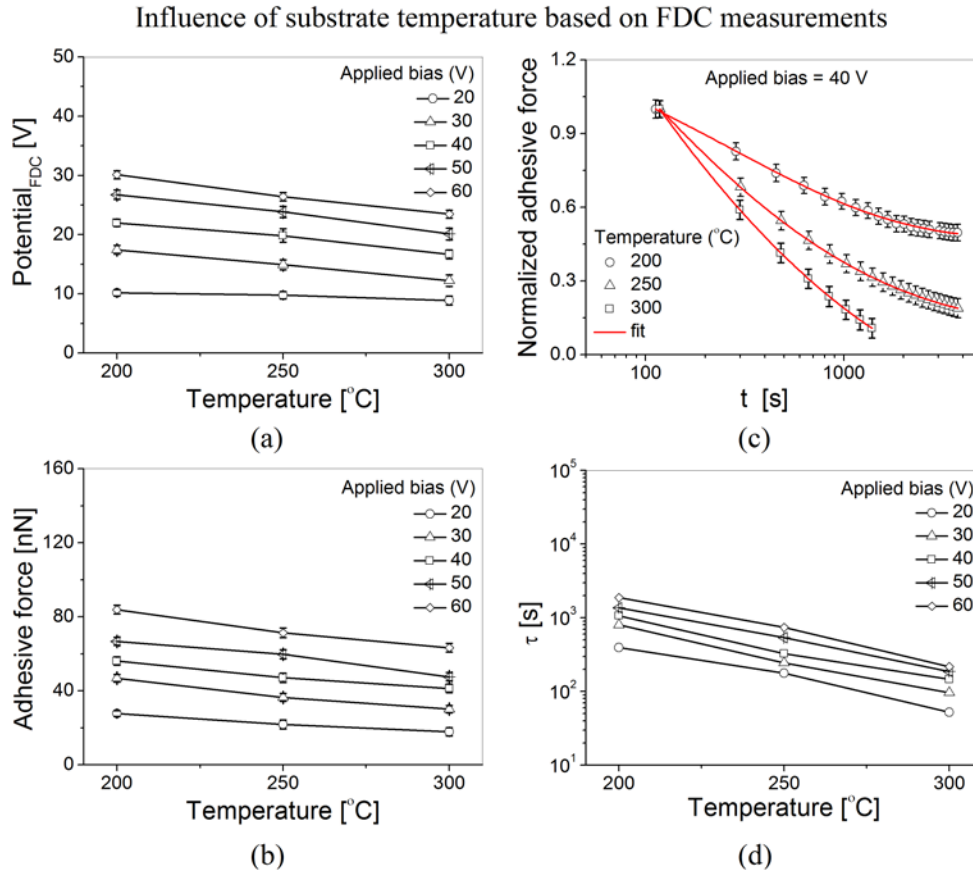


Figure 6.9. The influence of substrate temperature on the charging/discharging processes as measured from the FDC measurements for charges which were injected using different voltage: (a) measured surface potential, (b) adhesive force, (c) an example of adhesive force decay with time for charges injected using the same voltage, and (d) the decay time constant.

### 6.5.3 Influence on material stoichiometry

The FT-IR spectra for  $\text{SiN}_x$  films deposited using different substrate temperatures is shown in **Fig. 6.10a**. Increasing the deposition temperature from 200 °C to 300 °C leads to non-pronounced fall-down of the N/Si atomic ratio (from 0.694 to 0.681) as shown from **Table 6.1** and **Fig. 6.10b**. From the FT-IR spectra, the LO mode of Si-N at  $1027 \text{ cm}^{-1}$  at 250 °C increases to  $1051 \text{ cm}^{-1}$  at 300 °C, and oppositely the N-H rocking vibration becomes weak ( $1188 \text{ cm}^{-1}$  at 250°C,  $1181 \text{ cm}^{-1}$  at 300°C). In this case, the highest deposition temperature demonstrated a similar effect as in  $\text{SiN}_x$  films deposited using the maximum deposition RF power (100 W). The increased deposition temperature tends to reduce the reaction of ammonia, and also reduce the content of hydrogen in all plasma deposited materials, which leads to a more preferred formation of nitrogen and silicon  $\text{N}_x\text{-Si-H}$  bonds ( $x \geq 2$ ). Since the nitrogen is more electronegative than

silicon, the incorporation of nitrogen leads to an increase in the frequency of the absorption peak. Although the shift of N-H stretching vibrations is not conspicuous, it is believed that it is due to the emergence of the  $\text{NH}_2$  asymmetric mode. This becomes evident considering that the  $\text{NH}_2$  bending mode at about  $1539\text{ cm}^{-1}$  disappeared at the highest investigated substrate temperature,  $300\text{ }^\circ\text{C}$ .

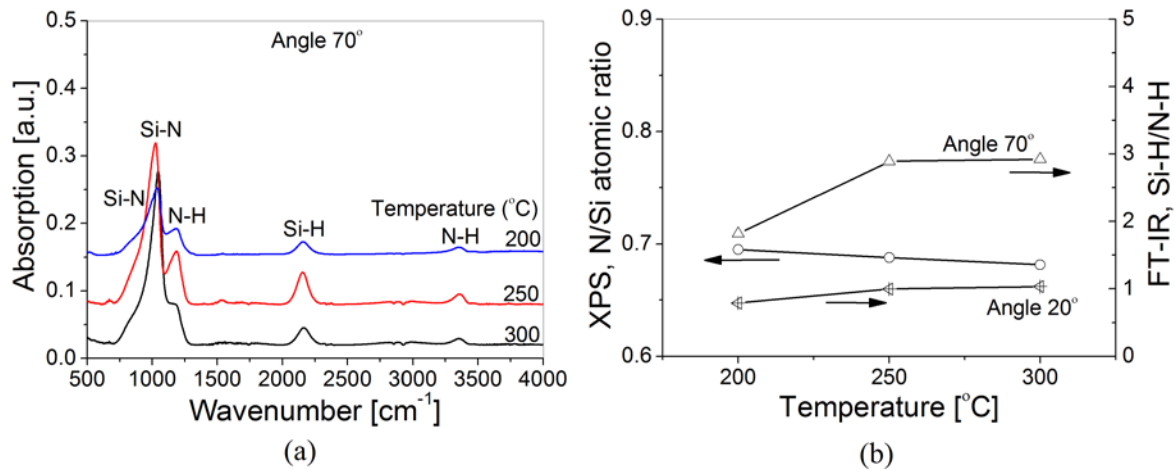


Figure 6.10. FT-IR and XPS data for  $\text{SiN}_x$  films deposited using different substrate temperature: (a) FT-IR spectra for  $\text{SiN}_x$  films deposited using different substrate temperature at an angle of  $70^\circ$ , and (b) N/ Si atomic ratio obtained from XPS analysis and the relative intensity Si-H (around  $2157\text{ cm}^{-1}$  at  $70^\circ$ ,  $2160\text{ cm}^{-1}$  at  $20^\circ$ ) versus N-H (around  $3348\text{ cm}^{-1}$  at  $70^\circ$ ,  $3350\text{ cm}^{-1}$  at  $20^\circ$ ) from FT-IR.

#### 6.5.4 Discussion

From KPFM and FDC measurements, it is concluded that increasing the substrate temperature results in slightly reducing the injected charge density and making the charge collection process relatively faster [133]. This indicates that the charge redistribution may be relatively larger with a higher deposition temperature resulting in attaining equilibrium between the charge injection and redistribution at smaller surface potential amplitude as explained earlier. From the data presented in [80], the measured TSDC current at 300 K for the  $\text{SiN}_x$  deposited at  $200\text{ }^\circ\text{C}$  is slightly larger compared to at  $300\text{ }^\circ\text{C}$ . This agrees with the results obtained from the KPFM and FDC measurements which were performed at room temperature. As seen from the FT-IR and XPS data, increasing the deposition temperature from  $200\text{ }^\circ\text{C}$  to  $300\text{ }^\circ\text{C}$  results in a non-pronounced variation in the N/Si atomic ratio. This also shows a good agreement with the data presented in [80] where the N/Si exhibits a relatively small variation and also does not have a consistent trend versus the deposition temperature in the range from  $200\text{ }^\circ\text{C}$  to  $300\text{ }^\circ\text{C}$ .

The difference between the charging/discharging processes for SiN<sub>x</sub> films deposited using different substrate temperatures could be attributed to several reasons. First, increasing the substrate temperature from 200 °C to 250 °C enhances the Si-H/N-H and slightly increases silicon content of the SiN<sub>x</sub> film (**Fig. 6.10b**). This tends to induce a high density of free charge centers which cause the reduced injected charge density and the faster discharging process as measured by KPFM and FDC. At 300 °C, the silicon content continues to increase. On the other hand, the increased deposition temperature is known to cause desorption of hydrogen in PECVD SiN<sub>x</sub>, which results in reducing the hydrogen content in the film as shown from **Fig. 6.10b**. For example, it was reported that the hydrogen content decreases from 26.88% for SiN<sub>x</sub> films deposited at 200 °C to 11.66% for films deposited at 340 °C [81]. For this reason the possible contribution from hydrogen migration to the dielectric charging in SiN<sub>x</sub> films deposited using different substrate temperatures cannot be overruled. Hydrogen can diffuse in the SiN<sub>x</sub> films, and this results in more induced defects, which may lead to a faster discharging process.

The second reason is attributed to the influence of the dielectric film stress on the material electrical properties, and hence on the dielectric charging. Increasing the deposition temperature results in changing the film stress from compressive stress for films deposited at 100 °C to tensile when the deposition was performed at 300 °C [69]. It was also reported that the residual stress of SiN<sub>x</sub> films increases from 110 MPa to 530 MPa as the SiN<sub>x</sub> film growth temperature increases from 200 °C to 340 °C [81]. The deposition temperature and pressure was also reported to have a considerable effect on the material structure and mechanical properties of deposited thin films [141, 142]. The third reason could be attributed to the difference in trap concentrations between the SiN<sub>x</sub> samples deposited at different temperatures [80]. Here, it should be emphasized that presently there is no report on the dependence of the SiN<sub>x</sub> charge trap concentration and properties on the material stoichiometry and bandgap. Finally, increasing the deposition temperature results in reducing the SiN<sub>x</sub> film conductivity as reported in [81] because hydrogen is known for its chemical reactivity creating Si–H bonds rather than N–H bonds [36]. This is expected also to affect the charging injection as well as the discharging process. Many of these hypotheses require further investigation in order to fully understand the influence of the deposition temperature on the dielectric charging.

All investigated SiN<sub>x</sub> films in this study indicates that there is a high concentration of Si-H and N-H bonds. This further indicates that there is a high concentration of silicon matrix that is

not bound to nitrogen, which can in principle give rise to silicon cluster nucleation. This is in agreement with the results discussed above which show that the investigated  $\text{SiN}_x$  films in this study are all silicon-rich with N/Si ratio much smaller than the stoichiometric one (1.33). Changing the gas ratio has a much stronger effect on the material composition and structural properties, and consequently on the electrical properties on  $\text{SiN}_x$  films, compared to the effect of RF power and substrate temperature. Comparing the  $\text{SiN}_x$  layers deposited with variable RF power and substrate temperature at the same gas ratio ( $r = 0.45$ ), it is evident that their compositions remain almost in the same domain ( $\text{N/Si} \approx 0.7$ ). Further investigation is currently in progress for the  $\text{SiN}_x$  films deposited with the extreme deposition parameters (RF power 100 W, substrate temperature 300 °C) which have a microscopic structural change.

The characterization results obtained from KPFM (on the scale of a single asperity) and FDC (which includes the meniscus effect) reveal a very good agreement regarding the influence of the deposition gas ratio, RF power, and substrate temperature. Actually, this is not surprising since the meniscus force, which is considered the main difference between the FDC-based characterization and KPFM, is minimized in the FDC experiments. This was done through dehydrating the  $\text{SiN}_x$  samples, and then by performing the FDC experiments at relatively low humidity [143].

In electrostatic MEMS/NEMS switches, the reliability is usually determined from the shift in the device C-V characteristics which is controlled by the injected charge density in the dielectric film during the down-state. In addition, the relaxation time constant of the trapped charges during the up-state determines the performance degradation of the switch on the long term. Thus, both the injected charge density and the relaxation time determines the switch lifetime. The optimum dielectric material for electrostatic MEMS/NEMS devices that have minimal charging is the one with smallest injected charge density and fastest discharging process. Based on this study, this corresponds to the  $\text{SiN}_x$  films deposited using the highest gas ratio ( $r = 0.8$ ) which is expected to result in a smaller shift in the C-V characteristics and a faster recovery of the injected charge compared to other investigated dielectric materials. It becomes visible now to propose a figure of merit for MEMS dielectrics based on injected charge density and the relaxation time determined from the KPFM or FDC measurements.

## **6.6 Summary**

The influence of PECVD deposition conditions on the dielectric charging in SiN<sub>x</sub> films was investigated. Numerous SiN<sub>x</sub> films were deposited using different recipes including variable silane/ammonia ratio, RF power, and substrate temperature. The charging/discharging processes in bare SiN<sub>x</sub> films were studied using the KPFM-TF and FDC-TF methods. Furthermore, FT-IR and XPS characterization were used to determine the chemical bonds and compositions, respectively of the investigated dielectric films. The key conclusions from this chapter are the following:

- KPFM and FDC lead to similar conclusions regarding the charging/discharging processes in SiN<sub>x</sub> films deposited using different gas ratio, RF power, and temperature.
- For all SiN<sub>x</sub> films, the KPFM surface potential decay follows the stretched exponential law, while the FDC adhesive force decay fits with the square of the stretched exponential law.
- Increasing the SiH<sub>4</sub>/NH<sub>3</sub> ratio results in a considerable decrease in the injected charge density and the decay time constant (attributed to increasing the Si content in SiN<sub>x</sub> films as revealed from FT-IR and XPS).
- Increasing the Si content results in higher leakage current, concentration of defects, and number of charge trapping centers (charge redistribution paths increase, the equilibrium of charge injection/redistribution is attained at smaller surface charge density).
- Varying the RF power has a small impact on the charging/discharging processes (agrees with FT-IR and XPS data which show similar SiN<sub>x</sub> stoichiometry for different RF power).
- Increasing the RF power leads to higher density and distribution of defects in SiN<sub>x</sub> films (results in higher redistribution currents and relatively faster charge decay).
- Increasing the substrate temperature results in relatively smaller injected charge density and faster discharging process (though FT-IR and XPS show little change in the material stoichiometry content).
- Higher deposition temperature leads to relatively larger charge redistribution paths (attributed to reducing the hydrogen content, changing trap concentrations, increasing the film stress, and reducing the film conductivity).
- The influence of gas ratio on the charging/discharging process is much larger compared to the effect of substrate temperature and RF power (agree with FT-IR and XPS data).

Considering the lack of available information on the dependence of SiN<sub>x</sub> charge trap concentration and electrical properties on the material stoichiometry and its relation to the dielectric deposition conditions, this work could help to determine which dielectric is more robust for electrostatic MEMS/NEMS devices with better reliability.

*The superiority of the learned man over the devout worshipper is like that of the full moon to the rest of the stars (i.e., in brightness). The learned are the heirs of the Prophets who bequeath neither dinar nor dirham (i.e., money) but only that of knowledge; and he who acquires it, has in fact acquired an abundant portion.*

*Prophet Muhammad (PBUH)*

## **7 The influence of environment medium, relative humidity, and contaminants on charging/discharging processes**

### **7.1 Introduction**

The impact of the environment medium and relative humidity on the dielectric charging/discharging processes in electrostatic MEMS/NEMS devices has not been entirely understood as explained in chapter 2. Most reported work targeting this issue was performed using the conventional characterization techniques of actual MEMS devices which suffer from serious limitations and don not allow deeper investigation as mentioned in chapter 2. Therefore, a complementary study on the nanoscale becomes essential. This chapter presents the influence of the environment gases, relative humidity, and, for the first time, the environment level of purification on the charging/discharging processes in PECVD SiN<sub>x</sub> films. The assessment was performed on the nanoscale using the KPFM-TF characterization method described in chapter 3.

The chapter is organized as follows. First, the used SiN<sub>x</sub> samples and the measurement conditions are described. Then, the impact of the relative humidity on KPFM measurement accuracy is investigated to validate the employed experiments. This is followed by discussing the charging/discharging processes in air and nitrogen under different humidity levels. Finally, the impact of environment level of purification is explained.

### **7.2 Experimental**

The investigated samples consist of HF PECVD SiN<sub>x</sub> films with 200 nm thickness deposited over Au/Ti (200 nm/50 nm) layers, which were evaporated over Si substrates. A

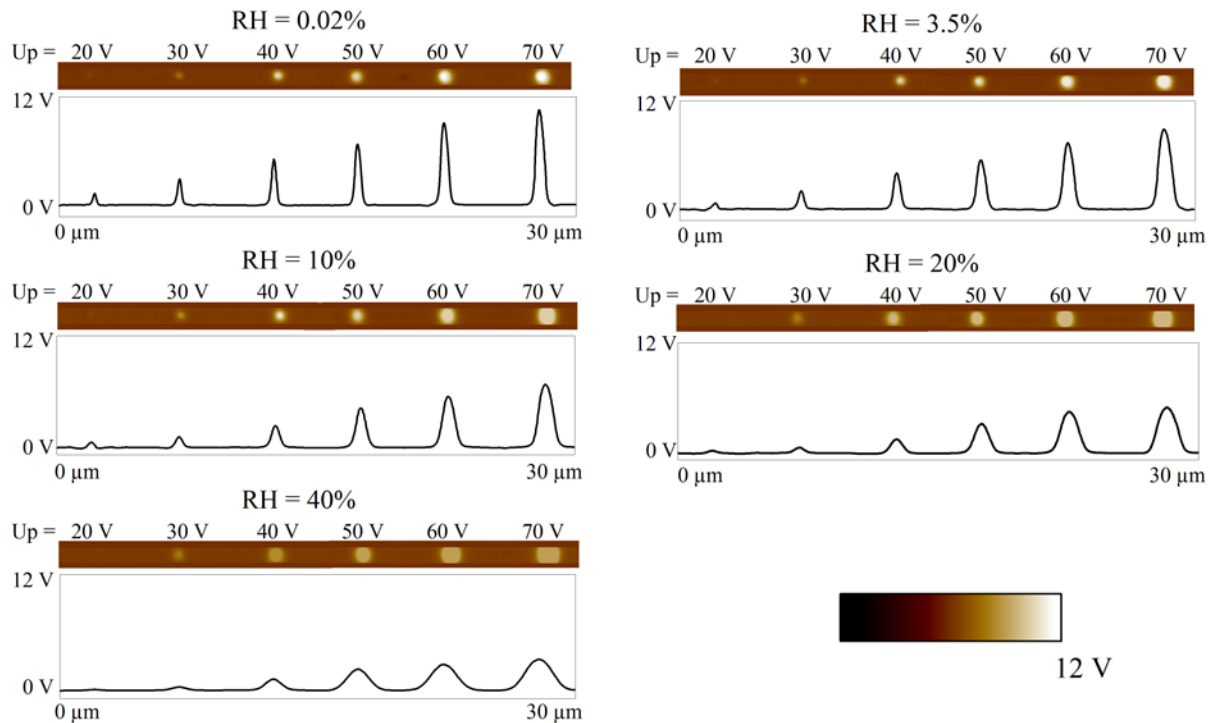
generic layer structure of the investigated samples (HF-Evap Au) is shown in **Fig. 3.2b**, and the details of each layer are presented in **Table 3.1**. The SiN<sub>x</sub> films were deposited using the standard HF recipe (see **Table 3.2**) in different PECVD runs from other SiN<sub>x</sub> films employed in previous chapters with almost one year difference in the deposition dates. The charging/discharging processes were assessed using the KPFM-TF method explained in chapter 3 which allows studying the induced surface potential distribution with high lateral resolution. Charges were injected in separate points over the SiN<sub>x</sub> films by applying voltage pulses of defined amplitude,  $U_p$ , and duration,  $T_p$ , to the AFM tip in tapping mode (**Fig. 3.4b**). The pulse duration,  $T_p$ , was fixed to 1 s while the pulse amplitude,  $U_p$ , was varied from 20 V to 70 V with a 10 V step. After completing the charge injection step, the discharging process was studied through monitoring the decay of the induced surface potential for 3.5 hours. For all experiments, the time interval between the end of charge injection step and the beginning of the KPFM measurements was fixed to be 30 s.

The environment control system used for these experiments is shown in **Fig. 3.11**. The influence of three different environmental parameters on the dielectric charging was investigated. First, the effect of the environment medium was explored through measuring the induced surface potential under both air and nitrogen environments. Second, the influence of relative humidity was investigated through performing the KPFM experiments under different relative humidity levels (0.02%, 3.5%, 10%, 20% and 40% RH) for both air and nitrogen environments. Finally, the impact of the environment level of purification was studied through engaging two gas purifiers: a hydrocarbon trap and an oxygen filter. Before each KPFM experiment, both the SiN<sub>x</sub> sample and the AFM tip went through two cycles of heating (150 °C) and cooling steps under vacuum in order to reduce the effect of the adsorbed water film over the surfaces of the tip and the sample on the KPFM potential measurements.

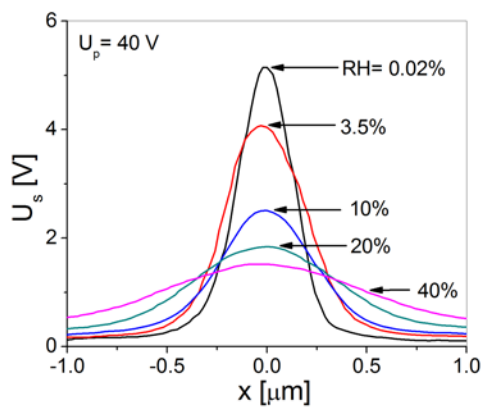
### **7.3 Impact of relative humidity on KPFM measurement accuracy**

An example of the KPFM-TF surface potential maps measured under different relative humidity levels for different pulse amplitude,  $U_p$  in air is presented in **Fig. 7.1a**. Also, the corresponding surface potential profiles for  $U_p = 40$  V are shown in **Fig. 7.1b**. It is obvious from the figures that as relative humidity increases for a given  $U_p$ , the potential distribution becomes less confined (FWHM increases) while the measured potential peak amplitude,  $U_s$ , decreases. When KPFM experiments are performed under different relative humidity levels, two factors

could affect the measured surface potential. First, the relative humidity inside the AFM chamber may influence the electrostatic force between the AFM tip and the sample surface, resulting in changing the measured surface potential. Second, the adsorbed water layer which exists over the dielectric surface and/or the AFM tip at higher humidity levels could shield the KPFM surface potential as reported in [78]. In order to investigate the impact of these two effects on our measurements a complete set of experiments were performed.



(a)



(b)

Figure 7.1. (a) KPFM surface potential maps measured in air under different relative humidity levels, and (b) the corresponding potential profiles for  $U_p = 40$  V.

**Figure 7.2** shows the results obtained from the first part of the abovementioned experiments which consists of three consecutive steps designated A, B, and C. First a low relative humidity level (3.5%) was employed inside the AFM chamber in order to start step A of the experiment where charges were injected using three different pulse amplitudes  $U_p$ ; 30 V, 40 V, and 50 V. Then, the  $U_s$  and FWHM of the induced surface potential profile monitored with time were analyzed. Next, the relative humidity was increased to 20% in order to start step B. In this step the monitoring of the evolution of both  $U_s$  and FWHM resulting from the charge injection in step A is resumed. After that, the humidity was adjusted to the level employed in step A (3.5% RH). Step C is then executed where the measurements of the surface potential resulting from the charge injection in step A is resumed.

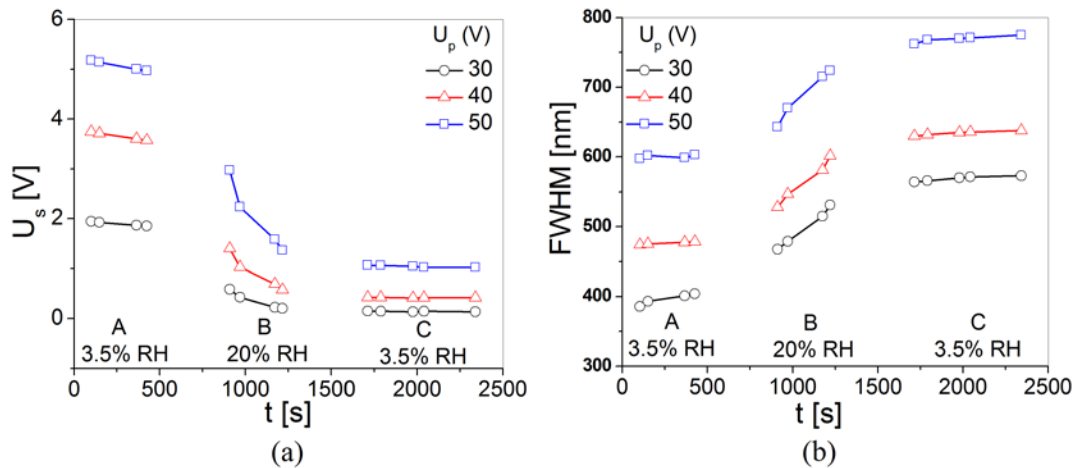


Figure 7.2. The surface potential amplitude  $U_s$  (a) and distribution FWHM (b) measured under a designed sequence of relative humidity levels.

Comparing the evolution of  $U_s$  and FWHM in **Fig. 7.2** for steps A and B, two remarks could be made. First, as the relative humidity increases the measured potential amplitude,  $U_s$ , decreases abruptly while the lateral spreading of surface potential, FWHM, increases remarkably. Second, the measured rate of  $U_s$  decrease or FWHM increase is increased considerably as the relative humidity increases. This has been observed for the measured surface potential from the three investigated pulse amplitudes,  $U_p$ . The measured  $U_s$  and FWHM at step C do not return to their original values measured at the end of step A. Besides, the rate of  $U_s$  decrease or FWHM increase is reduced again to comparable values of the rates observed in step A. This can lead us to the conclusion that our KPFM measurements are not affected by the

relative humidity inside the AFM chamber and the measured  $U_s$  and FWHM represent the real surface potential of the dielectric film.

The second part of the experiments targets the impact of the adsorbed water layer on the dielectric surface and/or the AFM tip at higher humidity levels. An external square wave ( $1 V_{\text{ptp}}$ ) was applied to the AFM chuck which was connected to the bottom Au layer over which the  $\text{SiN}_x$  film was deposited. Then, the surface potential was measured over the dielectric surface under two different relative humidity levels which are 0.02% and 40%, and using two different samples. Then, for the 40% measurement the  $\text{SiN}_x$  sample was stored inside the AFM chamber under 40% RH for 5 hours, longer than the observation time window (3.5 hours). The results show that the measured KPFM surface potential for both samples is the same and as the amplitude of the applied external pulse. This result indicates that the surface potential shielding by the adsorbed water layer reported in [78] does not exist, at least in our KPFM measurements. This may be attributed to a small thickness of the adsorbed water layer due to the surface properties of the  $\text{SiN}_x$  sample and/or the AFM tip or due to the limited storage time at higher humidity.

#### **7.4 Air versus nitrogen under different relative humidity levels**

In this section, the impact of the environment gases, mainly air and nitrogen will be presented. For both environments, charges were injected using different pulse amplitudes,  $U_p$ , and the induced surface potential was measured under different relative humidity levels. In the first two subsections, the charging process is discussed based on the  $U_s$  and FWHM values measured directly after the charging step. This is followed by presenting the evolution of both  $U_s$  and FWHM with time, which represent the discharging process.

##### *7.4.1 Surface potential distribution (FWHM)*

The measured FWHM as a function of the relative humidity for air and nitrogen environments is shown in **Fig. 7.3a, b**, respectively. The FWHM increases with the relative humidity for both air and nitrogen environments and for charges injected under different  $U_p$ . The figures also highlight that the rate of increase in FWHM with  $U_p$  is more pronounced at higher relative humidity levels, especially in the nitrogen environment. The data dispersion in the measured FWHM is found to increase with relative humidity due to increasing the adsorbed water layer from both surfaces of the sample and the AFM tip at larger humidity levels. This is in

agreement with previous studies [79] where the reproducibility of KPFM signals was considerably improved by the thermal treatment of the samples and its associated removal of the adsorbed water film. The difference between the measured FWHM in air and in nitrogen under different relative humidity levels is shown in **Fig. 7.3c**. It is evident that the surface potential distribution is more confined (smaller FWHM) in nitrogen than in air at different relative humidity. Finally, the reproducibility of the measured FWHM is found to be better in nitrogen compared to air for a given humidity and  $U_p$ .

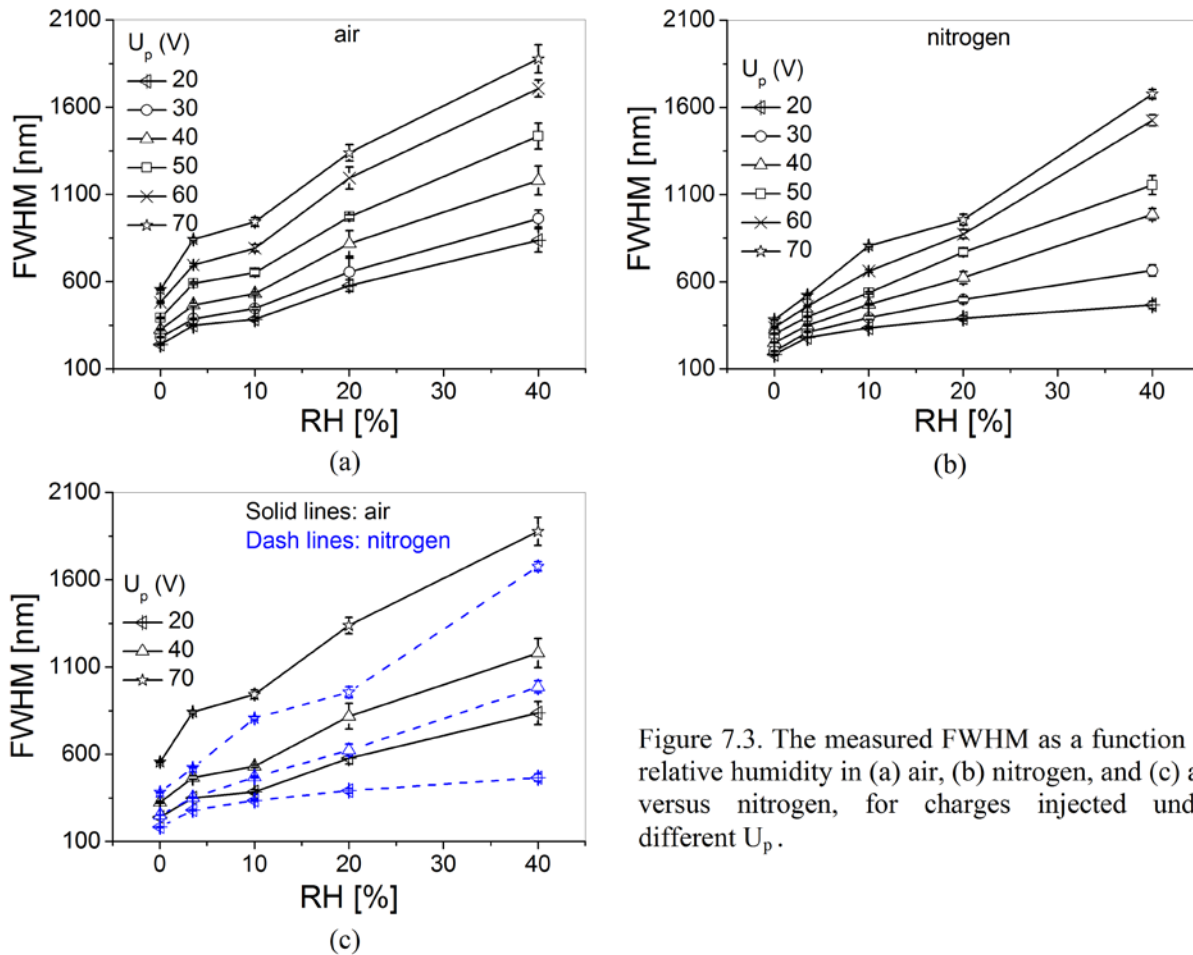


Figure 7.3. The measured FWHM as a function of relative humidity in (a) air, (b) nitrogen, and (c) air versus nitrogen, for charges injected under different  $U_p$ .

The impact of the relative humidity on the surface potential distribution can be directly related to the difference in conductivity of the adsorbed water film, hence the amount of the surface charge which exists on the dielectric surface as the humidity changes [144]. Ellipsometry measurements showed that at room temperature the adsorbed water layer thickness on a mica substrate could increase up to 2 nm in the relative humidity range between 80% and 100% [145].

Furthermore, the measured surface potential distribution follows the electric field distribution which exists between the AFM tip and the SiN<sub>x</sub> surface during the charging step. As reported in [146], the distribution of the electric field just under the tip becomes less concentrated as the adsorbed water increases at higher humidity levels. Therefore, the induced surface potential is expected to follow the less confined electric field distribution which exists at higher relative humidity levels resulting in larger FWHM values. Another contribution could be attributed to the expansion of the apparent AFM tip curvature radius by the adsorbed water layer during the charge injection step at higher relative humidity levels [78, 79].

The FWHM values alone cannot provide a complete view of the injected charge density in the dielectric film and must be integrated with the measured surface potential amplitude,  $U_s$ , which is presented in the following subsection.

#### 7.4.2 *Surface potential amplitude ( $U_s$ )*

The surface potential amplitude,  $U_s$ , measured under different relative humidity levels in air and in nitrogen is shown in **Fig. 7.4a, b**, respectively. For both environments, the measured  $U_s$  decreases with increasing the relative humidity, and this could be observed for charges injected using different  $U_p$ . Similar to what has been observed for the FWHM data, the reproducibility of  $U_s$  is improved for smaller humidity levels in both air and nitrogen environments.

The decrease in the measured  $U_s$  as the relative humidity increases can be explained as follows. During the charge injection step, the electric field distribution between the AFM tip and the SiN<sub>x</sub> surface becomes less confined as the adsorbed water layer increases, when employing higher relative humidity levels as explained in the previous subsection. This might correspond to smaller electric field intensities with increasing the relative humidity level. Since the injected charge density, and hence the induced surface potential  $U_s$ , is proportional to the applied electric field intensity, it becomes obvious that smaller potential amplitude  $U_s$  will be induced as the relative humidity increases. These results are in agreement with the KPFM measurements for mica substrates reported in [145]. In addition, the adsorbed water layer features a high dielectric constant. This causes the apparent distance between the AFM tip and the sample surface to be smaller than the actual distance, and in consequence, increasing the capacitance between the tip and the sample surface. From Eq. 3.1, the increase of the capacitance results further in increasing

the  $\partial C/\partial z$  term which in turn leads to increasing the main electrostatic force component,  $F_{\omega}$ , resulting in measuring larger surface potential,  $U_s$ . Since the measured  $U_s$  decreases with the relative humidity, it is concluded that the increase in the capacitance value due to the adsorbed water layer is less effective than the less confined electric field distribution which exists during the charge injection step. Another reason could be attributed to the difference in charge relaxation time when changing the relative humidity. After the charge injection step, the charged area is scanned, and then the peak  $U_s$  is located normally at the centre of the resulting KPFM map. As will be mentioned in the next subsection, the decay of the surface potential becomes faster as relative humidity increases. Thus, the time required to reach the centre of the charged area (around 100 s) will feature larger decay at higher humidity, resulting in measuring a smaller surface potential.

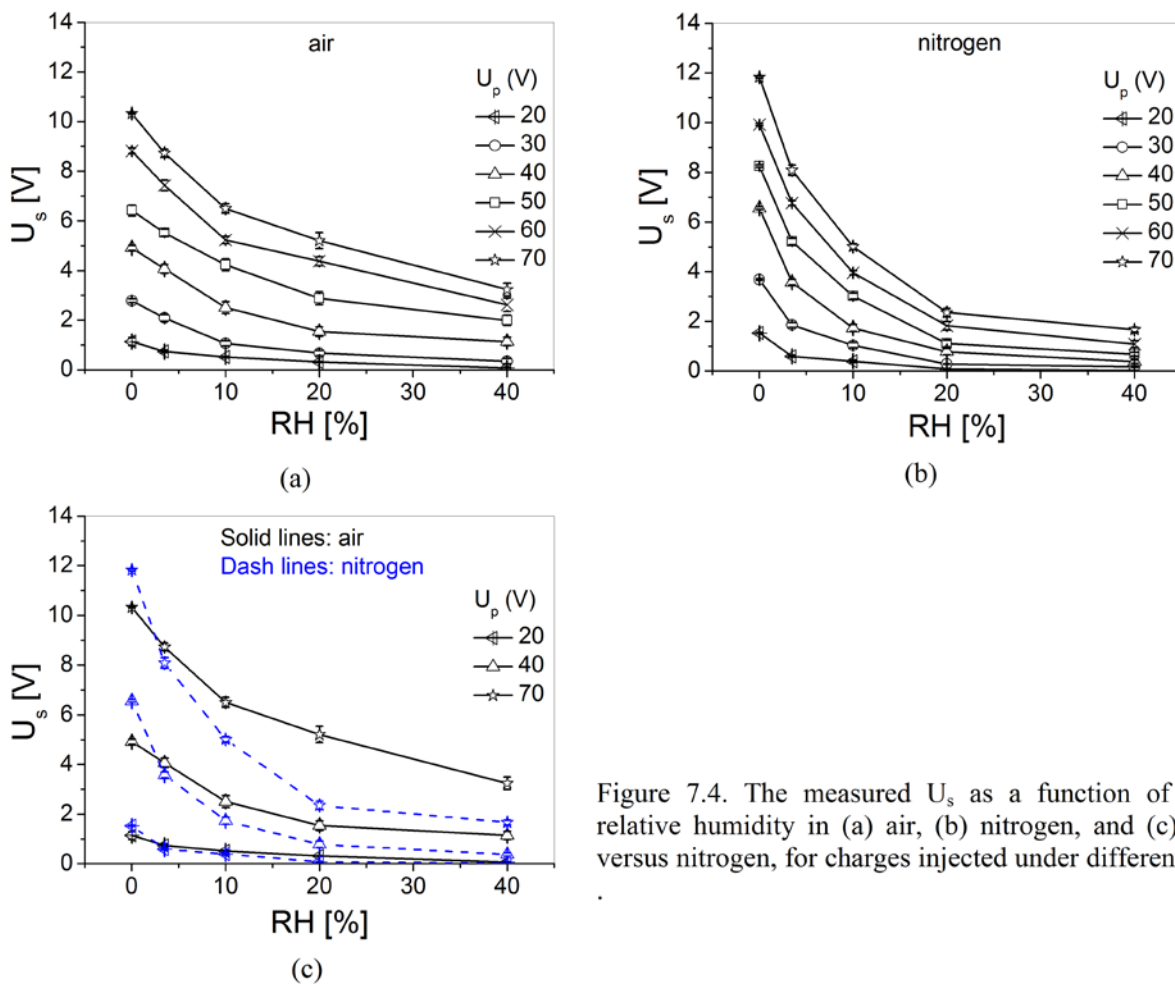


Figure 7.4. The measured  $U_s$  as a function of the relative humidity in (a) air, (b) nitrogen, and (c) air versus nitrogen, for charges injected under different  $U_p$

Since increasing the relative humidity results in reducing the potential amplitude,  $U_s$  (**Fig. 7.4**) and increasing the FWHM (**Fig. 7.3**), area integration was performed for the induced surface potential profiles in order to estimate the impact of humidity on the injected charge density [147]. The results are plotted in **Fig. 7.5** and highlight that the potential integral, consequently the injected charge density inside the  $\text{SiN}_x$  film, increases remarkably with the relative humidity. This could be observed for charges injected under different  $U_p$  in both air and nitrogen environments. The line fitting of the potential integral versus the relative humidity shows that the slope of increase in the injected charge density with humidity is independent of the applied pulse amplitude,  $U_p$ .

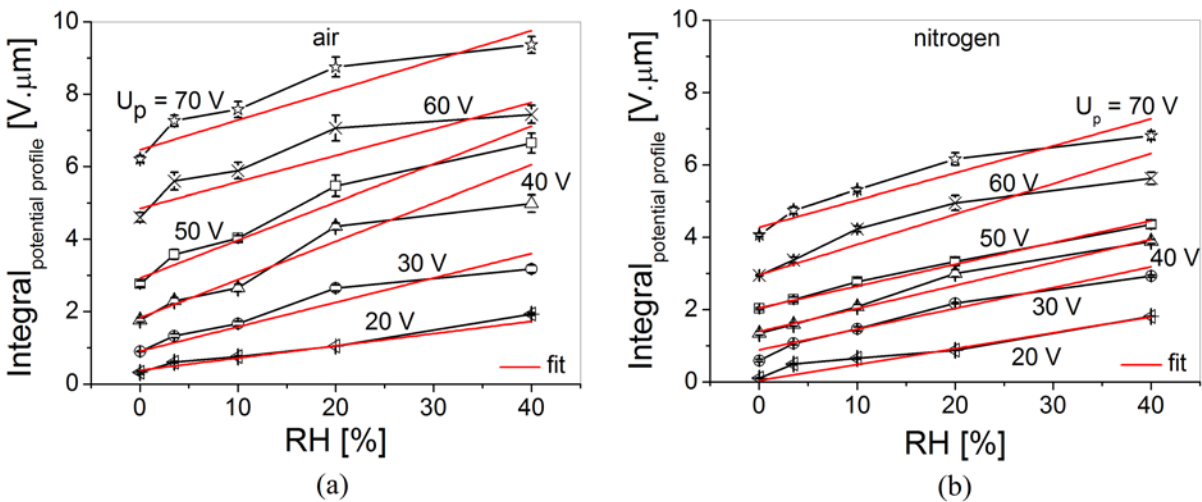


Figure 7.5. The potential profile integral as a function of the relative humidity in (a) air, (b) nitrogen, for charges injected under different  $U_p$ .

A comparison between the surface potential,  $U_s$ , measured in air and in nitrogen under different relative humidity is presented in **Fig. 7.4c**. Excluding the 0.02% RH, the measured  $U_s$  is smaller in nitrogen compared to air for all other relative humidity levels and for all applied  $U_p$ . Moreover, the difference between the measured  $U_s$  in air and in nitrogen increases with the applied pulse amplitude,  $U_p$ . It could be observed also that the reproducibility of the measured  $U_s$  is better in nitrogen than in air under all applied  $U_p$  and for all relative humidity levels, as has been found for the FWHM parameter. Recalling from **Fig. 7.3c** that smaller FWHM is measured in nitrogen than in air for all investigated humidity levels, it becomes clear that the injected charge density is smaller in nitrogen than in air for the same pulse amplitude,  $U_p$ , and relative

humidity level. This is evident from the comparison between the potential profile integral of air (**Fig. 7.5a**) and nitrogen (**Fig. 7.5b**) including the results of 0.02% RH.

The difference between the injected charge density in air and nitrogen might be attributed to the difference in charging due to gas discharge between the AFM tip and the underlying electrode through the  $\text{SiN}_x$  film. According to Wibbeler et al. [19], gas discharges in the capacitive air gap of silicon cantilever actuators were observed although their electrodes were covered with a PECVD  $\text{SiO}_2/\text{Si}_3\text{N}_4$ . Thus, when a discharge occurs in the gap between the AFM tip and the dielectric surface, an avalanche of free electrons and ions is generated. They traverse the gap and are stopped and neutralized by charge exchange at the dielectric surface instead of reaching the underlying electrode resulting in accumulation of the generated free electrons and ions at the dielectric surface. The gas discharge phenomenon was reported to depend on the gap environment [148]. Gas discharge measurements performed in air and nitrogen at atmospheric pressure indicate that the Paschen's law is not applicable at an electrode gap spacing smaller than  $4 \mu\text{m}$  [149]. Moreover, the difference between air and nitrogen gas discharge has not been investigated in a gap below  $0.5 \mu\text{m}$ . A typical example of this small gap is a MEMS switch with the movable electrode in the down position is in contact with the dielectric layer, which is simulated in our study by the AFM tip which comes almost in contact with the  $\text{SiN}_x$  surface during the charging step.

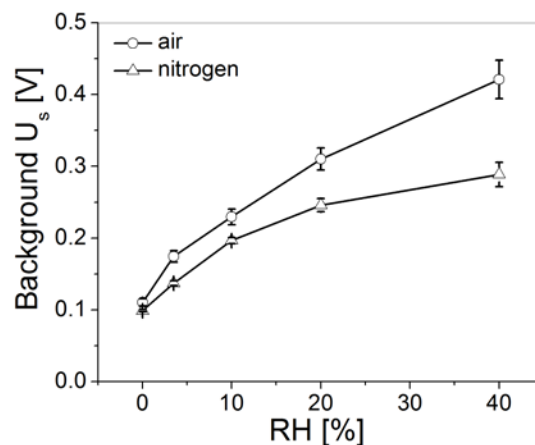


Figure 7.6. The measured background surface potential as a function of relative humidity in air and nitrogen environments.

Furthermore, the measured background surface potential (the potential in areas where no charge was injected) is found to increase with the relative humidity in both air and nitrogen environments as shown in **Fig. 7.6**. This agrees with the previously reported KPFM measurements in air for InAs thin films [79] and further indicates that surface charges increase with increasing relative humidity level. This is attributed to the polarization in the adsorbed water layer which cancels the DC bias applied between the sample and the AFM tip. The figure also highlights that the background potential in air is larger than in nitrogen under all investigated relative humidity. Finally, for nitrogen the background potential starts to saturate at 40% RH while in air the measured potential tends to increase.

Based on the presented KPFM measurements related to the charging process, a nitrogen environment and a smaller relative humidity are more favorable in order to reduce the dielectric charging process. These results agree well with the reported results for electrostatic capacitive MEMS switches. However, the discharging process must be explored as well in order to draw a concrete conclusion, and this is the goal of the following two subsections.

#### 7.4.3 *Surface potential decay*

The evolution of the measured surface potential amplitude,  $U_s$ , with time under different relative humidity in air and nitrogen environments is discussed in this subsection. **Figure 7.7** presents selected potential decay data obtained in air (left) and in nitrogen (right) at three different humidity levels; 0.02%, 10%, and 40%. The surface potential evolution was observed for around 3.5 hours under all investigated humidity levels except for the 40% RH, which was observed for approximately 30 minutes only. This is because the surface potential decays very fast at this high humidity level, and the measured  $U_s$  reaches less than 85% of its initial value after around 30 min in both air and nitrogen environments as could be seen from the figure.

The surface potential decay follows the stretched exponential law (Eq. 4.3),  $\exp[-(t/\tau)^\beta]$ , as presented in previous chapters. This has been observed for charges injected using different  $U_p$ , under all investigated relative humidity levels, and for both air and nitrogen environments as shown in **Fig. 7.7**. For different  $U_p$ , the tails of the potential curves become closer with time indicating that the charge gradient decreases and tends to be equal in the long time range due to the discharging process. As the relative humidity increases, the potential curves' tails become closer with time too, and this is more obvious in nitrogen than in air. Basically, the larger relative

humidity levels overwhelm the impact of  $U_p$ , and this becomes more pronounced in the long time range due to the charge collection process. Finally, for the same relative humidity and  $U_p$ , the measured  $U_s$  for nitrogen at the end of the observation time window is found to be always smaller than the corresponding value in measured air.

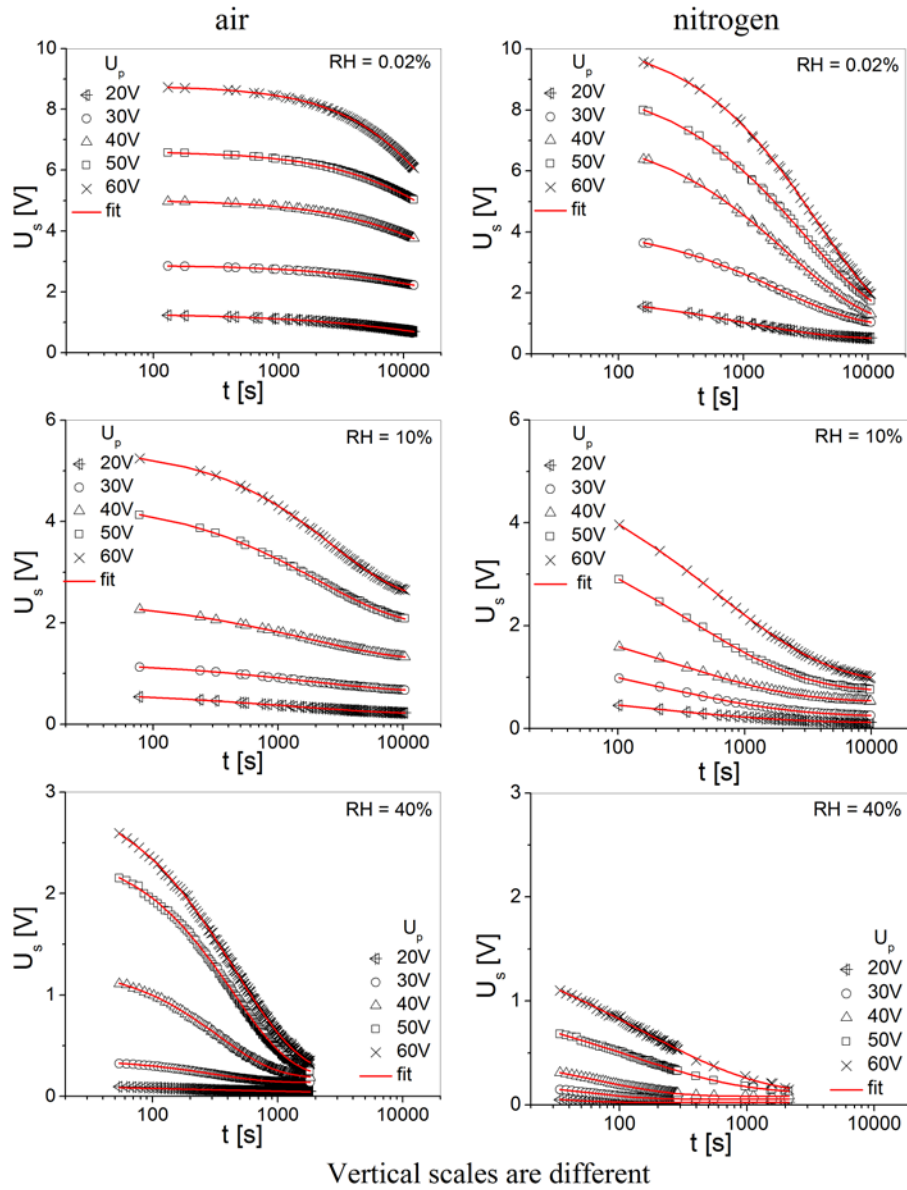


Figure 7.7. Surface potential decay with time measured in air (left) and nitrogen (right) under selected relative humidity levels for charges injected using different  $U_p$ .

The decay time constants,  $\tau$ , and stretch factors,  $\beta$ , calculated from fitting the surface potential decay with Eq. 4.3 is plotted as a function of the relative humidity in **Fig. 7.8**. The

decay time constant  $\tau$  decreases with the relative humidity indicating that injected charges decay faster as the humidity increases as shown in **Fig. 7.8a**. This could be observed for both air and nitrogen environments and for charges which were injected under different  $U_p$ . There are several reasons for charge decay, which are usually classified into two main groups: internal and external decay. The internal decay takes place through tunneling towards the injecting metal electrodes and further through transport and diffusion [128]. The external decay is due to the neutralization of surface charges, which can be caused by the adsorption of counterions from the surrounding medium or by charge loss due to its electrical conductivity. In the case of air and nitrogen environments the amount of available counterions and the electrical conductivity of the medium are both influenced by the relative humidity. Since the internal charge decay is not affected by a change of the environmental conditions, the observed decrease in  $\tau$  with increasing the relative humidity in both air and nitrogen is attributed mainly to the surface charge decay. As the relative humidity increases, the surface charge decays faster for two reasons. The first reason is the faster neutralization of surface charges with the external medium. Second, as humidity increases, the thickness of adsorbed water film over the  $\text{SiN}_x$  surface increases too, resulting in a faster charge loss due to the larger conductivity of the water film. On the other hand, **Fig. 7.8a** highlights that  $\tau$  increases with increasing  $U_p$ . This could be observed for all humidity levels and in air and nitrogen environments and is attributed to combined contribution of the Poole-Frenkel and Trap Assisted Tunneling effects as explained in chapter 5.

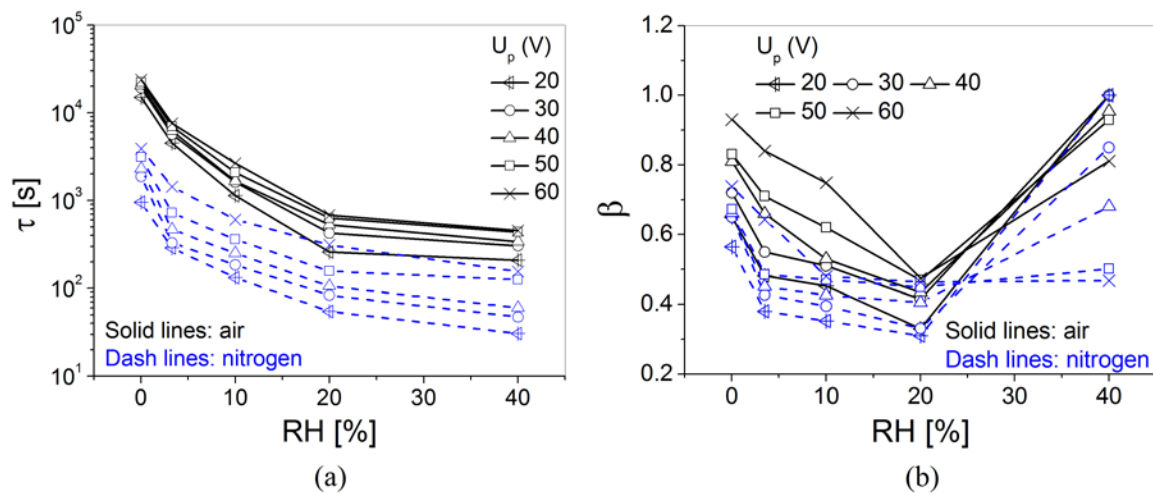


Figure 7.8. (a) The decay time constants,  $\tau$ , and (b) stretch factors,  $\beta$ , calculated from  $U_s$  decay with time in air and nitrogen environments under different relative humidity levels.

**Figure 7.8b** shows that for both air and nitrogen environments the stretch factor,  $\beta$ , decreases with increasing the relative humidity except for the 40% RH. This inconsistency in  $\beta$  values for the 40% RH measurements has been observed even after repeating the KPFM experiment at 40% RH several times in both air and nitrogen environments. As explained in chapter 3, the surface potential decay data is extracted from multiple KPFM potential maps which results from a continuous scanning of the charged areas with time. However, the potential decay is very fast at 40% RH, and the measured potential reaches less than 15% of its initial value for both air and nitrogen after 30 min only. Therefore, the area scanning was not possible at this high humidity level since it leads to an insufficient number of data points which increases the data fitting error. Instead, a continuous line scanning with time was performed at the center of charged positions. Such type of scanning is exposed to x and y drift observed for commercial AFM instruments. Therefore, the results obtained at 40% RH have less accuracy compared to the measurements performed at other smaller humidity levels.

On the other hand, the value of the stretch factor,  $\beta$ , was expected to decrease with increasing  $U_p$  as obtained from the KPFM and C/DCT measurements presented in previous chapters. However, **Fig. 7.8b** shows that the trend of  $\beta$  versus  $U_p$  in air and nitrogen is the opposite of what was expected for all relative humidity levels except for the 40% RH (the one with less accuracy). It has been observed also from the adhesive force decay data measured using the FDC technique and presented in chapter 4 that there is no consistent trend for  $\beta$  versus the applied electric field used during the charging step. This indicates that the increase of  $\beta$  with  $U_p$  observed for the KPFM experiments in the present chapter or the inconsistent trend of  $\beta$  found from the FDC measurements either have no microscopic meaning or cannot be directly linked to the discharging mechanism. Although the values of stretch factors  $\beta$  could sometimes provide important information about the involved discharging mechanisms, the key parameter for determining the reliability and the lifetime of electrostatic MEMS switches is the relaxation time,  $\tau$ , and not  $\beta$ . Thanks to the stretched exponential equation employed in this thesis, a consistent trend for the relaxation time versus different technological and operational conditions has been obtained.

The decay time constant,  $\tau$ , for nitrogen environment is smaller compared to air as shown in **Fig. 7.8a**, which indicates faster charge decay in nitrogen. This could be observed for all humidity levels and for charges injected under different  $U_p$ . **Figure 7.8b** depicts also that the

stretch factor,  $\beta$ , is smaller in nitrogen compared to air for all relative humidity levels and  $U_p$ . The difference in decay time constant between air and nitrogen can be attributed to numerous reasons. First,  $\tau$  is found to increase with  $U_p$  or the electric field intensity. Since, the injected charge density increases with the applied electric field intensity, it becomes obvious that the decay time constant increases with increasing the injected charge density. As concluded from the previous section, the injected charge density in air is larger compared to nitrogen, for a given  $U_p$  and humidity level. Therefore,  $\tau$  should be smaller for nitrogen compared to air since the former has less injected charge density. The second reason behind the observed difference in  $\tau$  between air and nitrogen could be attributed to the difference in the amount of available counterions and the electrical conductivity of the medium for both environments. The number of available ions is expected to be higher in air than in nitrogen. Such ions are attracted by the external electric field of the charged sample and are randomly trapped over the  $\text{SiN}_x$  surface.

To sum up, the trapped charges decay faster in nitrogen environment than in air. Moreover, the relaxation time,  $\tau$ , is found to decrease for a smaller pulse amplitude,  $U_p$ , and/or a higher relative humidity level. In the next section, the time evolution of the surface potential distribution, FWHM, is discussed to complete the analysis of the charge collection process.

#### 7.4.4 Lateral charge redistribution (FWHM evolution with time)

The impact of the relative humidity on the lateral charge redistribution with time in air and nitrogen is shown in **Fig. 7.9a** and **Fig. 7.9b**, respectively. For all relative humidity levels and for air and nitrogen environments, the FWHM increases with time indicating that the injected charge spreads over the  $\text{SiN}_x$  surface. The FWHM evolution with time does not fit with the stretched exponential law (Eq. 4.3), and shows a large deviation especially at higher humidity levels. It could be also observed from the figures that the rate of increase in FWHM with time becomes larger as the relative humidity increases, for both air and nitrogen. As the relative humidity increases the thickness of adsorbed water film over the  $\text{SiN}_x$  surface increases too, resulting in a faster charge spreading over the dielectric surface due to the larger conductivity of the water film. Comparing the difference between the FWHM measured for different humidity levels at the beginning and the end of the observation time window for both air and nitrogen, it can be seen that the values of the FWHM for different humidity diverge in the long time range.

Comparing the FWHM evolution with time measured under different humidity in air (**Fig. 7.9a**) with the corresponding surface potential decay data in **Fig. 7.7**, it could be observed

that there is no correlation between the trend of the FWHM evolution with time and the  $U_s$  decay with time. Therefore, the decrease in relaxation time with increasing the relative humidity (**Fig. 7.8a**) cannot be attributed to the faster lateral charge spreading over the dielectric surface observed at larger humidity levels. Similar observations could be made for nitrogen environment.

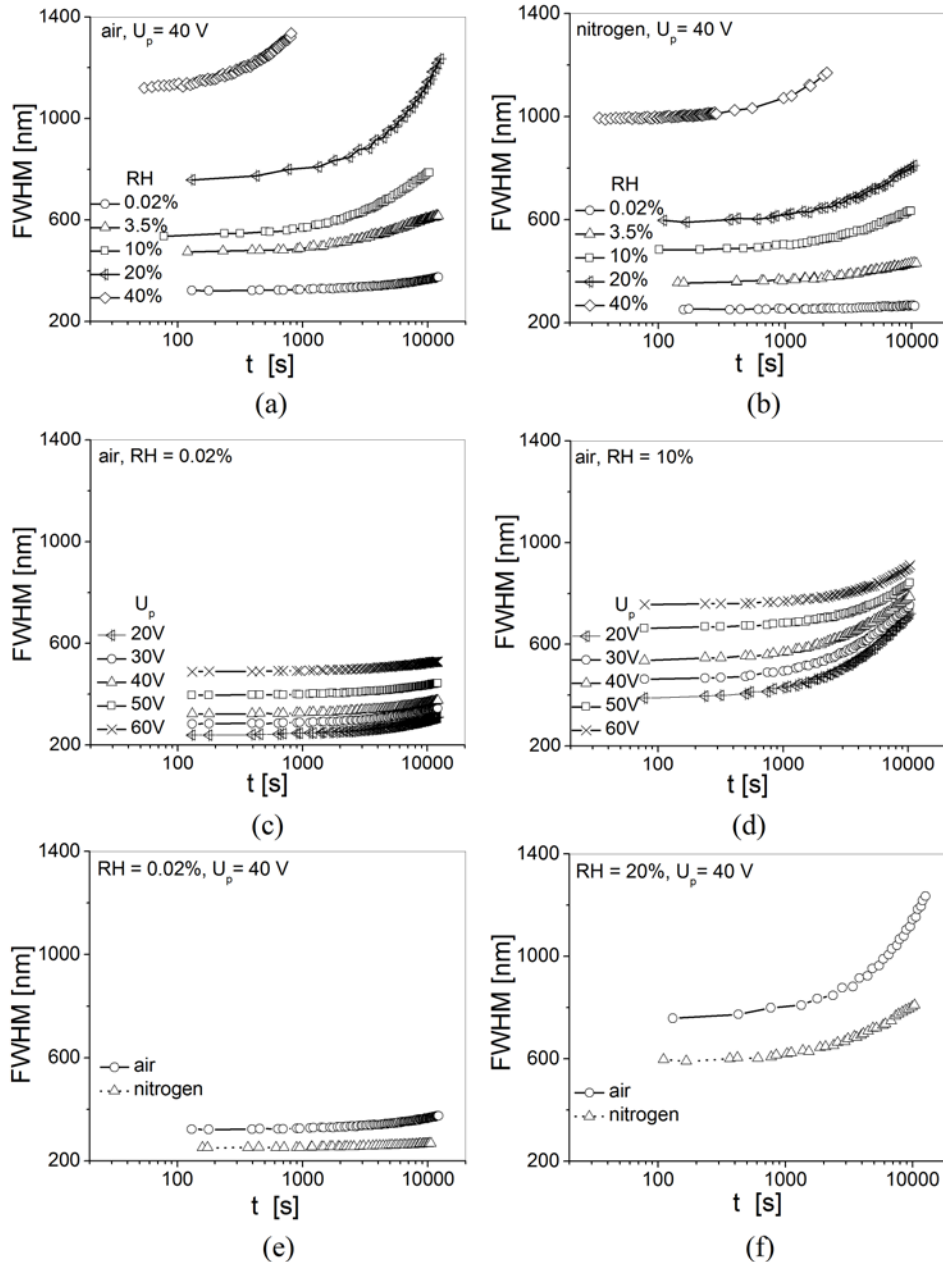


Figure 7.9. The effect of environment on the FWHM redistribution: FWHM evolution with time measured under different humidity in (a) air and (b) nitrogen; FWHM evolution with time measured in air for charges injected using different  $U_p$  under (c) 0.02% RH and (d) 10% RH; and FWHM evolution with time in air and nitrogen under (e) 0.02% RH and (f) 20% RH.

As the pulse amplitude,  $U_p$ , increases, lateral charge gradient increases too, and this is expected to affect the lateral charge redistribution with time over the  $\text{SiN}_x$  surface. In order to explore this effect, the time evolution of FWHM resulting from different pulse amplitude,  $U_p$ , is plotted in **Fig. 7.9c, d**. At small relative humidity levels (ex. 0.02%), the influence of  $U_p$  on the increasing rate of FWHM with time, though small, is still noticeable. Also, the difference between FWHM values for different  $U_p$  can be seen even after 3.5 hours. When increasing the humidity to 10% (**Fig. 7.9d**), the difference between the FWHM for different  $U_p$  starts to diminish indicating that the FWHM tends to be the same in the long time range. Thus, it can be concluded that the lateral charge redistribution with time is determined mainly by the relative humidity which overwhelms the impact of  $U_p$  especially at larger humidity levels.

When comparing the FWHM evolution with time for the 0.02% RH measured in air (**Fig. 7.9c**) with the corresponding surface potential decay at 0.02% RH in air (**Fig. 7.7**), it can be seen that for different values of  $U_p$ , the trend of FWHM evolution with time cannot be correlated with the trend of  $U_s$  decay with time. As mentioned earlier,  $U_p$  has a very small effect on the rate of increase of FWHM with time and the FWHM increases slightly faster with increasing  $U_p$ . Besides, from **Fig. 7.8a**,  $U_p$  has a remarkable impact on the decay time constant having the relaxation time increase with  $U_p$ . All of these remarks can lead us to the conclusion that the observed variation in the decay time constant when changing  $U_p$  is not attributed to the lateral charge spreading over the  $\text{SiN}_x$  surface. Similar conclusions can be drawn through comparing the FWHM evolution with time with the surface potential decay at 10% RH.

In contrast to the tails of FWHM curves with time presented in **Fig. 7.9a, b** where the FWHM for different relative humidity levels diverges in the long time range, the corresponding FWHM for different  $U_p$  converges for both small (**Fig. 7.9c**) and high (**Fig. 7.9d**) relative humidity levels. When changing  $U_p$  (**Fig. 7.9c, d**), the lateral charge gradient decreases with time resulting in having similar FWHM in the long time range while in case of changing the relative humidity (**Fig. 7.9a, b**) the employed humidity is kept constant during the whole observation time window resulting in higher lateral charge redistribution with time. Finally, similar remarks have been made in nitrogen environment regarding the impact of  $U_p$  on lateral charge redistribution with time.

A comparison between the lateral charge redistribution with time for air and nitrogen under two humidity levels is presented in **Fig. 7.9e** (0.02% RH) and **Fig. 7.9f** (20% RH). The

FWHM increase with time in air is slightly faster compared to nitrogen for both small (0.02%) and high (20%) humidity levels. This can be attributed to the expected higher number of available ions in air compared to nitrogen which is reflected on the conductivity of the adsorbed water layer in both environments. This is also supported by the larger background surface potential measured in nitrogen compared to air under different humidity levels (see **Fig. 7.6**). The expected higher conductivity of the adsorbed water film in the case of air than in nitrogen could increase the rate of FWHM spreading with time. Finally, since the FWHM measured in nitrogen is found to spread laterally slower than in air while  $U_s$  decays faster in nitrogen compared to air, it is further concluded that the difference in the decay time constant between air and nitrogen (**Fig. 7.8a**) is not attributed to the lateral charge redistribution over the dielectric surface with time.

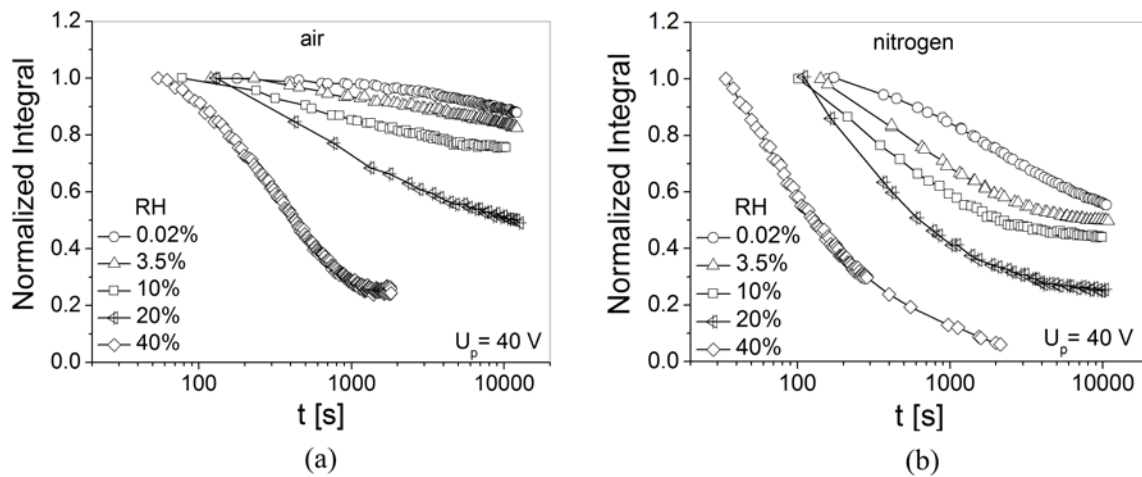


Figure 7.10. The evolution of the normalized potential profile integral with time in (a) air, and (b) nitrogen environments.

The integration of the obtained potential profiles with time was also performed for both air and nitrogen under different relative humidity levels. This is required to provide a comprehensive image for the discharging process since the evolution of  $U_s$  and FWHM with time shows an opposite trend [147]. The evolution of the normalized potential profile integral with time is plotted in **Fig. 7.10** and it shows obviously that the charge relaxation process is much slower in air (**Fig. 7.10a**) compared to nitrogen (**Fig. 7.10b**), following the trend of  $U_s$  decay with time (**Fig. 7.7**). For example, at 0.02% RH and at the end of observation time window, the potential integral is 87% and 55% for air and nitrogen environments, respectively,

from their initial values, while at 20% RH, the potential integral is 49% and 26% for air and nitrogen, respectively. Moreover, **Fig. 7.10** points out that increasing the relative humidity results in a faster discharging process in both air and nitrogen environments, and this also follows the  $U_s$  evolution with time under different humidity levels.

In view of the aforesaid KPFM results related to the charging and discharging processes, it is concluded that nitrogen is more favorable as a packaging environment for electrostatic MEMS switches compared to air in order to reduce the dielectric charging. The injected charge density in nitrogen is found to be smaller than in air for the same charge injection and measurement conditions. Moreover, the injected charges decay faster in nitrogen compared to air. These KPFM nanoscale results are supported by the lifetime measurements of electrostatic capacitive MEMS switches reported by [66] where the lifetime was reported to be a factor of about 100 longer in nitrogen than in air for different dielectric films including  $\text{SiN}_x$ .

Regarding the influence of the relative humidity, it is shown that the injected charge density in  $\text{SiN}_x$  films increases with humidity for both air and nitrogen environments (**Fig. 7.5**). Also, the discharge process becomes faster as the relative humidity increases (**Fig. 7.8**, **Fig. 7.10**), and this includes faster charge decay (**Fig. 7.7**) as well as faster charge lateral spreading (**Fig. 7.9**) over the dielectric surface. Finally, the background surface potential is found to increase with increasing relative humidity (**Fig. 7.6**). As reported in [85, 86], the measured shift in the actuation voltage for capacitive MEMS switches increases as the relative humidity increases. This increase in the actuation voltage shift with humidity could be explained in view of the KPFM results obtained in this study. Simply, it could be attributed to many reasons including the higher injected charge density, larger background potential, and faster lateral charge redistribution measured at larger humidity levels. There has been no published data on the time evolution of the actuation voltage shift or the measured capacitance for a comparable observation time window to the one used in this study after stressing MEMS switches under different relative humidity levels in order to be compared to the discharging process rates measured by KPFM. On the other hand, as the relative humidity increases the adhesive force between the switch bridge and the dielectric surface is expected to increase [93, 150, 151, 152], and might become comparable to the existing electrostatic force. This effect will be investigated in details in chapter 8.

There are two main differences between air and nitrogen environments which are the composition and the contamination level. Air is composed mainly of three gases; nitrogen (78.084%), oxygen (20.946%), and argon (0.9340%). The remaining gases are often referred to as trace gases [153], among which are the greenhouse gases such as water vapor, carbon dioxide, methane, nitrous oxide, and ozone. The second difference between the employed air and nitrogen in our study is the level of purification. The air environment used in our experiments is a normal lab-air while the nitrogen environment is taken from a liquid nitrogen tank with a fairly high level of purification. Hence, the level of local contamination is expected to be higher in case of air compared to nitrogen environment. Both of these differences between air and nitrogen might affect the charging and discharging processes and are investigated in the next section.

### **7.5 Influence of oxygen, organics and hydrocarbon contaminants**

In this section the impact of the oxygen gas as well as the hydrocarbon contaminants on the charging and discharging processes is discussed. Two types of gas purifiers were used; an oxygen trap and a hydrocarbon filter (see **Fig. 3.11**). The engaged oxygen trap [154] is designed to remove the oxygen from non-oxidizing gas streams such as He, Ar, N<sub>2</sub>, H<sub>2</sub> or CH<sub>4</sub>, and it cannot be used with an air line. The trap consists of a high-capacity filter filled with copper-based adsorbent which forms copper oxide in the presence of oxygen, and no gas is generated. The employed hydrocarbon filter [154] is filled with activated charcoal, one of the most effective adsorbents for organics and hydrocarbons. It is used in these experiments with both air and nitrogen streams to remove the organic and hydrocarbon contaminants at room temperature except methane.

There are two main reasons behind selecting the abovementioned gas purifiers. First, the oxygen trap was used because KPFM measurements indicate that there is a big difference between air and nitrogen environments regarding both the charging and discharging processes, as shown in the previous section. Since the main difference between air and nitrogen is the oxygen, it becomes essential to completely remove this component from the employed nitrogen environment, if there is any. The oxygen trap was installed with the nitrogen stream only as it cannot be used with the air line. The hydrocarbon filter was used with both air and nitrogen lines in order to investigate the influence of some of the environmental contaminants on the charging and discharging processes. To minimize the impact of the relative humidity for this set of

measurements, the KPFM experiments were performed under the lowest possible relative humidity level in our environmental setup which is 0.02%.

### 7.5.1 Impact on charging process

**Figure 7.11** introduces the measured  $U_s$  and FWHM at 0.02% RH under normal lab-air and nitrogen lines with and without employing the two investigated gas purifiers. Plugging the hydrocarbon filter with the air line results in a noticeable change in the measured FWHM, while the change in  $U_s$ , though exists, is hardly noticed. This could be observed for all investigated pulse amplitudes,  $U_p$ . When the same filter is plugged with the nitrogen line, the resulting difference in both  $U_s$  and FWHM becomes too small to be observed. Basically, this was expected as the normal lab-air used in these experiments is not purified properly while the nitrogen comes from a liquid nitrogen tank with a high purification level. These results indicate that the organics and hydrocarbons contaminants could affect the dielectric charging process in electrostatic MEMS switches employing  $\text{SiN}_x$  films and having an air packaging environment.

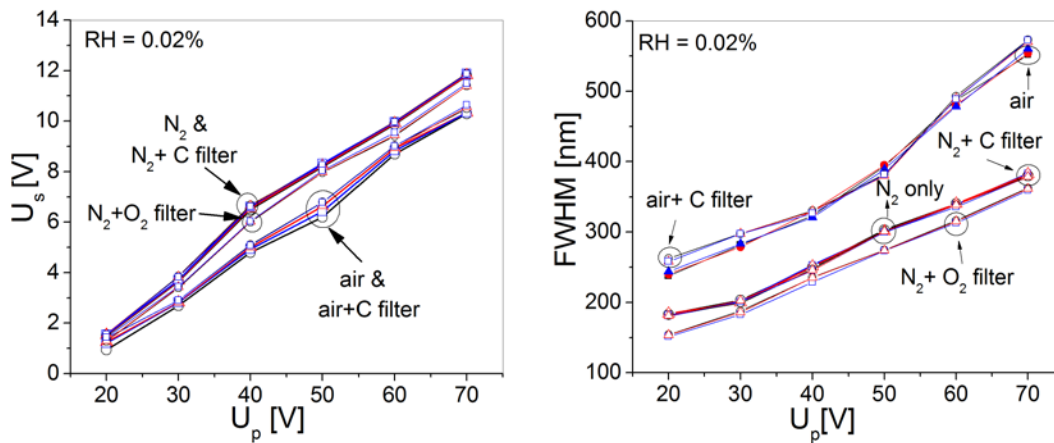


Figure 7.11. Impact of using the oxygen filter and hydrocarbons trap on  $U_s$  and FWHM for air and nitrogen environments.

When the oxygen filter is plugged with the nitrogen line, the measured  $U_s$  and FWHM decrease considerably for all investigated  $U_p$  as shown in **Fig. 7.11**. This clearly indicates that the injected charge density in the  $\text{SiN}_x$  film becomes smaller when using the oxygen filter, for a given  $U_p$  and relative humidity level. Furthermore, for the nitrogen measurements the influence of using the oxygen trap is found to be more pronounced than the effect of using the hydrocarbon trap. During the preparation of liquid nitrogen, oxygen atoms with different percentage

depending on the preparation methodology could be trapped. These atoms were filtered out in our experiments using the oxygen trap. Based on these results we can conclude that the oxygen gas plays an important role in determining the charging mechanisms in SiN<sub>x</sub> films. This could be further supported by the results presented in the previous section where a considerable difference has been observed between air and nitrogen with respect to the charging process.

### *7.5.2 Impact on discharging process*

The influence of using the two employed gas filters on the discharging process has also been investigated. The induced surface potential resulting from charge injection using different  $U_p$  was monitored for 3.5 hours. This was performed under normal lab-air and nitrogen lines and when the investigated gas purifiers were engaged. **Fig. 7.12** summarizes the values of the decay time constant,  $\tau$ , and stretch factor,  $\beta$ , calculated from fitting the surface potential decay with Eq. 4.3 for different filter combinations with both air and nitrogen environments. Plugging the hydrocarbon filter with the air line results in reducing the decay time constant  $\tau$  considerably. In other words, removing the hydrocarbon contaminants from the environment leads to faster charge decay. Depending on local contamination, the surface of a dielectric can be capable of localized charge storage for a considerable time. Also, the stretch factor,  $\beta$ , decreases when using the hydrocarbon trap with the air line. On the contrary, the hydrocarbon filter has almost no effect on both  $\tau$  and  $\beta$  when plugged with the nitrogen line. This is also expected as the employed lab-air is not as pure as the used nitrogen gas. Finally, comparing the influence of the hydrocarbon filter on the charging process (**Fig. 7.11**) and discharging process (**Fig. 7.12**) for measurements performed in air, it is clear that the impact of the hydrocarbon contaminants is more pronounced in the discharging process.

When the oxygen trap is engaged with the nitrogen line the decay time constant  $\tau$  decreases considerably compared to their values obtained under a normal nitrogen stream as shown in **Fig. 7.12**. This could be supported by the results shown in the previous section where the decay time constants are found to be shorter in nitrogen than in air (see **Fig. 7.8**). In addition, the stretch factor,  $\beta$ , decreases when employing the oxygen trap with the nitrogen line, which is also supported by the results presented in the previous section where the stretch factor is found to be smaller in nitrogen than in air. This can lead us to the conclusion that the oxygen plays a significant role during the discharge process, even when existing with a small amount which is

the case of the employed purified nitrogen gas. The considerable difference in both the charging and discharging process parameters observed when using the oxygen trap with the nitrogen line and/or using the hydrocarbon filter with the air line could be attributed to the influence of both the oxygen gas as well as the hydrocarbon contaminants. Thus, the difference between the charging and discharging processes observed in the previous section can be also attributed to the oxygen gas and local environment contaminants in addition to the previously mentioned reasons.

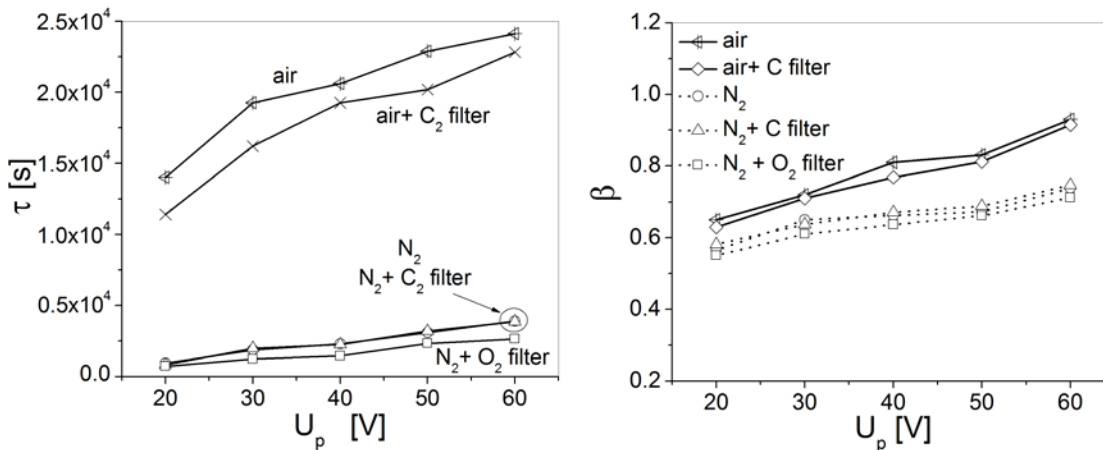


Figure 7.12. Influence of using the oxygen filter and hydrocarbons trap on the decay time constant,  $\tau$ , and the stretch factor,  $\beta$ , for air and nitrogen environments.

In summary, we have shown that it is not only the dielectric material and/or the employed relative humidity or environment medium which could influence the charging and discharging processes, but also the environment contaminants as well as different gas components could play a significance role. Since the injected charge density is smaller and the decay time constant is shorter when plugging the oxygen filter with the nitrogen line and/or the hydrocarbon filter with the air line, it becomes obvious that a well prepurified nitrogen gas could reduce considerably the dielectric charging phenomenon in electrostatic MEMS switches, and in consequence increases the device lifetime. The applied pulse duration,  $T_p$ , used in the experiments under discussion is limited to 1 s only, which is too short compared to the normally applied stressing time for actual MEMS switches. It is therefore concluded that for actual MEMS devices, the influence of the purification level of the packaging environment is expected to be more pronounced compared to the measured difference in this study.

## **7.6 Summary**

The influence of three environmental parameters, which are the environment medium, relative humidity, and environment level of purification on the charging and discharging processes was investigated. The assessment was performed using the KPFM-TF technique. The KPFM experiments were performed in two environment mediums (normal lab-air and nitrogen), under various relative humidity levels (from 0.02% to 40%), and using two types of gas purifiers (an oxygen trap and a hydrocarbon filter). The most important conclusive remarks from the present chapter are the following:

- Larger stress voltage results in higher injected charge density and slower discharging process (observed for air and nitrogen and for all investigated relative humidity levels).
- There is no correlation between the time evolution of FWHM and  $U_s$ . So, the discharging process is not attributed to lateral charge redistribution over the dielectric surface with time.
- Increasing the relative humidity results in larger injected charge density and faster discharge process in air and nitrogen (humidity affects the adsorbed water film conductivity, surface charge amount and neutralization with the external medium, and electric field distribution).
- The KPFM results obtained in this study explains the reported increase in actuation voltage shift for electrostatic MEMS switches with increasing the relative humidity.
- Nitrogen is more favorable than air as a packaging environment for electrostatic MEMS to reduce the dielectric charging (nitrogen has smaller injected charge density and faster discharging process). This agrees with the reported lifetime data for MEMS switches.
- The differences in charging/discharging processes between air and nitrogen are attributed to the variation in the gas discharge, amount of available counterions, electrical conductivity of the medium, and the surface charge for both environments.
- The environment contaminants and gas compositions affect the charging/discharging processes significantly.
- The injected charge density is smaller and the discharging process is faster when plugging the oxygen filter with the nitrogen line and/or the hydrocarbon filter with the air line.
- A well prepurified nitrogen or air environments could reduce the dielectric charging in electrostatic MEMS devices considerably.

The outcome of such study is very useful in specifying the requirements of proper packaging schemes for electrostatic MEMS/NEMS devices with minimal charging and hence improved reliability.

*To be nobody but yourself in a world which is doing its best, night and day, to make you everybody else means to fight the hardest battle which any human being can fight; and never stop fighting.*

*Edward Estlin Cummings  
1894 – 1962, American Poet*

## **8 Characterization of different stiction mechanisms**

### **8.1 Introduction**

In this chapter, the influence of the tribological phenomena, mainly adhesion and friction, at the interface of the MEMS switches movable electrode and the dielectric film is studied for the first time. Furthermore, the multiphysics coupling between these phenomena and the dielectric charging failure mechanism is investigated. This further leads to an in-depth understanding of different stiction mechanisms in electrostatic MEMS switches. In these devices, stiction can be caused by two main mechanisms: the dielectric charging and the meniscus formation resulting from the adsorbed water film between the switch movable electrode and the dielectric. The effect of each mechanism and their interaction were investigated by measuring the adhesion and friction forces under different electrical stress conditions and relative humidity levels. An atomic force microscope (AFM) was used to perform the adhesion and friction measurements on the nanoscale. The study provides an accurate explanation for the literature reported lifetime measurements of electrostatic MEMS switches. Though the present investigation targets mainly MEMS switches, it could be extended to include other electrostatic MEMS devices.

The chapter is organized as follows. The procedures of measuring the adhesive and friction forces are presented first. Next, the impact of the relative humidity on adhesive and friction forces when no bias is applied is discussed. This is followed by discussing the influence of the applied bias on adhesion and friction under different humidity levels.

## 8.2 Experimental

The investigated samples consist of PECVD SiN<sub>x</sub> films with 300 nm thickness deposited over Au/Ti (200 nm/50 nm) layers, which were evaporated on Si substrates. The layer structure of the samples (HF-Evap Au) is shown in **Fig. 3.2b**, and the details of each layer are presented in **Table 3.1**. The SiN<sub>x</sub> films were deposited using the standard HF recipe presented in **Table 3.2**.

The adhesion and friction experiments were performed under different relative humidity levels in order to study the individual effect of meniscus formation. The environment control system used for these experiments is shown in **Fig. 3.11**. For each humidity level, the adhesive and friction forces between the AFM tip and the SiN<sub>x</sub> surface were measured while different bias amplitudes were applied to the Au layer underneath the SiN<sub>x</sub> film (see subfigure in **Fig. 8.1a**). Due to the dielectric charging phenomenon, the SiN<sub>x</sub> film is charged and this results in an induced surface potential over the dielectric film. Thus, the applied bias in these experiments corresponds to the voltage used to actuate the MEMS switch and/or the induced surface potential over the dielectric film due to the dielectric charging. The adhesion and friction measurements were conducted using highly doped Si tips (FORTA-10).

### 8.2.1 Adhesive force and water film thickness measurements

The Force-distance curve (FDC) measurements were used to measure the adhesive force between the AFM tip and the SiN<sub>x</sub> film as well as the adsorbed water layer thickness over the SiN<sub>x</sub> surface [20, 143]. An example of the force-distance curve for the investigated samples is presented in **Fig. 8.1a** and it has been described in details in chapter 3. The piezo travel distance used in these experiments was 500 nm which is comparable to the air gap of actual MEMS switches. The adhesive force, which is the force needed to pull the tip away from the sample, is calculated from FDC by multiplying the vertical distance between E and F with the stiffness of the cantilever (Eq. 3.3) as described in **Fig. 8.1a**. Moreover, as the tip travels in the adsorbed water film from point B to C, it is deflected as well. For the AFM used in this study the tip deflection occurs in the same direction as the piezo travels. Therefore, the water film thickness is the sum of the deflection of cantilever ( $h_1$  in **Fig. 8.1a**) and the travel distance of the piezo ( $h_2$  in **Fig. 8.1a**) [20, 155, 156]. The force-volume method explained in chapter 3 was used in order to map the adhesive force between the sample and the AFM tip. For each sample, four adhesive maps were obtained in different locations over the dielectric surface. Also, for each map an area

of  $10\ \mu\text{m} \times 10\ \mu\text{m}$  square was scanned and divided into  $16 \times 16$  matrix positions. The adhesive force as well as the thickness of the water layer for each position is calculated from the obtained FDCs. This is followed by a statistical evaluation for each sample by averaging over the four measured adhesive force maps. **Figure 8.1b** presents an example of the obtained adhesive force map measured using the force-volume method.

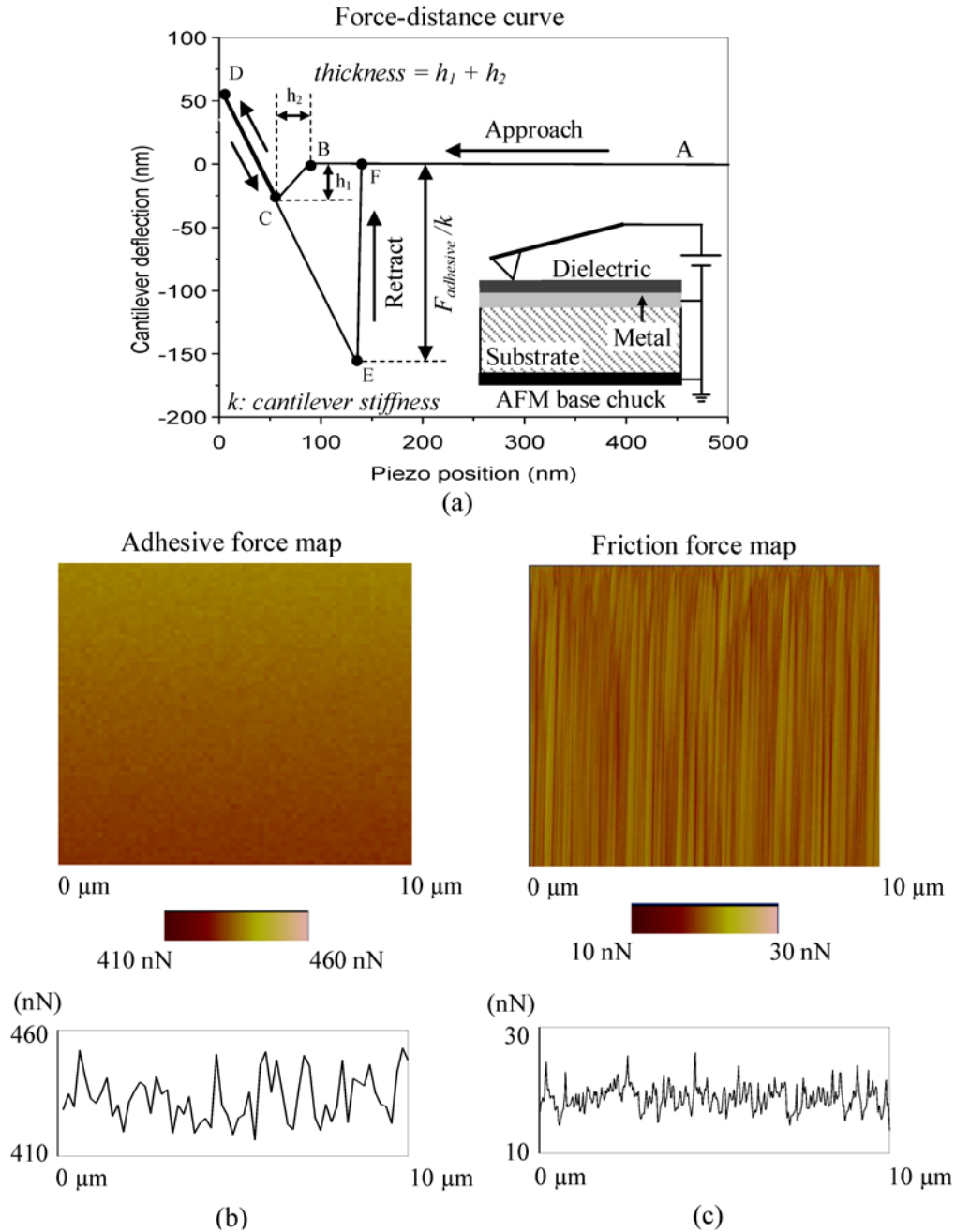


Figure 8.1. (a) Illustration of determining the adhesive force and the adsorbed water film thickness from force-distance curve; (b) an example of the obtained adhesive force maps and (c) friction force maps.

### 8.2.2 Friction force and coefficient of friction

In order to investigate the influence of the friction forces between the movable electrode of MEMS switch and the dielectric, the friction force between the AFM tip and the SiN<sub>x</sub> surface was measured under different normal loads. The friction force measurements were conducted by scanning the AFM tip orthogonal to the cantilever axis over a scan length of 10 μm and at a scan rate of 1 Hz. The normal load was increases between 35 nN and 990 nN, and the friction force was measured at each increment. Furthermore, the quantitative measurement of friction force was calibrated by the method described in [20, 157]. **Figure 8.1c** shows an example of the obtained friction force maps. The friction force is given by [20]

$$F_{friction} = \mu_f (W + F_{adh}) \quad (8.1)$$

where  $\mu_f$  is the coefficient of friction,  $W$  is the applied normal load to the AFM tip, and  $F_{adh}$  is the adhesive force measured between the AFM tip and the sample. By plotting the friction force as a function of the normal load, an average value of the coefficient of friction,  $\mu_f$ , can be calculated from the slope of the linear fitting of the data.

### 8.3 Effect of meniscus formation when no bias is applied

The individual influence of the meniscus force was studied by measuring the adhesive and friction forces under different relative humidity levels. No bias was applied between the AFM tip and the sample for these experiments in order to completely eliminate the effect of the electrostatic force and dielectric charging. The used samples and AFM tips were dehydrated before performing these experiments through two cycles of heating (150 °C) and cooling steps under vacuum. Then, the samples were stored for 60 min under each investigated relative humidity level before performing the measurements. Increasing the relative humidity increases the adsorbed water layer thickness over the dielectric surface, and results in enhancing the meniscus formation. The reason behind the dehydration step is to remove a considerable amount of the previously adsorbed water molecules over the dielectric surfaces, and therefore study mainly the influence of the 60 min storage time under different relative humidity levels.

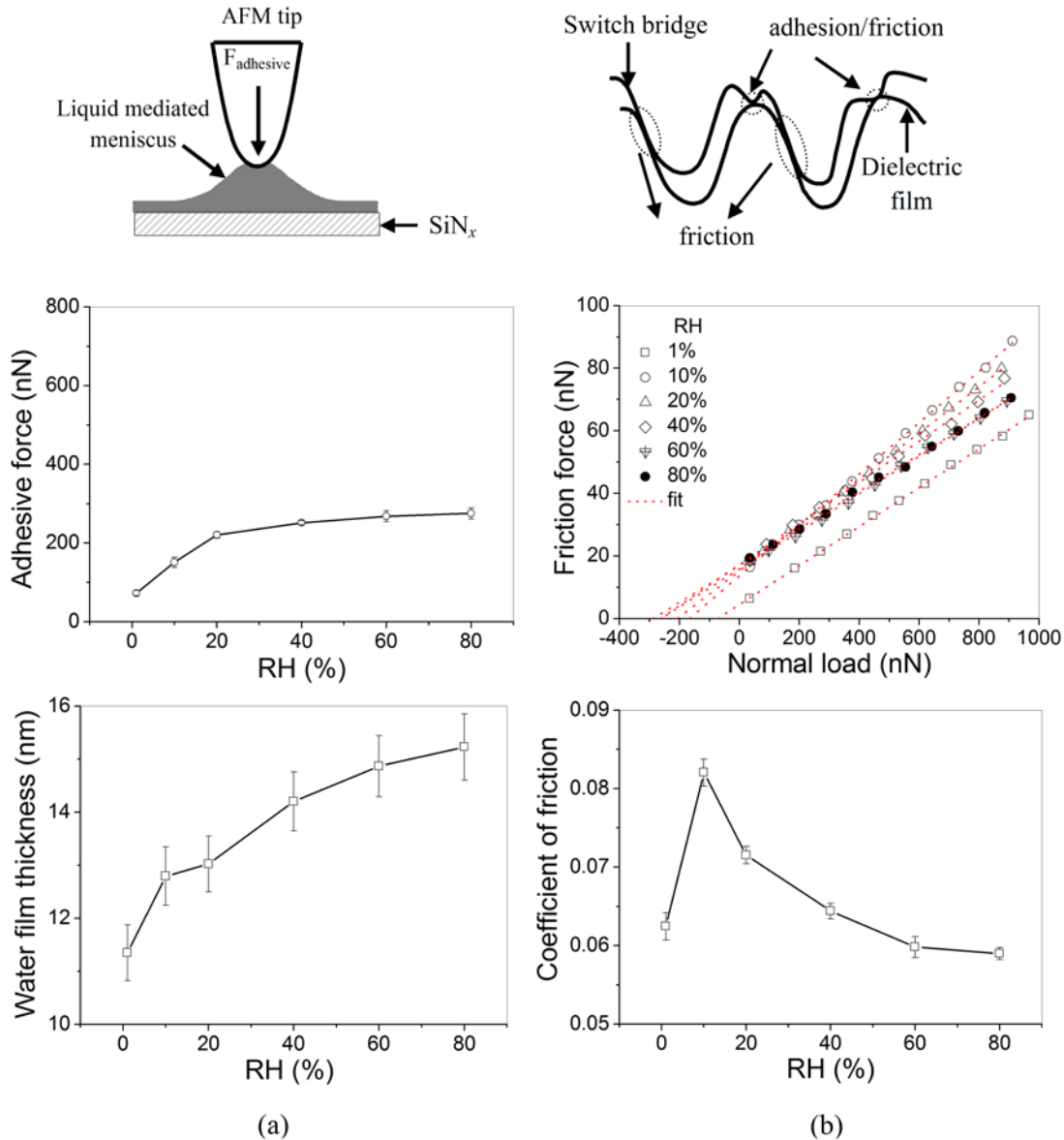


Figure 8.2. The influence of the relative humidity on (a) the adhesive force between the AFM tip and the  $\text{SiN}_x$  surface, the adsorbed water layer thickness over the dielectric film, and (b) the friction force measured at different normal loads and the coefficient of friction.

The impact of the relative humidity on the adhesion and friction between the tip and the  $\text{SiN}_x$  surface is presented in **Fig. 8.2**. **Figure 8.2a** (top) shows that the adhesive force increases considerably when the relative humidity increases from 1% to only 20%, and the increase tends to saturate at larger humidity levels. The measured thickness of the adsorbed water film over the  $\text{SiN}_x$  surface is also found to increase with the relative humidity as shown in **Fig. 8.2a** (bottom). The measured adhesive force presented in **Fig. 8.2a** results only from the meniscus formation between the AFM tip and the dielectric surface (see the cartoon in **Fig. 8.2a**). The increase of the

water film thickness enhances the meniscus formation, and consequently results in increasing the adhesive force. Though the measured increase in the water film thickness when increasing the relative humidity from 1% RH to 80% RH is relatively small, the adhesive force increases considerably in this humidity range. The measured increase in the water film thickness presented in **Fig. 8.2a** results from a storage time of only 60 min at the employed relative humidity. Increasing the storage time is expected to increase the water film thickness, and hence further increase the adhesive force. In addition, when relative humidity increases the meniscus becomes easier to form and more difficult to rupture, and hence the adhesive force becomes longer ranged [158]. In other words, the water bridge can persist at a longer tip-sample distance before the bridge rupture. This leads to stronger attractive capillary force between the tip and the sample, and hence larger adhesive force with increasing the relative humidity.

It is widely believed that the adhesive force between the switch movable electrode (the bridge) and the dielectric film is the main reason behind stiction in electrostatic capacitive MEMS switches. The influence of friction force is usually neglected since there is no sliding motion between the bridge and the dielectric. For this reason, the influence of the friction between the switch bridge and the dielectric film on MEMS switches reliability has not been experimentally investigated before. The cartoon in **Fig. 8.2b** points out that any two surfaces that are full of asperities and move vertically against each other could have also friction at the sidewalls of asperities. Basically, this scenario resembles the interface between the MEMS switch bridge and the dielectric film, and therefore the friction at this interface needs also to be investigated.

The measured friction force as a function of normal load under different humidity levels is shown in **Fig. 8.2b** (top). The reproducibility associated with the measured friction force at each normal load is generally within  $\pm 3$  percent. An approximately linear response could be observed in the load range of 35–990 nN for measurements performed under different humidity levels [20]. The coefficient of friction,  $\mu_f$ , at each relative humidity is calculated from slope of the friction force versus the normal load as given in Eq. 8.1, and the results are presented in **Fig. 8.2b** (bottom). The data shows that the coefficient of friction,  $\mu_f$ , increases sharply when increasing the relative humidity from 1% to only 10%. This increase is attributed to the considerable increase in the adhesive force measured at 10% as shown in **Fig. 8.2a**. When the relative humidity increases beyond 10% RH, the coefficient of friction,  $\mu_f$ , is found to decrease in

spite of the measured increase in the adhesive force in this humidity range. This indicates that at larger relative humidity (beyond 10% RH in our case) the water film acts as a lubricant material [20, 150]. The considerable change in the adhesive force when relative humidity increases to only 20% and in the coefficient of friction,  $\mu_f$ , when humidity increases to only 10% indicates that the  $\text{SiN}_x$  material is very sensitive to any tiny amount of water molecules adsorbed over its surface.

In **Fig. 8.2b** (top), the non-zero value of the friction force at zero external load is due to the adhesive forces. Based on the relationship that exists between the friction force and adhesive force (Eq. 8.1), the adhesive force at each relative humidity can be calculated also from the friction data presented in **Fig. 8.2b** (top). The adhesive force values are obtained from the horizontal intercepts of the friction force versus normal load curves at a zero value of friction force [94]. A good agreement has been found in the trend of the adhesive force versus relative humidity calculated from the friction data and from the FDC measurements.

#### **8.4 Effect of applied bias on adhesive and friction forces**

The influence of the electrostatic force between the bridge of the MEMS switch and the dielectric film on the adhesion and friction forces is discussed in this section. This electrostatic attractive force results from the voltage used to actuate the switch and/or the induced surface potential due to the dielectric charging phenomenon. The study was performed by measuring the adhesive and friction forces between the AFM tip and the  $\text{SiN}_x$  surface while an electrical bias was applied to the Au layer underneath the  $\text{SiN}_x$  film (see subfigure in **Fig. 8.1a**). In order to validate the FDC measurements under different applied bias, the FDC-MEMS method described in chapter 3 was first used to measure the adhesive force over a charged dielectric film implemented in an electrostatic capacitive MEMS switch. For this experiment, MEMS switches with high frequency (HF) PECVD  $\text{SiN}_x$  films of 300 nm thickness were used (**Fig. 8.3a**). The switch was actuated first for 2 min using 40 V. Next, the suspended Au bridge was removed in order to have the  $\text{SiN}_x$  surface naked (**Fig. 8.3b**). The FDC measurements were used then to map the adhesive force in different positions over the charged dielectric film. **Figure 8.3c** shows an optical image for the suspended Au bridge over the scanned area while **Fig. 8.3d** presents the obtained adhesive force map for the charged  $\text{SiN}_x$  surface over the same area. It is obvious from the adhesive map that the adhesive force in the contact areas is much larger compared to the etch holes positions, and therefore the holes' locations are easily identified. Charge injection takes

place in contact areas only, and this results in larger induced surface potential and consequently higher adhesive force in contact areas compared to holes positions. The correlation between the etch holes positions in the adhesive force map and in the optical image of the suspended electrode is quite clear.

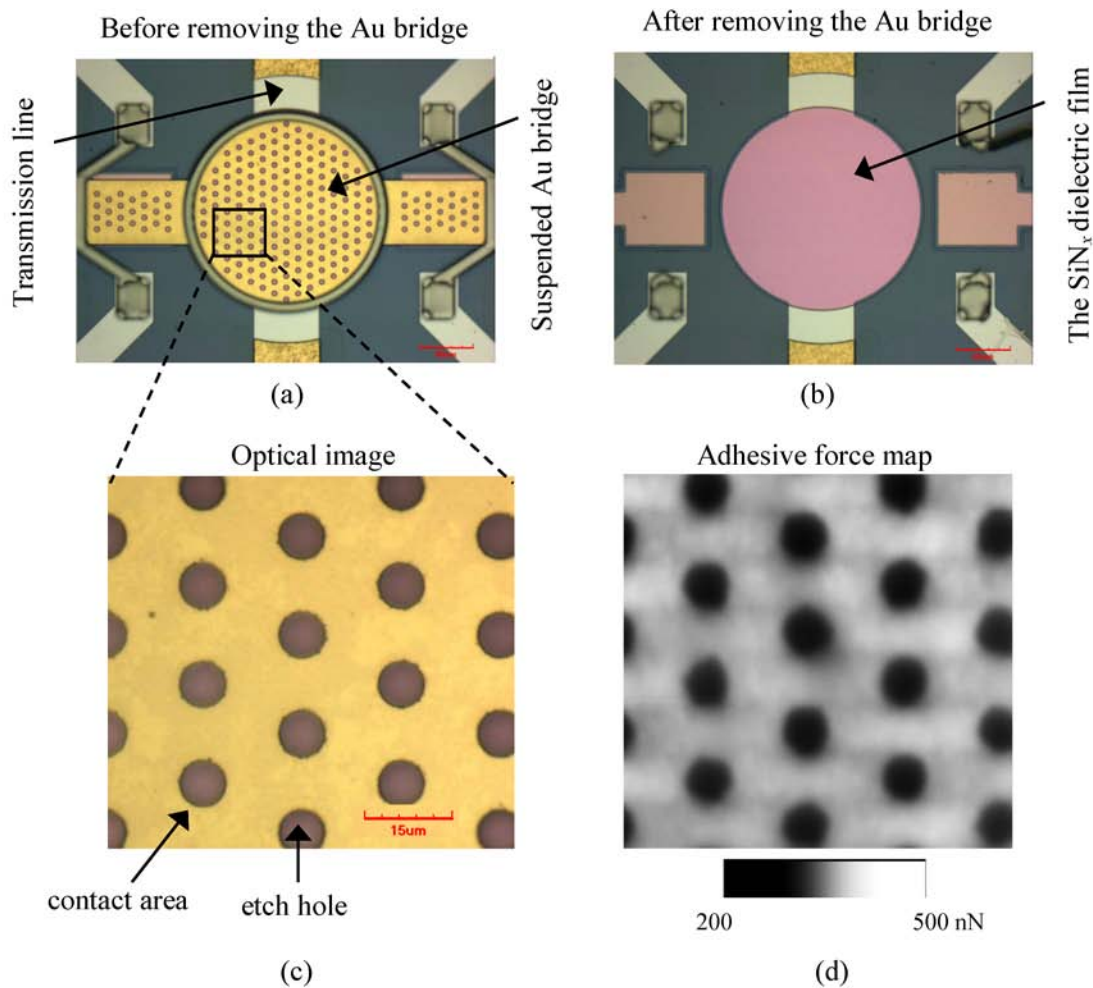


Figure 8.3. The MEMS switch used for the experiment [163] (a) before removing the suspended Au bridge, and (b) after removing the bridge; (c) An optical image of the bridge over the scanned area; and (d) the obtained adhesive force map over the charged SiN<sub>x</sub> surface for the same area.

The separate and combined effect of the two stiction mechanisms induced by the electrostatic force and by the meniscus force were studied by using three different groups of samples (A, B, and C). Group A and B were dehydrated just before performing the experiments through two cycles of heating (150 °C) and cooling steps under vacuum. This removes a considerable amount of the adsorbed water over the dielectric surface. Then, group A was measured under a very low relative humidity level (1%), while group B was stored under high

relative humidity (60%) for 60 min, and then was measured under 60% RH. Group C was not dehydrated, and was measured under a low humidity level (1%) similar to group A. The thickness of the adsorbed water layer for group A is therefore smaller than groups B and C. Consequently, the contribution of the meniscus force to the measured adhesive and friction forces is expected to be much smaller for group A compared to groups B and C. Also, the interaction between the stiction resulting from the meniscus force and the stiction caused by the electrostatic force is expected to be much smaller in group A compared to groups B and C. Comparing groups A and B, the influence of the water molecules adsorbed during a time duration of 60 min under high relative humidity (60%) could be assessed. Furthermore, the comparison between groups A and C reveals the influence of the annealing step.

An example of the FDC data obtained under different applied bias for groups A and B is presented in **Fig. 8.4**. When bias is applied, the tip moves towards the  $\text{SiN}_x$  surface under an additional force which is the attractive electrostatic force. The approach data shown in **Fig. 8.4a** highlights that as the applied bias increases, the cantilever starts to deflect toward the sample surface at much far distance from the tip-sample interaction region due to the electrostatic attractive force. Also, the piezo position at which the mechanical instability of the cantilever occurs is found to increase with the applied bias. In other words, the tip is snapped down towards the  $\text{SiN}_x$  surface from a larger tip-sample separation as the applied bias increases. This is attributed to the further increase in electrostatic force as the tip approaches the sample surface. As the applied bias increases, the tip-sample distance at which the attractive electrostatic force could overwhelm other countering forces will increase too. These remarks have been made for both sample groups A (**Fig. 8.4a** left) and B (**Fig. 8.4a** right).

The retract data in **Fig. 8.4b** depicts that the piezo position at which the elastic force of the cantilever becomes equivalent to the adhesive force (point E in **Fig. 8.1a**) increases with the applied bias. The larger electrostatic force obtained for higher bias requires larger tip-sample separation in order to be reduced and to become equivalent to the mechanical restoring force. The figure also highlights that when no bias is applied the cantilever returns directly to its original position (point F in **Fig. 3a**). With the applied bias, the cantilever returns to an intermediate point, and then starts to approach its original position gradually. This is similar to the gradual deflection observed for the approach data, and is attributed to the electrostatic attractive force. The larger cantilever deflection measured at higher bias indicates that the

adhesive force between the tip and the  $\text{SiN}_x$  sample increases with the applied bias. This has been observed for both sample groups A (**Fig. 8.4b** left) and B (**Fig. 8.4b** right).

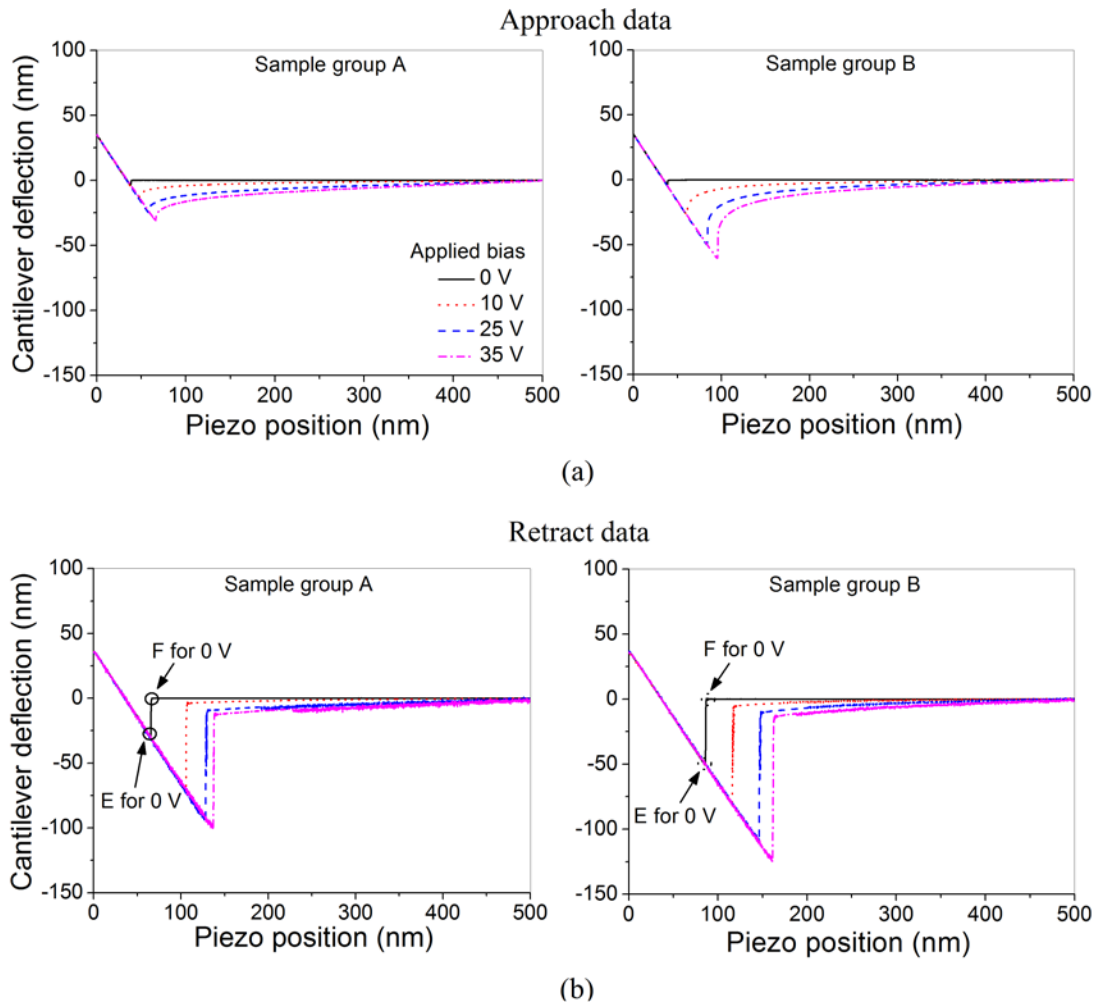


Figure 8.4. (a) The approach and (b) retract data measured under different applied bias for sample group A (left) and sample group B (right).

**Figure 8.5** presents the measured adhesive force under different applied bias for the three mentioned sample groups (A, B, and C). When no bias is applied, **Fig. 8.5a** highlights that the adhesive force measured for group B is larger compared to groups A and C. Due to the storage step of group B under higher relative humidity (60%), the thickness of the adsorbed water film is higher compared to group A. This results in larger meniscus formation, and hence larger meniscus force in group B compared to group A. In addition, the higher relative humidity employed in group B leads to stronger attractive capillary force compared to groups A and C as explained earlier. For the three groups, the adhesive force is found to increase with the applied

bias as shown in **Fig. 8.5a**. This increase is attributed to the increase in the attractive electrostatic force between the AFM tip and the  $\text{SiN}_x$  surface as the applied bias increases. In addition, the increase in the adhesive force with bias is found to be very small for group A compared to groups B and C. In these experiments, the adhesive force was measured while the bias is applied. Therefore, the  $\text{SiN}_x$  film is charged due to the applied bias, and this results in an induced surface potential over the dielectric surface. This surface potential reduces the effective applied bias between the AFM tip and the sample. Therefore, it becomes essential to measure the induced surface potential over the dielectric films for the three sample groups in order to investigate accurately the influence of the electrostatic force. The induced surface potential was measured using the novel FDC-based method as described in chapter 3 and the results are shown in **Fig. 8.5b**.

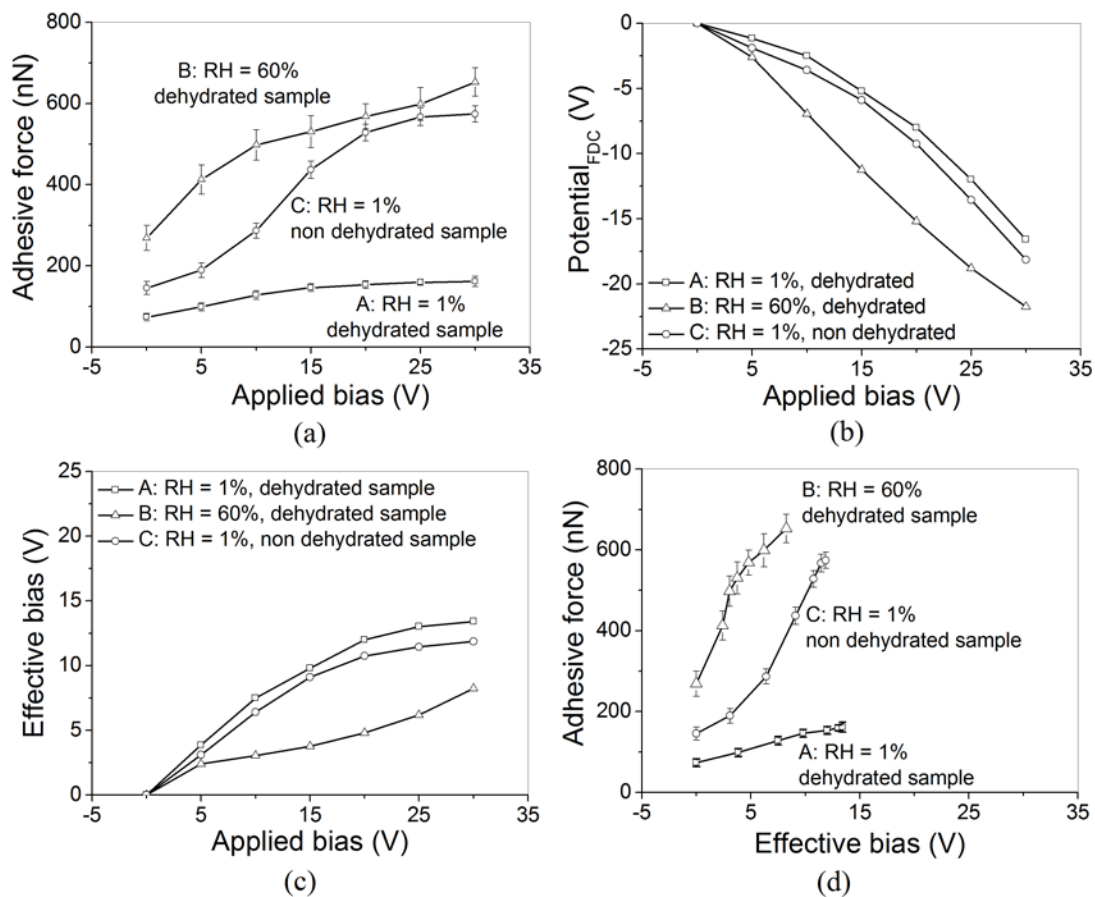


Figure 8.5. The effect of the applied bias on adhesive force for sample groups A, B and C: (a) the adhesive force versus the applied bias, (b) the measured surface potential induced over the dielectric films, (c) the calculated effective applied bias versus the applied bias, and (d) the measured adhesive force as a function of the effective applied bias.

The measured surface potential for group B is much larger than group C, which in turn has higher potential than group A. Since the thickness of the adsorbed water layer in group A is much smaller compared to group C, it becomes obvious that the more the adsorbed water molecules over the dielectric surface is, the higher the dielectric charging will be. Also, since the relative humidity employed in group B is much larger compared to groups A and C, larger humidity results in much higher injected charge density in the dielectric film. These results agree quite well with the dielectric charging study performed for SiN<sub>x</sub> films under different relative humidity levels using KPFM [75, 159]. The obtained results agree also with the larger shift in the actuation voltage measured for capacitive MEMS switches operated at larger relative humidity levels as reported in [85, 86]. The small difference in the measured surface potential between groups A and C compared to the large difference between groups A and B indicates that the influence of the relative humidity on the dielectric charging is much higher than the impact of the adsorbed water film thickness. Due to the induced surface potential, the effective applied bias between the AFM tip and the sample surface will decrease. The effective applied bias for each sample is calculated from the difference between the applied bias and the measured surface potential, and the results are plotted in **Fig. 8.5c**.

Three main differences exist between sample groups A and B: the adsorbed water film thickness, the relative humidity employed during the experiment, and the induced surface potential. **Figure 8.5c** shows that for a given applied bias, the effective bias is much smaller for group B compared to group A, and this is attributed to the higher induced surface potential in group B compared to group A (**Fig. 8.5b**). Therefore, the electrostatic attractive force for group B is much smaller than group A for all investigated applied bias. In spite of that, the adhesive force measured under different bias for group B is found to be much larger compared to group A. The measured adhesive force as a function of the effective bias is shown in **Fig. 8.5d**. It is evident from the figure that at the same effective bias, hence the same electrostatic force, the adhesive force for group B is much larger compared to group A. Also the increase in the adhesive force with the effective bias is much higher for group B compared to group A. Therefore, the difference in the trend of the adhesive force versus the applied bias between both groups cannot be attributed to the electrostatic attractive force. Moreover, the relatively small difference in the adhesive force between the two groups when no bias is applied clearly indicates that the large difference between both groups at higher bias cannot be explained by the liquid

mediated meniscus formation. Since the individual impact of the attractive electrostatic force and the liquid mediated meniscus formation does not explain the high difference in the adhesive force between groups A and B, there must be other adhesion mechanisms.

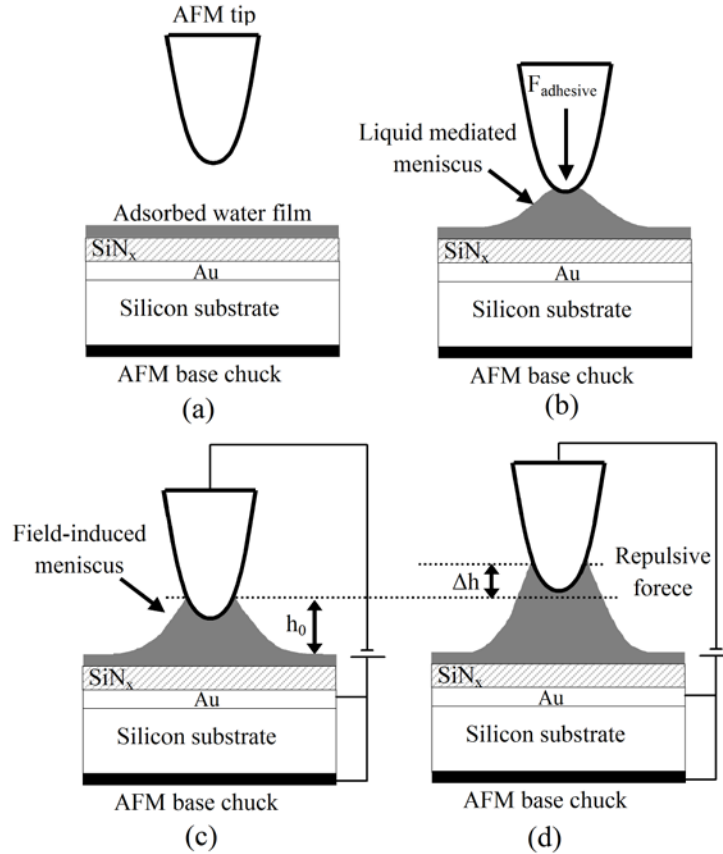


Figure 8.6. Different mechanisms of meniscus formation between the AFM tip and the sample surface: (a) initial stage where the tip is far from the sample surface, (b) formation of liquid mediated meniscus when the tip comes in contact with the adsorbed water film, (c) formation of field-induced meniscus when bias is applied between the AFM tip and the sample, and (d) the tip is pushed far from the surface due to the repulsive hydrodynamic force.

There are different mechanisms behind the meniscus formation. **Figure 8.6a** shows the AFM tip before reaching the sample surface. When the mechanical instability occurs (between points B, C in **Fig. 8.1a**), the tip jumps into contact with the adsorbed water film and wicks up around it to form a meniscus (**Fig. 8.6b**). This is called liquid mediated meniscus. It was also reported that the adsorbed water film between the AFM tip and the sample surface grows under the influence of the electric field, forming a meniscus that becomes unstable when a critical field is reached [96, 97, 98]. At this point, the meniscus suddenly forms a bridge between the tip and surface as shown in **Fig. 8.6c**. This is called a field-induced meniscus. Water will condense just

under the tip because the field is a maximum at this location relative to the rest of the sample surface. When the critical electric field is reached, condensation will accelerate until the liquid surface contacts the tip. Being attracted by the electric field, the meniscus generates a repulsive hydrodynamic force which counters the electrostatic force on the tip [160]. The imbalance of the forces leads to an increase of the tip-surface separation as highlighted in **Fig. 8.6d**. The increase in the water film at the tip-surface junction due to the applied bias is given by [160]

$$\Delta h = \frac{V^2}{K} \left[ C_0 \frac{R^2}{h_0^2} - C_1 \ln\left(\frac{D}{h_0}\right) \right] \quad (8.2)$$

where  $V$  is the applied bias,  $K$  is spring constant of the AFM tip,  $R$  is the end radius of the tip,  $h_0$  is the initial tip-surface separation before meniscus formation,  $C_0$  is a constant related to the properties of the water, and  $C_1$  and  $D$  are constants related to the shape and dimension of the tip [161, 162]. Upon meniscus impact, the tip moves upward from its initial height by 20 nm [160]. It then oscillates due to the restoring and damping forces until it finally stabilizes at an equilibrium height of 10 nm. Other modeling study shows that the height of the water film under the tip almost doubles upon the formation of the field-induced meniscus [97]. The height increase is found also to increase considerably for higher humidity levels. From **Fig. 8.2a**, the adsorbed water film thickness increases from 11.35 nm to 15.23 nm only when the relative humidity increases from 1% to 80%. The increase in the water film thickness caused by field-induced meniscus is therefore much higher compared to the increase in the water film thickness caused by increasing the relative humidity. Also, due to the attraction of water molecules towards the tip under the electric field, the volume of the meniscus surrounding the tip will increase considerably. Therefore it could be concluded that the field-induced meniscus and its resulting considerable increase in the water film volume surrounding the tip will result in increasing the adhesive force between the AFM tip and sample surface considerably. Also, the influence of the field-induced meniscus on the adhesive force is expected to be much higher compared to the liquid mediated meniscus formed when no bias is applied.

The threshold electric field required to induce the formation of liquid bridges between a metallic tip and a flat metallic sample is given by [98]

$$E_{th} = \sqrt{\frac{2KT\rho\varepsilon \ln(1/RH)}{m\varepsilon_0(\varepsilon - 1)}} \quad (8.3)$$

where  $\rho$ ,  $m$ ,  $\varepsilon$  are the molecular density, molecular mass and dielectric constant of the liquid, respectively,  $RH$  is the employed relative humidity, and  $\varepsilon$  is the dielectric constant of the liquid. For water, Eq. 8.3 takes the form

$$E_{th} = 3.5\sqrt{\ln(1/RH)} \quad \text{V/nm} \quad (8.4)$$

When the tip radii of the AFM tip is large enough,  $E_{th} = V_{th}/D$ , where  $V_{th}$  is the threshold voltage, and  $D$  is the distance at which the field-induced meniscus forms. Based on Eq. 8.3, for a given tip-sample separation, the required threshold field for the formation of water bridges decreases considerably when the relative humidity increases. For example, at 5 nm tip-sample separation, the calculated value of  $V_{th}$  for relative humidity levels of 1% and 60% are found to be 24.7 V and 8.2 V, respectively. Though Eq. 8.3 is derived for metallic tip and sample surfaces, it can be applied in this study after considering the measured effective bias between the AFM tip and the  $\text{SiN}_x$  dielectric surface presented in **Fig. 8.5c**.

**Figure 8.5d** shows that for sample group B the adhesive force increases considerably at relatively small effective bias (around 5 V), and this increase is attributed to the field-induced meniscus formation. The considerable increase in adhesive force indicates obviously that the threshold field required to induce the formation of liquid bridges between AFM tip and the  $\text{SiN}_x$  surface has been reached. This is supported by the small calculated value of the threshold voltage at 60% relative humidity which is 8.2 V. In addition, higher relative humidity would lead to a stronger attractive capillary force since the adhesive force becomes longer ranged as explained earlier. According to that, the field-induced meniscus can persist at a longer tip-sample separation before bridge rupture [158]. Therefore the adhesive force measured at 60% relative humidity (group B) will increase considerably by the field-induced meniscus formation. For group A of samples, the maximum effective bias is found to be larger compared to group B as shown in **Fig. 8.5d**. In spite of that the increase in the adhesive force with the effective bias for group A is found to be smaller compared to group B. This indicates that for group A the threshold field required for the field-induced meniscus has not been reached by the range of applied bias used in these experiments. Comparing the adhesive force for groups A and B at higher bias, it can be concluded that at higher relative humidity levels the adhesive force resulting from the field-induced meniscus is much higher compared to the adhesive force caused by the attractive electrostatic force and/or the liquid mediated meniscus.

Two categories of capacitive MEMS switches (switch-A and switch-B) are assumed, which employ the sample groups A and B. In other words, switch-A is dehydrated under vacuum and then measured at 1% relative humidity similar to sample group A. Switch-B is also dehydrated under vacuum and then stored and measured under 60% relative humidity similar to sample group B. When no bias is applied and assuming that the surfaces of both the dielectric film and the switch bridge come in contact with each other, the interface will look like **Fig. 8.7a** and **Fig. 8.7b** for switch-A and switch-B, respectively. The figures show that the interfaces of both switches have many contacting and near-contacting asperities. Also the liquid mediated meniscus formation in switch-B is much higher than switch-A. This results in larger adhesive force between the switch bridge and the dielectric film in switch-B compared to switch-A as shown in **Fig 4a** for samples A and B.

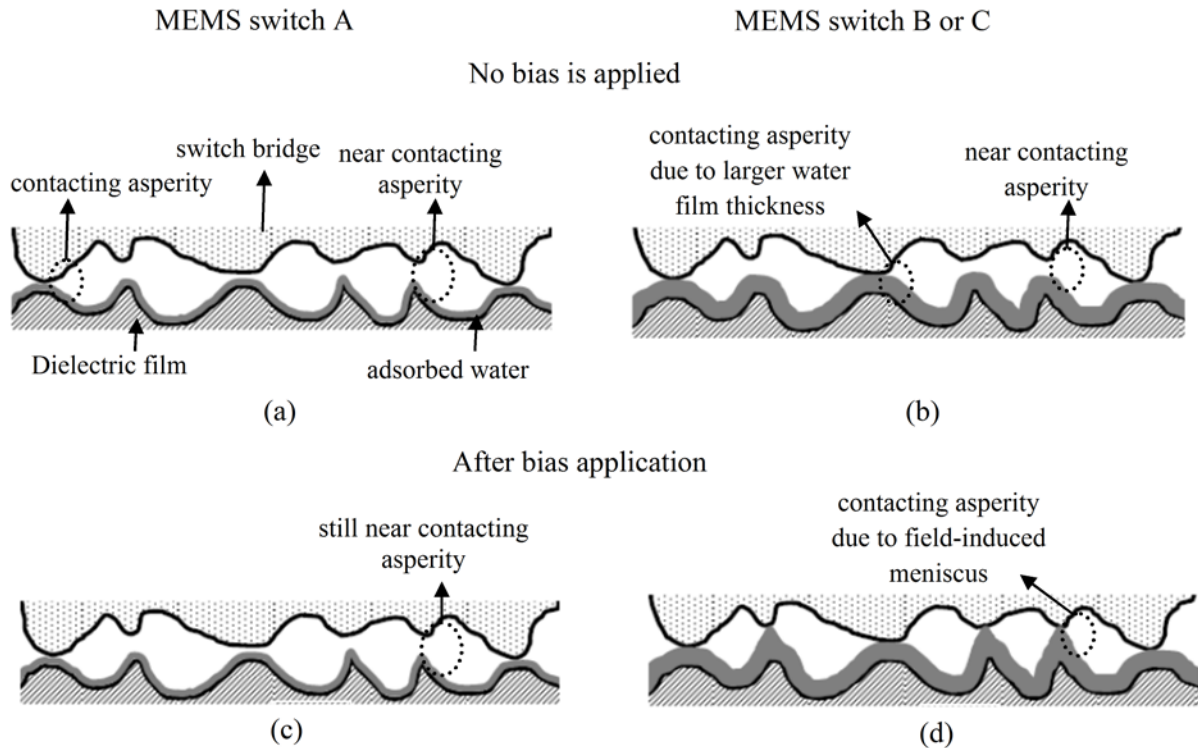


Figure 8.7. A cartoon showing the meniscus formation at the interface between the switch bridge and the dielectric film when no bias is applied for (a) MEMS switch of type A and (b) MEMS switch of type B or C, and after the bias application for (c) MEMS switch of type A and (d) MEMS switch of type B or C.

When bias is applied in order to actuate the switch, field-induced meniscus will be formed in the positions of contacting and near-contacting asperities for switch-B (**Fig. 8.7d**).

This might also occur in switch-A if the actuation voltage is large enough to reach the threshold voltage (**Fig. 8.7c**). Under any condition, the formation of the field-induced meniscus will be much higher in switch-B compared to switch-A, similar to the obtained results for samples B and A. This results in the formation of a water meniscus between the near-contacting asperities in switch-B as shown in **Fig. 8.7d**. Also, the volume of liquid mediated meniscus previously formed at the contacting asperities will increase in switch-B. When the applied bias is removed, the adhesive force between the switch bridge and the dielectric layer occurs under the effect of induced surface potential over the dielectric surface. As presented earlier, the induced surface potential in sample B is much larger compared to sample A. Therefore, the enhancement of the field-induced meniscus in switch-B is much larger compared to switch-A. Also, the attractive electrostatic force in switch-B will be much higher compared to switch-A. Based on this analysis, the adhesive force between the switch bridge and the dielectric film will be much higher in switch-B compared to switch-A. Considering the effect of the contacting asperities as well as the influence of the near-contacting asperities in switch-B, the difference between the adhesive force between switch-A and switch-B will be extremely higher compared to the difference measured between samples A and B in this study.

Based on the previous analysis, the adhesion or stiction between the switch bridge and the dielectric will be much faster in switch-B compared to switch-A, if both switches are stressed using the same bias and for the same time duration. This explains why MEMS switches operated at larger relative humidity have shorter lifetimes as reported in [66]. For switch-B, the main mechanism behind the stiction is the field-induced meniscus formation which is enhanced by the dielectric charging phenomenon. In other words, the electrostatic attractive force between the switch bridge and the dielectric film which results from the dielectric charging is not the main reason behind stiction in switch-B, as it is widely believed. For MEMS switch-A, if the induced surface potential reaches the critical threshold, field-induced meniscus will be formed, and the high resulting adhesive force will cause the switch stiction. If the induced surface potential in the long time range does not reach the threshold voltage, the stiction will be caused by the electrostatic attractive force. In this study, the induced surface potential is found to be 16.6 V when using a bias of 30 V for a very short time. As presented in [76], the induced surface potential increases almost exponentially with the charge injection duration. Therefore, the

threshold voltage might be reached also for switch-A under normal operation conditions for MEMS switches.

The influence of the sample annealing step could be assessed from the comparison between sample groups A and C. **Figure 8.5a** highlights that the increase in the adhesive force with the applied bias for sample group C is much higher compared to group A. The measured surface potential for group C is found to be slightly larger compared to group A as shown in **Fig. 8.5b**. This results in relatively smaller effective bias, hence electrostatic force, for group C compared to group A (**Fig. 8.5c**). The difference in adhesive force between both groups when no bias is applied is found to be also relatively small. Therefore the higher increase rate of adhesive force with the applied bias for group C compared to group A cannot be explained by the liquid mediated meniscus and/or by the electrostatic attractive force. Obviously, the difference between both groups is attributed to the field-induced meniscus formation. The adsorbed water film thickness over the dielectric surface for group C is larger compared to group A due to the dehydration step under vacuum performed for group A. Gómez-Monivas et al. [97] reported that the adsorbed water film thickness does not affect the field-induced meniscus formation. However, the increasing rate of adhesive force with the effective bias in group C compared to group A (**Fig. 8.5d**) clearly indicates that the field-induced meniscus is enhanced by increasing the adsorbed water film thickness. This could lead to the conclusion that the main source of adhesion or stiction for sample group C is the field-induced meniscus formation, and not the attractive electrostatic force or the liquid mediated meniscus force.

Once again, two MEMS switches are assumed, switch-A and switch-C, which resembles the investigated samples A and C, respectively. There are two main differences between switch-A and switch-C: the adsorbed water film thickness and surface potential induced by the dielectric charging. When no bias is applied, the higher thickness of the adsorbed water film in switch-C compared to switch-A will result in larger adhesive force for switch-C. This is attributed to increasing the volume of the meniscus surrounding the contacting asperities at the bridge/dielectric interface. Bridging the gap between near-contacting asperities by the thicker water film in switch-C compared to switch-A will result also in larger adhesive force in switch-C (see **Fig. 8.7a, b**). When bias is applied to actuate switch-C, the volume of the meniscus surrounding the contacting asperities will further increase due to the field-induced meniscus formation (**Fig. 8.7d**). Also, bridging the near-contacting asperities by water will be further

supported by the field-induced meniscus in switch-C. This is because the gap between the near-contacting asperities will be smaller due to the thicker water film in switch-C, and therefore the threshold voltage will be smaller. Thus the field-induced meniscus formation is expected to increase considerably with the adsorbed film thickness, and to be much higher in switch-C compared to switch-A.

From **Fig. 8.5c**, the induced surface potential in switch-C is slightly larger than switch-A. This relatively small difference results from charge injection for a very short time. With normal operating conditions of MEMS switches, the actuation time is much larger, and hence induced surface potential would be higher as reported in [76]. Therefore, in the long term the induced surface potential for switch-C will be much higher than switch-A. Therefore, the impact of the field-induced meniscus in switch-C will be much larger compared to switch-A. Based on this analysis the stiction between the switch bridge and the dielectric film for switch-C will be much faster compared to switch-A. This explains why annealing MEMS switches increases the device lifetime as reported by Czarnecki et al. [84]. Furthermore, it is concluded that the main reason behind the stiction of MEMS switch-C is not the dielectric charging itself, but it is the field-induced meniscus formation enhanced by the dielectric charging.

As presented in **Fig. 8.5b**, the induced surface potential in sample group B is much larger compared to group C due to the higher relative humidity employed for group B. This results in a smaller effective bias, hence smaller electrostatic force, for group B compared to group C. In spite of that the measured adhesive force under different applied bias (**Fig. 8.5a**) and the slope of increase of adhesive force versus the effective bias (**Fig. 8.5d**) is found to be comparable for both groups. This indicates that the adhesive force measured under different applied bias for both groups B and C results from the same mechanism which is the field-induced meniscus formation.

The influence of the applied bias on the friction force between the AFM tip and the  $\text{SiN}_x$  sample for sample groups A and B is presented in **Fig. 8.8**. The friction force is found to increase exponentially with the applied bias as highlighted in **Fig. 8.8a**. This has been observed for different applied mechanical normal loads and for both groups A and B. Also the increase trend of the friction force as a function of the applied bias for both groups is almost identical. As explained earlier, the adhesive force between the AFM tip and the sample surface increases with the applied bias (**Fig. 8.5a**). As given by Eq. 8.1, the friction force increases with increasing the adhesive force. As the applied bias increase, the normal load between the tip and the sample

surface also increases due to the larger attractive electrostatic force. The additional normal load under different applied bias was measured, and the results are shown in **Fig. 8.8b**. It is obvious that the normal load increases exponentially with the applied bias. From Eq. 8.1 and **Fig. 8.2b** (top), the relation between the friction force and the normal load is linear. Based on that, the exponential increase in the friction force with the applied bias shown in **Fig. 8.8a** is attributed to the measured exponential increase of the normal load versus the applied bias.

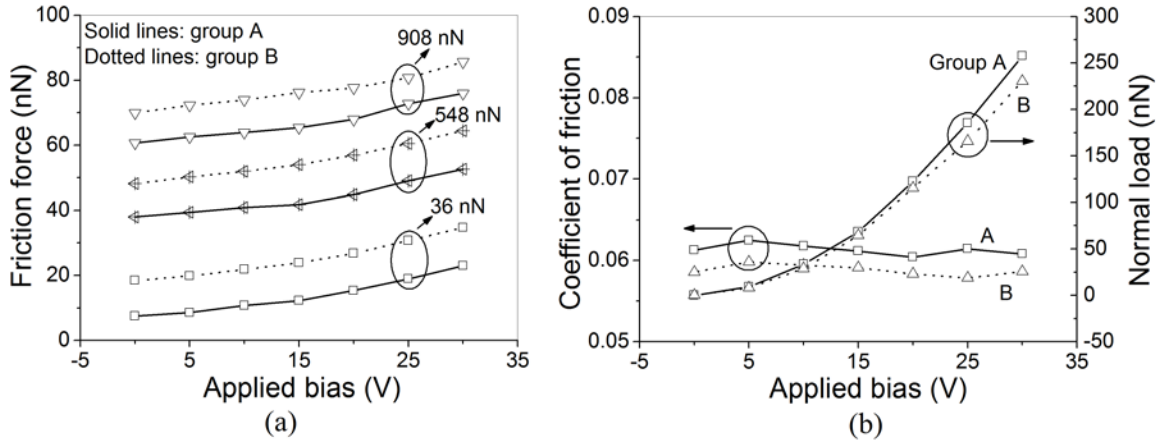


Figure 8.8. The impact of the applied bias on the friction force and the coefficient of friction for samples A and B: (a) the friction force as function of the applied bias under different normal loads, and (b) the measured additional normal load and the calculated coefficient of friction versus the applied bias.

The calculated coefficient of friction under different applied bias for groups A and B is shown in **Fig. 8.8b**. It is clear that the applied bias has a minimal impact on the coefficient of friction for both groups. In addition, the difference in the coefficient of friction calculated for both groups is found to be small for all applied bias values. This is attributed to the lubricant behavior of the adsorbed water layer in group B as explained earlier. Comparing **Fig. 8.2b** (bottom) and **Fig. 8.8b**, it is evident that the applied bias has a minimal effect on the coefficient of friction compared to the influence of relative humidity. Also, comparing **Fig. 8.5a** and **Fig. 8.8a** shows that the applied bias and hence the dielectric charging affects mainly the adhesive force and not the friction force. Therefore, it could be concluded that the adhesive force and not the friction force is the main force component which determines the lifetime of electrostatic capacitive MEMS switch.

## 8.5 Summary

The adhesive and friction forces were measured on the nanoscale under different relative humidity and electrical stress conditions in order to study the influence of the tribological phenomena at the interface of the MEMS switch suspended electrode and the dielectric on the reliability of these devices. The individual impact of the charging induced stiction and meniscus induced stiction in electrostatic MEMS switches has been presented for the first time. Also, the interaction between the two stiction mechanisms has been discussed. The main conclusive remarks from this chapter are the following:

- The adhesive force, and not the friction force, is the main force component which determines the lifetime of electrostatic MEMS switches.
- When the dielectric layer is not electrically stressed, the adhesive force induced by meniscus formation due to the adsorbed water layer is relatively small.
- When bias is applied, the adhesive force increases considerably for non-annealed dielectric films even when measured at very low humidity due to the field-induced meniscus formation.
- For the annealed samples, the contribution of the field-induced meniscus is very high when the sample is stored under large humidity level even for short storage duration.
- These results explain why MEMS switches operated at larger relative humidity have shorter lifetimes, and why annealing MEMS switches increases the device lifetime.

To sum up, the study reports a new possible failure mechanism that could causes stiction in electrostatic MEMS/NEMS devices, the electric field-induced meniscus, and explains how to reduce its effects.

*Man's mind, once stretched by a new idea, never  
regains its original dimensions.*

*Oliver Wendell Holmes  
1809 – 1894, American author and physician*

### **Conclusions**

The thesis presents a comprehensive study of the dielectric charging failure mechanism and provides an in-depth investigation for different tribological effects, for example stiction, in electrostatic MEMS/NEMS. These phenomena affect the reliability of several electrostatic MEMS devices, especially capacitive MEMS switches, which are the case study for this thesis. The influence of various parameters on the charging/discharging processes in PECVD SiN<sub>x</sub> films was investigated. This includes the impact of the dielectric film thickness, dielectric deposition conditions, substrate, electrical stress conditions, environment medium, environment contaminants, and the relative humidity. A large variety of samples were studied including bare dielectric films, MIM capacitors, and MEMS switches. A complete package of novel nanoscale characterization techniques based on KPFM and FDC measurements were proposed and used to investigate the charging phenomenon in addition to the conventional assessment methods. The obtained electrical results were explained in view of the material characterization data of FT-IR and XPS. Finally, the stiction mechanisms were studied by measuring the adhesive and friction forces on the nanoscale under different electrical stress and relative humidity levels.

The proposed assessment methods were correlated and compared with the C/DCT and TSDC techniques. The C/DCT, KPFM, and FDC-based characterization methods reveal that both the injected charge density in the dielectric film and the relaxation time constant increase with the charging electric field. The FDC-TF and KPFM-TF techniques are shown to efficiently simulate charge injection and collection through a single asperity where the AFM tip doesn't contribute to the charge injection/collection processes. Both FDC-TF and FDC-MIM were used

to study the charge build-up with time during the charging process as well as the charge collection during discharging. This resembles an important advantage for these techniques over KPFM methods which cannot investigate the charging process with time. The FDC-MIM methodology exhibits a considerable advantage over FDC-TF simulating the real scenarios of charging/discharging in MEMS switches which take place in the whole dielectric area simultaneously. The KPFM-MIM and KPFM-MEMS methods lead to comparable decay time constants. Similar observation has been made for the FDC-MEMS and FDC-MIM techniques. Therefore, MIM capacitors and MEMS switches can lead to similar conclusions regarding the electrical properties of MEMS dielectric films when assessed properly using KPFM or FDC. This recommends the application of KPFM-MIM and FDC-MIM as powerful and low cost characterization tools for studying the charging phenomenon in MEMS.

The stretched exponential equation fits properly with the charging/discharging current transients measured by C/DC, the induced surface potential decay measured by KPFM, and the charging/discharging adhesive force decay measured by FDC. In all cases, the calculated time constant increases with the experiment time window. Due to the different charge collection processes in the abovementioned assessment methods, the resulting discharging time constant from these techniques vary significantly. Thus, in C/DCT, the charge collection by the injecting electrodes reveals always shorter relaxation times. In contrast, in KPFM and FDC methods, hence in MEMS, the injected charges are collected by the opposite electrodes which lead to longer relaxation time. Using the TSDC method allows determining the time constant dispersion over a wide range of values simultaneously, and so it could be used as a complementary characterization tool to the KPFM, FDC and C/DCT methods.

Larger injected charge density has been measured for thicker dielectric films compared to thinner ones for a given stress electric field although FT-IR and XPS reveal comparable material stoichiometry for  $\text{SiN}_x$  films with different thicknesses. Also,  $\text{SiN}_x$  films with different thicknesses show a similar discharging behavior when stressed with the same electric field. As a result, thicker  $\text{SiN}_x$  films are preferable for MEMS switches with reduced dielectric charging. Moreover, the  $\text{SiN}_x$  films deposited over metal layers and over Si substrates have the same material stoichiometry as obtained from FT-IR and XPS. Yet, the  $\text{SiN}_x$  films deposited over metal layers exhibit larger injected charge density and faster charge collection process compared to the  $\text{SiN}_x$  deposited over silicon substrates. This has been attributed mainly to the presence of

## CONCLUSIONS

---

the depletion region, interface states and the more pronounced MWS effect in  $\text{SiN}_x$  samples deposited directly over silicon. It also explains the reported data in literature related to the considerable influence of the substrate charging on the shift in pull-in voltage and lifetime of MEMS switches. The induced surface potential and adhesive force and their decays measured by KPFM and FDC are almost identical for  $\text{SiN}_x$  films deposited over evaporated gold, electrochemically-deposited gold and evaporated titanium. Those  $\text{SiN}_x$  films show a comparable material stoichiometry as found from FT-IR and XPS data. It is therefore concluded that the work function and roughness of the underlying metal layer have almost no effect on the charging/discharging of the dielectric.

The electric field intensity and the pulse duration are the main dominant parameters in determining the injected charge density in  $\text{SiN}_x$  films that have similar material stoichiometry. The injected charge density and the relaxation time are found to be higher when charges are injected using larger electric field and/or longer charging durations. This agrees with the measurement results obtained from the charging study of capacitive MEMS switches. The injected charge density is larger and the charge relaxation time is longer when the  $\text{SiN}_x$  dielectric film is charged using negative voltage compared to positive voltage. This also explains the shift in the C-V characteristics for MEMS switches actuated using bipolar signals.

Varying the PECVD deposition conditions of the  $\text{SiN}_x$  films shows a very high impact on the charging/discharging processes. The injected charge density and the relaxation time decreases with increasing the silane/ammonia ratio. This is attributed to increasing the silicon content in the investigated  $\text{SiN}_x$  films with increasing the gas ratio as observed from FT-IR and XPS data, which results in larger leakage current, higher concentration of defects and larger number of charge trapping centers. Charge redistribution paths, therefore, increase, with the silicon content in the  $\text{SiN}_x$  film and consequently the redistribution current will be larger and will lead to a smaller charge density at the dielectric surface. For these reasons, the charge injection/redistribution equilibrium, which determines the injected charge density measured by KPFM or FDC, will be attained at a smaller surface charge density with larger gas ratio. The difference in the injected charge density for  $\text{SiN}_x$  samples deposited using different RF power, though small, cannot be fully explained based on the data obtained by FT-IR and XPS, which highlights that the material stoichiometry of these films are quite similar. The density and distribution of defects in  $\text{SiN}_x$  films is expected to be larger as the deposition RF power

increases. This results in larger charge redistribution paths, higher redistribution currents, and consequently faster charge decay as the deposition RF power increases.

What's more, increasing the substrate temperature results in slightly reducing the injected charge density and making the charge collection process relatively faster, in spite of the non-pronounced variation in N/Si atomic ratio for these samples as obtained by FT-IR and XPS. This indicates that the charge redistribution is relatively larger with higher deposition temperature which results in attaining the charge injection/redistribution equilibrium at smaller charge density at the dielectric surface. This is attributed mainly to reducing the hydrogen content in the SiN<sub>x</sub> film, increasing the film stress, changing trap concentrations, and reducing film conductivity when deposition temperature increases. Both KPFM and FDC measurements leads to similar conclusions regarding the influence of gas ratio, RF power, and temperature on the charging/discharging processes in the investigated SiN<sub>x</sub> films. Based on these techniques, it was shown that the influence of gas ratio on the charging/discharging process in SiN<sub>x</sub> films is much larger compared to the effect of substrate temperature and RF power. This is in good agreement with the results obtained from FT-IR and XPS which highlights that the reactive gas ratio has a larger influence on the SiN<sub>x</sub> material stoichiometry compared to the effect of RF power or substrate temperature. Finally, the HF SiN<sub>x</sub> is more reliable with respect to the dielectric charging compared to the LF SiN<sub>x</sub> since the HF material has smaller injected charge density and faster charge decay. This has been attributed to the more silicon content, density of defects, and random spatial distribution of the layers in HF SiN<sub>x</sub>.

Increasing the relative humidity results in larger injected charge density and faster discharging process in air and nitrogen environments. The increase of the injected charge density with the relative humidity are attributed to many reasons among which are the conductivity of the adsorbed water film, the amount of the surface charge which exists on the dielectric surface, and finally the less confined electric filed distribution between the tip and the sample surface as the adsorbed water layer increases, when employing higher relative humidity levels. In addition, the decrease in relaxation time for both air and nitrogen with increasing humidity is attributed mainly to the faster neutralization of surface charges with the external medium as well as to the conductivity increase of adsorbed water film over the SiN<sub>x</sub> surface. In view of the KPFM nanoscale results obtained in this study, the reported increase in the measured shift in actuation voltage for capacitive MEMS switches with increasing relative humidity in previous studies

## CONCLUSIONS

---

could be explained. No correlation has been observed between the trend of evolution of the KPFM potential distribution and the surface potential decay with time. Therefore, it is concluded that the charge collection is not attributed to lateral charge redistribution over the dielectric surface.

Nitrogen environment is shown to be more favorable as a packaging environment compared to air to reduce the dielectric charging in electrostatic MEMS. The injected charge density in nitrogen is smaller than in air for the same charge injection voltage and environment conditions. This is partially attributed to the difference between air and nitrogen in charging due to the gas discharge in the gap between the AFM tip volume and the underlying electrode. On the other side, faster charge decay has been observed in nitrogen compared to air, which agrees with the reported lifetime measurements for capacitive MEMS switches. The difference in relaxation time between air and nitrogen are due to several reasons including the difference in the amount of available counterions, the electrical conductivity of the medium, surface charge, and finally the injected charge density for both environments. Additionally, smaller injected charge density and shorter decay time constant have been observed when plugging the oxygen filter with the nitrogen line and/or the hydrocarbon filter with the air line. For measurements performed in air, the impact of the hydrocarbon contaminants is more pronounced in the discharging process. When the oxygen trap is engaged with the nitrogen line the relaxation time decreases considerably indicating the significant role that oxygen plays during the discharge process even when existing with a small amount. It is therefore concluded that high purified nitrogen or air packaging environments could reduce the dielectric charging in MEMS remarkably.

Nanotribological measurements performed under different relative humidity and several electrical stress conditions reveal that the adhesive force, and not the friction force, is the main force component which determines the lifetime of electrostatic capacitive MEMS switch. Moreover, the adhesive force resulting from the electric field-induced meniscus is found to be a dominant stiction mechanism. The adhesive force induced by meniscus formation due to the adsorbed water layer is found to be relatively small when the dielectric layer is not electrically stressed. When the bias is applied and/or the dielectric film is charged, the adhesive force increases considerably for dielectric films which have not been annealed even when measured at a very low humidity level, due to the field-induced meniscus mechanism. For the annealed samples, the contribution of the field-induced meniscus is found to be very high when the sample

is stored under larger relative humidity even for a shorter storage time. This explains why annealing MEMS switches increases the device lifetime, and why MEMS switches operated at larger relative humidity have shorter lifetimes. Therefore, the electric field-induced meniscus should be recognized as a possible failure mechanism for electrostatic MEMS/NEMS devices.

In summary, the thesis provides a deeper insight to the influence of various key parameters on the charging phenomenon based on novel characterization methodologies. It also reports a new possible failure mechanism, the field-induced meniscus, that could cause stiction in electrostatic MEMS. The thesis highlights that the integration between results from KPFM on the level of a single asperity, FDC on the level of multi asperity including tribological effects, C/DCT and TSDC on the device level resembles complementary characterization tools for a better understanding of the charging related failure mechanisms in MEMS. In addition, KPFM and FDC provide proper explanations for the reported measurement results from actual MEMS devices, which further emphasizes the usefulness of these low cost assessment methods. Considering the lack of available information on the topic, it is believed that the present thesis opens the door towards building more reliable electrostatic MEMS/NEMS devices.

*It is not hard to learn more. What is hard is to unlearn when you discover yourself wrong.*

*Martin H. Fischer*

*1879 – 1962, German-born American physician and author*

### **Conclusions**

Les travaux présentés dans cette thèse portent sur l'étude des mécanismes de défaillance dans les micro-commutateurs RF à contact capacitif et à actionnement électrostatique qui sont liés au chargement des diélectriques et en intégrant une analyse approfondie des effets tribologiques. Les phénomènes de charge/décharge ont été étudiés pour des films de nitrure de silicium obtenus par PECVD dans différentes conditions (épaisseur, conditions de dépôts, type de substrat) et pour différentes conditions de tests (niveau et signe de la contrainte électrique, humidité, contamination). Une large variété de dispositifs ont été analysés tels que les films sur substrats, les capacités MIM (Métal-Isolant-Métal) et les micro-commutateurs. Des techniques à l'échelle nanométrique basées sur la microscopie à force atomique (KPFM : Kelvin Probe Force Microscopy, FDC : Force-Distance Curves) ont été utilisées et comparées aux méthodes plus conventionnelles (C/DCT : Charge/Discharge Current Transient, TSDC : Thermally Stimulated Depolarization Current). Les résultats obtenus ont ensuite été analysés à l'aide des propriétés structurales des diélectriques obtenues par XPS et par FTIR. Finalement les mécanismes de collage ont été étudiés en mesurant les forces de friction et d'adhésion à l'aide de l'AFM pour différents niveaux de contrainte électrique et pour différents taux d'humidité.

Ces nouvelles techniques, utilisant la pointe de l'AFM pour l'injection des charges, ont montré qu'elles permettaient de reproduire fidèlement les phénomènes présents dans les MEMS, à savoir l'injection à travers la rugosité de surface et la collection des charges par l'électrode présente sous le diélectrique. La pointe de l'AFM ne contribue pas également de manière significative au déchargement lors des injections effectuées en mode contact intermittent. Tous

les résultats obtenus avec des structures MIM amènent aux mêmes conclusions concernant le comportement des diélectriques que celles obtenues avec des MEMS. Ceci permet de mener des études de chargement plus rapidement grâce à la complexité plus faible des structures MIM. La technique FDC présente par ailleurs plusieurs avantages par rapport à la technique KPFM : une mise en œuvre plus simple, la possibilité de suivre le procédé de chargement au cours du temps grâce à la simultanéité de l'injection et de la mesure de la force de contact, une gamme de chargements beaucoup plus élevés qui correspond plus à ceux présents dans les MEMS.

La cinétique de chargement et déchargement a été modélisé, avec toutes les techniques utilisées, par une équation exponentielle à puissance variable avec une excellente corrélation par rapport aux mesures. Le temps de relaxation des charges obtenus diffère notablement suivant la technique utilisée pour le suivi du déchargement. Pour la technique classique (C/DCT) les charges sont collectées par l'électrode supérieure de la capacité MIM et le temps de relaxation est donc inférieur. Pour les techniques AFM (KPFM et FDC), les charges sont collectées par l'électrode inférieure (comme dans le cas réel des MEMS) et le temps de relaxation est plus long. Mais dans tous les cas, le temps de relaxation augmente si on augmente la durée de la fenêtre d'observation. Ceci est certainement lié à la présence de plusieurs mécanismes de relaxation avec des énergies d'activation différentes. La technique classique de TSDC peut ainsi donner des informations complémentaires par rapport aux autres techniques.

Le chargement de films de  $\text{SiN}_x$  obtenus par PECVD a été étudié pour différentes conditions d'élaboration et par les différentes techniques décrites précédemment. Les conclusions obtenues sont décrites dans ce paragraphe. La densité de charge injectée et le temps de relaxation de ces charges augmentent avec l'intensité du champ électrique, avec la durée d'injection et pour des tensions négatives. Ces résultats sont en accord avec ceux obtenus sur les études de fiabilité menées sur des micro-commutateurs à contact capacitif. Pour un niveau de stress électrique identique (même champ électrique) appliqué sur un film de  $\text{SiN}_x$ , la densité de charge injectée augmente avec l'épaisseur du diélectrique mais le temps de relaxation reste comparable. Il est donc préférable d'utiliser une épaisseur de diélectrique la plus élevée possible pour limiter les problèmes de chargement dans les MEMS.

Le type de matériau présent sous le diélectrique a également un impact sur le chargement. Un dépôt sur du métal présente une densité de charge injectée plus élevée et un temps de relaxation plus court que ceux obtenus avec un dépôt sur silicium. Nous avons montré que la

## CONCLUSIONS

---

stœchiométrie du diélectrique était identique dans les deux cas et ce comportement est attribué principalement à la présence d'une région de déplétion et d'état d'interfaces plus importants dans le cas du silicium. Ceci explique les résultats obtenus dans la littérature concernant l'influence du chargement par le substrat en silicium dans les micro-commutateurs RF. Par contre peu d'effets significatifs ont été trouvés en fonction du type de métal (or évaporé, or électrodéposé, titane) présent sous le diélectrique ni en fonction de la rugosité du métal.

L'impact du rapport des gaz, de la puissance RF, de la fréquence RF (HF ou BF), de la température du substrat sur la cinétique de chargement/déchargement a également été analysé. Les paramètres les plus importants sont ceux qui modifient la stœchiométrie du dépôt de  $\text{SiN}_x$  (rapport du débit de gaz, fréquence RF). Plus le diélectrique est riche en silicium (débit de  $\text{SiH}_4/\text{NH}_3$  élevé,  $\text{SiN}_x$  HF), plus la densité de charges et le temps de relaxation sont faibles. Ceci est attribué à un courant de fuite plus important, à une concentration de défauts plus grande et un nombre plus important de pièges dans le diélectrique. L'écoulement des charges à travers le volume du diélectrique est donc augmenté ce qui donne une plus faible concentration de charges à la surface du diélectrique.

Le chargement de films de  $\text{SiN}_x$  a été étudié pour différentes conditions environnementales de tests. Les conclusions obtenues sont décrites dans ce paragraphe. L'augmentation du niveau d'humidité (aussi bien sous air que sous azote) entraîne une augmentation de la densité de charge et une diminution du temps de relaxation. Ceci est attribué à la présence du film d'eau adsorbé à la surface. Celui-ci entraîne une augmentation de la quantité de charges injectées grâce à une plus forte conductivité électrique de surface et à un champ électrique moins confiné. La diminution du temps de relaxation est attribuée à la neutralisation plus rapide des charges par ce film d'eau. Ces résultats confirment les études reportées dans la littérature sur l'augmentation du chargement dans les micro-commutateurs RF lorsque le taux d'humidité augmente.

Nous avons montré également que l'azote était plus favorable que l'air pour réduire le chargement (densité de charge et temps de relaxation plus faible) dans les diélectriques, ce qui est confirmé par les études de fiabilité sur les micro-commutateurs RF de la littérature. Ceci peut être attribué aux propriétés différentes des deux gaz qui entraîne une modification de l'injection entre la pointe AFM et la surface et de la neutralisation des charges en surface. Par ailleurs, l'utilisation de filtres (à oxygène ou à hydro-carbonnes), sur la ligne de gaz entraîne une

diminution de la densité de charge et du temps de relaxation. Cet effet est plus prononcé pour l'air que pour l'azote. Le packaging des MEMS doit donc être très bien contrôlé pour minimiser le chargement des diélectriques.

Des études de nanotribologie ont été menées grâce à la technique FDC. Nous avons montré tout d'abord que les forces d'adhésion étaient prépondérantes devant les forces de friction. S'il est bien connu que la présence d'humidité augmente les forces d'adhésion, nous avons mis en évidence que les forces d'adhésion augmentaient considérablement lorsqu'un champ électrique était couplé avec cette humidité. Ceci est lié à la formation d'un ménisque d'eau (entre la pointe de l'AFM et la surface du diélectrique), dont la hauteur augmente avec le champ électrique. La surface de contact s'en trouve donc augmentée. Ceci explique clairement l'importance de la suppression de toute présence d'humidité pour améliorer la fiabilité des MEMS. Le recuit des échantillons avant caractérisation permet de réduire considérablement ce phénomène en désorbant le film d'eau présent à la surface.

En résumé, cette thèse a permis d'identifier les paramètres clés qui gouvernent le chargement des diélectriques grâce à une nouvelle méthodologie de caractérisation basée sur l'utilisation de l'AFM. Différentes techniques ont été développées (KPFM, FDC) aussi bien sur des films diélectriques que sur des capacités MIM et sur des MEMS et ont été comparées aux techniques classiques (C/DCT, TSDC). Il apparaît clairement que ces nouvelles techniques apportent un nouvel éclairage sur l'étude du chargement des diélectriques et permettent de mieux appréhender la complexité des phénomènes tout en ne nécessitant pas de dispositifs complexes à fabriquer.

*The important thing in science is not so much to obtain new facts as to discover new ways of thinking about them.*

*Sir William Bragg  
1862 – 1942, British physicist and chemist  
Nobel Prize for Physics in 1915*

### **Outlook**

Further validation of the proposed characterization techniques in this thesis is still required and could be made through comparing the results from these methods to the measurements of actual MEMS devices that have the same dielectric films. For this purpose, a complete set of electrostatic capacitive MEMS switches with selected SiN<sub>x</sub> films and underlying metal layers from the investigated ones in the present work are currently under fabrication. This includes switches with different dielectric thickness, dielectric deposition conditions, and underlying metals. The charging phenomena in these switches will be characterized based on monitoring the shift of the bias for capacitance minimum to reduce the contribution of the mechanical part of the switch to the measurements, and the results will be correlated to the KPFM and FDC data presented in this thesis. Following this validation, a 2D and 3D study for the influence of different deposition parameters on the charging/discharging processes and on the material stoichiometry of SiN<sub>x</sub> films could be performed. So, instead of changing individually a single deposition parameter at a time, two and then three parameters will be varied simultaneously, and the influence on the electrical and chemical properties of the deposited films will be studied. This should help to determine the optimum deposition conditions of PECVD SiN<sub>x</sub> films that lead to minimal charging. On the other hand, other material characterization techniques rather than FT-IR and XPS used extensively in this thesis should be employed to provide a better insight to the material stoichiometry of the investigated dielectrics films. We have seen for example that the hydrogen content cannot be quantified using FT-IR and XPS.

While performing this study, we had to decide whether to investigate a specific dielectric material ‘in-depth’ and propose several novel characterization techniques or to introduce a single assessment method and then use it to study several dielectric materials. As the thesis shows, the former approach has been selected and only SiN<sub>x</sub> material has been investigated while a complete package of novel characterization methods have been introduced. Hopefully, we were right taking this decision! It is time now to start applying these methods to study the charging in different dielectric materials, of course following the required validation mentioned above. In addition to the KPFM and FDC based techniques proposed in this thesis, other AFM based assessment methods could be introduced to further investigate the charging in MEMS thanks to the available variety of these measurements. For example, conductive AFM (CAFM), tunneling AFM (TUNA), scanning spreading resistance microscopy (SSRM), and scanning capacitance microscopy (SCM) might be useful tools for this purpose.

The results of this thesis have been presented in many international reviewed conferences (ex. Transducers, IRPS, ESREF, MRS, and AVS) where it has been our pleasure to find several companies and laboratories worldwide showing high interest in using our proposed characterization techniques to improve the reliability of their MEMS devices. The clear message behind such interest is the lack of available knowledge on several reliability concerns of MEMS especially those related to the charging failure mechanisms. This necessitates the introduction of novel assessment methodologies that originate, in most of cases, from *creative* solutions. In other words, we need to *think out of the box* to improve the MEMS reliability.

*We should be careful to get out of an experience only the wisdom that is in it - and stop there; lest we be like the cat that sits down on a hot stove-lid. She will never sit down on a hot stove-lid again - and that is well; but also she will never sit down on a cold one anymore.*

Mark Twain  
1835 – 1910, American author and humorist

## References

- [1] Hartzell, A. L., M. Silva, and H. Shea (2011), *MEMS Reliability*, Springer, New York, USA.
- [2] Tabata, O., and T. Tsuchiya (2008), *Reliability of MEMS: Testing of Materials and Devices*, Wiley-VCH, Weinheim, Germany.
- [3] EDFAS Desk Reference Committee (2011), *Microelectronics Failure Analysis Desk Reference*, sixth edition, ASM International, Cleveland, Ohio, USA.
- [4] De Wolf, I. (2006), "Reliability of MEMS," *Proc. of the 7th Int. Conf. on Thermal, Mechanical and Multiphysics Simulation and Experiments in Micro-Electronics and Micro-Systems (EuroSime 2006)*, pp. 1-6.
- [5] <http://www.iec.ch/>.
- [6] <http://www.landandmaritime.dla.mil/programs/milspec/ListDocs.asp?BasicDoc=MIL-STD-883>.
- [7] Tanner, D. M. (2009), "MEMS reliability: Where are we now?," *J. Microelectron. Reliab.* **49**, 937–940.
- [8] Rebeiz, G. M. (2003), *RF MEMS theory, design, and technology*, John Wiley & Sons, Inc., Hoboken, New Jersey.
- [9] Yao, J. (2000), "RF MEMS from a device perspective," *J. Micromech. Microeng.* **10**, R9.
- [10] Yao, Z., S. Chen, S. Eshelman, D. Denniston and C. Goldsmith (1999), "Micromachined low-loss microwave switches," *J. Microelectromech. Syst.* **8**, 129-134.
- [11] Rebeiz, G. and J. Muldavin (2001), "RF MEMS switches and switch circuits," *IEEE Microw. Mag.*, **2**, 59-71.
- [12] Newman, H. (2002), "RF MEMS switches and applications," *2002 IEEE Int. Reliability Physics Symposium Proc.*, pp. 111-115, IEEE, New York.
- [13] Pacheco, S., C. Nguyen and L. Katehi (1998), "Micromechanical electrostatic K-band switches," *1998 IEEE MTT-S Int. Microwave Symp. Dig.*, pp. 1569-1572, IEEE, New York.
- [14] Goldsmith, C., D. Forehand, Z. Peng, J. Hwang and I. Ebel (2007), "High-cycle life testing of RF MEMS switches," *2007 IEEE MTT-S Int. Microwave Symp. Proc.*, pp. 1805-1808, IEEE, New York.

- [15] Puyal, V., D. Dragomirescu, C. Villeneuve, J. Ruan, P. Pons and R. Plana (2009), "Frequency Scalable Model for MEMS Capacitive Shunt Switches at Millimeter-Wave Frequencies," *IEEE Trans. Microw. Theory Tech.* **57**, 2824-2833.
- [16] Mihailovich, R., M. Kim, J. Hacker, E. Sovero, J. Studer, J. Higgins and J. DeNatale (2001), "MEM relay for reconfigurable RF circuits," *IEEE Microwave and Wireless Components Letters* **11**, 53-55.
- [17] Modlinski, R., A. Witvrouw, P. Ratchev, A. Jourdain, V. Simons, H. Tilmans, J. Den Toonder, R. Puers and I. De Wolf (2004), "Creep as a reliability problem in MEMS," *J. Microelectron. Reliab.* **44**, 1733-1738.
- [18] Oya, Y., A. Okubora, M. Van Spengen, P. Soussan, S. Stoukatch, X. Rottenberg, P. Ratchev, H. Tilmans, W. De Raedt and E. Beyne (2004), "A reliable and compact polymer-based package for capacitive RF-MEMS switches," *International Electron Devices Meeting*, pp. 31-34, IEEE, New York.
- [19] Wibbeler, J., G. Pfeifer and M. Hietschold (1998), "Parasitic charging of dielectric surfaces in capacitive microelectromechanical systems (MEMS)," *Sens. Actuator A-Phys.* **71**, 74-80.
- [20] Bhushan, B. (2011), *Nanotribology and Nanomechanics I - Measurement Techniques and Nanomechanics*, third edition, Springer-Verlag, Heidelberg, Germany.
- [21] Goldsmith, C., J. Ehmke, A. Malczewski, B. Pillans, S. Eshelman, Z. Yao, J. Brank and M. Eberly (2001), "Lifetime characterization of capacitive RF MEMS switches," *2001 IEEE MTT-S Int. Microwave Symp. Proc.*, pp. 227-230, IEEE, New York.
- [22] Man, K. (1999), "MEMS reliability for space applications by elimination of potential failure modes through testing and analysis," *Proc. of SPIE MEMS reliability for Critical and Space applications, Vol. 3880*, (eds. R. A. Lawton, W. M. Miller, G. Lin and R. Ramesham), pp. 120-129, SPIE, Bellingham, Washington.
- [23] ESA Endorfins project, Contract no 18613/05/NL/1A.
- [24] Reid, J. and R. Webster (2002), "Measurements of charging in capacitive microelectromechanical switches," *Electron. Lett.* **38**, 1544-1545.
- [25] Rottenberg, X., B. Nauwelaers, W. De Raedt and H. Tilmans (2004), "Distributed dielectric charging and its impact on RF MEMS devices," *Proc. of the 34th European Microw. conf.*, pp. 77-80, IEEE, New York.
- [26] Van Spengen, W., R. Puers, R. Mertens and I. Wolf (2004), "A comprehensive model to predict the charging and reliability of capacitive RF MEMS switches," *J. Micromech. Microeng.* **14**, 514-521.
- [27] Melle, S., D. De Conto, D. Dubuc, K. Grenier, O. Vendier, J. Muraro, J. Cazaux and R. Plana (2005), "Reliability modeling of capacitive RF MEMS," *IEEE Trans. on Microw. Theory Tech.* **53**, 3482-3488.
- [28] Yuan, X., J. Hwang, D. Forehand and C. Goldsmith (2005), "Modeling and characterization of dielectric-charging effects in RF MEMS capacitive switches," *2005 IEEE MTT-S Int. Microwave Symp. Dig.*, pp. 753-756, IEEE, New York.
- [29] Czarnecki, P., X. Rottenberg, R. Puers, I. De Wolf, (2006) "Effect of gas pressure on the lifetime of capacitive RF MEMS switches," *Proc. of the 19th IEEE Int. Conf. on Micro Electro Mechanical Systems (MEMS)*, pp. 890-893, IEEE, New York.
- [30] X. Rottenberg, I. De Wolf, B. K. J. C. Nauwelaers, W. De Raedt, and H. A. C. Tilmans, (2007) "Analytical model of the DC actuation of electrostatic MEMS devices with

- distributed dielectric charging and nonplanar electrodes," *IEEE/ASME J. Microelectromech. Syst.*, **16**, 1243-1253.
- [31] Olszewski, Z., R. Duane, and C. O'Mahony, (2008) "A study of capacitance-voltage curve narrowing effect in capacitive microelectromechanical switches," *Appl. Phys. Lett.* **93**, Art. #094101.
- [32] Vandershueren, J. and J. Casiot in: P. Braunlich, Ed. (1979), *Topics in Applied Physics: "Thermally stimulated relaxation in solids"*, Springer-Verlag, Heidelberg, Germany.
- [33] Van Turnhout, J., in: G.M. Sessler, Ed. (1987), *Topics in Applied Physics: "Electrets"*, **33**, ch. 3, pp. 81-216, Springer-Verlag, Berlin.
- [34] Kao, K. C. (2004), "Dielectric Phenomena in Solids, With Emphasis on Physical Concepts of Electronic Processes," *Elsevier Academic Press*.
- [35] Ramprasad, R. (2003), "Phenomenological theory to model leakage currents in metal-insulator-metal capacitor systems," *Phys. Status Solidi B-Basic Solid State Phys.* **239**, 59-70.
- [36] Lamhamdi, M., J. Guastavino, L. Boudou, Y. Segui, P. Pons, L. Bouscayrol and R. Plana (2006), "Charging-Effects in RF capacitive switches influence of insulating layers composition," *J. Microelectron. Reliab.* **46**, 1700-1704.
- [37] Zaghoul, U., G. Papaioannou, F. Coccetti, P. Pons and R. Plana (2009), "Dielectric charging in silicon nitride films for MEMS capacitive switches: Effect of film thickness and deposition conditions," *J. Microelectron. Reliab.* **49**, 1309-1314.
- [38] Frenkel, J. (1938), "On pre-breakdown phenomena in insulators and electronic semiconductors," *Physical Review* **54**, 647-648.
- [39] Harrell, W.R., and J. Frey (1999), "Observation of Poole-Frenkel effect saturation in SiO<sub>2</sub> and other insulating films," *Thin Solid Films* **352**, 195-204.
- [40] Cherki, C., R. Coelho and R. Nannoni (1972), "Influence of interfacial tunnel exchange on dielectric losses in thin amorphous insulating films," *Physica Status Solidi (a)*, **2**, 785-796.
- [41] Perera, R., A. Ikeda, R. Hattori and Y. Kuroki (2003), "Trap assisted leakage current conduction in thin silicon oxynitride films grown by rapid thermal oxidation combined microwave excited plasma nitridation," *J. Microelectronic Engineering*, **65**, 357-370.
- [42] Yuan, X., S. Cherepko, J. Hwang, C. L. Goldsmith, C. Nordquist, and C. Dyck (2004), "Initial Observation and Analysis of Dielectric-Charging Effects on RF MEMS Capacitive Switches," *International Microwave Symposium*, pp. 1943-1946.
- [43] Melle, S., F. Flourens, D. Dubuc, K. Grenier, P. Pons, F. Presseccq, J. Kuchenbecker, J. L. Muraro, L. Bary, and R. Plana (2003), "Reliability overview of RF MEMS devices and circuits," *Proc. 33rd Eur. Microwave Conf.*, pp. 37-40.
- [44] Papaioannou, G., M. Exarchos, V. Theonas, G. Wang and J. Papapolymerou (2005), "Temperature study of the dielectric polarization effects of capacitive RF MEMS switches," *IEEE Trans. Microw. Theory Tech.* **53**, 3467-3473.
- [45] Lisec, T., C. Huth, and B. Wagner (2004), "Dielectric material impact on capacitive RF MEMS reliability," *34th European Microwave Conf.*, pp. 73 - 76.
- [46] Papaioannou, G. J., and T. Lisec (2007), "Dielectric charging process in AlN RF-MEMS capacitive switches," *Proc. 2nd European Microwave Integrated Circuits Conf.*, pp. 540-543.

- [47] Papandreou, E., G. Papaioannou, and T. Lisec (2009), "A correlation of capacitive RF-MEMS reliability to AlN dielectric film spontaneous polarization," *International Journal of Microwave and Wireless Technologies* **1**, 43-47.
- [48] Blondy, P., A. Crunteanu, A. Pothier, P. Tristant, A. Catherinot, and C. Champeaux (2007), "Effects of Atmosphere on the Reliability of RF-MEMS Capacitive Switches," *European Microwave Integrated Circuits Conf.*, pp. 548-551.
- [49] Rottenberg, X., H. Jansen, P. Fiorini, W. De Raedt, and H. Tilmans (2002), "Novel RFMEMS capacitive switching structures," *32nd European Microwave Conf.*, pp. 1-4.
- [50] Luo, J.K., M. Lin, Y.Q. Fu, L. Wang, A.J. Flewitt, S.M. Spearing, N.A. Fleck, and W.I. Milne (2006), "MEMS based digital variable capacitors with a high-k dielectric insulator," *Sensors and Actuators A*, **132**, 139–146.
- [51] Tsauro, J., K. Onodera, T. Kobayashi, Z.-J. Wang, S. Heisig, R. Maeda, and T. Suga (2005), "Broadband MEMS shunt switches using PZT/HfO<sub>2</sub> multi-layered high k dielectrics for high switching isolation," *Sensors and Actuators A*, **121**, 275–281.
- [52] Daigler, R., E. Papandreou, M. Koutsourelis, G. Papaioannou and J. Papapolymerou (2009), "Effect of deposition conditions on charging processes in SiN<sub>x</sub>: Application to RF-MEMS capacitive switches," *J. Microelectron. Eng.* **86**, 404-407.
- [53] Lau, S., J.M. Shannon and B.J. Sealy (1998), "Changes in the Poole–Frenkel coefficient with current induced defect band conductivity of hydrogenated amorphous silicon nitride," *J Non-Cryst Solids* **277-230**, 533–537.
- [54] Shannon, J., S. C. Deane, B. McGarvey, and J. N. Sandoe (1994), "Current induced drift mechanism in amorphous SiN<sub>x</sub>:H thin film diodes," *Appl. Phys. Lett.* **65**, 2978.
- [55] Nieuwesteeg, K., J. Boogaard, G. Oversluizen and M. Powell (1992), "Current stress induced asymmetry in hydrogenated amorphous silicon n i n devices," *J. Appl. Phys.* **71**, 1290-1297.
- [56] Yuan, X., Z. Peng, J. Hwang, D. Forehand and C. Goldsmith (2006), "Acceleration of dielectric charging in RF MEMS capacitive switches," *IEEE Trans. on Dev. and Mat. Reliability* **6**, 556-563.
- [57] Duenas, S., H. Castan, J. Barbolla, R.R. Kola, and P.A. Sullivan (2000), "Electrical characteristics of anodic tantalum pentoxide thin films under thermal stress," *Microelec. Reliab.*, **40**, 659-662.
- [58] Allers, K.-H., P. Brenner, and M. Schrenk (2003), "Dielectric reliability and material properties of Al<sub>2</sub>O<sub>3</sub> in metal insulator metal capacitors (MIMCAP) for RF bipolar technologies in comparison to SiO<sub>2</sub>, SiN and Ta<sub>2</sub>O<sub>5</sub>," *Proc. Bipolar/BiCMOS Circuits and Tech. Meeting*, 35-38.
- [59] Afanas'ev, V.V., and A. Stesmans (2004), "Injection induced charging of HfO<sub>2</sub> insulators on Si," *Materials Science and Engineering B* **109**, 74-77.
- [60] Puzzilli, G., and F. Irrera (2007), "Long time transients in hafnium oxide," *J. Microelectronic Engineering*, **84**, 2394–2397.
- [61] Talbi, F., F. Lalam, and D. Malec (2007), "DC conduction of Al<sub>2</sub>O<sub>3</sub> under high electric field," *J. Phys. D: Appl. Physics*, **40**, 3803–3806.
- [62] Ruffner, J.A., P.G. Clem, B.A. Tuttle, D. Dimos, and D.M. Gonzales (1999), "Effect of substrate composition on the piezoelectric response of reactively sputtered AlN thin films," *Thin Solid Films*, **354**, 256-261.
- [63] Papaioannou, G., and R. Plana, in: M. Mukherjee, Ed. (2010), *Advanced Microwave and Millimeter Wave Technologies Semiconductor Devices Circuits and Systems: "Physics of*

- Charging in Dielectrics and Reliability of Capacitive RF-MEMS Switches*" InTech, Rijeka, Croatia.
- [64] Ruan, J., G. J. Papaioannou, N. Nohier, N. Mauran, M. Bafleur, F. Coccetti and R. Plana (2008), "ESD failure signature in capacitive RF MEMS switches," *J. Microelectron. Reliab.*, **48**, 1237-1240.
- [65] Nieminen, H., J. Hyyrylainen, T. Veijola, T. Ryhanen and V. Ermolov (2005), "Transient capacitance measurement of MEM capacitor," *Sensors and Actuators A* **117**, 267–272.
- [66] Van Spengen, W., P. Czarnecki, R. Poets, J. Van Beek and I. De Wolf (2005), "The influence of the package environment on the functioning and reliability of RF-MEMS switches," *Proc. 2005 IEEE Int. Reliability Physics Symposium*, pp. 337-341, IEEE, New York.
- [67] Exarchos, M., V. Theonas, P. Pons, G.J. Papaioannou, S. Melle, D. Dubuc, F. Cocetti, and R. Plana (2005), "Investigation of charging mechanisms in Metal-Insulator-Metal structures," *J. Microelectronics Reliability*, **45**, 1782–1785.
- [68] Lamhamdi, M., P. Pons, U. Zaghoul, L. Boudou, F. Coccetti, J. Guastavino, Y. Segui, G. Papaioannou and R. Plana (2008), "Voltage and temperature effect on dielectric charging for RF-MEMS capacitive switches reliability investigation," *J. Microelectron. Reliab.* **48**, 1248-1252.
- [69] Papandreou, E., M. Lamhamdi, C. M. Skoulikidou, P. Pons, G. Papaioannou and R. Plana (2007), "Structure dependent charging process in RF MEMS capacitive switches," *J. Microelectron. Reliab.* **47**, 1812-1817.
- [70] Lamhamdi, M., L. Boudou, P. Pons, J. Guastavino, A. Belarni, M. Dilhan, Y. Segui and R. Plana (2007), "Si<sub>3</sub>N<sub>4</sub> thin films properties for RF-MEMS reliability investigation," *Proc. of the International Solid-State Sensors, Actuators and Microsystems Conference (TRANSDUCERS 2007)*, pp. 579-582, IEEE, New York.
- [71] Belarni, A., M. Lamhamdi, P. Pons, L. Boudou, J. Guastavino, Y. Segui, G. Papaioannou and R. Plana (2008), "Kelvin probe microscopy for reliability investigation of RF-MEMS capacitive switches," *J. Microelectron. Reliab.* **48**, 1232-1236.
- [72] Herfst, R., P. Steeneken, J. Schmitz, A. Mank and M. van Gils (2008), "Kelvin probe study of laterally inhomogeneous dielectric charging and charge diffusion in RF MEMS capacitive switches," *2008 IEEE Int. Reliability Physics Symposium Proc. 46th Annual (IRPS 2008)*, pp. 492-495, IEEE, New York.
- [73] Zaghoul, U., A. Abelarni, F. Coccetti, G. Papaioannou, R. Plana and P. Pons (2008), "Charging processes in silicon nitride films for RF-MEMS capacitive switches: The effect of deposition method and film thickness," *Microelectromechanical Systems-Materials and Devices II*, MRS Proc. Vol. 1139, (eds. S. M. Spearing, S. Vengallatore, N. Sheppard and J. Bagdahn), pp. 141-146, Material Research Society (MRS), Pennsylvania.
- [74] Zaghoul, U., A. Belarni, F. Coccetti, G. Papaioannou, L. Bouscayrol, P. Pons and R. Plana (2009), "A comprehensive study for dielectric charging process in silicon nitride films for RF MEMS switches using Kelvin probe microscopy," *2009 Int. Solid-State Sensors, Actuators and Microsystems Conf. (TRANSDUCERS)*, pp. 789-793, IEEE, New York.
- [75] Zaghoul, U., G. Papaioannou, F. Coccetti, P. Pons and R. Plana (2009), "Effect of Humidity on Dielectric Charging Process in Electrostatic Capacitive RF MEMS Switches Based on Kelvin Probe Force Microscopy Surface Potential Measurements,"

- Microelectromechanical Systems-Materials and Devices III*, MRS Proc. Vol. 1222, (eds. J. Bagdahn, N. Sheppard, K. Turner and S. Vengallatore), pp. 39-44, Material Research Society(MRS), Pennsylvania.
- [76] Zaghoul, U., F. Coccetti, G. Papaioannou, P. Pons and R. Plana (2010), "A novel low cost failure analysis technique for dielectric charging phenomenon in electrostatically actuated MEMS devices," *2010 IEEE Int. Reliability Physics Symp.*, pp. 237-245, IEEE, New York.
- [77] Jacobs, H., H. Knapp and A. Stemmer (1999), "Practical aspects of Kelvin probe force microscopy," *Rev. Sci. Instrum.* **70**, 1756-1760.
- [78] Sugimura, H., Y. Ishida, K. Hayashi, O. Takai and N. Nakagiri (2002), "Potential shielding by the surface water layer in Kelvin probe force microscopy," *Appl. Phys. Lett.* **80**, 1459-1461.
- [79] Ono, S., M. Takeuchi and T. Takahashi (2001), "Kelvin probe force microscopy on InAs thin films grown on GaAs giant step structures formed on (110) GaAs vicinal substrates," *Appl. Phys. Lett.* **78**, 1086-1088.
- [80] Tavassolian, N., M. Koutsourelis, E. Papandreou, G. Papaioannou, B. Lacroix, Z. Liu, and J. Papapolymerou (2009), "The effect of silicon nitride stoichiometry on charging mechanisms in RF-MEMS capacitive switches," *IEEE Trans. Microwave Theory Tech.* **57**, 3518 - 3524.
- [81] Herth, E., B. Legrand, L. Buchaillet, N. Rolland, and T. Lasri (2010), "Optimization of SiNX: H films deposited by PECVD for reliability of electronic, microsystems and optical applications," *J. Microelectron. Reliab.* **50**, 1103-1106.
- [82] Koutsourelis, M., N. Tavassolian, G. Papaioannou, and J. Papapolymerou (2011), "Dielectric charging in capacitive microelectromechanical system switches with silicon nitride," *Appl. Phys. Lett.* **98**, Art. # 093505.
- [83] Shea, H. R., A. Gasparyan, H. B. Chan, S. Arney, R. E. Frahm, D. López, S. Jin, and R. P. McConnell (2004), "Effects of electrical leakage currents on MEMS reliability and performance," *IEEE Trans. Device Mater. Reliab.* **4**, 198 - 207.
- [84] Czarnecki, P., X. Rottenberg, P. Soussan, P. Ekkels, P. Muller, P. Nolmans, W. De Raedt, H. Tilmans, R. Puers and L. Marchand (2009), "Effect of substrate charging on the reliability of capacitive RF MEMS switches," *Sens. Actuator A-Phys.* **154**, 261-268.
- [85] Peng, Z., X. Yuan, J. Hwang, D. Forehand and C. Goldsmith (2006), "Top vs. bottom charging of the dielectric in RF MEMS capacitive switches," *Proc. of Asia-Pacific Microw. Conf.*, IEEE, New York.
- [86] Peng, Z., C. Palego, J. Hwang, C. Moody, A. Malczewski, B. Pillans, D. Forehand and C. Goldsmith (2009), "Effect of Packaging on Dielectric Charging in RF MEMS Capacitive Switches," *2009 IEEE MTT-S Int. Microwave Symp. Dig.*, pp. 1637-1640, IEEE, New York.
- [87] Peng, Z., C. Palego, J.C.M Hwang, D.I. Forehand, C.L. Goldsmith, C. Moody et al. (2009), "Impact of humidity on dielectric charging in RF MEMS capacitive switches," *IEEE Microwave and Wireless Components Letters*, **19**, 299-301.
- [88] Bhushan, B. (2010), *Springer Handbook of Nanotechnology*, third edition, Springer-Verlag, Heidelberg, Germany.
- [89] Bhushan, B. (2007), "Nanotribology and nanomechanics of MEMS/NEMS and BioMEMS/BioNEMS materials and devices," *J. Microelectron. Eng.*, **84**, 387-412.

## REFERENCES

---

- [90] Kima, S.H, D. B. Asaya, and M. T. Duggerb (2007), "Nanotribology and MEMS," *Nanotoday*, **2**, 22-29.
- [91] Man, K.F., B.H. Stark, R. Ramesham (1998), "A Resource Handbook for MEMS Reliability," *Rev. A, JPL Press*, Jet Propulsion Laboratory, California Institute of Technology, Pasadena, CA.
- [92] Bhushan, B., and H. Liu (2001), "Nanotribological properties and mechanisms of alkylthiol and biphenyl thiol self-assembled monolayers studied by AFM," *Phys. Rev. B* **63**, 245412.
- [93] Bhushan, B., H. Liu and M. S. Hsu (2004), "Adhesion and friction studies of silicon and hydrophobic and low friction films and investigation of scale effects," *ASME J. Tribol.* **126**, 583-590.
- [94] Liu, H., B. Bhushan (2003), "Nanotribological characterization of molecularly thick lubricant films for applications to MEMS/NEMS by AFM," *Ultramicroscopy* **97**, 321–340.
- [95] Bhushan, B., and C. Dandavate (2000), "Thin-film friction and adhesion studies using atomic force microscopy," *J. Appl. Phys.* **87**, 1201.
- [96] Calleja, M., M. Tello, and R. García (2002), "Size determination of field-induced water menisci in noncontact atomic force microscopy," *J. Appl. Phys.* **92**, 5539-5542.
- [97] Gómez-Monivas, S., J. J. Sáenz, M. Calleja, and R. Garcia (2003), "Field-Induced Formation of Nanometer-Sized Water Bridges," *Phys. Rev. Lett.* **91**, 056101.
- [98] Sacha, G. M., A. Verdaguer, and M. Salmeron (2006), "Induced Water Condensation and Bridge Formation by Electric Fields in Atomic Force Microscopy," *J. Phys. Chem. B*, **110**, 14870-14873.
- [99] Goldsmith, C. L., Z. Yao, S. Eshelman, and D. Denniston, (1998) "Performance of Low-Loss RF MEMS Capacitive Switches," *IEEE Microwave and Guided Wave Letters*, **8**, 269-271.
- [100] Muldavin, J. B. and G. M. Rebeiz (2000) "High-isolation CPW MEMS shunt switches; Part 1: Modeling," *IEEE Transactions on Microwave Theory and Techniques*, **48**, 1045-1052.
- [101] Madou, M. J. (2011), *Fundamentals of Microfabrication and Nanotechnology*, third edition, CRC Press, Boca Raton, Florida.
- [102] Harsh, K.F., et al., Harsh, K. F., W. Zhang, V.M. Bright, and YC Lee, (1999) "Flip-chip assembly for Si-based RF MEMS," *Proc. of the IEEE Int. Conf. on Microelectromech. Sys.*, pp. 273-278. 1999, IEEE.
- [103] Milanovic, V., M. Maharbiz, A. Singh, B. Warneke, N. Zhou, H. K. Chan, and K.S.J. Pister (2000) "Microrelays for batch transfer integration in RF systems," *Proc. of the IEEE 13th Annual Int. Conf. on Microelectromech. Sys.*, pp. 787-792.
- [104] Villeneuve, C., P. Pons, V. Puyal, and R. Plana (2010), "Planarization optimization of RF-MEMS switches with a gold membrane," *J. Micromech. and Microeng.* **20**, Ar. #064013.
- [105] Jacobs, H. O., H. F. Knapp, S. Müller and A. Stemmer (1997), "Surface potential mapping: A qualitative material contrast in SPM," *Ultramicroscopy* **69**, 39-49.
- [106] DeVecchio, D. and B. Bhushan (1998), "Use of a nanoscale Kelvin probe for detecting wear precursors," *Rev. Sci. Instrum.* **69**, 3618-3624.

- [107] Bhushan, B. and A. Goldade (2000), "Measurements and analysis of surface potential change during wear of single-crystal silicon (100) at ultralow loads using Kelvin probe microscopy," *App. Surf. Sci.* **157**, 373-381.
- [108] Liscio, A., V. Palermo, D. Gentilini, F. Nolde, K. Müllen, and P. Samorí (2006), "Quantitative measurement of the local surface potential of p-conjugated nanostructures: a Kelvin Probe Force Microscopy study," *Adv. Funct. Mater.*, **16**, 1407-1416.
- [109] Dianoux, R., F. Martins, F. Marchi, C. Alandi, F. Comin, and J. Chevrier (2003), "Detection of electrostatic forces with an atomic force microscope: Analytical and experimental dynamic force curves in the nonlinear regime," *Phys. Rev. B*, **68**, 045403. .
- [110] Yan, M., and G. H. Bernstein (2006), "Apparent height in tapping mode of electrostatic force microscopy," *Ultramicroscopy*, **106**, 582-586.
- [111] Ziegler, D., N. Naujoks, and A. Stemmer (2008), "Feed-forward compensation of surface potential in atomic force microscopy," *Rev. Sci. Instrum.* **79**, Art. #063704.
- [112] Jacobs, H. O., P. Leuchtmann, O. J. Homan and A. Stemmer (1998), "Resolution and contrast in Kelvin probe force microscopy," *J. Appl. Phys.* **84**, 1168-73. .
- [113] Yokoyama, H., and T. Inoue (1994), "Scanning Maxwell stress microscope for nanometre-scale surface electrostatic imaging of thin films," *Thin Solid Films* **242** 33-39.
- [114] Zaghoul, U., B. Bhushan, G.J. Papaioannou, F. Coccetti, P. Pons, and R. Plana (2011), "Nanotribology-based novel characterization techniques for the dielectric charging failure mechanism in electrostatically actuated NEMS/MEMS devices using force-distance curve measurements," *J. Colloid and Interface Science*, doi:10.1016/j.jcis.2011.08.005 (in press).
- [115] Kohlrausch, R., *Ann. Phys. (Leipzig)* 12:393 (1847); G. Williams and D. C. Watts, *Trans. Faraday Soc.* 66:80 (1970); J. Jackle, *Phil. Mag. B* 56:113, 1987.
- [116] Phillips, J. (1996), "Stretched exponential relaxation in molecular and electronic glasses," *Rep. Prog. Phys.* **59**, 1133-1207.
- [117] Zaghoul, U., B. Bhushan, F. Coccetti, P. Pons, and R. Plana (2011), "Kelvin probe force microscopy-based characterization techniques applied for electrostatic MEMS/NEMS devices and bare dielectric films to investigate the dielectric and substrate charging phenomena," *J. Vac. Sci. Technol. A* **29**, Art.# 051101.
- [118] Gritsenko, V., D. Gritsenko, Yu. Novikov, R. Kwok, and I. Bello (2004), "Short-range order, large-scale potential fluctuations, and photoluminescence in amorphous SiNx", *Journal of Experimental and Theoretical Physics* **98**, 760-769.
- [119] Yoshida, K., I. Umezu, N. Sakamoto, M. Inada, A. Sugimura (2002), "Effect of structure on radiative recombination processes in amorphous silicon suboxide prepared by rf sputtering," *J. of Applied Physics* **92**, 5936.
- [120] Iacona, F., C. Bongiorno, C. Spinella (2004), "Formation and evolution of luminescent Si nanoclusters produced by thermal annealing of SiOx films," *J. of Applied Physics* **95**, 3723.
- [121] Bisquert, J., and G. Garcia-Belmonte (2001), "Analysis of the power-law response in the fractal dielectric model by thermally stimulated currents and frequency spectroscopy," *J. Appl. Phys.* **89**, 5657.
- [122] Gun'koa, V.M., V.I. Zarkoa, E.V. Goncharuka, L.S. Andriykoa, V.V. Turova, Y.M. Nychiporuka, et al (2007), "TSDC spectroscopy of relaxational and interfacial phenomena," *Advances in Colloid and Interface Science*, **131**, 1-89.

## REFERENCES

---

- [123] Zaghoul, U., G. Papaioannou, B. Bhushan, F. Coccetti, P. Pons, and R. Plana (2011), "New insights into reliability of electrostatic capacitive RF MEMS switches," *Int. J. of Microwave and Wireless Technologies*, doi:10.1017/S1759078711000766.
- [124] Simmons, J. G. (1967), "Poole-Frenkel Effect and Schottky Effect in Metal-Insulator-Metal Systems," *Phys. Rev.* **155**, 657-660.
- [125] Zaghoul, U., M. Koutsourelis, H. Wang, F. Coccetti, G. Papaioannou, P. Pons and R. Plana (2010), "Assessment of dielectric charging in electrostatically driven MEMS devices: A comparison of available characterization techniques," *J. Microelectron. Reliab.* **50**, 1615-1620. .
- [126] Jeong, D. S., and C. S. Hwang (2005), "Tunneling current from a metal electrode to many traps in an insulator," *Phys. Rev. B* **71**, Art. #165327.
- [127] Mardivirin, D., D. Bouyge, A. Crunteanu, A. Pothier and P. Blondy (2008), "Study of Residual charging in dielectric less capacitive MEMS switches," *2008 IEEE MTT-S Int. Microwave Symp. Dig.*, pp. 33-36, IEEE, New York.
- [128] Sessler, G.M., (1987), *Electrets*, second edition, Springer topics in applied physics Vol.33, Springer-Verlag, Berlin, Germany.
- [129] Peng, Z., X.B. Yuan, J.C.M. Hwang, D.I. Forehand, and C.L. Goldsmith (2007), "Superposition Model for Dielectric Charging of RF MEMS Capacitive Switches Under Bipolar Control-Voltage Waveforms," *IEEE Trans. Microw. Theory Tech.*, **55**, 2911-2918.
- [130] Peng, Z., X.B. Yuan, J.C.M. Hwang, D.I. Forehand, C.L. Goldsmith (2007), "Dielectric Charging of RF MEMS Capacitive Switches under Bipolar Control-Voltage Waveforms," *IEEE Intl Microwave Symp Dig.*, pp. 1817-1820, IEEE, New York.
- [131] Mardivirin, D., D. Bouyge, A. Crunteanu, A. Pothier and P. Blondy (2008), "Study of Residual charging in dielectric less capacitive MEMS switches," *IEEE MTT-S Int. Microwave Symp. Dig.*, pp. 33-36, IEEE, New York.
- [132] Papaioannou, G., F. Coccetti and R. Plana (2010), "On the Modeling of Dielectric Charging in RF-MEMS Capacitive Switches", *10th topical meeting on silicon monolithic integrated circuits in RF Systems (SIRF)*, New Orleans, pp.108-111.
- [133] Zaghoul, U., G.J. Papaioannou, B. Bhushan, H. Wang , F. Coccetti, P. Pons, and R. Plana (2011), "Effect of deposition gas ratio, RF power and substrate temperature on the charging/discharging processes in PECVD silicon nitride films for electrostatic NEMS/MEMS reliability using atomic force microscopy," *IEEE/ASME J. Microelectromechanical Systems* (in press).
- [134] Zaghoul, U., G. J. Papaioannou, F. Coccetti, P. Pons and R. Plana (2010), "A systematic reliability investigation of the dielectric charging process in electrostatically actuated MEMS based on Kelvin probe force microscopy " *J. Micromech. Microeng.* **20**, Art.# 064016.
- [135] Zaghoul, U., G.J. Papaioannou, H. Wang, B. Bhushan, F. Coccetti, P. Pons, and R. Plana (2011), "Nanoscale characterization of the dielectric charging phenomenon in PECVD silicon nitride thin films with various interfacial structures based on Kelvin probe force microscopy," *Nanotechnology* **22**, Art.# 205708.
- [136] Carrada, M., A. Zerga, M. Amann, J. J. Grob, J. P. Stoquert, A. Slaoui, C. Bonafos, and S. Scham (2008), "Structural and optical properties of high density Si-ncs synthesized in SiNx:H by remote PECVD and annealing ," *Mater. Sci. Eng., B* **147**, 218-221.

- [137] Petersen, M., and Y. Roizin (2006), "Density functional theory study of deep traps in silicon nitride memories," *Appl. Phys. Lett.* **89**, Art. # 053511.
- [138] Vishnyakov, A. V., Yu. N. Novikov, V. A. Gritsenko, and K. A. Nasyrov (2009), "The charge transport mechanism in silicon nitride: Multi-phonon trap ionization," *Solid-State Electron.* **53**, 251-255.
- [139] Cen, Z. H., T. P. Chen, L. Ding, Y. Liu, J. I. Wong, M. Yang, Z. Liu, W. P. Goh, Z. H. F. R. Zhu, and S. Fung (2009), "Evolution of electroluminescence from multiple Si-implanted silicon nitride films with thermal annealing," *J. Appl. Phys.* **105**, Art. # 123101.
- [140] Ackaerta, J., R. Charavela, K. Dhondta, B. Vlachakisa, L. De Scheppera, M. Millecama, et al. (2008) "MIMC reliability and electrical behavior defined by a physical layer property of the dielectric," *J. Microelectron. Reliab.* **48**, 1553-1556.
- [141] Thornton, J. A. (1977), "High rate thick film growth," *Ann. Rev. Mater. Sci.*, **7**, 239-260.
- [142] Bhushan, B., and B. K. Gupta (1991), *Handbook of Tribology: Materials, Coatings, and Surface Treatments*, McGraw-Hill, New York.
- [143] Zaghloul, U., B. Bhushan, P. Pons, G.J. Papaioannou, F. Coccetti, and R. Plana (2011), "Nanoscale characterization of different stiction mechanisms in electrostatically driven MEMS devices based on adhesion and friction measurements," *J. Colloid and Interface Science* **358**, 1-13. .
- [144] Mesquida, P. (2002), "Charge Writing with an Atomic Force Microscope Tip and Electrostatic Attachment of Colloidal Particles to the Charge Patterns", Doctor of Technical Sciences, ETH, Zurich, Swizerland.
- [145] Bluhm, H., T. Inoue and M. Salmeron (2000), "Formation of dipole-oriented water films on mica substrates at ambient conditions," *Surf. Sci.* **462**, L599-L602.
- [146] Ohara, K. and Y. Cho (2004), "Effect of the surface adsorbed water on the studying of ferroelectrics by scanning nonlinear dielectric microscopy," *J. Appl. Phys.* **96**, 7460-7463.
- [147] Zaghloul, U., G.J. Papaioannou, B. Bhushan, F. Coccetti, P. Pons, and R. Plana (2011), "On the reliability of electrostatic NEMS/MEMS devices: Review of present knowledge on the dielectric charging and stiction failure mechanisms and novel characterization methodologies," *Microelectron. Reliab.* **51**, 1810-1818.
- [148] Strong, F., J. Skinner and N. Tien (2008), "Electrical discharge across micrometer-scale gaps for planar MEMS structures in air at atmospheric pressure," *J. Micromech. Microeng.* **18**, Art.# 075025.
- [149] Dhariwal, R., J. Torres and M. Desmulliez (2000), "Electric field breakdown at micrometre separations in air and nitrogen at atmospheric pressure," *IEE Proceedings-Science, Measurement and Technology* **147**, pp. 261-265.
- [150] Bhushan, B. and S. Sundararajan (1998), "Micro/nanoscale friction and wear mechanisms of thin films using atomic force and friction force microscopy," *Acta Mater.* **46**, 3793-3804.
- [151] Liu, H. and B. Bhushan (2003), "Adhesion and friction studies of microelectromechanical systems/nanoelectromechanical systems materials using a novel microtriboapparatus," *J. Vac. Sci. Technol.* **21**, 1528-1538.
- [152] Bhushan, B. (2002), *Introduction to Tribology*, Wiley, New York.
- [153] Jacob, D. J. (1999), *Introduction to Atmospheric Chemistry*, Princeton University Press, New Jersey.

## REFERENCES

---

- [154] <http://www.chromres.com>.
- [155] Bhushan, B., H. Lee, S. C. Chaparala and V. Bhatia (2010), "Nanolubrication of sliding components in adaptive optics used in microprojectors," *Applied Surface Science*, **256** 7545–7558.
- [156] Tang, W., B. Bhushan and S. Ge (2010), "Friction, adhesion and durability and influence of humidity on adhesion and surface charging of skin and various skin creams using atomic force microscopy," *Journal of Microscopy*, **239**, 99–116.
- [157] Palacio, M. and Bhushan, B. (2010), "Normal and Lateral Force Calibration Techniques for AFM Cantilevers," (*invited*) *Crit. Rev. Solid State and Mater. Sci.* **35**, 73-104.
- [158] Yumei, M., X. Zhang, W. Wang (2009), "Capillary liquid bridges in atomic force microscopy: Formation, rupture, and hysteresis," *J. Chem. Phys.* **131**, 184702.
- [159] Zaghoul, U., B. Bhushan, P. Pons, G. Papaioannou, F. Coccetti and R. Plana (2011), "On the Influence of Environment Gases, Relative Humidity and Gas Purification on Dielectric Charging/Discharging processes in Electrostatically Driven MEMS/NEMS Devices," *Nanotechnology* **22**, Art.# 035705.
- [160] Xie, X. N., H. J. Chung, D. M. Tong, C. H. Sow, and A. T. S. Wee (2007), " Field-induced meniscus dynamics and its impact on the nanoscale tip-surface interface," *J. Appl. Phys.* **102**, 084313.
- [161] Yokoyama, H., T. Inoue, and J. Itoh (1994), "Nonresonant detection of electric force gradients by dynamic force microscopy," *Appl. Phys. Lett.* **65**, 3143.
- [162] Belaidi, S., P. Girard, and G. Leveque (1997), "Electrostatic forces acting on the tip in atomic force microscopy: Modelization and comparison with analytic expressions," *J. Appl. Phys.* **81**, 1023.
- [163] <http://www.amicom.info>.

*Experience is not what happens to a man. It is what a man does with what happens to him.*

*Aldous Leonard Huxley  
1894 – 1963, English critic and novelist  
in “Texts and Pretexts”*

## **Nomenclature**

AFM	<u>A</u> tom <u>i</u> c <u>f</u> orce <u>m</u> icroscope
C/DCT	<u>C</u> harge/ <u>d</u> ischarge <u>c</u> urrent <u>t</u> ransients
CPW	<u>C</u> oplanar <u>w</u> ave guide
DCT	<u>D</u> ischarge <u>c</u> urrent <u>t</u> ransients
ECD Au	<u>E</u> lectrochemically- <u>d</u> eposited gold
Evap Au	<u>E</u> vaporated gold
Evap Ti	<u>E</u> vaporated titanium
FA	<u>F</u> ailure <u>a</u> nalysis
FDC	<u>F</u> orce- <u>d</u> istance <u>c</u> urve
FDC-MEMS	<u>F</u> orce- <u>d</u> istance <u>c</u> urve applied to study charging in <u>m</u> icro- <u>e</u> lectrom <u>e</u> chanical systems
FDC-MIM	<u>F</u> orce- <u>d</u> istance <u>c</u> urve applied to study charging in <u>m</u> etal- <u>i</u> nsulator- <u>m</u> etal capacitors
FDC-TF	<u>F</u> orce- <u>d</u> istance <u>c</u> urve applied to study charging in bare dielectric <u>t</u> hin <u>f</u> ilms
FMEA	<u>F</u> ailure <u>m</u> ode and <u>e</u> ffects <u>a</u> nalysis

FT-IR	<u>F</u> ourier <u>t</u> ransform <u>i</u> nfra- <u>r</u> ed spectroscopy
FWHM	<u>F</u> ull <u>w</u> idth at <u>h</u> alf <u>m</u> aximum
HF	<u>H</u> igh <u>f</u> requency PECVD deposition recipe
HF Evap Au	<u>H</u> igh <u>f</u> requency SiN <sub>x</sub> deposited over <u>e</u> vap <u>o</u> rated gold
HF Si	<u>H</u> igh <u>f</u> requency SiN <sub>x</sub> deposited directly over silicon substrate
HF SiN <sub>x</sub>	SiN <sub>x</sub> films deposited using the <u>h</u> igh <u>f</u> requency PECVD deposition recipe
KPFM	<u>K</u> elvin <u>p</u> robe <u>f</u> orce <u>m</u> icroscopy
KPFM-MEMS	<u>K</u> elvin <u>p</u> robe <u>f</u> orce <u>m</u> icroscopy applied to study charging in <u>m</u> icro- <u>e</u> lectro <u>m</u> echanical <u>s</u> ystems
KPFM-MIM	<u>K</u> elvin <u>p</u> robe <u>f</u> orce <u>m</u> icroscopy applied to study charging in <u>m</u> etal- <u>i</u> nsulator- <u>m</u> etal capacitors
KPFM-TF	<u>K</u> elvin <u>p</u> robe <u>f</u> orce <u>m</u> icroscopy applied to study charging in bare dielectric <u>t</u> hin <u>f</u> ilms
LF	<u>L</u> ow <u>f</u> requency PECVD deposition recipe
LF Evap Au	<u>L</u> ow <u>f</u> requency SiN <sub>x</sub> deposited over <u>e</u> vap <u>o</u> rated Au
LF Si	<u>L</u> ow <u>f</u> requency SiN <sub>x</sub> deposited directly over silicon substrate
LF SiN <sub>x</sub>	SiN <sub>x</sub> films deposited using the <u>l</u> ow <u>f</u> requency PECVD deposition recipe
LO mode	<u>L</u> ongitudinal <u>o</u> ptical mode
MEMS	<u>M</u> icro- <u>e</u> lectro <u>m</u> echanical <u>s</u> ystems
MIM	<u>M</u> etal- <u>i</u> nsulator- <u>m</u> etal
MWS	<u>M</u> axwell- <u>W</u> agner- <u>S</u> illars
NEMS	<u>N</u> ano- <u>e</u> lectro <u>m</u> echanical <u>s</u> ystems
PECVD	<u>P</u> lasma- <u>e</u> nhanced <u>c</u> hemical <u>v</u> apor <u>d</u> eposition
PF	<u>P</u> oole- <u>F</u> renkel

## NOMENCLATURE

---

RF	<u>R</u> adio <u>f</u> requency
RH	<u>R</u> elative <u>h</u> umidity
SCM-PIT	<u>S</u> canning <u>c</u> apacitance <u>m</u> icroscopy- <u>p</u> latinum <u>i</u> ridium <u>t</u> apping
TAT	<u>T</u> rap <u>a</u> ssisted <u>t</u> unneling
TF	<u>T</u> hin <u>f</u> ilms
TO mode	<u>T</u> ransverse <u>o</u> ptical mode
TSDC	<u>T</u> hermally <u>s</u> timulated <u>d</u> epolarization <u>c</u> urrent
XPS	<u>X</u> -ray photoelectron <u>s</u> pectroscopy

*I am always doing that which I cannot do, in order that I may learn how to do it.*

*Pablo Picasso  
1881 – 1973, Spanish Artist and Painter*

### **Biography**

Usama Zaghoul Heiba received the B.Sc. degree in electrical engineering from the Faculty of Electronics Engineering, Menoufia University, in 2002, and the M.Sc. degree in electrical engineering from the Faculty of Engineering, AinShams University, Cairo, Egypt, in 2006. In January 2008, he joined the Laboratoire d'Analyse et d'Architecture des Systèmes (LAAS) - the Centre National de la Recherche Scientifique (CNRS), and the Université de Toulouse, France, where he is currently working towards the Ph.D. degree in micro- and nanosystems, jointly with the Nanoprobe Laboratory for Bio- and Nanotechnology and Biomimetics (NLBB), The Ohio State University, Columbus, Ohio, USA. During his Ph.D. studies, he invented several nanoscale and macroscale characterization techniques based on different scanning probe microscopy measurements to study the dielectric charging and stiction failure mechanisms in electrostatic MEMS/NEMS devices. Moreover, he designed and developed the micro-fabrication process of two packaging schemes for RF MEMS devices.

Before starting the Ph.D, Usama was with the Electronics Research Institute (ERI) in Cairo, where he joined the Microelectronics Department as a Research Assistant in 2003. While at ERI, he was involved in the design and fabrication of tunable RF MEMS inductors and capacitors for reconfigurable wireless systems. From September 2004 to June 2005, he was a full time student at the Information Technology Institute (ITI) in Cairo, where he received a diploma in VLSI circuit design and CAD tools development. Starting from June 2005, he had an internship for seven months at the MEMS and Microsensors Laboratory, CEERI, Pilani, India, where he was involved in the micro-fabrication process development of several MEMS-based pressure and acoustic sensors. From June 2006 to December 2007, he was with SoftMEMS as a MEMS Physical Design Engineer. His research interests include design, modeling, fabrication, packaging, and reliability of MEMS/NEMS devices.